# Medium Range Structure and Structural Changes of Glass and Liquid $Ge_xSe_{1-x}$ Investigated by Raman Spectra

(ラマン分光によるガラス、液体 $Ge_xSe_{1-x}$ の
中距離構造および構造変化の研究)

by

Yong WANG　王勇

Dissertation in Physics

The Osaka University
Graduate School of Science

January, 1997

# Contents

# List of Figures

# List of Tables

# Acknowledgments

I would like to express my sincere thanks to Prof. Kazuo Murase for giving me the opportunity to promote this interesting work, and for his warm encouragement, helpful guidance and enlightening discussions. I am so much grateful to Prof. Sadao Takaoka for his continuous encouragement and advice. My special thanks are due to Dr. Osamu Matsuda for his instruction, technical support, fruitful ideas and inspired discussions. I am indebted to Dr. Kenichi Oto for his valuable suggestions and discussions.

My thanks are also extended to Prof. Koichi Inoue, Prof. Satoshi Hashimoto and Dr. Norimasa Umesaki for their very kind suggestions, technical support and fruitful ideas.

I am very grateful to Mr. Mitsutaka Nakamura, Mr. Yoshiki Wada, Mr. Yuichi Saito for their help in preparing the specimens and Raman measurement. It is a pleasure to thank all the members of the Murase group for their friendly encouragement and stimulating discussions.

I am very grateful to the Ikenaka Foreign Student Scholarship and 99 Asian Student Scholarship Foundation for their five-years financial support.

# Abstract

Structures of chalcogenide glass, super cooled liquid and liquid ( SCL ), as well as phase-transitions among them, have been intensively investigated by Raman spectra in the microscopic and/or mesoscopic point of view. Chalcogenide glasses $Ge_xSe_{1-x}$ which are the typical network glasses can be easily prepared. By changing the Ge composition, the structural dimensionality can be varied and by using different preparation methods, the *variety* of medium-range structure can be realized.

In the first part, the structure and thermal structural changes in $Ge_xSe_{1-x}$ which include the glass-transition, re-crystallization and melting are investigated by measuring the Raman spectra in a sequence of increasing temperature from 20 °C to 850 °C. Different temperature dependencies of the Raman spectra are demonstrated for the samples with different Ge compositions from $x = 0$ to 0.33.

In Se glass and Ge-poor $Ge_xSe_{1-x}$ ( $x \leq 0.07$ ) glasses, it has been found that the dominant structure is $(Se)_n$ chains where the glassy state involves parallel Se–Se chain regions and non-parallel chain regions. The decrease of viscosity above the glass-transition temperature $T_g$ causes large configurational fluctuations in the parallel region of $(Se)_n$ chains to broaden the corresponding vibrational Raman band at 235 $cm^{-1}$. In the $Ge_xSe_{1-x}$ ( $0.10 \leq x \leq 0.20$ ), the Raman intensity ratio $I_{GeSe4/2}/I_{Se}$ increases with increasing temperature above the $T_g$, probably because the leading structural units become $GeSe_{4/2}$ tetrahedra which easily move and coalesce with each other to form the crystalline embryo in the SCL state. In $Ge_xSe_{1-x}$ ( $x = 0.10, 0.15$ ), where no crystalline spectra has been observed, the crystalline $GeSe_2$ like crystalline embryo is found to fade away fairly below the melting point.

The typical medium-range structure in the glassy and liquid $GeSe_2$ is considered as a topologically crystalline layer-like fragment. In the glassy state, the lone pair Se–Se interactions between the two successively quasi-stacked fragments somewhat restrains the Raman intensity of the $A_1^C$ band which relates to the edge-sharing $GeSe_{4/2}$ tetra-

hedra. The fact that with increasing temperature the intensity ratio of the $A_1^C$ band to the $A_1$ band increases quickly from 1:3 to 1:1 in the super-cooled liquid is related to a drastic decrease of the interaction between the layer-like fragments. The onset of the increase is considered to be at the glass-transition temperature.

In the Ge composition region of $0.04 < x < 0.18$, neither the crystalline Se nor the $GeSe_2$ has been observed in the experimental time periods up to 10 hours owing to the long relaxation time for their crystallization. With the Ge composition increasing above 0.04, the population of $GeSe_{4/2}$ tetrahedra, whose structure is rather stable than the $(Se)_n$ chains at the experimental temperature, is large enough to easily prevent the $(Se)_n$ chains from crystallization owing to chain crossing. It should be noted that the relaxation time for the crystallization of $GeSe_2$ showing an essential change at $x = 0.18$ ( average coordination number $\langle r \rangle = 2.37$ ) which is very close to the rigidity percolation threshold value $x = 0.2$ ( $\langle r \rangle = 2.4$ ) basing on the Phillips–Thorpe constraint theory.

In the second part, to obtain the information of the structural variety occurred in the preparation, the photo-induced crystallization ( PIC ) processes are investigated by analyzing the time-resolved Raman spectra. In the PIC processes, the structural changes of the illuminated portion are cooperatively promoted by the photons and phonons from the initial various structures. The fact that the threshold temperature for the PIC process is lower in the sample with a slower cooling rate is reasonable to be considered that its medium-range structure is more similar to the crystalline nuclei, or easier to transform into crystalline nuclei than those samples with faster cooling rates.

In the last part, toward the understanding of the relaxation processes of excited electrons, the photoluminescence spectra of both the crystalline and glassy $GeSe_2$ have been studied in the temperature range from 10 K to 250 K with the excitation photon energies of 1.93~2.81 eV. In the glass, a new result that with increasing temperature the spectral widths first decrease in the low temperature region and then increase in the high region, is qualitatively interpreted basing on a configurational coordinate energy diagram model.

# Chapter 1

# Introduction

Science of glass, super-cooled liquid ( SCL ), crystal and liquid, and transitions among them, involves a wide range of attractive subjects in the condensed matter physics. Theoretical considerations relate glass-forming tendencies and the global profile of glassy structures to the average coordination number $\langle r \rangle$. Phillips first proposed that glass formation is easiest when the coordination number $\langle r \rangle = 2.4$ [1]. Later Thorpe suggested that the rigidity percolation threshold value is located at the coordination number near $\langle r \rangle = 2.4$ in the covalent network glass in the meanfield consideration [2]. The character of a covalent network undergoes a qualitative change from being partially deformable $\langle r \rangle < 2.4$ to being rigid at $\langle r \rangle = 2.4$. The critical behavior has been investigated in many situations in the glass system [3-11].

Angell classified the super-cooled liquid behavior during cooling between *strong* and *fragile* [12-15], and indicated that the canonical characteristics of relaxing liquids are correlated through the fragility. It has been found that at $\langle r \rangle = 2.4$ in glass-forming liquid the *fragility* which is introduced from a $T_g$-scaled Arrhenius plot for the viscosity is minimum [10].

From the vibrational dynamics of glasses in the low-energy frequency range from 5 to 100 $cm^{-1}$, the cooperative motions of atoms over correlation lengths in the nanometer range ( a kind of the medium-range ) is reflected [16-22]. An apparent correspondence among the *boson peak*, the excess of heat capacity and the plateau of thermal conductivity in low temperature has been shown. The Debye model fails to interpret the behavior of vibrational density of states ( VDOS ) in this low-energy regime which means that VDOS corresponds more closely to a fractal or disordered system than to an averaged continuum. A strong relation between the vibrational dynamics and the fragility has

been confirmed in several experiments.

Chalcogenide glasses which contain chalcogen elements ( S, Se, and Te ) and usually elements of group IV and/or V ( Si, Ge, P, As, etc. ) can be easily prepared. The coordination numbers of chalcogen atoms are usually *2* and those of group IV and/or V are *4* and/or *3*, respectively. With varying the compositions, the average coordination number $\langle r \rangle$ can be changed from *2* to *4* basing on the glass–forming region of each chalcogenide glass. In the chalcogenide network glass, Raman and Mössbauer experiments confirmed that the topologically ordered cluster-network model, which allows a partial break of the chemical order, is more suitable than the chemically ordered continuous-random-network model. In the structure factor of x-ray and neutron diffractions, the first sharp diffraction peak is observed which may be related to a corresponding medium-range structure. In chalcogenide glasses, the photoluminescence spectra usually show a large Stokes-shift which suggests the existence of strong electron-phonon interactions. These covalent glasses exhibit a number of photo-induced structural changes [23-36] due to their peculiar structures. Understanding the mechanism of these photo-induced effects will also advance applications in a lot of fields. For example, the photo-induced doping phenomenon [23-25] relates to finding suitable resist-materials which are used in making fine structure with micron or sub-micron size, and the photo-induced amorphization [26] and crystallization [27] phenomena relate to the application of optical recorder media.

The characteristic chalcogenide semiconductor, $Ge_xSe_{1-x}$, can be easily prepared in glassy form over a wide range of the composition $x$ ( $0 \sim 0.42$ ) by quenching melts [38]. In this glass system, the coordination number $\langle r \rangle$ can be arranged from 2 to 2.84 which covers the rigidity percolation threshold $\langle r \rangle = 2.4$ at $x = 0.2$. Though the structures and the structural changes in $Ge_xSe_{1-x}$ have been studied by numerous techniques, the details have not been clarified yet. By studying the Raman spectra which involves the information not only of the short-range structure but also of the medium-range structure, the structural changes between the glassy and SCL forms, or the SCL and crystalline forms will be clarified as a function of temperature. Furthermore according to the Raman spectra and spectral changes in the phase transitions, the structural models can be practically constructed.

For clarifying the structure and structural changes in $Ge_xSe_{1-x}$ we proceeded to this work with following three ways.

In the first part of this work ( chapter 4, 5 ), we report the structures and structural changes in $Ge_xSe_{1-x}$ ( $0 \leq x \leq 0.33$ ) in a sequence of increasing temperatures from

20 °C to 850 °C by Raman scattering. The Raman spectra shows drastic changes when the structures change at some characteristic temperatures such as the glass-transition temperature $T_g$, the re-crystallization temperature $T_c$ and the melting point $T_m$. Our results will be very advantageous not only for a general understanding of the structural relation and transformations among glassy, crystalline, and liquid phases on micro– and mesoscopic view points but also for the investigation of the photo-induced crystallization ( PIC ) process.

In the second part ( chapter 6 ), we report the PIC process in glassy $GeSe_2$ thin films ( $\sim 1\mu$m ) which are prepared in different cooling rates by quenching in ice water or in air. Basing on the crystallizability from glasses in different preparations, structural differences in micro– and/or mesoscopic scales in the glasses have been clarified. Our results suggest that the PIC measurement is very useful to interpret the glass structure.

In the last part ( chapter 7, 8 ), the relaxation processes of the excited states in glassy and crystalline $GeSe_2$ are studied by photoluminescence measurements in a temperature range of 10~250 K with varying excitation energy from 1.93 eV to 2.81 eV. Both in glassy and crystalline $GeSe_2$, the relaxation processes of the excited electrons are interpreted by using configuration coordinate energy diagrams.

Before we go to discuss the results of the three parts, it is necessary to take a view ( chapter 2 ) of historical backgrounds about the structures in glassy and crystalline $Ge_xSe_{1-x}$, the PIC process in amorphous $GeSe_2$ films and a general understanding of relaxation processes of excited states in glassy and crystalline $GeSe_2$. And in chapter 3, the experimental procedures are described.

# Chapter 2

# Historical Backgrounds

In this chapter we review various aspects of the glassy state, in particular, its medium-range structure and the transition between the glass and super-cooled liquid states. The necessary knowledge to proceed to this work, such as the understanding of vibrational and electronic properties for $Ge_xSe_{1-x}$ and the photo-induced crystallization process in amorphous $GeSe_2$ film is also introduced.

## 2.1 General Aspects of Glasses

Glasses have the properties of liquids in terms of their lack of the long-range ordered structure and the properties of solids in terms of atomic movements. Though glasses are widely used in various fields, a clear picture of glasses has not been given.

An important beginning towards understanding glasses at a basic level was made in 1979 when Phillips laid a foundation of a constraint theory. He asserted that for covalently bonded networks, a mechanical critical point occurs when the number of constraints per atom $n_c$ equals the degree of freedom $n_d$ of the network, i.e.,

$$n_c = n_d. \tag{2.1}$$

The idea was cast in the language of a percolation theory by Thorpe who recognized that the Phillips optimum glass forming condition ( equation 2.1 ) represents a rigidity percolation threshold in a meanfield sense. For a 3-dimensional system, the glass forming condition or the percolation threshold value can be expressed by the average coordination number $\langle r \rangle = 2.4$. The character of a covalent network undergoes a qualitative from being partially deformable at $\langle r \rangle < 2.4$ to being stiff at $\langle r \rangle = 2.4$.

Direct evidence for a qualitative change of vibrational density of states ( VDOS ) at $\langle r \rangle = 2.4$ in $Ge_xAs_ySe_{1-x-y}$ glasses has emerged from the inelastic neutron scattering measurements [3]. The average coordination number $\langle r \rangle$ is obtained by

$$\langle r \rangle = r_{Ge} \times x + r_{As} \times y + r_{Se} \times (1 - x - y), \tag{2.2}$$

where the $r_{Ge}(= 4)$, $r_{As}(= 3)$, $r_{Se}(= 2)$ are the coordination numbers of Ge, AS and Se atoms, respectively. Figure 2.1, taken from Ref. [3], shows the VDOS as a function of $\langle r \rangle$. The prominent band peaked at about 5 meV in g–Se ( $\langle r \rangle = 2.0$ ) is related to the floppy vibrational modes which has $\langle r \rangle$ dependencies in the $\langle r \rangle < 2.4$ system. These floppy modes vanish when $\langle r \rangle = 2.4$ where the rigidity percolation occurs. Lamb-Mössbauer $f$-factors, Mössbauer site intensity ratios [4,5], molar volumes [6] and Raman $A_1$ mode frequencies in glassy $Ge_xSe_{1-x}$ [7] and infrared $F_2$ mode spectra in Ge–Se–Sn system [8,9], all provide persuasive evidence for the rigidity percolation threshold to occur near $\langle r \rangle = 2.4$ at $x = 0.2$.

Angell classified the super-cooled liquid behavior of glass-formers during cooling between *strong* and *fragile*, depending on the departure from the Arrhenius behavior of the average of the relaxation time, $\tau$, [13-15]. The fragility, $m$, was defined by the slope of the curve $\log \tau = f(T_g/T)$ at $T=T_g$, where $T_g$ is the glass transition temperature. It was indicated that the canonical characteristics of relaxing liquids are correlated through the fragility. The relaxation time $\tau$ usually can be expressed by the viscosity $\eta$. Figure 2.2, taken from Ref. [14], shows the $\log \eta \sim T_g/T$ plot of various glass formers. The $T_g$s are the calorimetric glass transition temperatures. A schematic representation of the potential energy versus the configuration space variable for glass formers has been introduced to explain the strong and fragile behaviors as shown in Fig. 2.3 taken from Ref. [15]. Thermodynamically fragile system exhibits substantial changes of the local structure corresponding to a much high density of minima on the hypersurface as indicated in Fig. 2.3 ( parts (b) and (d) ).

In Ref. [20] a strong indication has been shown that the excess heat capacity and thermal conductivity plateau at low temperature ( $\sim$ 1 K ), the excess Raman scattering or boson peak have the same origin which is related to the phonon localization. All the related localization sizes, of cohesive domains in a non-continuous network, are in common. It has been found that the glass network is more continuous ( or the localization size is smaller ) for fragile than for strong glass-formers. Basing on the behaviors of thermal conductivity plateau at low temperature, which is due to the tunneling sys-

tems ( TS ), it was indicated that in glasses obtained from fragile liquids, the high TS concentration is a consequence of rapid quenching, for avoiding the crystallization [20].

The excess heat capacity $\Delta C_p$ measured at $T_g$ implies a magnitude for the structural degradation corresponding to the fragility. In Ge–Se–As glasses, the minimum of the heat capacity $\Delta C_p$ at the average coordination number $\langle r \rangle = 2.4$ is correlated with a minimum fragility [10]. Figure 2.4, taken from [10], shows the plots of activation energies for viscosity, enthalpy and $\Delta C_p$ in Ge–Se–As glasses versus $\langle r \rangle$. In each case at $\langle r \rangle = 2.4$, all the characters reach their minima. In this system on a semiquantitative level, the strong–to–fragile ( variably non–Arrhenius ) transport behavior shows strong relations to rigidity percolation described by the varying of $\langle r \rangle$.

## 2.2 Vibrational and Electronic Properties of $Ge_xSe_{1-x}$

### 2.2.1 Vibrational Spectra in Crystalline and Glassy $GeSe_2$

#### The Atomic Arrangements in Crystalline $GeSe_2$

In the crystalline $GeSe_2$ there are two polymorphic modifications which are high-temperature form HT–$GeSe_2$ and low-temperature form LT–$GeSe_2$. In both of these two modifications, the basic structural unit is a $GeSe_{4/2}$ tetrahedron. The HT-$GeSe_2$ is a layer-formed crystal ( two dimensional, 2D ) [48-50]. Figure 2.5 shows the atomic arrangement in a mono-layer of HT–$GeSe_2$, where the tetrahedra are connected by sharing the corner or by sharing the edge [51]. The LT-$GeSe_2$ is considered to have a similar structure to the LT-$GeS_2$ structure from the resemblance between their Raman spectra [33], as shown in Fig. 2.6, but a full X–ray analysis of the structure has not been done yet. Figure 2.7 illustrates the schematic network connection in LT-$GeS_2$ [52]. In LT-$GeS_2$, the unit cell contains four corner-sharing tetrahedral chains: two, ( –1–7–1–7– ) and ( –3–9–3–9– ), are along [001], and the other two, ( –2–4–2–4– ) and ( –8–10–8–10– ), are along the [101]. The chains are connected by corner-sharing tetrahedra, 5, 6, 11, and 12, in a three-dimensional structure ( 3D ). The essential difference between the two modifications is that the high-temperature form includes edge-sharing connections, while the low-temperature form is composed of corner-sharing tetrahedra only. The HT-$GeSe_2$ can be prepared more easily than the LT-$GeSe_2$ and in the PIC processes

Table 2.1: Band gap values of c–$GeSe_2$.( From Ref. [54] )

| T ( K ) | $E_g$ ( eV ) | |
|---|---|---|
| | $E \parallel a$ | $E \parallel b$ |
| 300 | 2.50 | 2.49 |
| 77 | 2.675 | 2.685 |
| 4.2 | 2.725 | 2.735 |

the photo-induced crystals are almost in high-temperature form Refs. [32,33]. In this paper, we use the word "crystal" or c–$GeSe_2$ to represent the layer-formed crystalline $GeSe_2$ for simplicity, except described otherwise.

### Optical Properties in Crystalline and Glassy $GeSe_2$

In c–$GeSe_2$, a strongly anisotropic optical properties has been reported [53] where the transmittance of the visible light propagating normal to the (001) surface of single crystal has been measured. In the absorption spectra which are measured with the light polarized parallel to the $a$ axis ( $E \parallel a$, curve 1 in Fig. 2.8 ) at 4.2K, they found an exciton absorption peak at 2.854 eV. But in the $E \parallel b$ spectrum ( curve 2 ) such exciton absorption peak is not observed. The exciton absorption peak energy decreases with increasing temperature as shown in Fig. 2.9. At room temperature, the exciton transition energy is about 2.7 eV. Table 2.1 shows the temperature dependence of the band gap values which are obtained from the absorption spectra with $\alpha^2 \sim h\nu$ plot [54]. The absorption spectra of the $Ge_xSe_{1-x}$ ( $0 \leq x \leq 0.33$ ) glasses, crystalline Se and c–$GeSe_2$ reported in Ref. [55] are shown in Fig. 2.10. In Refs. [57] and [58] the dielectric functions of g–$GeSe_2$ have been measured and found that the electronic structure of g–$GeSe_2$ is very similar to that of layer-formed crystalline $GeSe_2$.

### Medium-Range Structure in Glassy and Liquid $GeSe_2$

In g–$GeSe_2$ a medium-range structure ( MRS ) has been strongly impressed with the neutron and X-ray scattering experiments [59-62]. In the diffraction studies, from the first sharp diffraction peak ( FSDP ) in the structure factor $S(k)$, the MRS can be proposed. Figure 2.11 shows $S(k)$ of neutron scattering in amorphous $GeSe_2$ [62]. The FSDP appears at 1.01 $\mathring{A}^{-1}$ relating to a correlation length of about 6.22 $\mathring{A}$. This FSDP

which relates to the MRS is also preserved in liquid. However, the atomic arrangement of the g–$GeSe_2$ has not been declared.

From the investigation of the Raman spectra where the vibrational properties are contained, the manner of the atomic connections can be obtained to improve the understanding of the MRS. Figure 2.12 shows the Raman spectra for the parallel ( H,H ) and perpendicular ( H,V ) polarization in the backscattering configuration in the g–$GeSe_2$ at 50 K [36]. The vibration band with the peak energy at 203 $cm^{-1}$ is related to the symmetric breathing motions of chalcogen atoms at $GeSe_{4/2}$ tetrahedra. This vibrational band is named $A_1$ band. The low-energy side band at 180 $cm^{-1}$ is due to the vibrational mode at Ge–Ge bond, called as a wrong bond for the broken chemical order, in the ethane like cluster. As the chemical order is broken in the stoichiometic glass, $GeSe_2$, the chalcogen–chalcogen vibrational modes also appear. The peaks at 247 $cm^{-1}$ and 145 $cm^{-1}$ have been identified as the Se–Se stretching mode ( CS ) and bending mode ( CB ), respectively. The higher energy side band at 220 $cm^{-1}$ of the $A_1$ peak is called the companion $A_1$ line ( $A_1^C$ ). These results suggest that the basic structural units in g–$GeSe_2$ are the $GeSe_{4/2}$ tetrahedra. Beside the $GeSe_{4/2}$ tetrahedra, there are appreciable amount of Se–Se and Ge–Ge wrong bonds.

To study how the $GeSe_{4/2}$ tetrahedra connect in the MRS and what structures relate to the $A_1$ and $A_1^C$ modes, it is useful to get information from the investigation of the Raman spectra in c–$GeSe_2$. Figure 2.13(b)$\sim$(e) are the Raman spectra of c–$GeSe_2$ which were measured at two polarization configurations, $c(a,a)\bar{c}$ and $c(b,b)\bar{c}$, by using two excitation energies [63-67]. Only one intense peak, labeled $A$, was observed at 211 $cm^{-1}$ using 514.5 nm excitation. It should be mentioned that the 211 $cm^{-1}$ peak has an asymmetric tail on the high-energy side [68]. As there is a weak side peak at 217 $cm^{-1}$ in the highly-resolved spectra in the low temperature measurement [69], the asymmetric tail has been considered to be related to the weak peak at 217 $cm^{-1}$( $A^*$ ) at low temperature. A resonant Raman effect, where $A$ and $A^*$ intensities change depending on the excitation energy, especially in the $c(a,a)\bar{c}$ polarization configuration has been reported in Ref. [51]. For example, the $A^*$ peak increases remarkable with 457.9 nm ( 2.71 eV ) excitation in the $c(a,a)\bar{c}$ configuration, as shown in Fig. 2.13(b). Figure 2.14 shows the excitation energy dependence of the intensity ratio $A^*$:$A$. In the $c(a,a)\bar{c}$ configuration, the ratio shows a strong peak at about 2.7 eV, where a bulk exciton transition was observed in the $E \parallel a$ absorption spectrum. On the other hand, there is no notable structure in the ratio of the $c(b,b)\bar{c}$ configuration [65] or in the $E \parallel b$

absorption spectrum ( Fig. 2.8 ).

To determine the structural assignment of the fundamental bands $A$ and the $A^*$ in crystal, as well as the $A_1$ and $A_1^C$ bands in amorphous, in Refs. [39,40] the Raman spectra of c–$GeSe_2$ have been investigated from a simple model calculation using a combination of a valence-force-field ( VFF ) and a bond polarizability ( BP ). The interatomic potential $U$ was described by the Keating potential [70],

$$U = \frac{1}{2}k_1 \sum_i (\frac{\delta r_i}{r_i})^2 + \frac{1}{2}\sum_{i \neq j} k_x (\frac{\delta(\vec{r_i} \cdot \vec{r_j})}{r_i r_j})^2, \tag{2.3}$$

where $r_i$ is the bond-length of a bond $i$, $\delta r_i$ is the displacement, and $x$ indicates the species ( Ge or Se ) of central atom which has neighboring bonds $i$ and $j$. To calculate the Raman intensities, they assigned to each Ge–Se bond an ellipsoidal bond polarizability whose magnitude $\alpha$ was assumed to depend on the bond length,

$$\alpha_k = \alpha_k + \delta\alpha_k (\frac{\delta r}{r}), \tag{2.4}$$

where $k$ indicates longitudinal ( l ) or transverse ( t ) to the bond direction. The ellipsoidal polarizability which comes from lone-pair electrons of chalcogen atoms ( Se ) was also considered. Ref. [39] presents the whole assignments of the ellipsoidal bond polarizability.

At first, the VFF-BP calculation was carried out in one layer of the c–$GeSe_2$. Figure 2.13(f) shows the calculated ( using VFF-BP ) Raman intensities with the vertical bars. The mode 45 corresponds to the $A$ band and the mode 48 to the $A^*$ band [39]. The atomic motions in mode 48 are illustrated in Fig. 2.15. The layer is composed of four basic $GeSe_{4/2}$ tetrahedra: $C_1$, $C_2$, $E_1$, and $E_2$. The motions of all the other tetrahedra have been obtained by the $A_g$ symmetrical transformation of these four. In the mode 48, the edge-sharing tetrahedra $E_1$ and $E_2$ vibrate in a symmetric breathing motion, while the corner- sharing tetrahedra $C_1$ and $C_2$, which belong to a chain structure, move almost rotationally. On the other hand in mode 45, whose atomic motions are shown in Fig. 2.16, the tetrahedra $C_1$ and $C_2$ vibrate in a symmetric breathing motion, while the tetrahedra $E_1$ and $E_2$ vibrate not in the breathing motion. Since both these two modes, 45 and 48, are due to in-phase breathing motions of the tetrahedra, it is reasonable that they have comparable intensities as shown in Fig. 2.13(f). Though the positions of the calculated modes are well agreed with the experimental results, the calculated intensity of the mode 48 is much stronger than the experimental intensity of the $A^*$ vibrational mode in Fig. 2.13(c)$\sim$(e).

To explain the peculiar weakness of $A^*$ peak in the usual non-resonant Raman spectra, an extended VFF-BP model ( E-VFF-BP ) is proposed [40]. A natural extension of VFF-BP is obtained by taking the interlayer interactions between the two successive layers in the layer-formed crystalline $GeSe_2$. In Fig. 2.17, the interlayer interactions are supposed as due to the Se–Se weak 'bonds' with the van der Waals forces, labeled A, B, and B′ in broken lines. Though there is no covalent bond between these Se atoms, the assignment of these weak bonds are considered as follows:
1) the distance between these Se atoms is about 4 Å which is almost equivalent to the second nearest Se–Se distance of $GeSe_{4/2}$ tetrahedra;
2) the lone-pair orbits of the two Se atoms are almost parallel.
Under the above two conditions, the overlap integral of lone-pair orbitals will become large. A bond polarizability, which is similar to the ordinal bonds, is assigned to these three weak bonds, while the force constant of these weak bonds is ignored for simplicity. As a result the calculated $A^*$ intensity is notably reduced as shown in Fig. 2.18(b). Thus the calculated spectra agree well with the experimental spectra Fig. 2.18(c).

The intensity ratio of $A^*$:$A$ in various kinds of disordered $GeSe_2$ crystals is much larger than that in the single crystal under the non-resonant condition ( Fig. 2.14 ). It is probable that with increasing disorder the interlayer interaction, which restrains the vibrational intensity of $A^*$ mode, becomes weak so that the intensity ratio of $A^*$:$A$ is enlarged.

Figure 2.19 shows the calculated phonon dispersion curves and the vibrational density of the states ( VDOS ) for c–$GeSe_2$. The dispersion of the uppermost branch, which corresponds to the mode 48, is small. The vibrations in the mode 48 are quasi-localized at the edge-sharing tetrahedra $E_1$ and $E_2$ in Fig. 2.15. In the VDOS, this branch leads to a rather narrow peak at 215 $cm^{-1}$. On the other hand, the mode 45 is an extended mode in the chain structure ( $C_1$ and $C_2$ ) because of the large dispersion corresponding to the mode 45. Thus the mode 45 gives a broad peak at about 205 $cm^{-1}$ merging with the other branches.

In the crystal, the momentum selection rule for the Raman process should be considered so that only the near-Γ-point modes can contribute to the Raman spectra. In the amorphous spectrum, however, the momentum selection rule is broken. Although the VDOS is calculated in c–$GeSe_2$, the total VDOS has a doublet peak which resembles the Raman spectrum of the glass ( the $A_1$ and $A_1^C$ peaks ). Here we assume that the calculated VDOS can be embodied in the spectrum of the glass ap-

proximately. One can find that in the g–$GeSe_2$ the Raman spectral line shape around 200~220 $cm^{-1}$ ( Fig. 2.13(a) ) is very similar to the VDOS calculated in c–$GeSe_2$. The $A_1$ and $A_1^C$ vibrational modes are assigned to the structures of corner-sharing and edge-sharing tetrahedra, respectively. Thus the MRS in amorphous $GeSe_2$ is concluded as a topologically layered crystalline-like fragments which involve the corner-sharing and edge-sharing tetrahedra.

### 2.2.2 Structure and Vibrational Properties of Se

#### Structure of Crystalline Se

In the crystalline Se there are two polymorphic modifications which are monoclinic and trigonal forms. The monoclinic Se ( mc–Se ) is a molecular crystal based on $Se_8$ ring. The trigonal Se ( tc–Se ) is in two enantiomorphous modifications, in right- and left-handed helical chains. The helical chain is periodic with a three-atom unit cell and has trigonal symmetry about the chain axis as shown in Fig. 2.20 [71]. Each atom has two near neighbors at distance $r_1$ and $r_2$ with an angle $\theta$ between the bond vectors, while the interchain distance is $r_3$, as listed in Table 2.2. In the helical chains the sense of the dihedral angles $\psi$ between adjacent bonding plane is preserved along the chain. In contrast, the sense or phase of the dihedral angles alternates in the $Se_8$ ring of mc–Se. In both the helical chain and eight-member ring structure, the dihedral angle $\psi$ is almost the same, approximately 102 degrees. This is fixed by a chemical bonding constraint: minimization of the Coulomb repulsion between the lone-pair electrons on nearest neighbor sites. The tc–Se lattice is highly anisotropic, because of the covalent intrachain bonding and weak van der Waals forces with small covalent contributions between the chains. With increasing disorder from tc–Se, the intrachain distances $r_1$ and $r_2$ remain practically the same while the interchain distance $r_3$ increases ( Table 2.2 ).

#### Medium-Range Structure in Amorphous Se

The generally accepted structural model for amorphous Se ( a–Se ) also maintains the same dihedral angles for the chemical bonding constraint, and includes two 'molecular' species. One kind of species is the chain structure where the phase relation between pairs of adjacent dihedral angles is random. The other is the ring-like structure where the relative phase alternates. The low temperature Raman spectrum of a–Se is shown

Table 2.2: Intrachain distances $r_1$, $r_2$ and interchain distance $r_3$ for three Se modifications. The vitreous state was prepared by quenching the melts in ice water, while the red amorphous Se was obtained by reducing the cooled ( ~5 °C ) $H_2SeO_3$ with $[N_2H_6]SO_4$ ( From Ref. [71] ).

| Se-modification | $r_1$ [Å] | $r_2$ [Å] | $r_3$ [Å] |
|---|---|---|---|
| Trigonal | 2.31 | 3.69 | 3.46 |
| Vitreous | 2.32 | 3.69 | 3.69 |
| Red amorphous | 2.32 | 3.69 | 3.86 |

Table 2.3: Raman-active fundamental vibrational modes in a–Se proposed in Refs. [73,74].

| Position ( $cm^{-1}$ ) | assignment | |
|---|---|---|
| | in Ref. [73] | in Ref. [74] |
| 112 | $Se_8$, $A_1$ | $Se_8$-fragment $A_1$ |
| 235 | polymeric chain, $A_1$ | not mentioned |
| 255 | $Se_8$, $A_1$ | $Se_8$-fragment $A_1$ |

in Fig. 2.21 [72]. The most intense feature of the spectrum is the broad band centered at 250 $cm^{-1}$ upon which is superposed by a low energy shoulder at 235 $cm^{-1}$. In Ref. [73] the vibrational modes have been identified by studying the infra-red and Raman spectra of tc–, mc– and a–Se. An assignment of the fundamental vibrational modes in a–Se Raman spectra is proposed as the description shown in the central column of Table 2.3. In this model the $Se_8$ ring structure is proposed to rather exist in g–Se, but in the later experiment it is not agreed.

Keezer et al. analyzed the dissolution of a–Se in $CS_2$, and they indicated that the $Se_8$ ring-fraction in a–Se may indeed be quite small. Then Lucovsky and Galeener refined their medium-range structural model which is shown in Figs. 2.22 and 2.23 [74,75]. Their structural model bases on the chains which include the local segments with both the cis– and trans–coupling configuration. The important difference between the local atomic structure in the rings and helical chains is the phase relationship between adjacent pairs of dihedral angles. These phase relations are described in terms

of cis- and trans- coupling where the two local configuration show the difference only in the placement of atoms 5 and 5′ ( Fig. 2.22 ). In the cis-coupling geometry, the dihedral angles alternate in phase, and the structure closes on itself to form $Se_8$ ring molecules. On the other hand, the trans-coupling arrangement maintains the sense of the dihedral angles to lead the helical configuration of potentially infinite extent. The trans-coupling configuration has only one $A_1$ mode with a frequency of $\sim$255 $cm^{-1}$, a bond-stretching vibration with the atomic motion in the bonding plane. In contrast, the cis-coupling configuration has two $A_1$ modes, the bond-stretching mode at $\sim$255 $cm^{-1}$ and the bond-bending vibration with a frequency of $\sim$112 $cm^{-1}$ where the atomic motion is perpendicular to the bonding plane. In their chain model, the local molecular order are in a chain segment with trans-coupling configuration, and in $Se_8$-fragment with the cis-coupling configuration, as shown in Fig. 2.23. Suzuki [76] and Misawa [77] studied the structure of liquid and amorphous Se by pulsed neutron diffraction using an electron LIANC. They concluded that the structure was best described by a model where the long chains included cis- and trans- coupled regions.

Figure 2.24, which was reported in Ref. [78], shows the changes of the Raman spectra during laser induced transformation from the amorphous to the crystalline state. A gradual intensity redistribution for the peaks at 255 $cm^{-1}$ and 235 $cm^{-1}$ ( labeled 237 $cm^{-1}$ in Ref. [78] ) without a frequency shift is observed as the irradiation power increases. With the radiation power increasing, the peak at 255 $cm^{-1}$ degenerates into the plateau, while the peak at 235 $cm^{-1}$ simultaneously narrows and becomes the dominant spectral feature. At the last stage of the transformation, the Raman spectrum becomes practically indistinguishable from the spectrum of tc-Se. The results support that the vibrational mode at 235 $cm^{-1}$ is related to a chain structure which is more similar to the tc-Se structure than the chain structure corresponding to the vibrational mode at 255 $cm^{-1}$.

### 2.2.3 Properties of Glassy $Ge_xSe_{1-x}$

Glassy $Ge_xSe_{1-x}$, which exhibits no sharp X-ray diffraction lines, can easily be prepared by quenching from melts in the range of $0 \leq x \leq 0.42$ [38]. Phillips has proposed that the molecular structure of melt-quenched $Ge_xSe_{1-x}$ is much more ordered than a continuous random network. In $Ge_xSe_{1-x}$ glasses, their physical properties, such as the glass-transition temperature $T_g$, the melting point $T_m$, and the optical band gap, depend on the composition ratio. The optical property has been shown in Fig. 2.10 where

the variation of the composition $x$ induces significant changes of the optical absorption edge. With the Ge content increasing from 0 to 0.33, the optical absorption edge shifts to higher energy side. A phase diagram of Ge–Se system has been summarized in Ref. [55] according to many works' results [80-83], as shown in Fig. 2.25. For the Ge concentration in the range of 0∼0.08, the $T_m$ maintains at about 220 °C. When the Ge concentration increases from $x = 0.08$, the $T_m$ increases in a monotonic way up to $x = 0.33$. It has been reported by Koós and Kósa Somogyi [79] that $T_g$ increases with the Ge composition $x$ changing from 0 to 0.33 as shown in Fig. 2.26 where the average coordination number $\langle r \rangle$ is used instead of the Ge composition $x$. All these variations of the physical properties are related to the structural change.

In Ref. [55] the Raman spectra have been measured, as shown in Fig. 2.27, and verified that at the composition $x \leq 0.33$ the coordination numbers of Ge and Se atoms are equal to 4 and 2, respectively. Three fundamental peaks appear in the Raman spectra of the glasses at 195 $cm^{-1}$, 215 $cm^{-1}$ and 250 $cm^{-1}$. The vibrational band $A_1$ with the peak at 195 $cm^{-1}$, which is attributed to the breathing motion of corner-sharing $GeSe_{4/2}$ tetrahedra, appears at the whole composition except in pure Se. The $A_1^C$ band with the peak at 215 $cm^{-1}$, which is assigned to the edge-sharing $GeSe_{4/2}$ tetrahedra, increases slowly in the region of $x \leq 0.20$, and rapidly as $x$ approaches to 0.33.

These $x$ dependence of the three vibrational bands at $x \leq 0.33$ suggests that the glass structure is locally similar either to Se-chain structure, or to the $GeSe_{4/2}$ tetrahedral structure. The amount of local $GeSe_{4/2}$ tetrahedral structure obviously increases with increasing Ge content. In the region of $x > 0.33$, the $A_1^C$ band decreases gradually up to $x = 0.42$, where the vibrational intensity of Ge–Ge bond increases [55,56].

As a typical chalcogenide glassy system, mentioned in the chapter 1, $Ge_xSe_{1-x}$ shows many rigidity percolation related aspects at $\langle r \rangle$=2.4 under which the structure is easily reformed. In addition, important results have been obtained that the normal and inverse photo-emission spectra change abruptly at $\langle r \rangle$=2.4 in glassy $Ge_xSe_{1-x}$ [11] as shown in Fig. 2.28. The distinct change of the normal and inverse photo-emission spectra is reasonably assumed to reflect the threshold between the nucleation and subsequent growth of the $GeSe_{4/2}$ tetrahedra obtained clusters just after the percolation.

## 2.3 Photo-induced Crystallization

The PIC, which is one of the typical and drastic photo-induced structural changes in g–$GeSe_2$, was first reported in Refs. [27,28]. And then, some other works have studied it [29-36]. In Refs. [32-36] time-resolved Raman scattering studies have been made to intensively investigate the photo-induced crystallization process of the amorphous ( a– ) $GeSe_2$ films which are prepared by vacuum-evaporation deposition of bulk g–$GeSe_2$ onto glass substrates ( silica glass or Corning 7059 glass ). Figure 2.29 shows the time-resolved Raman spectra of a–$GeSe_2$. After an appropriate period, which is named latent period, the initial amorphous spectra gradually change into the crystalline spectra in two types with the irradiation time passed. In type A case only the 2D form grows, while in type B both the 2D and 3D forms grow. Type A was more frequently observed than the type B. In the type A case, the intense peak grows with the peak energy at about 210 $cm^{-1}$ which corresponds to the A peak of c–$GeSe_2$ ( 2D ). The growth curve, as shown in Fig. 2.30, is empirically fitted by

$$1 - \exp[-k(t - t_0)], \tag{2.5}$$

where $t_0$ is the latent period.

When laser light irradiates onto the sample, the temperature under the illuminated portion rises above the environmental temperature by the absorption of the light. These heating effect may confuse the investigation of the photo-process with the thermal process in the PIC. To distinguish these two processes in the PIC, the temperature of the irradiated portion is estimated from the position shift of the 211 $cm^{-1}$ band of the photo-induced crystals [33]. Lowering the irradiation power of the excitation light, the Raman peaks shift to higher energy side simultaneously. The 211 $cm^{-1}$ band of c–$GeSe_2$ at room temperature has a temperature coefficient of about –0.01 $cm^{-1}/K$. Extrapolating the peak position to power = zero where the temperature is considered to be equal to the environmental temperature, the temperature at the PIC process, $T_{pic}$, is estimated from

$$T_{pic} = \frac{E_P - E_0}{-0.01 \mathrm{cm}^{-1}/\mathrm{K}} + T_{room}, \tag{2.6}$$

where $E_P$ is the peak position of the 211 $cm^{-1}$ band at the irradiation power of $P$, $E_0$ is the peak position at the irradiation power extrapolating to 0, and the $T_{room}$ is the room temperature.

With the $T_{pic}$ being increased by rising the irradiation power, the latent period

becomes short which means the PIC occurs easily. On the other hand, the latent period becomes long near a certain threshold temperature $T_{pic}$ below which no PIC process has been observed. The threshold temperature $T_{pic}$ ( ~200 °C ) of the PIC is much lower than the threshold temperature ( ~325 °C ) for the thermal crystallization in the dark within several hours. To distinguish the photo-induced process from the thermal process, in Ref. [35] the electronic and thermal processes have been studied during the PIC of a–$GeSe_2$ with continuous or periodic light. A picture of the phonons and photons cooperatively promoting the PIC process, as shown in Fig. 2.31, has been proposed as follows: the electronic excitation successively converts the initial amorphous state into intermediate amorphous states; from the intermediate state, the thermally assisted development of the crystalline nuclei occurs by overcoming an energy barrier, A. On the other hand, the thermal crystallization process in the dark from the initial amorphous state to the crystalline nuclei requires an energy barrier, B which is higher than A, to be overcome.

## 2.4 Photoluminescence in Glassy and Crystalline $GeSe_2$

Photoluminescence ( PL ) investigation brings much information on relaxation processes of photo-excited electrons and/or holes in materials. In chalcogenide semiconductor, PL spectrum generally shows a broad Gaussian shaped luminescence band with its peak energy much lower than the peak energy of its excitation spectrum [41-45]. The difference between the two peak energies is called Stokes shift. For example, the peak energy of PL spectrum is about half of the band gap while that of the excitation spectrum is approximately equal to the band gap. The broad luminescence band in the Gaussian shape and the large Stokes shift are attributed to a strong electron-phonon interaction at the recombination center, according to the Mott-Davis-Street ( MDS ) model [41,84-87]. As for g–$GeSe_2$, PL band is shifted by about 0.1 eV towards lower energy and its FWHM is about 0.07 eV wider than that of c–$GeSe_2$, as shown in Fig. 2.32. The similarity of the PL spectra of g–$GeSe_2$ and c–$GeSe_2$ incites ones to relate the relaxation processes in two forms with a same kind of ways.

Most chalcogenide glasses exhibit fatiguing effects in which the intensity of the luminescence decreases with prolonged excitation. The extent of fatiguing and the

initial luminescence intensity of the g–$Ge_xSe_{1-x}$ ( $0.20 \leq x \leq 0.42$ ) is reported in Ref. [84] as shown in Fig. 2.33. The fatiguing is measured with a fixed excitation energy there. For $x > 0.33$ with Ge content increasing, the PL spectra intensity decreases and fatiguing is observed as the intensity being reduced to 30% of its initial value. On the other hand, for $x < 0.33$ the intensity of PL spectra fatigues very strongly to $<$ 10% of its initial value. $GeSe_2$ is found to be the only composition without discernible fatiguing. The fatiguing can be recovered by thermal annealing in the dark.

Thermal quenching of PL, where the intensity decreases with increasing temperature, yields information about the kinetics of the concurrent radiative and non-radiative recombination processes. The temperature dependence of the PL intensity in g–$GeSe_2$ and c–$GeSe_2$ is different. These thermal behaviors have alternatively been explained by the different models [43-45].

As a common explanation in the various models, photoluminescence line shape $S(\hbar\omega)$ is given by

$$S(\hbar\omega) = const. \times exp[-\frac{(\hbar\omega - E^* + 2W)^2}{\sigma^2}], \tag{2.7}$$

where $2W$ is the Stokes shift. The $S(\hbar\omega)$ is a Gaussian curve centered at $E^* - 2W$ with line width parameter $\sigma$ given by

$$\sigma = (2W\hbar\Omega_0)^{\frac{1}{2}}, \tag{2.8}$$

where $\Omega_0$ is a relevant vibrational frequency. With increasing temperature $T$, the occupancy of higher vibronic levels causes the line width $\sigma(T)$ to increase as ( Huang and Rhys [88] )

$$\sigma(T) = \sigma(0)(\coth(\frac{\hbar\Omega_0}{2kT}))^{\frac{1}{2}}. \tag{2.9}$$

In an amorphous material the energy level of a particular type of luminescent center may vary due to the disorder and this contributes to broadening of the luminescence band. If the disorder energy is described by a Gaussian of width $\sigma_D$, the luminescence band is also in Gaussian line with a width $\sigma_{am}$ of

$$\sigma_{am}^2 = \sigma_{ph}^2 + \sigma_D^2, \tag{2.10}$$

where $\sigma_{ph}$ is the contribution due to the phonon coupling for an appropriative vibronic level.

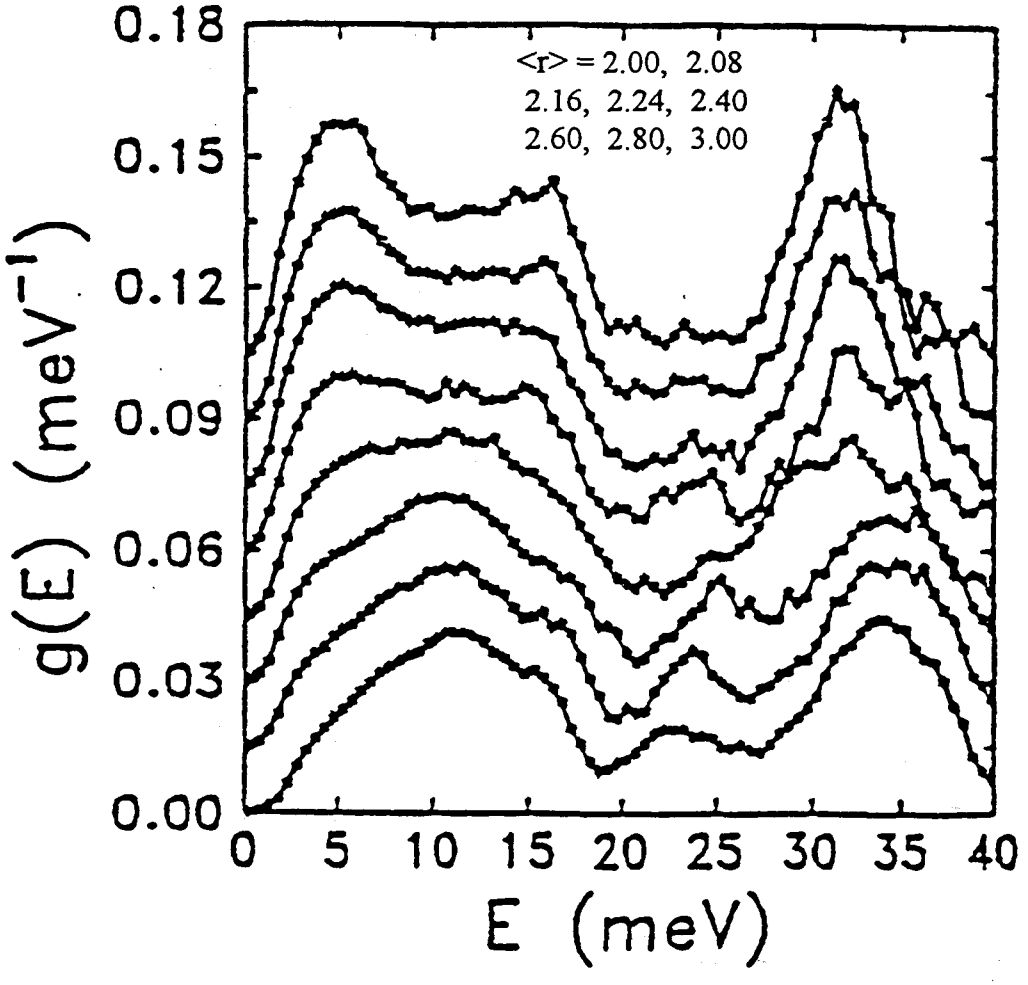


Figure 2.1: VDOS for Ge–Se–As glasses system. Starting from the bottom ( $\langle r \rangle$ = 3.00 ), successive curves have been shifted up to 0.015 units on the vertical scale. The top curve ( $\langle r \rangle$ = 2.0 ) is for pure Se glass. The other glasses in order are $\langle r \rangle$ = 2.08, $Ge_4Se_{96}$; $\langle r \rangle$ = 2.16, $Ge_5Se_{89}As_6$; $\langle r \rangle$ = 2.24, $Ge_{12}Se_{88}$; $\langle r \rangle$ = 2.40, $Ge_{7.5}Se_{67.5}As_{25}$; $\langle r \rangle$ = 2.60, $Ge_{23}Se_{63}As_{14}$; $\langle r \rangle$ = 2.80, $Ge_{31}Se_{51}As_{18}$; $\langle r \rangle$ = 3.00, $Ge_{39.5}Se_{39.5}As_{21}$. The peak at ~5 meV is identified as the floppy mode peak. ( From Ref. [3] ).

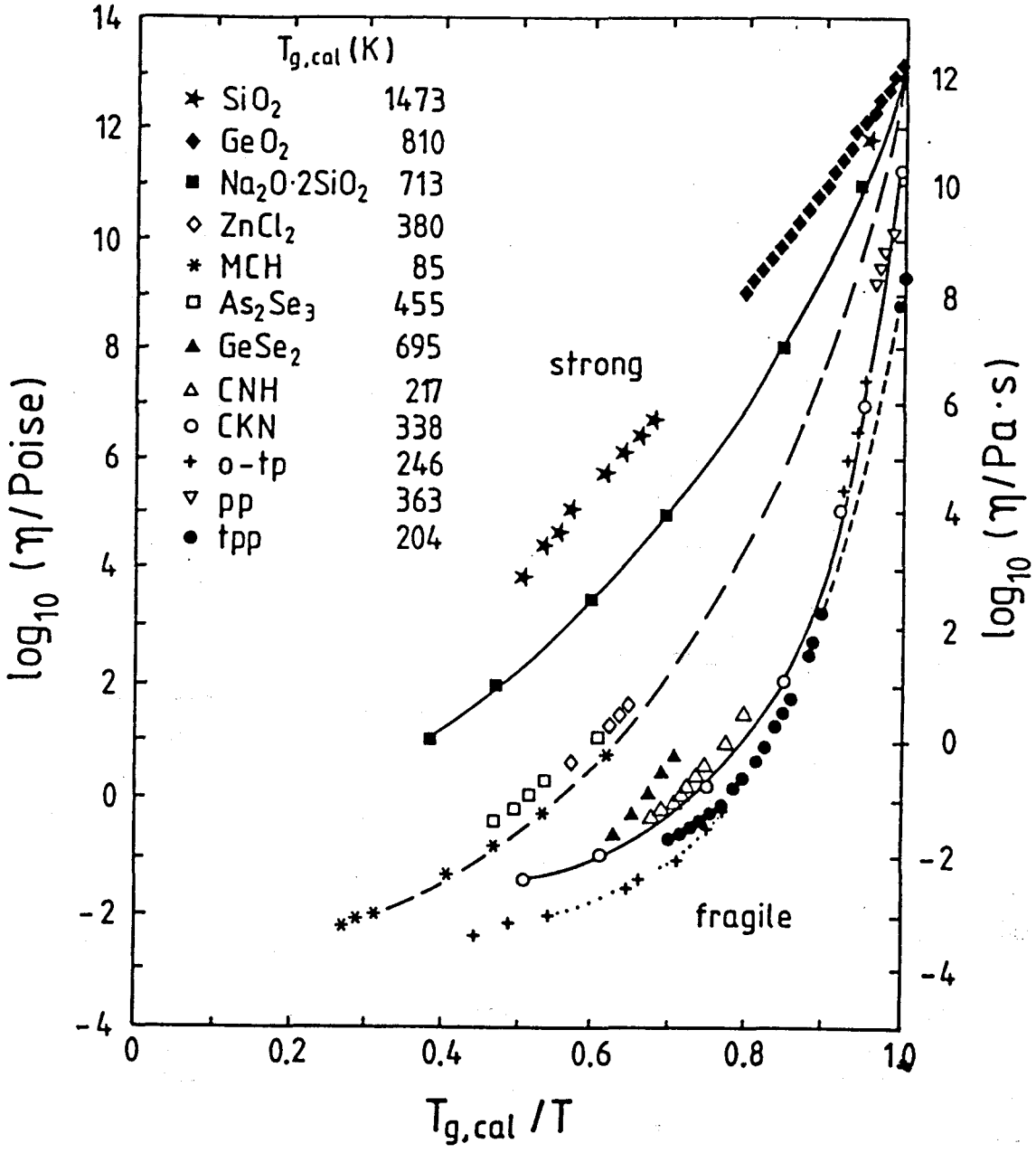


Figure 2.2: Arrhenius plot for the viscosity of a variety of super-cooled liquids. The inverse temperature scale has been normalized with respect to the calorimetric glass-transition temperature $T_g$. ( From Ref. [14] ).

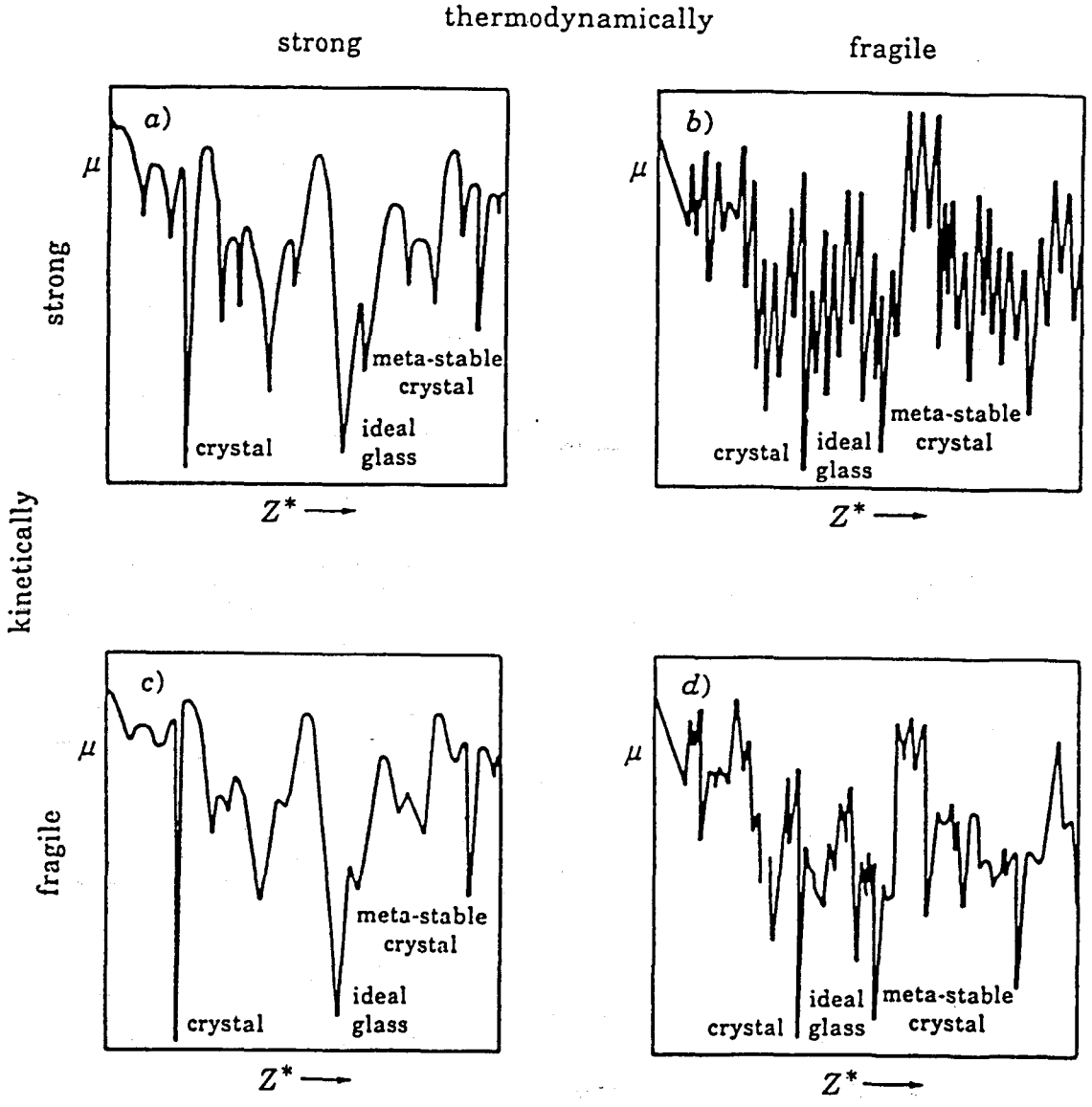


Figure 2.3: Schematic representation of the potential energy $\mu$ versus the configuration space variable $Z^*$ for strong and fragile glass-formers. This plot emphasizes the importance of variations in the density of minima as well as in the highness of barriers $\Delta\mu$ separating them. Thermodynamically strong behavior ( parts (a) and (c) ) is characterized by a relatively small number of minima on the hypersurface. Kinetically strong behaviors is observed for glass-formers that exhibit large barriers $\Delta\mu$ ( parts (a) and (b) ) while small barrier heights are associated with the kinetically fragile case ( From Ref. [15] ).

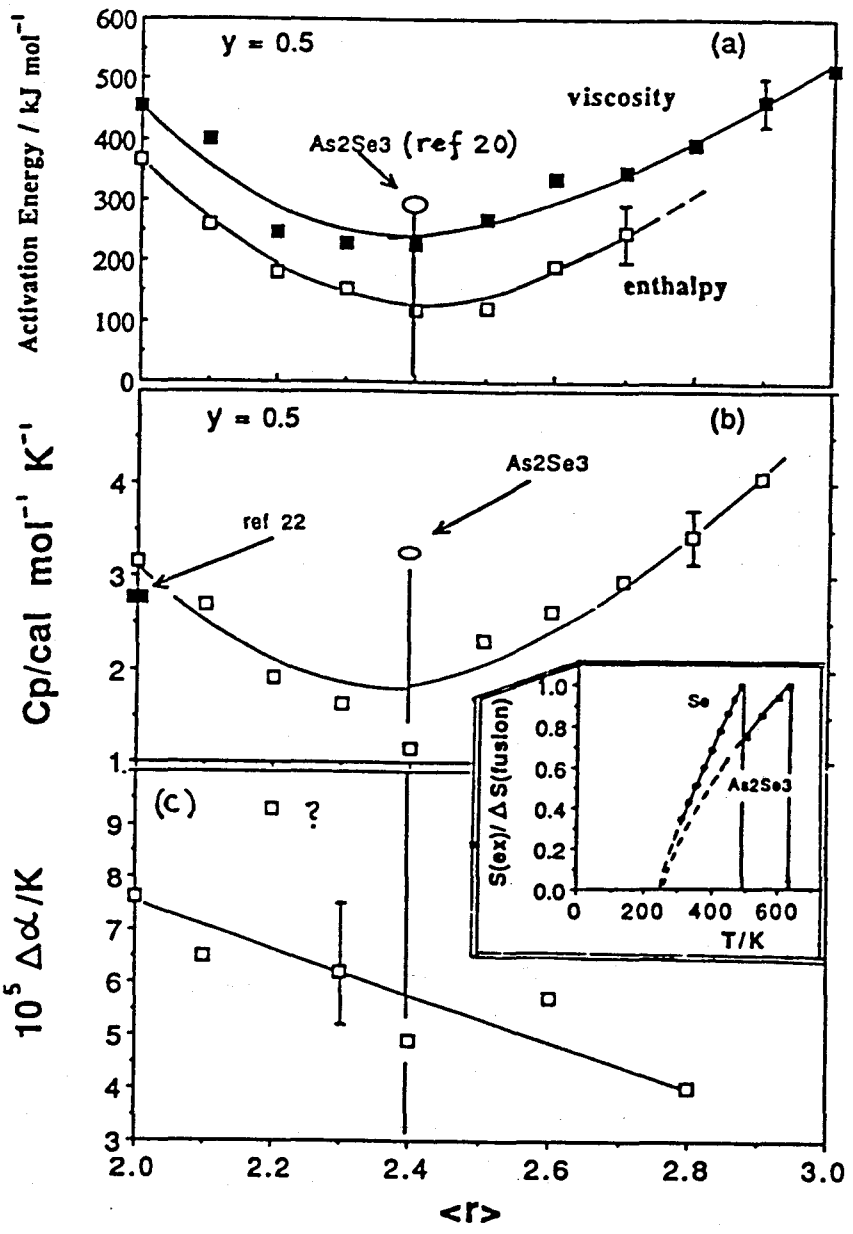


Figure 2.4: $\langle r \rangle$ dependence of key relaxational and thermodynamic properties of $Se_{1-x}(Ge_yAs_{1-y})_x$ liquids at $y = 0$ and 0.5: (a) Dependence of activation energies for viscosity and enthalpy relaxation. (b) Excess heat capacity $\Delta C_p$ measured at $T_g$ showing minima in each case at the rigidity percolation threshold $\langle r \rangle = 2.4$. (c) Excess expansion coefficient $\Delta\alpha$ showing *absence* of anomaly at $\langle r \rangle = 2.4$. Inset: Kauzmann plots for excess entropy in the case of $\langle r \rangle = 2.0$ ( pure Se ) and $\langle r \rangle = 2.4$ ( $As_2Se_3$ ) ( From Ref. [10] ).

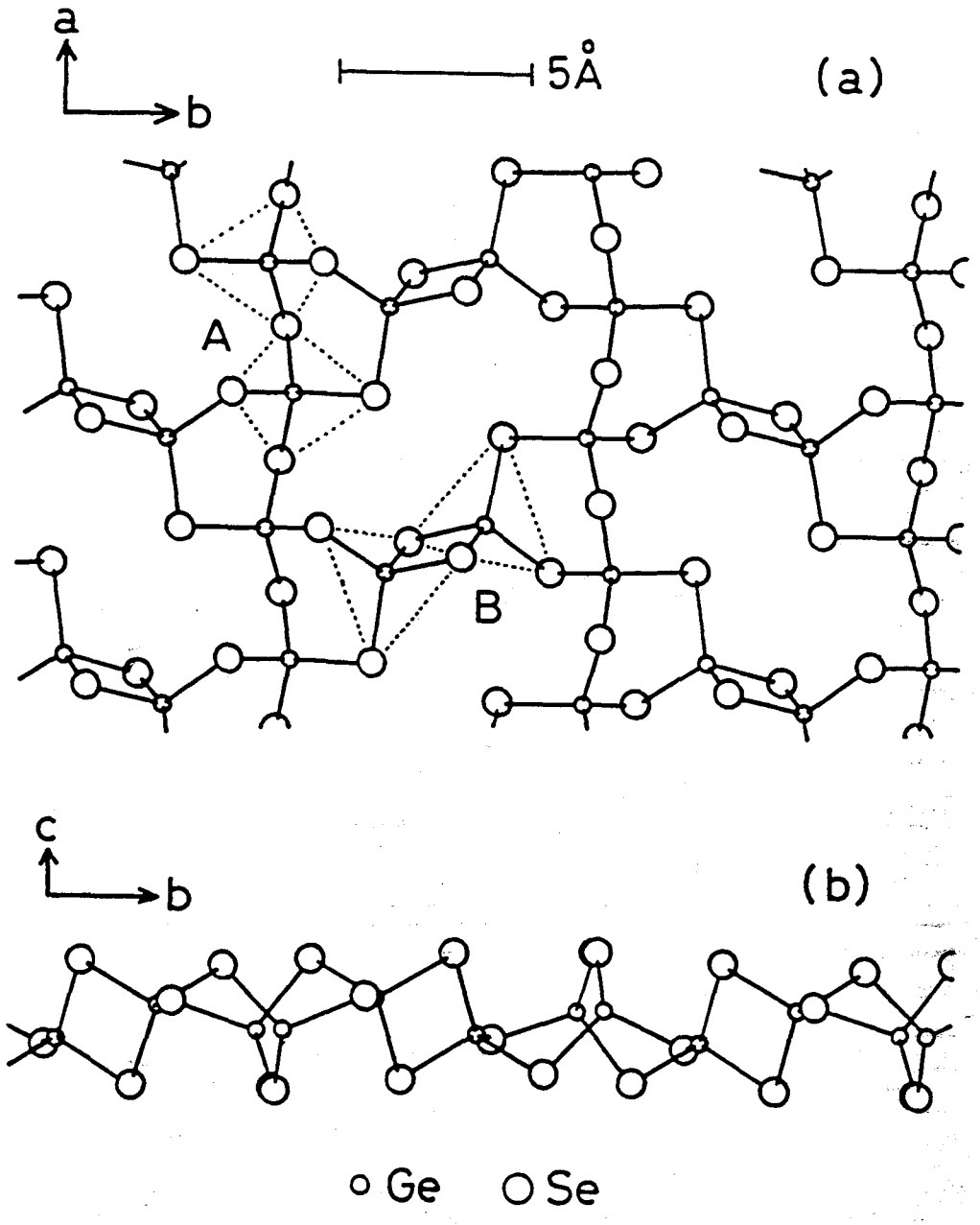


Figure 2.5: Atomic arrangement of one layer of HT-$GeSe_2$. Smaller circles are Ge atoms, and the larger ones are Se atoms. In the projection onto the (001)-plane (a), the $GeSe_{4/2}$ tetrahedra ( in broken lines ) are connected by sharing the corner, labeled A, or by sharing the edge, labeled B. (b) is a view along the [100]-direction ( From Ref. [51] ).

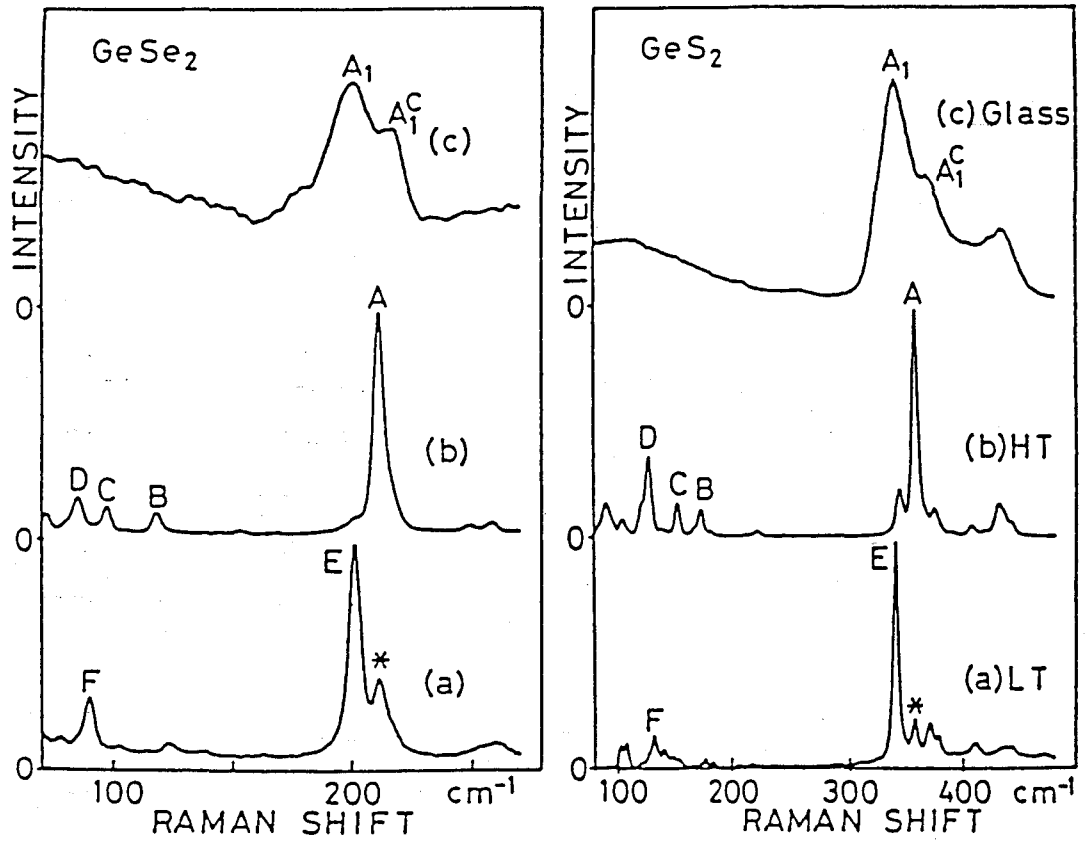


Figure 2.6: (A): Raman spectra of (a) LT-$GeSe_2$, (b) HT-$GeSe_2$, and (c) amorphous film are measured at room temperature by excitation energy of 2.41 eV. (B): Room temperature Raman spectra of (a) LT-$GeS_2$, (b) HT-$GeS_2$, and (c) glass. The line * is due to the contamination with HT-$GeSe_2$ or HT-$GeS_2$. The lines A~F in both (A) crystalline $GeSe_2$ and (B) crystalline $GeS_2$ are corresponding to each other ( From Ref. [33] ).

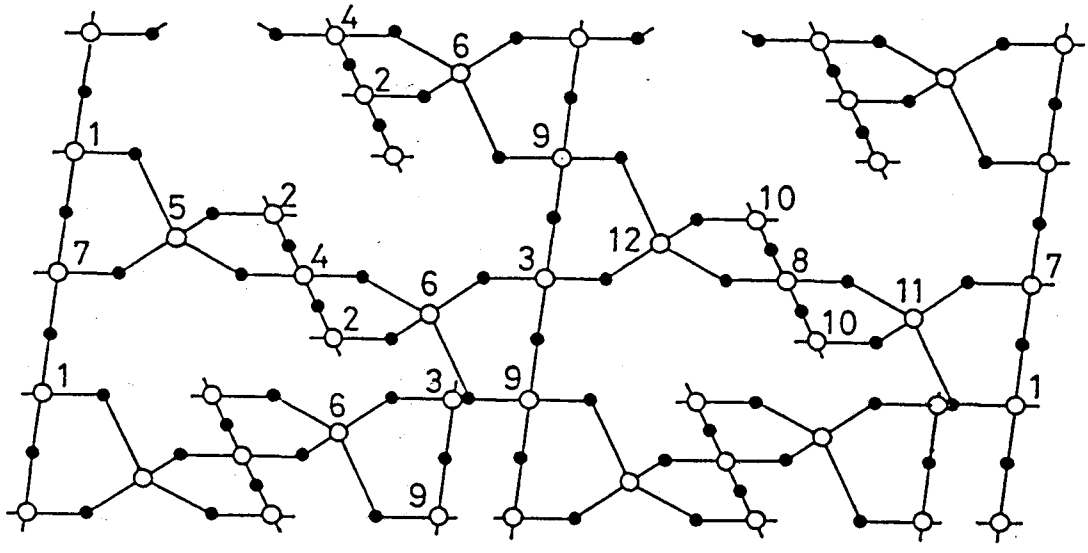


Figure 2.7: Schematic illustration of network connection in the LT-$GeS_2$. Open circles are Ge atoms and closed ones are S atoms. Numbers from 1 to 12 indicate the different $GeS_{4/2}$ tetrahedral sites in a unit cell. They are connected only by sharing corners to form a 3D-structure. The chains ( –7–1–7–1– ) and ( –3–9–3–9– ) are along with [001] direction, and the chains ( –2–4–2–4– ) and ( –8–10–8–10– ) are along with [101] direction in a different plane from the first two chains ( From Ref. [52] ).

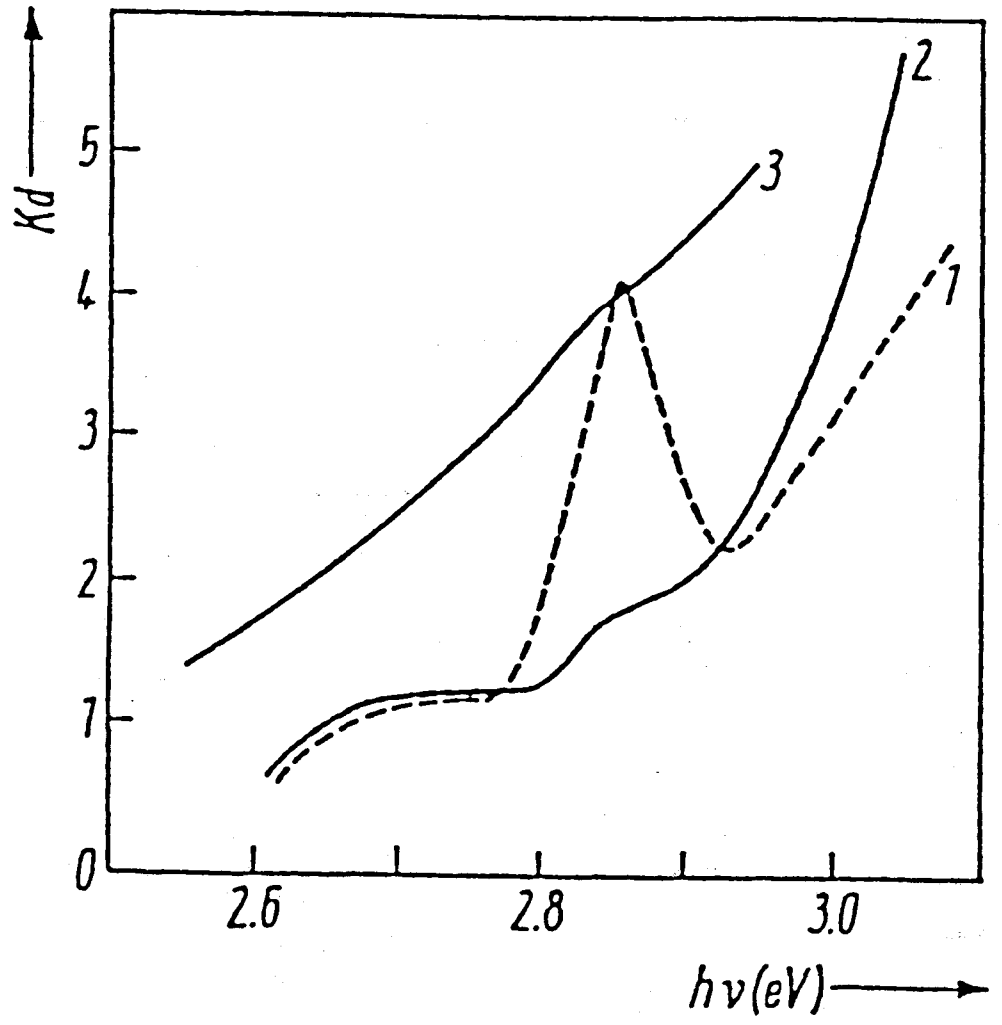


Figure 2.8: Absorption spectra of c–$GeSe_2$ in (1) $E \parallel a$ and (2) $E \parallel b$ polarization, and (3) amorphous $GeSe_2$ at 4.2 K. In the $E \parallel a$ polarization, an exciton absorption peak is observed at about 2.854 eV ( From Ref. [53] ).

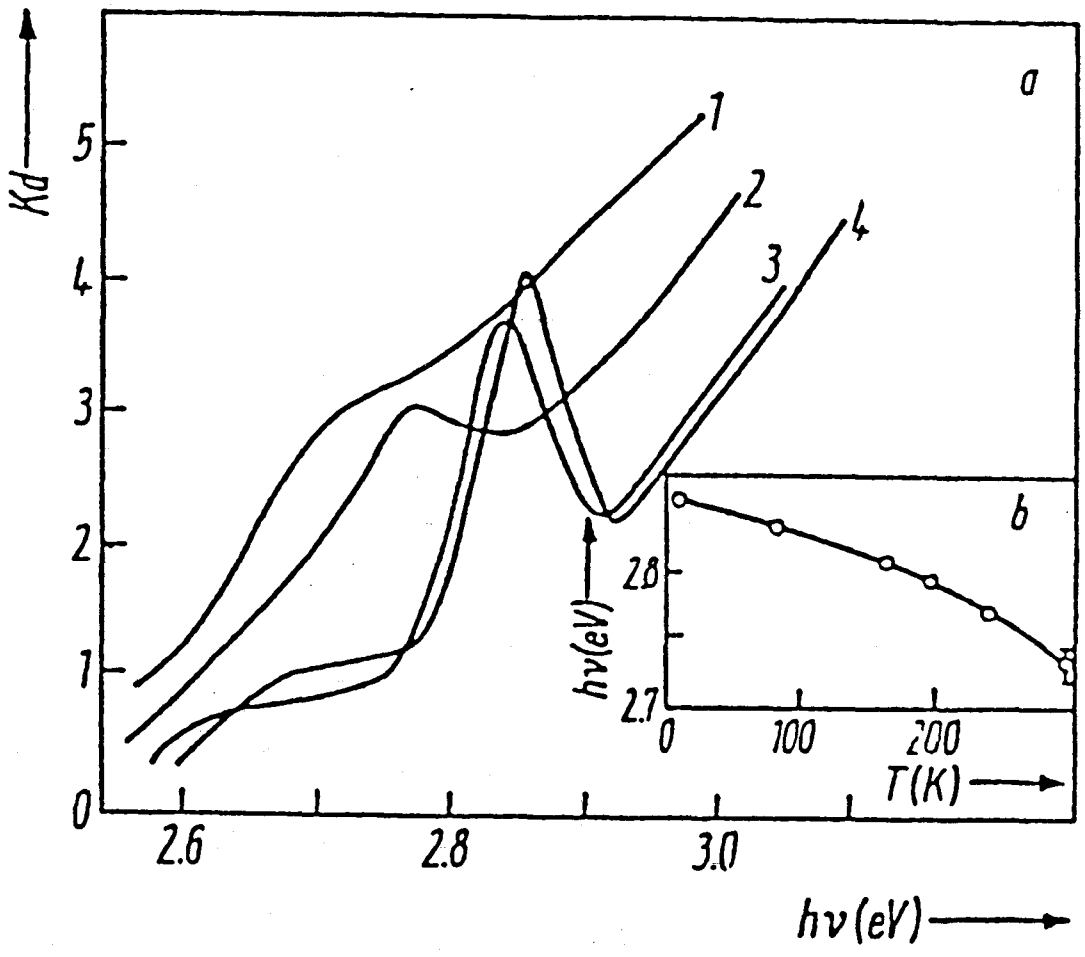


Figure 2.9: Absorption spectra of c–$GeSe_2$ in the $E \parallel a$ polarization, at (1) 300 K, (2) 240 K, (3) 77 K, and (4) 4.2 K. The inset shows temperature dependence of the exciton transition energy. The exciton absorption peak becomes sharp and shifts to higher energy side with decreasing temperature ( From Ref. [53] ).

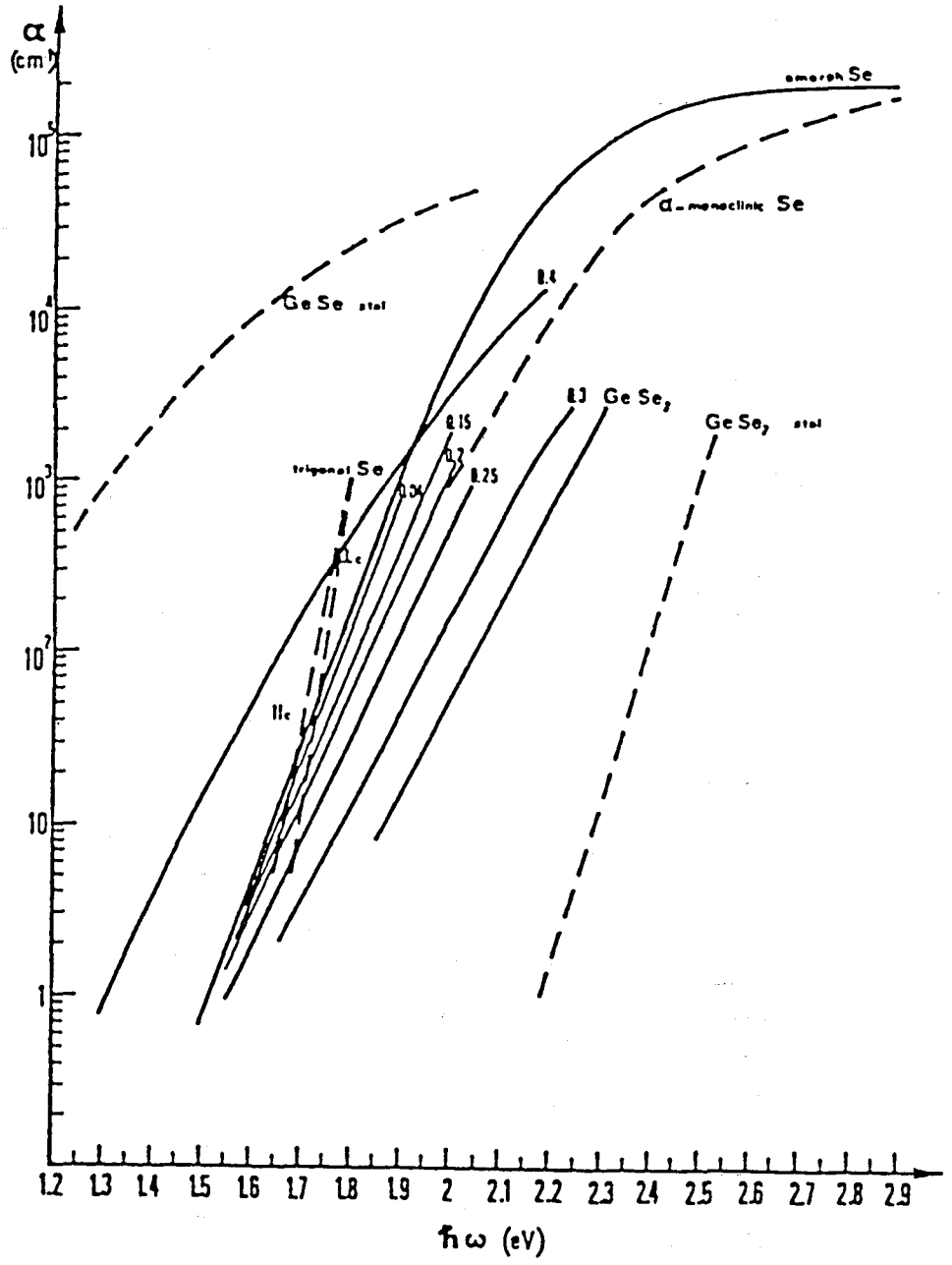


Figure 2.10: Optical-absorption edges of $Ge_xSe_{1-x}$ glasses. The absorption coefficient of g–$GeSe_2$ around 2 eV is about $10^2$ $cm^{-1}$ which is higher than that of c–$GeSe_2$ ( From Ref. [55] ).

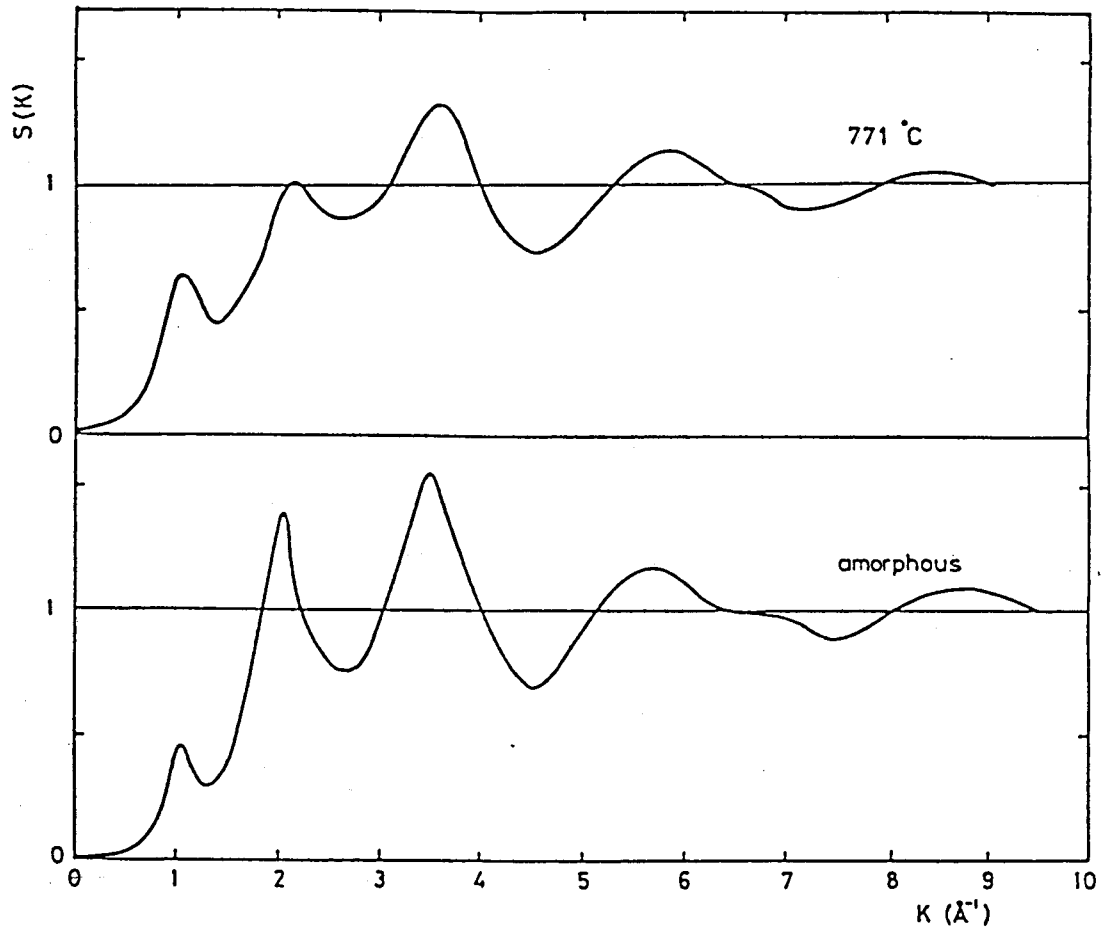


Figure 2.11: Structure factor $S(k)$ of amorphous $GeSe_2$ at room temperature and liquid $GeSe_2$ at 771 °C. The FSDP at 1.01 $\mathring{A}^{-1}$ relates to a correlation length of about 6.22 $\mathring{A}$ which corresponds to the characteristic scale of the MRS. The FSDP is preserved even in the liquid ( From Ref. [62] ).

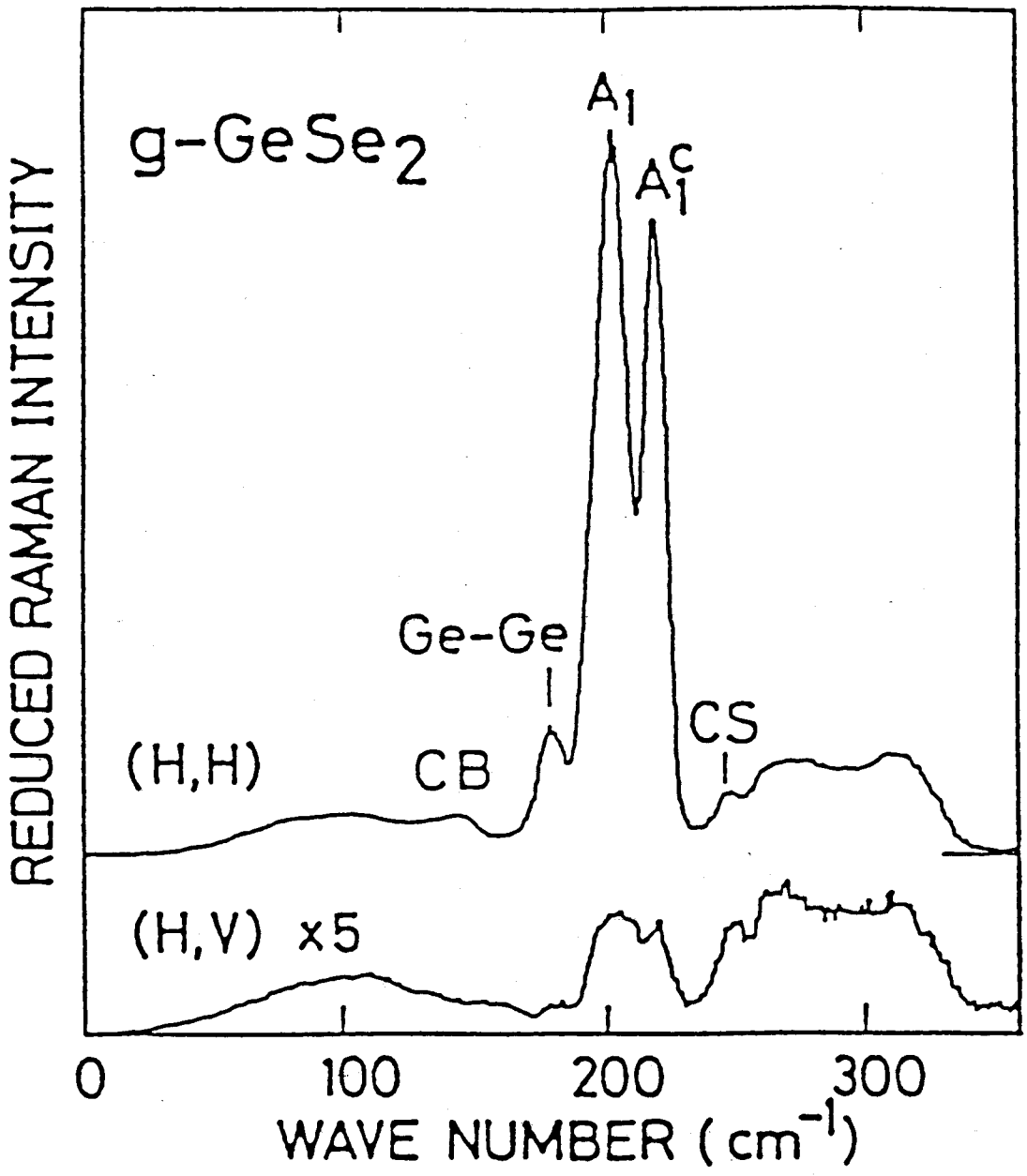


Figure 2.12: Raman spectra of g–$GeSe_2$ at 50 K with 6328 Å light excitation ( From Ref. [36] ).

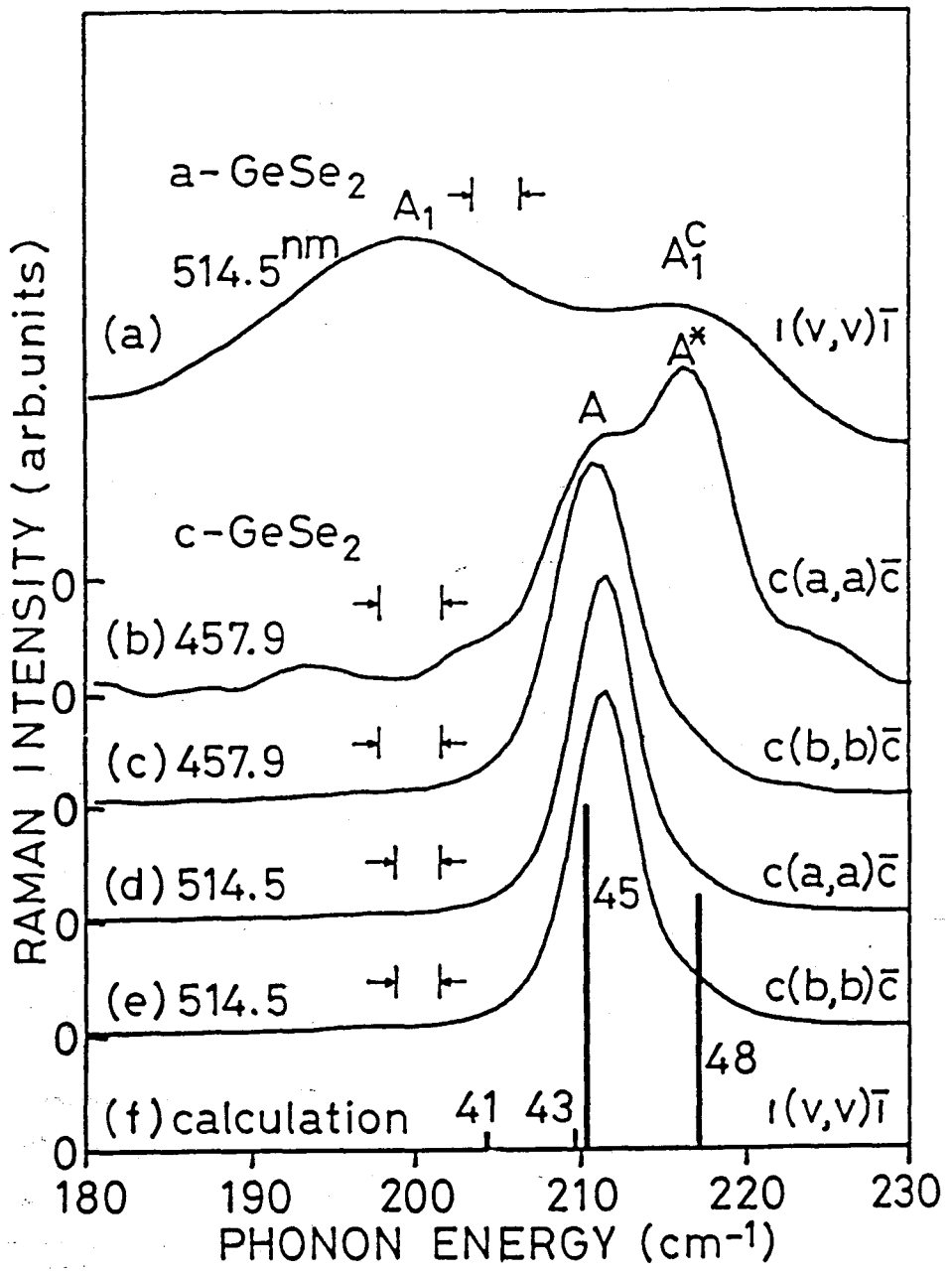


Figure 2.13: Comparison of the Raman spectra for $GeSe_2$ in the (a) amorphous and (b)~(e) crystalline forms. The vertical bars (f) show the calculated intensity for the crystalline Raman spectrum. The excitation wavelengths, spectral resolutions ( arrows ), and polarization conditions are also shown ( From Ref. [66] ).

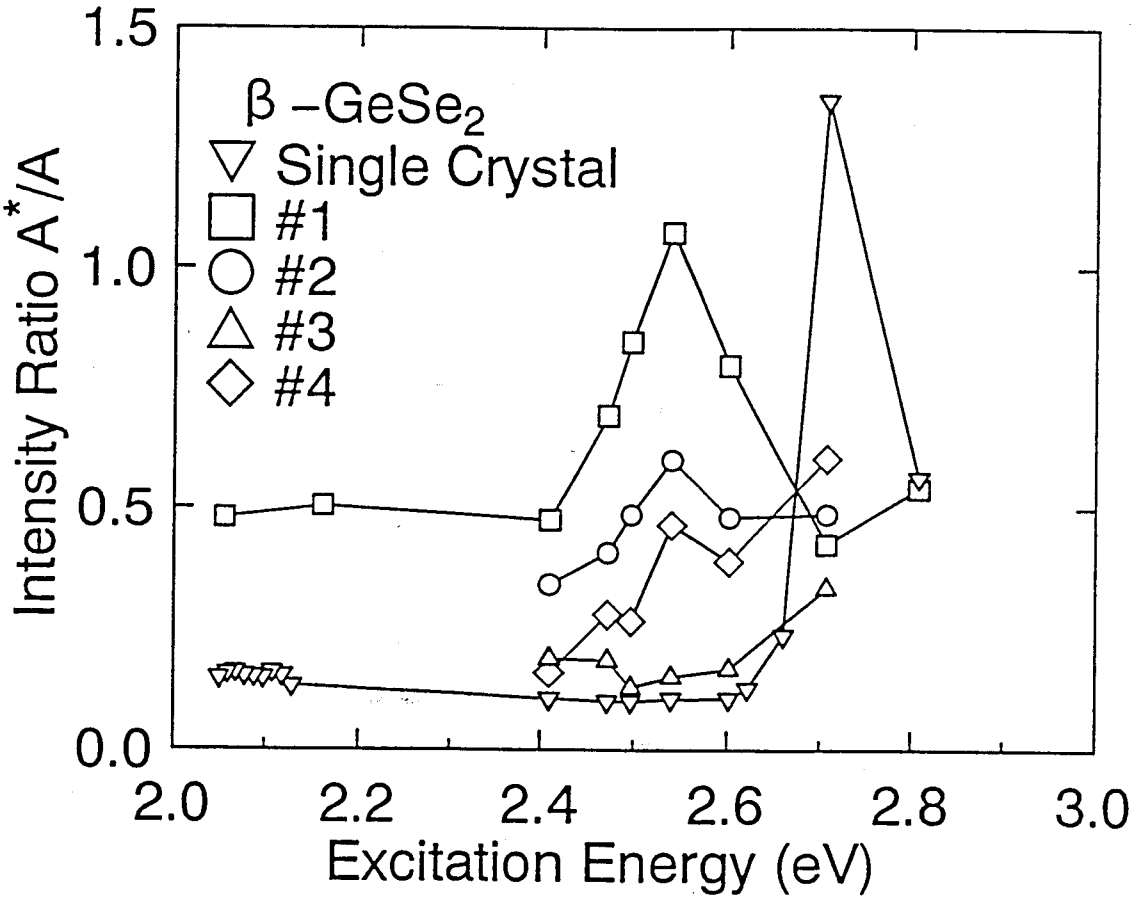


Figure 2.14: Intensity ratio $A^*$:$A$ for the single crystals and the small crystals ( #1–#4 ). The lines are guides to the eye. The spectra are strongly influenced by the degree of disorder in the crystals ( From Ref. [67] ).

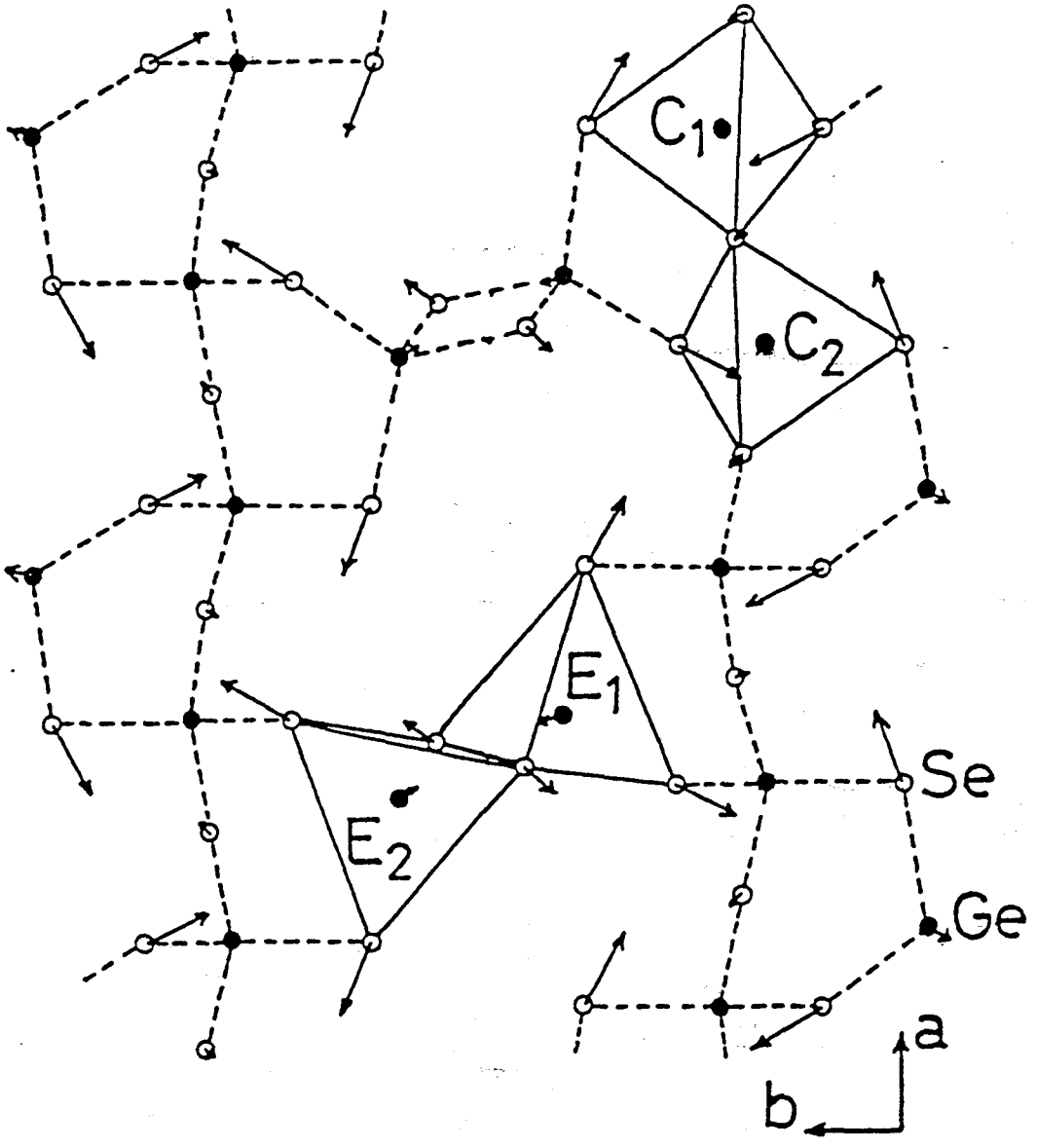


Figure 2.15: A c–$GeSe_2$ layer with the atomic motions in the mode 48 indicated by arrows. The tetrahedra $C_1$ and $C_2$ move almost rotationally, while the tetrahedra $E_1$ and $E_2$ vibrate in a symmetric breathing motion ( From Ref. [66] ).

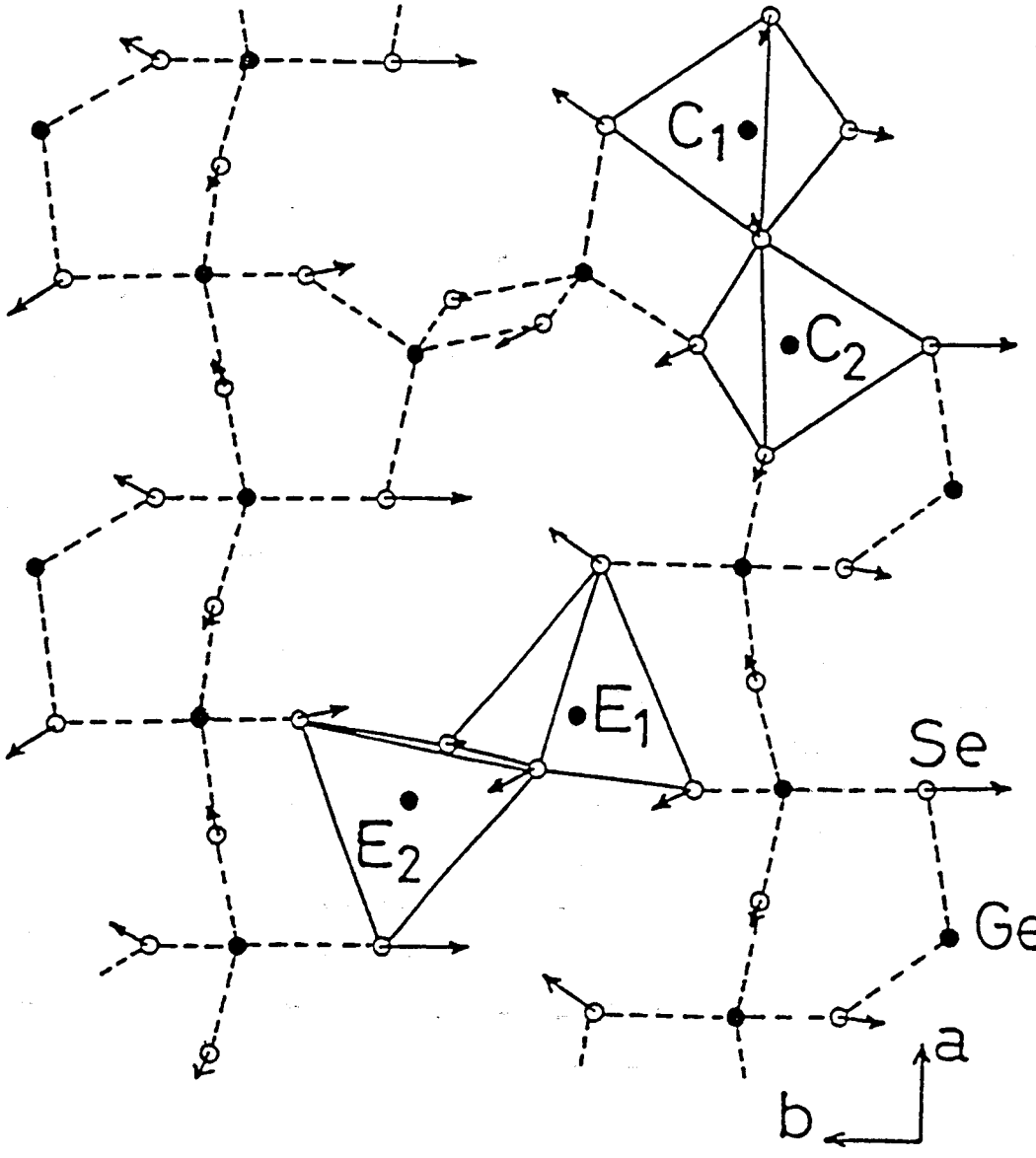


Figure 2.16: A c–$GeSe_2$ layer with the atomic motions in the mode 45 indicated by arrows. The tetrahedra $C_1$ and $C_2$ vibrate in a symmetric breathing motion, while the $E_1$ and $E_2$ vibrate not in breathing motion.

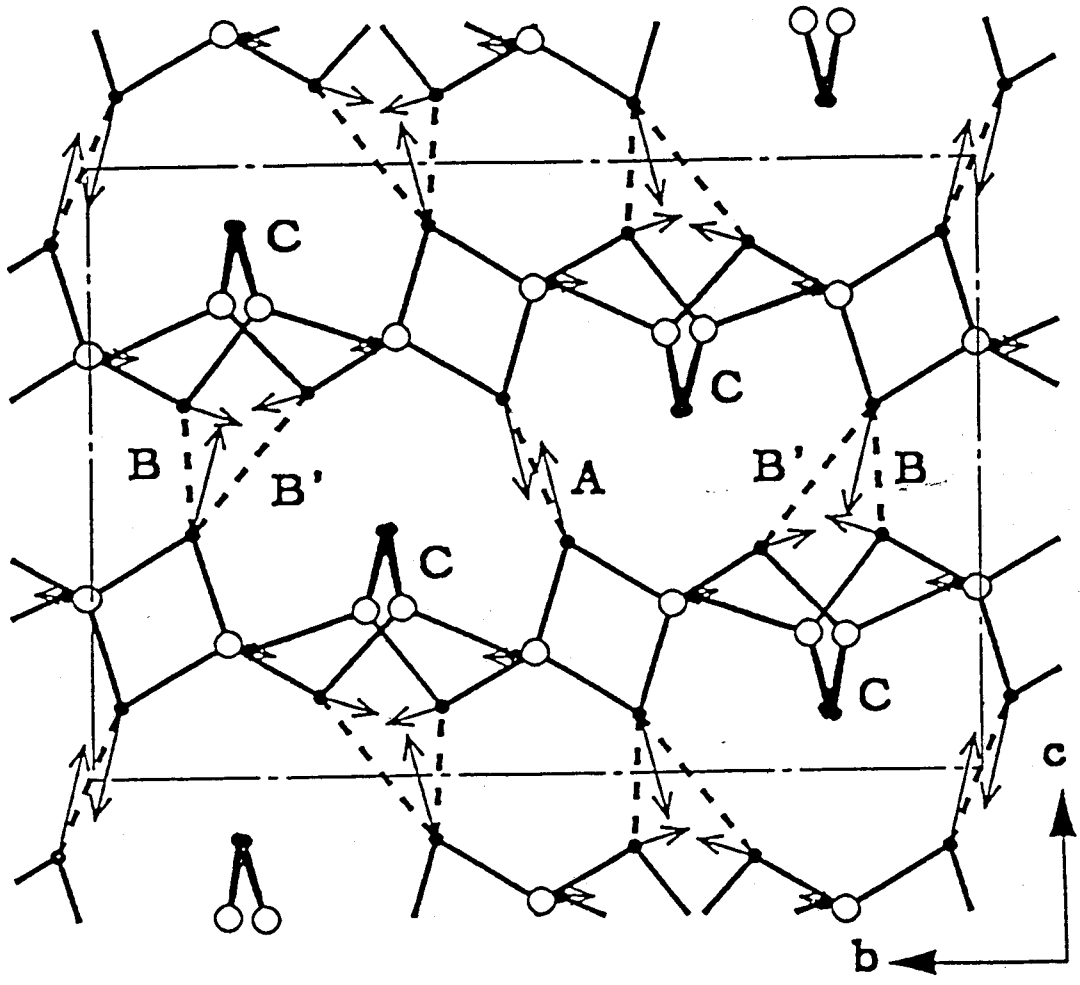


Figure 2.17: Projection of layered structure of c–$GeSe_2$ to [100] plane. Open circles indicate Ge atoms; black dots, Se atoms; and heavy lines, covalent bonds. Arrows indicate the atomic motions of the $A^*$ mode calculated by E-VFF-BP by taking Se–Se weak bonds, A, B, and B′ ( dashed lines ), into account ( From Ref. [40] ).

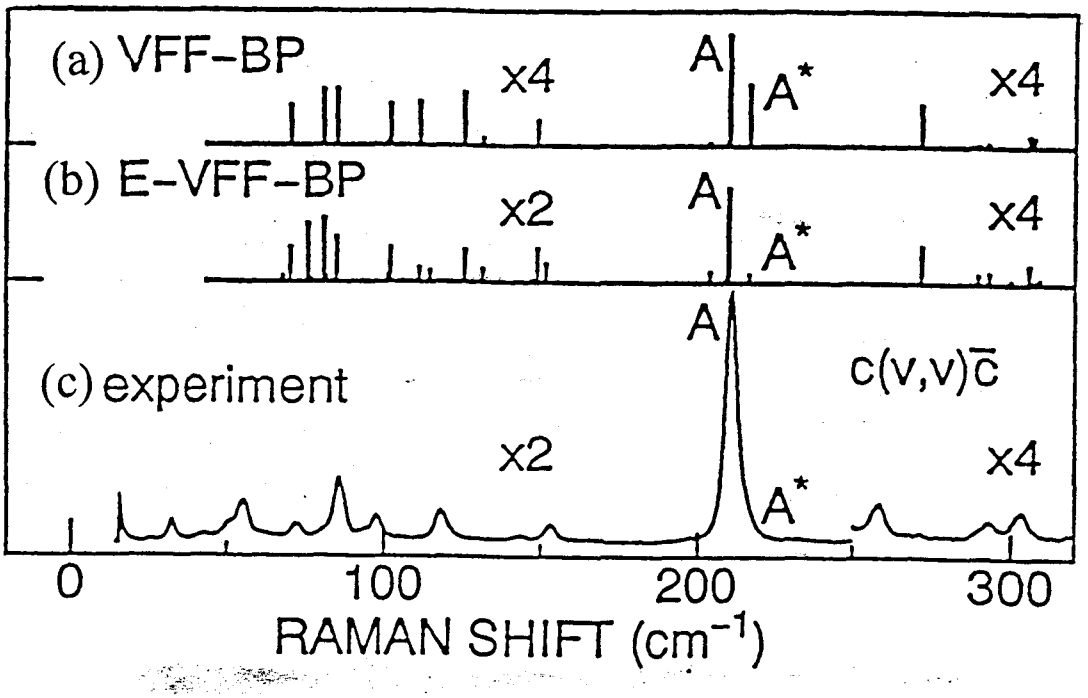


Figure 2.18: Raman intensity calculated for c–$GeSe_2$ by (a) VFF-BP and by (b) E-VFF-BP are compared with (c) the experimental spectra of c–$GeSe_2$ ( From Ref. [40] ).

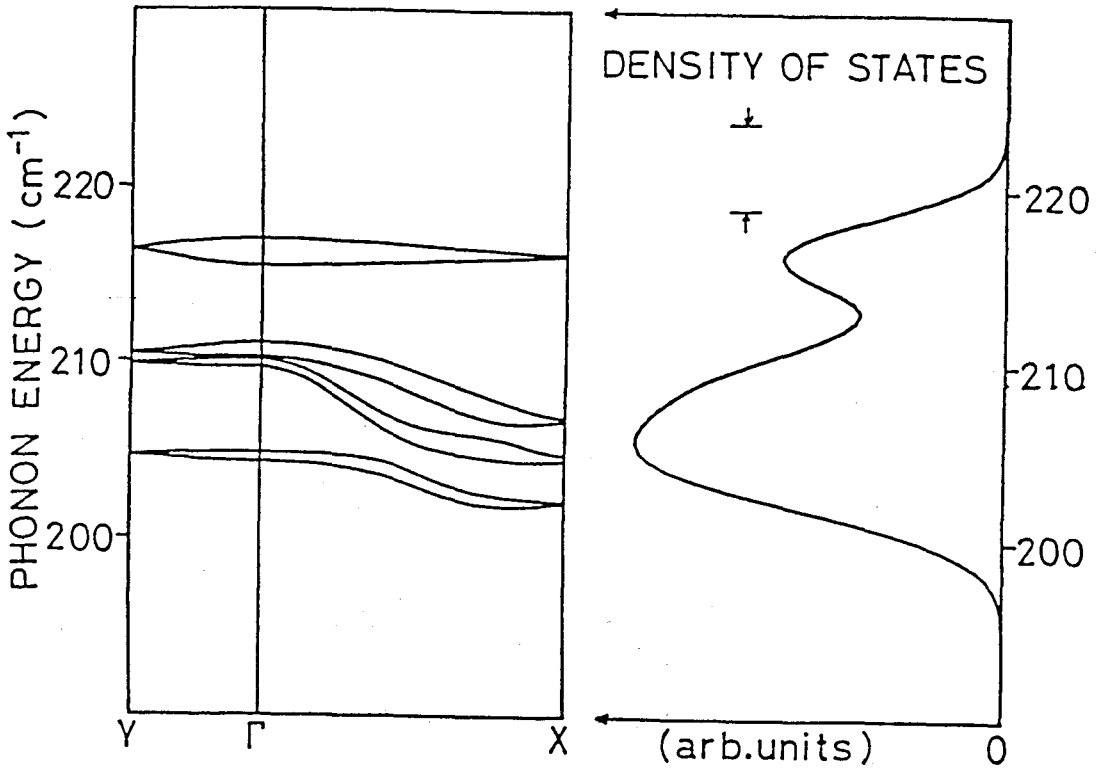


Figure 2.19: The phonon dispersion curve and the density of states for the VFF model. Eight branches, mode 41 $\sim$ mode 48, are shown. The density of states is calculated on the assumption of Gaussian peaks with a width of about 5 cm$^{-1}$ FWHM. In this model, the interlayer interaction are not included ( From Ref. [66] ).

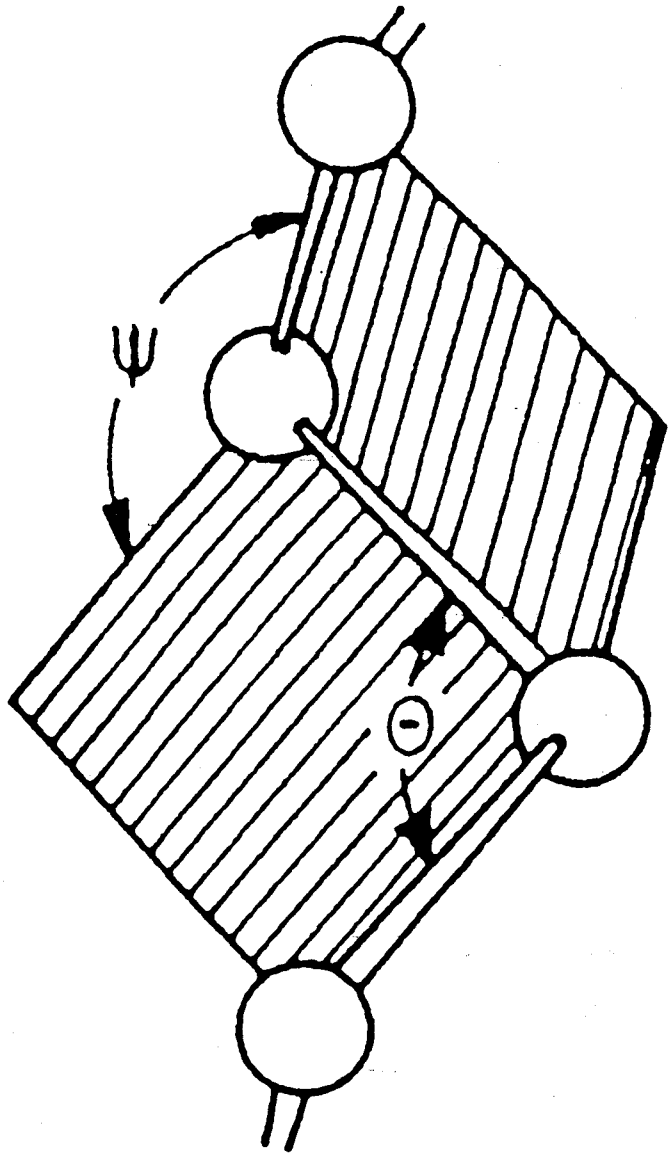

Figure 2.20: Local coordination of atoms for trigonal Se. $\theta$, indicates the angle between bond vectors of two nearest neighbor atoms, and $\psi$, the dihedral angle between adjacent bonding planes ( From Ref. [71] ).

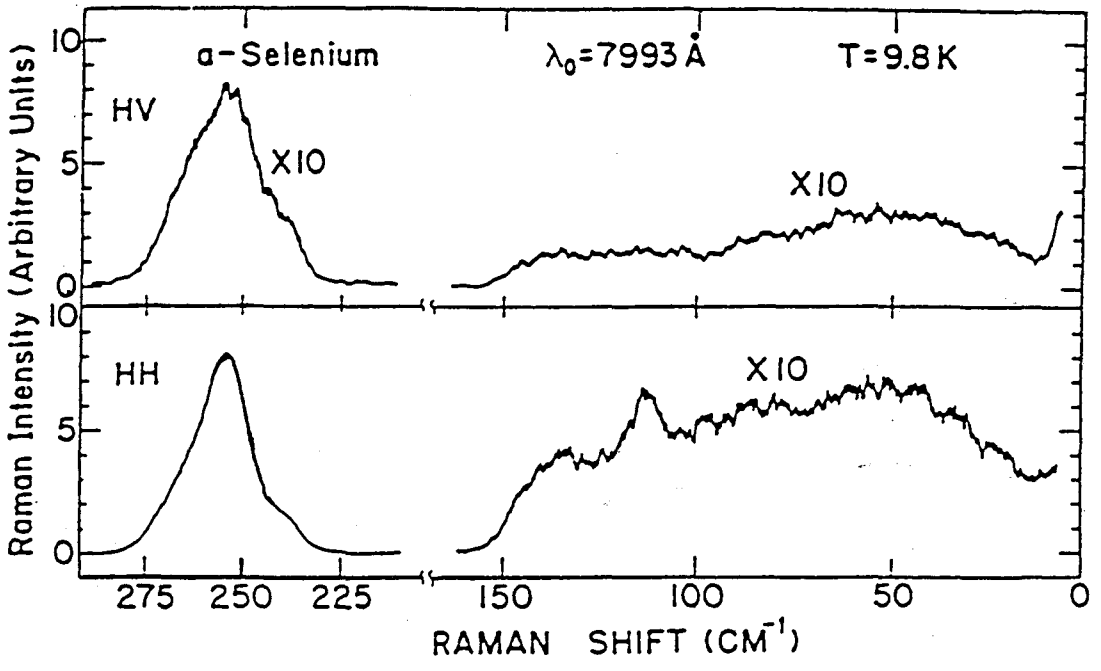


Figure 2.21: The transmission Raman spectra of bulk g–Se for HH and HV polarization. There is a lower energy shoulder at 235 $cm^{-1}$ beside the main vibration band at 255 $cm^{-1}$ ( From Ref. [72] ).

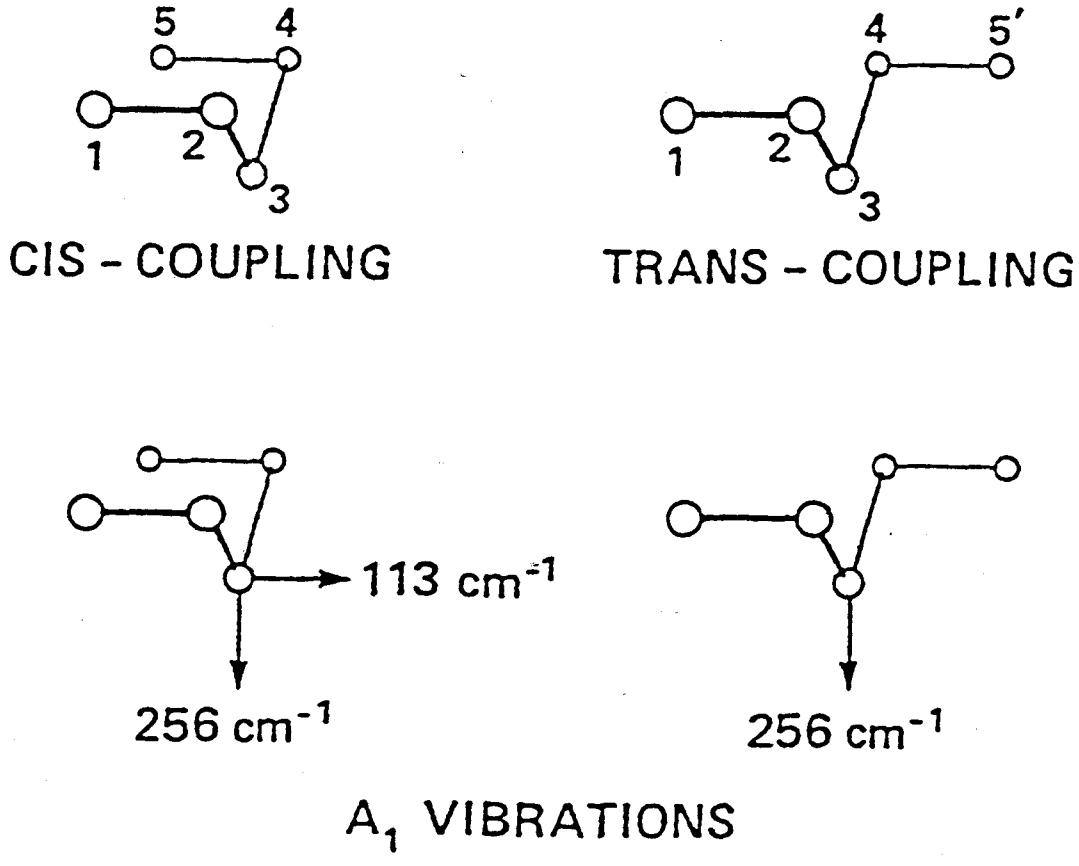


Figure 2.22: Cis- and trans-coupling configurations for molecular bonding in Se. The essential difference in the two configurations is in the placement of atoms 5 and 5'. In the cis-coupling the dihedral angles alternate in sign, while in the trans-coupling the sign is maintained. Also shown are the atomic displacements of the $A_1$ symmetry vibrational modes. For the cis-coupling there are two modes: the first with a displacement in the bonding plane, and the second mode with a displacement perpendicular to this plane. In contrast, the trans-coupling gives only one mode ( From Ref. [74] ).

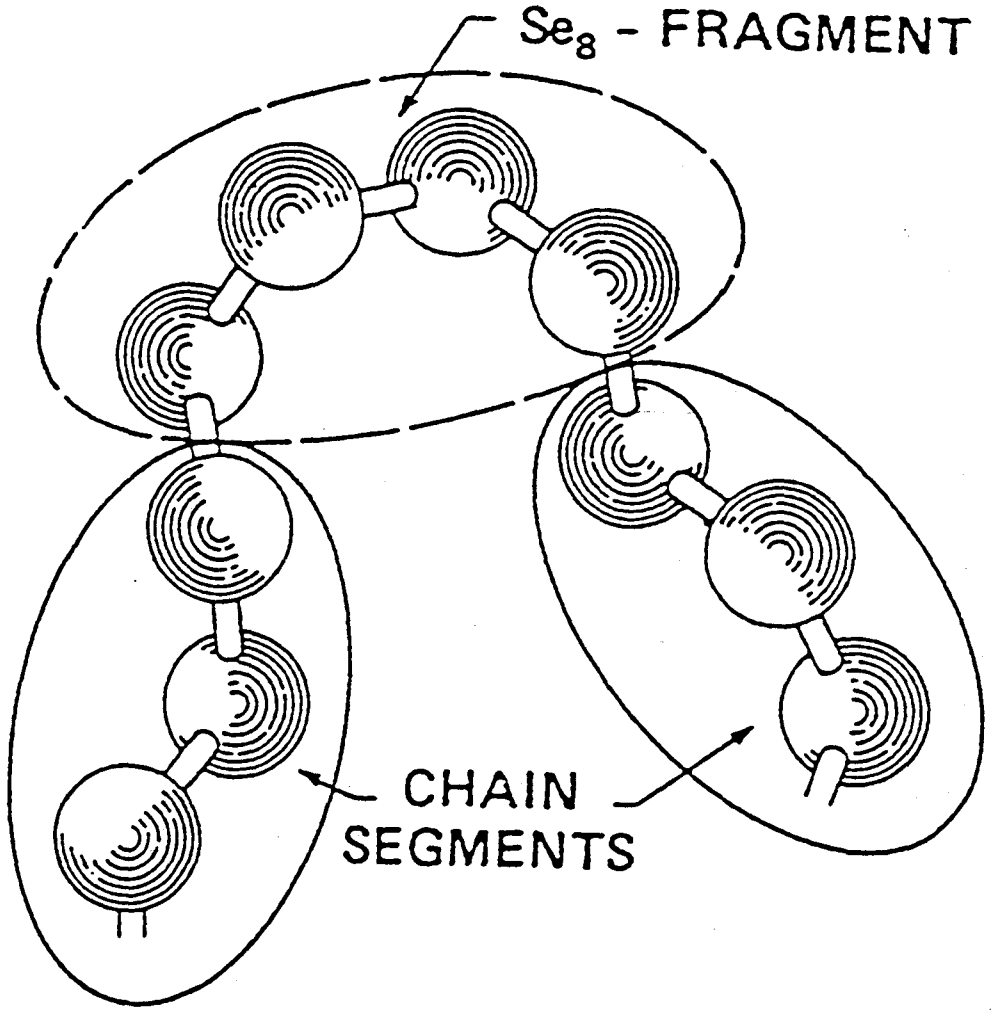


Figure 2.23: Local molecular order in a–Se chain where there are segments characterized by repetition of the same dihedral angle, the *chain-like* part in the sense of tc–Se, and segments characterized by alternating dihedral angles, the *ring-like* part in the sense of the $Se_8$ molecule ( From Ref. [74] ).

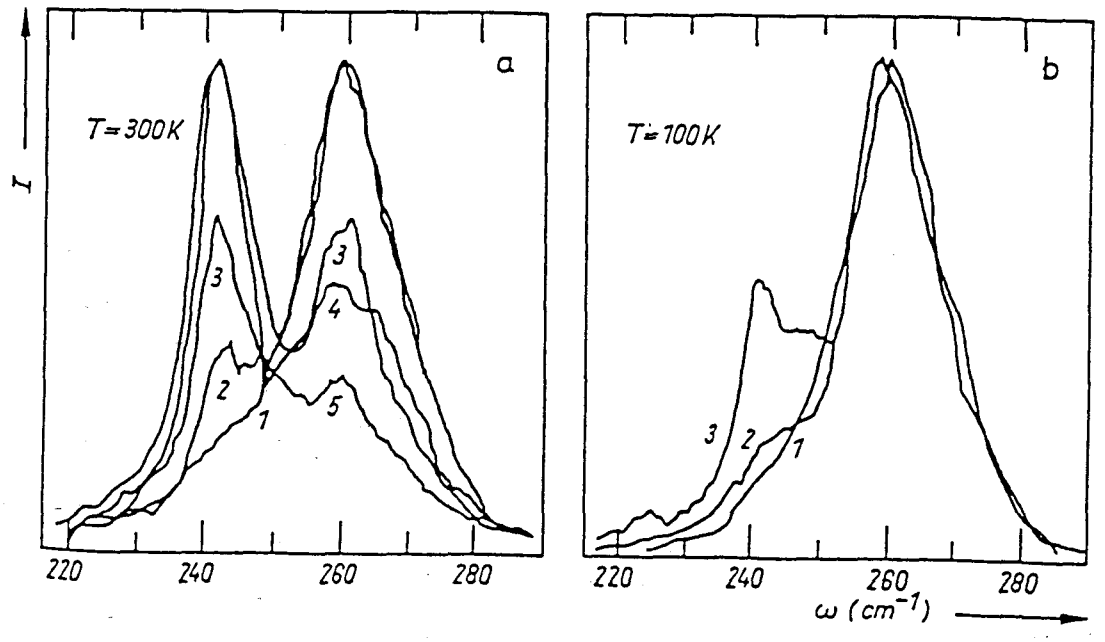


Figure 2.24: Transformation of Raman spectra of amorphous Se with increasing laser beam power. a) T = 300 K; Power P = (1) 4, (2) 6, (3) 7.5, (4) 10 mW, after cycle (4) sample is allowed to rest in the dark and then the spectrum (5) is recorded with P = 3 mW.

b) T = 100 K; P = (1) 5, (2) 20, (3) 25 mW ( From Ref. [78] ).

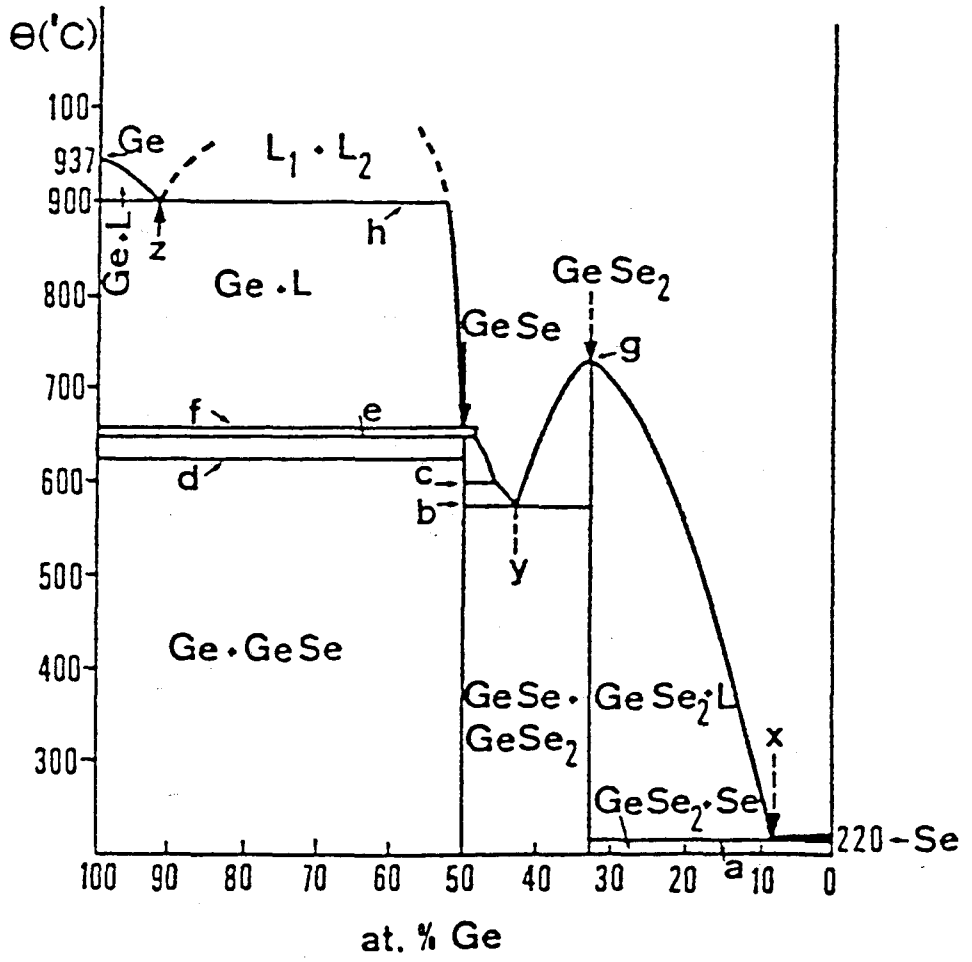


Figure 2.25: Phase diagram of Ge–Se system. a: 218 °C (2); b: 580 °C (3), 578 °C (4), 573 °C (5); c: 630 °C (3), 603 °C (5); d: 627 °C (5); e: 660 °C (4), 651 °C (5); f: 666 °C (4), 661 °C (5); g: 740 °C (3, 4, 5); h: 900 °C (4), 890 °C (5);
X: at.% Ge = 8 (2); Y: at. % Ge = 38 (3), 40~42 (4), 43 (5); Z: at.% Ge = 88~89 (4), 86 (5);
(2): Dembovsky et al. Ref. [80]; (3) vinogradova et al. Ref. [80]; (4) Ross et al. Ref. [82]; (5): Quenez et al. Ref. [83] ( From Ref. [55] ).

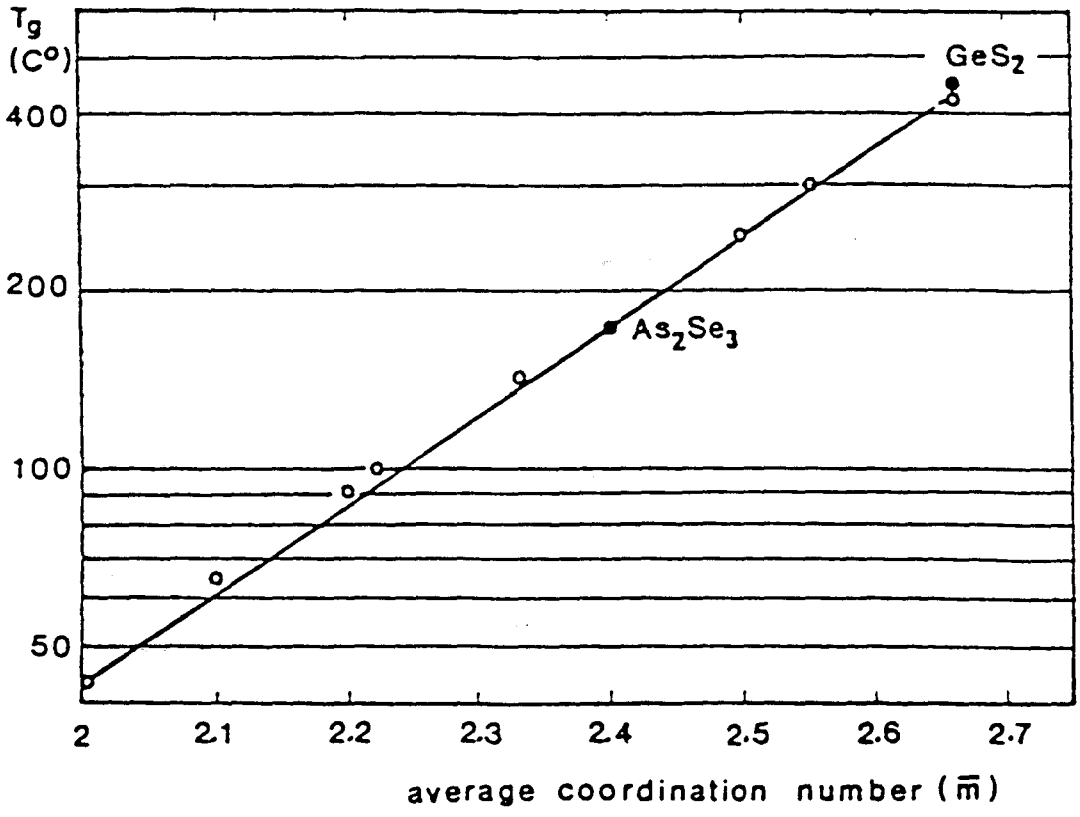


Figure 2.26: $T_g$ as a function of average coordination number $\bar{m}$ for $Ge_xSe_{1-x}$ glasses. $T_g$ values of $As_2Se_3$ and $GeS_2$ are also shown ( From Ref. [79] ).

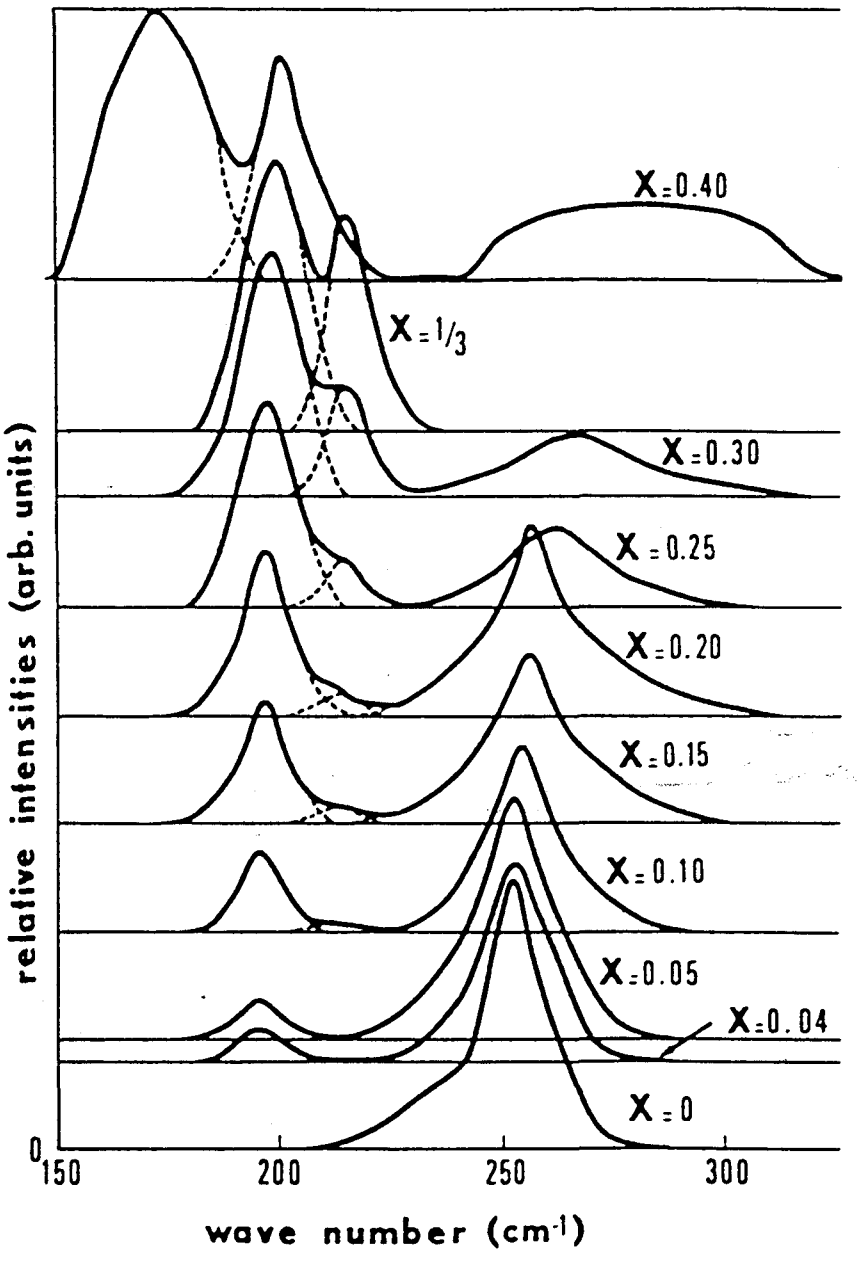


Figure 2.27: Raman spectra of $Ge_xSe_{1-x}$ ( $0 \leq x \leq 0.40$ ). The band $A_1$, corresponding to the vibration of $GeSe_{4/2}$ tetrahedra, appears in all $x$ except $x = 0$, while the band $A_1^C$ appears in the range of $0.10 \leq x \leq 0.33$ approximately ( From Ref. [55] ).

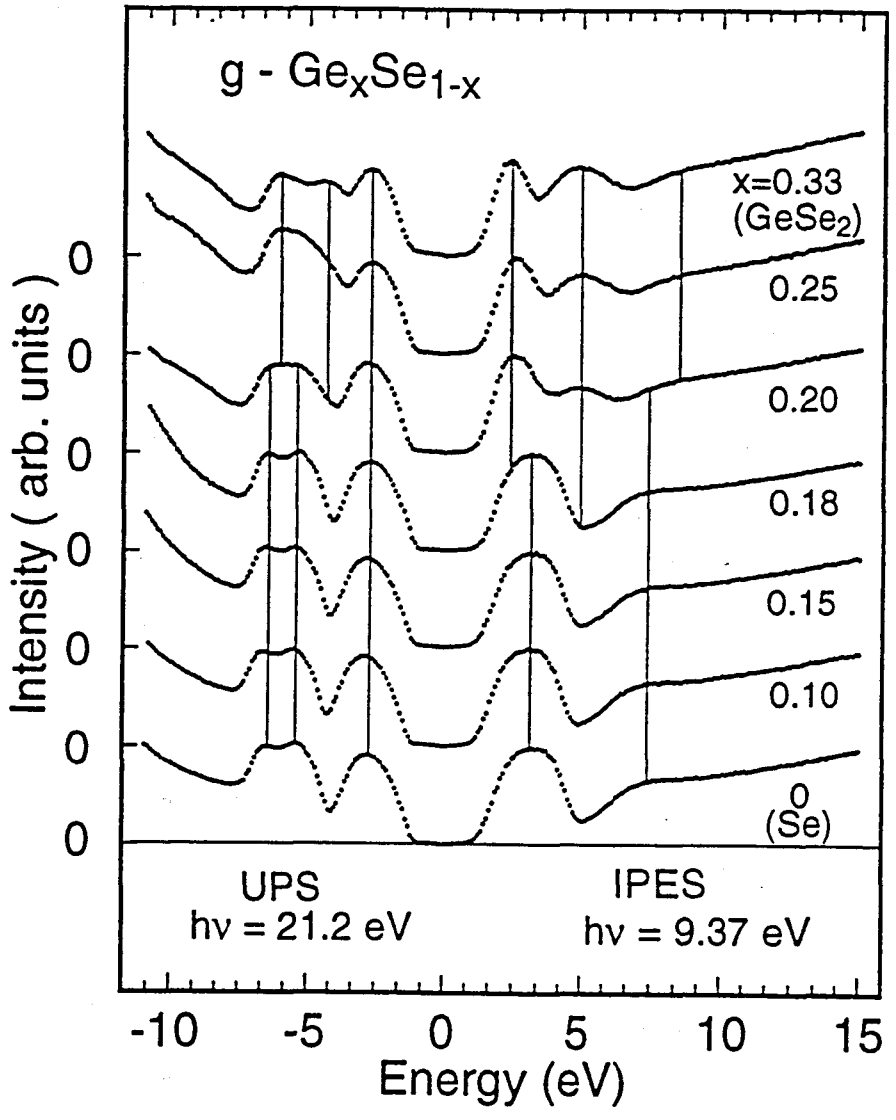


Figure 2.28: A series of the valence-band UPS and conduction-band IPES spectra of g–$Ge_xSe_{1-x}$ with $x$ from 0 to 0.33. Intensities of the UPS and IPES spectra are tentatively normalized at –2.7 eV, and 3.1 eV ( $x = 0$, 0.10, 0.15 and 0.18 ) and 2.4 eV ( $x = 0.20$, 0.25 and 0.33 ), respectively. Vertical bars indicate the positions of structures. Energies are referred to the Fermi level ( From Ref. [11] ).

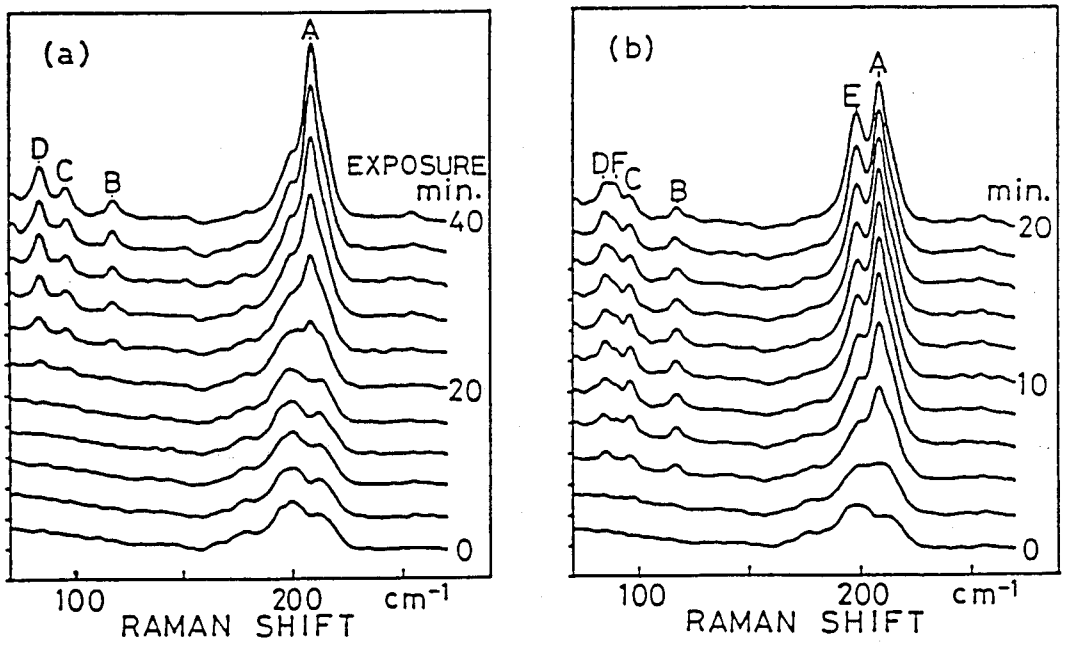


Figure 2.29: Time-resolved Raman spectra of PIC of the a–$GeSe_2$ representing two types of crystallization, (a) type (A), and (b) type (B). Exposure times are shown in the figure. Lines *A*, *B*, *C*, and *D* are due to the 2D form; lines *E* and *F* are due to the 3D form ( From Ref. [33] ).

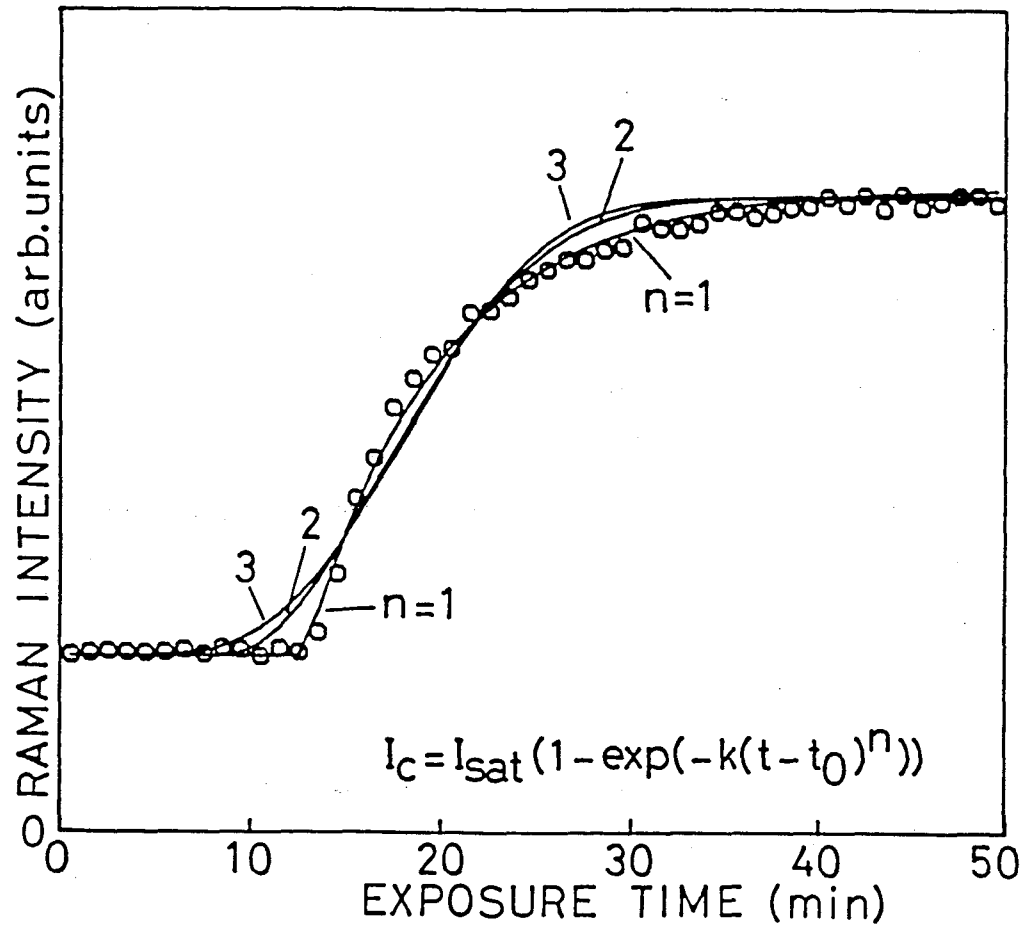


Figure 2.30: Growth curve of the 2D crystal in photo-induced crystallization type A by 22 mW incident laser power. The intensity at the A peak position are plotted. Solid lines illustrate the empirical fitting curves: $I_0[1 - \exp(-k(t - t_0)^n)]$. The best fit is obtained for $n = 1$ ( From Ref. [33] ).

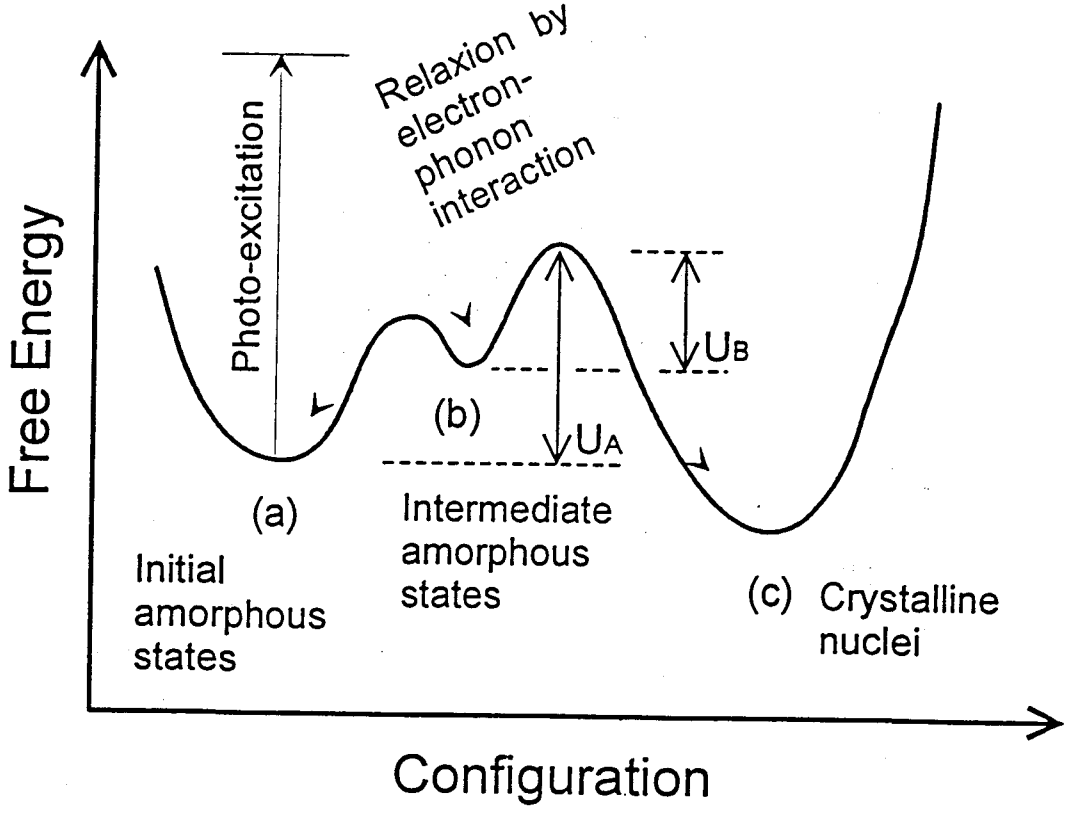


Figure 2.31: The diagram of the electronic and thermal processes during the latent period of the PIC process. ( From O. Matsuda used in the 6th International Conference on the Structure of Non-Crystalline Materials, Praha, Czech, 1994 ).

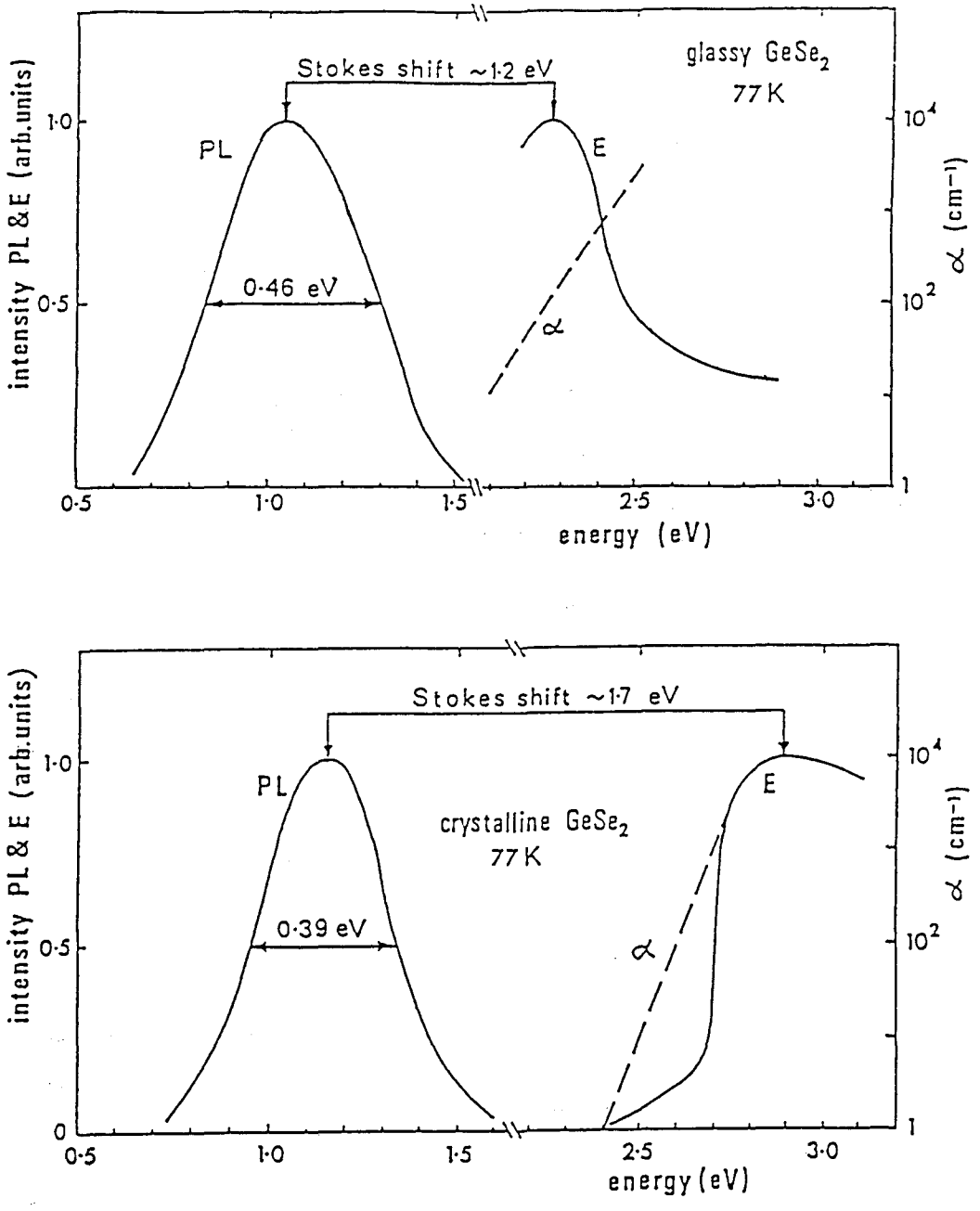


Figure 2.32: Photoluminescence, excitation and absorption spectra of glassy and single-crystalline $GeSe_2$ ( From Ref. [42] ).

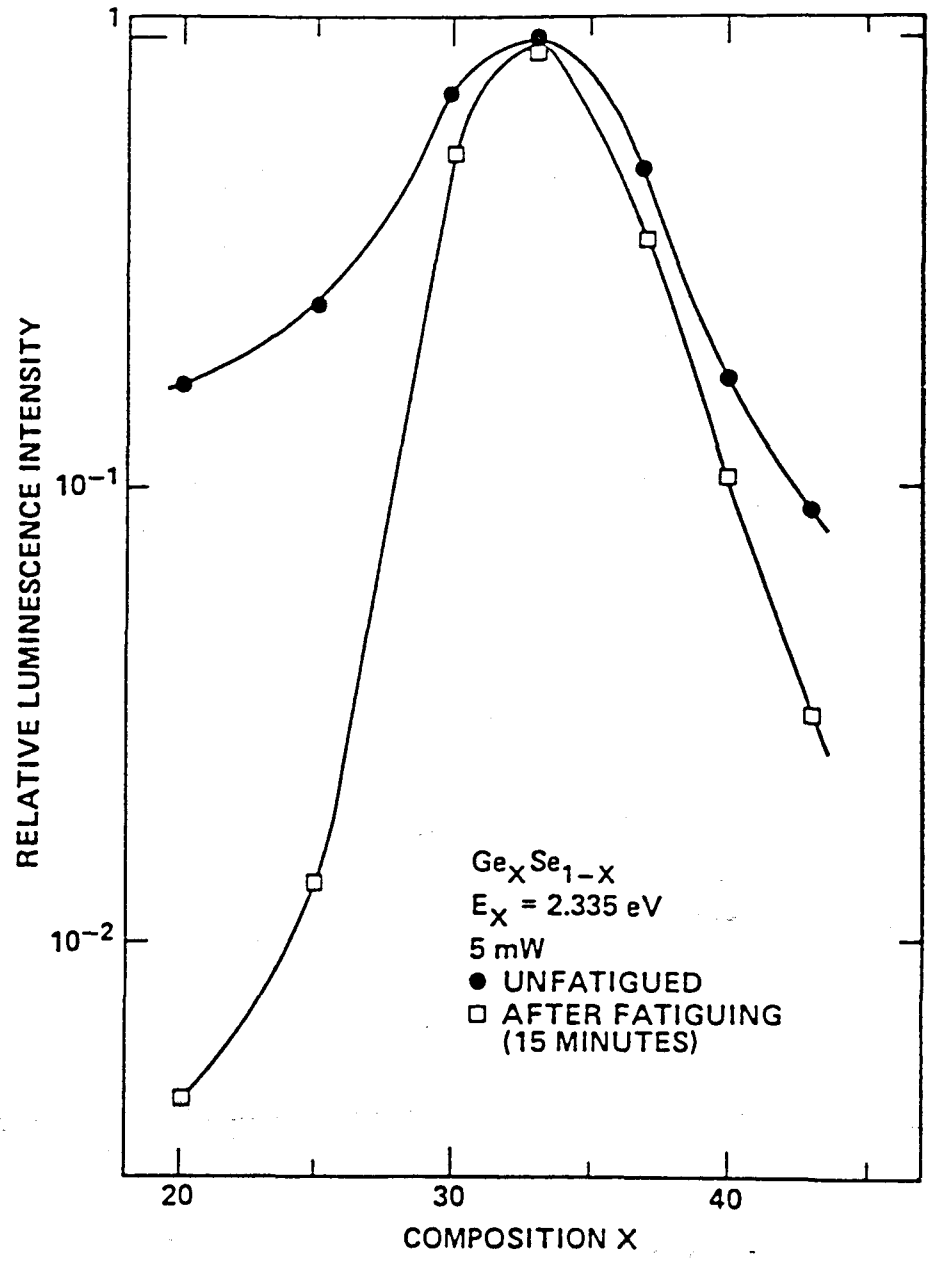


Figure 2.33: Luminescence intensity before and after fatiguing in $Ge_xSe_{1-x}$ glasses. The intensity before fatiguing is measured using a short pulse ( ~100 ms ) of excitation. Fatiguing then proceeded for 15 min. to be saturated substantially ( From Ref. [84] ).

# Chapter 3

# Experimental Procedures

## 3.1 Sample Preparation

For studying the Raman spectra of $Ge_xSe_{1-x}$ in the temperature range of 20 $\sim$ 850 °C which involves liquid state, thin film $Ge_xSe_{1-x}$ samples were prepared in an evacuated fused-silica cells. The photo-induced crystallization ( PIC ) was studied in thin films of $GeSe_2$. In photoluminescence ( PL ) measurement, bulk glassy ( g– ) and crystalline ( c– ) $GeSe_2$ were used.

### 3.1.1 Bulk Glassy $Ge_xSe_{1-x}$

Bulk g–$Ge_xSe_{1-x}$ samples were prepared by quenching melts. To obtain the bulk glasses of various compositions ( Table 3.1 ), the mixture of Ge and Se elements with 5N-grade in $x : (1-x)$ mole-ratio was sealed in evacuated fused-silica ampoules. These ampoules were put in a rocking electric furnace at 960 °C over 24 hours to make the two elements melt, and then they were thrown into the ice water quickly. The bulk g–$GeSe_2$ samples were cut in appropriate size ( thickness $\sim$1 mm ) for PL measurement.

### 3.1.2 Crystalline $GeSe_2$

A vapor phase growth method was used for preparing the $GeSe_2$ crystal from g–$GeSe_2$. An evacuated fused-silica ampoule, with the g–$GeSe_2$ sealed in, was kept at 700 °C for one week. The melting point of c–$GeSe_2$ is about 720 °C. For preparing the single crystalline $GeSe_2$, the temperature of one end of the ampoule was kept about 1 °C higher than the other end where the c–$GeSe_2$ grew. Polycrystalline ( pc– ) $GeSe_2$

was also prepared in similar growth method to that for the single crystal but with the temperature difference of the two ends in the ampoule larger than 5 °C. All the crystalline samples for PL measurement were not polished. The bulk single crystals were cut in appropriate size ( thickness ~1 mm ) with two natural-cleavage ( 001 ) surfaces

### 3.1.3 Thin Films of $Ge_xSe_{1-x}$

The g–Se thin film was made from 5N-grade Se element. For other films, with Ge composition of 0.04~0.33, we used the obtained bulk glasses of each compositions. Thin films of $Ge_xSe_{1-x}$ glasses were prepared by quenching from the melts. The Se element or bulk glasses were held in evacuated fused-silica cells where a narrow gap was defined by two parallel plates [89]. Figure 3.1(a)~(g) shows the processes of thin films' preparation. In the case of the Se sample, the cell containing Se was put in an electric furnace at 600 °C for 24 hours to make the narrow gap be completely permeated by the melting Se. Then the cell was thrown into the ice water and the melting Se was suddenly frozen in the narrow gap with the thickness of ~1 $\mu$m. Other films were also made in the same procedure as that of the Se film except the melting compounds were kept at 940 °C.

For the PIC measurement, the $GeSe_2$ samples were prepared in three different cooling rates by quenching in three different ways as follows.

1. For the fastest cooling rate, the film was made by quenching in ice water, as shown in Fig. 3.1(e).

2. For the slowest cooling rate, the film was made by quenching in air, as shown in Fig. 3.1(g).

3. For the medium cooling rate, we pulled the cell out of the furnace at 940 °C and immediately cooled it in a tube which was with an ice water bath, as shown in Fig. 3.1(f).

Table 3.1: $Ge_xSe_{1-x}$ samples prepared in this work are indicated by ○.

| $Ge_xSe_{1-x}$ | $x$ | Glass | | Crystal |
|---|---|---|---|---|
| | | bulk | thin film | |
| Se | 0 | | ○ | |
| $Ge_4Se_{96}$ | 0.04 | ○ | ○ | |
| $Ge_6Se_{94}$ | 0.06 | ○ | ○ | |
| $Ge_7Se_{93}$ | 0.07 | ○ | ○ | |
| $Ge_{10}Se_{90}$ | 0.10 | ○ | ○ | |
| $Ge_{15}Se_{85}$ | 0.15 | ○ | ○ | |
| $Ge_{18}Se_{82}$ | 0.18 | ○ | ○ | |
| $Ge_{20}Se_{80}$ | 0.20 | ○ | ○ | |
| $GeSe_2$ | 0.33 | ○ | ○ | ○ |

## 3.2 Raman Measurement

### 3.2.1 Study of Structural Changes

The Raman spectrum was investigated as a function of the sample temperature in the range from 20 °C to 850 °C. A dye-laser ( Rhodamine 6G ) and an Ar ion laser were used as excitation light sources whose energies cover the range of 1.93~2.71 eV. All Raman spectra were acquired in a back scattering configuration. The incident light was polarized vertically ( V ) to the plane of incident and scattering light. To prevent an additional temperature rise, the incident light was focused onto a rectangular region of about 5mm×0.1mm by a cylindrical lens with the light power about 8 mW. The scattered light was dispersed by a triple grating monochromator with the spectral resolution of about 1 $cm^{-1}$. Using a multi-channel photo-detector, the Raman spectrum was accumulated for 10 minutes at each temperature which was controlled within ±1 °C by an electric furnace for the optical measurement. The measurements were made in the sequence of increasing temperature. Generally, the temperature increasing rate between two successive measurement was 2~5 °C/min..

### 3.2.2 Photo-induced Crystallization

The Photo-induced crystallization ( PIC ) study was carried out in the thin films of $GeSe_2$. The 488 nm ( 2.54 eV ) light of the Ar ion laser, with the light power in the range of 5~50 mW, was focused onto the sample surface with a typical illumination region of about 50 $\mu$m in diameter by a spherical lens. Using the excitation light for the PIC as a Raman probe, the transformation of the Raman spectra during the PIC process was recorded in every 1 minute. All the PIC measurement were made at room temperature.

## 3.3 Photoluminescence Measurements

The PL spectra of the bulk glassy and crystalline $GeSe_2$ were excited by a dye laser, an Ar ion laser and a He-Cd laser with the light energy in the range of 1.93~2.81 eV. The excitation light was focused onto the bulk sample's surface with a typical illumination region of about 2 mm in diameter with the light power in the range of 10~30 mW. The PL emission was chopped ( 450 Hz ) and dispersed by a 20 cm single grating monochromator and detected by a liquid nitrogen cooled Ge PIN photo-diode. Detected signals were amplified ( 10~500 times ) and sent to a lock-in-amplifier.

In the lower temperature range ( 10~100 K ), the width of the slit was 1.25 mm which made the spectral resolution to ~0.01 eV at $\lambda = 1$ $\mu$m and in the higher temperature range ( 150~250 K ), the width of the slit was set at 2.5 mm or 5 mm where the spectral resolution were better than ~0.1 eV. The temperature of the samples was controlled by a gas-flow-type cryostat ( 10~250 K ).

Both in Raman and PL measurement, the sensitivity of overall measurement system was calibrated by measuring a halogen lamp whose spectra can be approximately regarded as the black-body radiation.

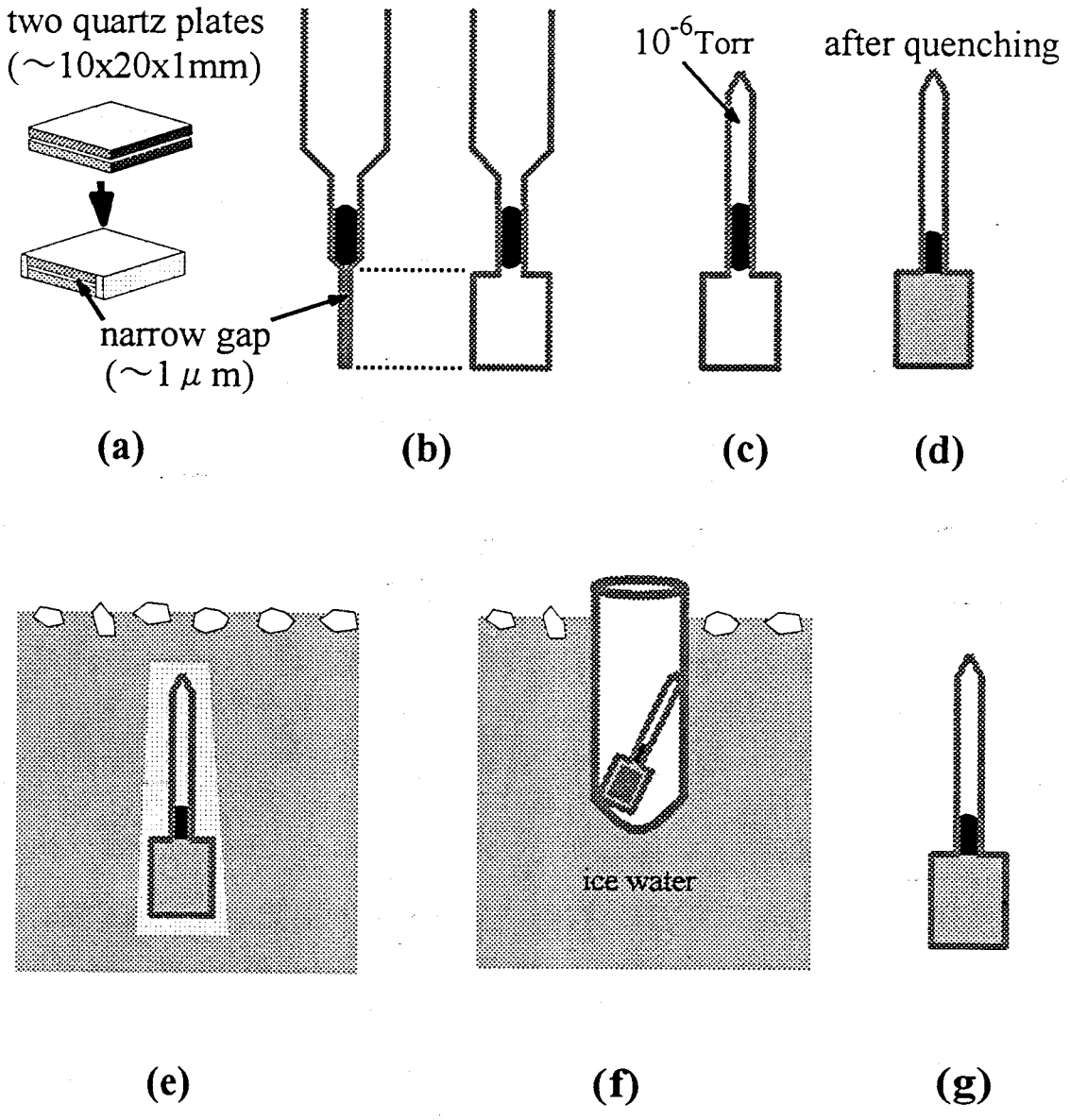


Figure 3.1: The processes of preparing the thin films. Se element or bulk glasses are held in the cell ( a ), ( b ) where a narrow gap is defined by two parallel plates. After ( c ) sealing the cell in a $10^{-6}$ Torr vacuum, ( d ) the thin films are prepared by quenching melts. ( e ) in ice water, ( f )in an ice water bath, and ( g ) in air, show the different cooling ways to obtain the glasses with different cooling rates in a sequence from fast to slow.

# Chapter 4

# Structural Changes at Glass-transition in $GeSe_2$

In this chapter, the Raman spectra of $GeSe_2$ are extensively studied in the temperature range from 30 °C to 730 °C. Our concern is the structure and structural changes at the glass-transition and melting. These phenomena should be related to the medium-range structure ( MRS ) which exists in both glassy ( g– ) and liquid ( l– ) $GeSe_2$ as described in chapter 2.

## 4.1 Results: Temperature Dependence of Raman Spectra

Figure 4.1 shows the Raman spectra of the $GeSe_2$ thin film at various temperatures below the crystallization temperature. The experiment is carried out in a sequence of increasing temperature mode. Three characteristic Raman bands of the g-$GeSe_2$, $A_G$, $A_1$ and $A_1^C$ are observed around 200 $cm^{-1}$. As we have mentioned in chapter 2, that the $A_1$ and $A_1^C$ bands are related to the breathing vibrational modes of the corner-sharing tetrahedra ( CST ) and the edge-sharing tetrahedra ( EST ) respectively, and the $A_G$ band is related to the stretching vibrational mode of the Ge–Ge wrong bonds. At temperatures lower than 350 °C, each spectrum is accumulated for 10 minutes at each temperature. Because the thermal crystallization for the amorphous $GeSe_2$ films prepared by vacuum evaporation occurs above 350 °C [33], the present measurement above 350 °C is carefully made in order not to overlook any crystallization process. In

the temperature range of 350~420 °C the accumulated time for a Raman measurement is about 2 hours at each temperature, except at 390 °C and 410 °C, where the spectra are monitored for over 16 hours. At each temperature, however, no notable time-dependent spectral change is observed. As shown in Fig. 4.1, the Raman bands $A_G$, $A_1$ and $A_1^C$ shift to the lower energy side with increasing temperature. By comparing the spectra at 30 °C with those at 420 °C, a significant change of the spectral shape comes to be obvious.

When the temperature is higher than 420 °C, the Raman band of c-$GeSe_2$ ( the *A* band in Fig. 2.7 ) begins to appear with the passage of time. In this work, the crystallization temperature $T_c$ is treated as the temperature at which the crystalline spectra appear. Figure 4.2 shows the time dependence of the integrated intensity of the *A* band at the crystallization temperatures ( $T_c$ ) 440 °C and 450 °C. The intensity of the *A* band is obtained by four-Gaussian band fitting of the spectra including the three amorphous components ( $A_G$, $A_1$, $A_1^C$ ) with a linear base line. At the $T_c$ = 450 °C, no notable change of the Raman spectra has been recorded in the first 10 minutes which corresponds to the latent period in the PIC process. Then, the intensity of the *A* band increases with the time passing and saturates after about 1 hour from the very beginning when we raise the temperature to 450 °C. At the $T_c$ = 440 °C we can not see the crystalline *A* band during the first 1 hour . After about 1 hour, the *A* band begins to grow gradually and saturates approximately after 20 hours. Obviously, the crystallization at 450 °C proceeds much faster than that at 440 °C. Once the specimen turns into the crystalline phase, the vibrational bands in crystalline Raman spectra shift with temperature by a coefficient -0.01 $cm^{-1}/K$ which is about the same value measured in bulk c-$GeSe_2$ [33].

Figure 4.3 shows the change of the Raman spectra around the melting point $T_m$. At 690 °C, the characteristic c-$GeSe_2$ *A* band appears clearly together with other crystalline vibrational bands on the lower energy side. The intensity of the *A* band becomes weaker with increasing temperature up to 710 °C. When the temperature is higher than 710 °C, the c-$GeSe_2$ *A* band disappears in the Raman spectra and the specimen is molten. By these results, the melting point $T_m$ is evaluated as 710 °C in this specimen. Raman spectra of l-$GeSe_2$ are accumulated for 1 hour at each temperature up to 730 °C. The spectra around 200 $cm^{-1}$ are similar to those at 420 °C.

## 4.2 Discussion

First we discuss the difference among the shapes of the spectra at 30 °C, 420 °C and at 730 °C. By fitting the Raman spectra with three Gaussians corresponding to the $A_G$, $A_1$ and $A_1^C$ bands at various temperatures ( in Fig. 4.4, the two curves for $A_1$ and $A_1^C$ are shown ), the ratio of the integrated intensities of $A_1^C$ and $A_1$ bands ( $A_1^C$:$A_1$ ) is obtained. The ratio $A_1^C$:$A_1$ has notable changes as shown in Fig. 4.5 (a). The glass-transition temperature $T_g$ have been determined to be 396 °C by using differential thermal analysis ( DTA ) for $GeSe_2$ bulk glass [28], and in Ref. [79] the $T_g$ has been declared as about 440 °C. In our results, the intensity of the $A_1^C$ and $A_1$ bands begin to change drastically at a temperature around 370 °C. As we shall see later in this chapter, the onset temperature is naturally related to the glass transition. So that the glassy, SCL, crystalline and liquid phases are separated by the characteristic temperatures: $T_g$( 370 °C ), $T_c$( 440 °C ) and $T_m$( 712 °C ).

In the glassy phase, the intensity ratio $A_1^C$:$A_1$ is kept at about 1:3 as shown in Fig. 4.5 (a). In the SCL phase, the ratio $A_1^C$:$A_1$ approaches 1:1 quickly with increasing temperature. It should be noted that the ratio $A_1^C$:$A_1$ in the liquid phase at 720 °C and 730 °C is similar to that in the SCL at 420 °C. From the temperature dependence of peak positions of the $A_1$ and $A_1^C$ bands in the glassy phase, we find that both the $A_1$ and $A_1^C$ bands in the g–$GeSe_2$ shift with the same temperature coefficient –0.017 $cm^{-1}$/K, which is almost twice of that in the c–$GeSe_2$. The peak positions of the $A_1$ and $A_1^C$ bands in the SCL and liquid $GeSe_2$ are near the extrapolated line from the temperature dependence of peak positions in the g–$GeSe_2$ as shown in fig. 4.5 (b). These results also support our view based on the $A_1$ and $A_1^C$ bands: there is a similar MRS in g– and l–$GeSe_2$.

It has been shown that the $A_1$ and $A_1^C$ bands are related to the CST and the EST, respectively [36]. It is hasty to conclude that the numbers of the CST and EST for g– and l–$GeSe_2$ are quite different in parallel with the fact that the intensity ratio $A_1^C$:$A_1$ of the glass differs from that of the liquid. In the neutron diffraction experiment, the numbers of the CST and EST in g– and l–$GeSe_2$ have been estimated to be comparable with each other [90,91].

Before considering the changes of the intensity ratio at the glass-transition, we should review the Raman spectra of c–$GeSe_2$ which has a layered form. In the Raman spectra, the origin of the $A$ and $A^*$ bands has been ascribed to the breathing vibration

of the CST and EST, respectively [36]. In the usual non–resonant Raman spectra of the single crystal, the $A^*$ band is weaker than the $A$ band [36]. As we have mentioned in chapter 2, it has been confirmed that the peculiar weakness of $A^*$ band is due to the interlayer interaction in the two neighboring layers by using a combination of a VFF and a BP model [40]. The intensity ratio $A^*$:$A$ in various kinds of disordered $GeSe_2$ crystals is much larger than that in the single crystal under the non-resonant condition [36]. Then, it is probable that with increasing disorder, the interlayer interaction becomes weak so that the intensity ratio of $A^*$:$A$ enlarges.

Now we return to the problem of the intensity ratio $A_1^C$:$A_1$ in the g– and l–$GeSe_2$. In the previous work [36], the $A_1$ and $A_1^C$ bands in g–$GeSe_2$ have been associated with the $A$ and $A^*$ bands in the crystals, respectively. According to the spectral shape and the temperature dependence of the $A_1^C$ and $A_1$ bands' peak energies, the MRS which is maintained in the g–, SCL–, and l–$GeSe_2$ should be similar to each other. Thus the rapid decrease of viscosity $\eta$ with increasing temperature above $T_g$ is mainly caused by a relaxation of the interlayer constraint between two successively stacked layer–like fragments. The relative flow of the layer–like fragments results in a decrease of the interlayer interaction. The decrease of the interaction should cause an increase of the intensity ratio $A_1^C$:$A_1$ from 1:3 to 1:1 similar to the increase of the ratio $A^*$:$A$ in crystals with increasing the disorder.

Let us now turn to discuss the observation in the thermal crystallization ( TC ) processes which start from glassy states. The crystallization is considered to occur by the processes of nucleation and growth of crystals; that is, it begins at and propagates from certain centers. All the reaction occurs at crystal–liquid interfaces. To describe the rate of crystallization, two constants have been used [92-96]: the frequency of appearance ( nucleation ), $I$, of crystallization centers and the rate, $u$, of propagation of the crystal–liquid interface from these centers. These two rates have been described by Turnbull and Hillig in a number of articles [92-94]. It was demonstrated that in the absence of specific structural or chemical energy barriers to reorganization of the liquid to form a nucleus, the nucleation rate $I$ at a given degree of undercooling ( below the melting point $T_m$ ) is,

$$I = nk_l \exp[-\frac{b}{T_f(\Delta T_r)^2}], \tag{4.1}$$

where $n$ is the number of molecules per unit volume in the sample, $k_l$ is the frequency with which a molecule jumps across the crystal–liquid interface, $T_f$ is the reduced temperature $T/T_m$, and $\Delta T_r$ is the degree of undercooling, while $b = 5.33\pi\alpha^3\beta$. The

two dimensionless parameters, $\alpha$ and $\beta$, depend to the samples; the former relates to the crystal–liquid surface tension and the heat of fusion, the latter the entropy of fusion. The Equation 4.1 leads to a maximum in nucleation rate versus temperature relation at the temperature $T_{nc}$. The growth rate of crystal, $u$, is determined by [93],

$$u = \frac{\kappa(\Delta T)^2}{4\pi T\sigma}, \tag{4.2}$$

where $\kappa$ is the thermal conductivity of the super-cooled liquid and $\sigma$ is the free energy/area of the growth-crystal surface. The growth rate also shows a maximum at the temperature $T_{gc}$. Basing on the equations 4.1 and 4.2, the nucleation rate and crystal growth rate take their characteristic temperature regions due to the different temperatures $T_{nc}$ and $T_{gc}$, respectively, in which these two phenomena can be observed in the experimental period of time. The growth of crystal is considerably influenced by the population of the crystallization centers. For a good glass-former, a small overlap of these two temperature regions is needed.

At the $T_c$ = 450 °C after the 10 minutes latent period, it costs about 1 hour for the intensity of the A band to saturate. On the other hand, at the $T_c$ = 440 °C the latent period prolongs to 1 hour and then for about 20 hours the intensity of A band saturates. In the above two TC processes, the essential difference is the $T_c$. First, during the latent period, it is considered that the crystalline nuclei develops and at the end the crystal grows where the crystalline peak appears in the spectra. The shorter latent period time suggests a faster $I$ for the nuclei appearance. The $I$ at $T_c$ = 450 °C is faster than that at $T_c$ = 440 °C. Secondly, from the period for the intensity of crystalline $A$ band saturating, the crystal growth rate $u$ can be obtained. The $u$ at $T_c$ = 450 °C is faster than that at $T_c$ = 400 °C. Thus, both the temperatures $T_{nc}$ and $T_{gc}$ are higher than 450 °C.

Last, in our thin g–$GeSe_2$ films, which are held in the quartz cell, only the 2D–crystal ( HT crystalline form ) is obtained at the current temperature increasing ratio. For an bulk glass which is prepared by quenching melts in evacuated fused-silica ampoules ( chapter 3 ), it has been reported that the 3D–crystal ( LT crystalline form ) is obtained in vacuum at 350 °C [97]. As we have mentioned in chapter 4.1 that though the sample have been kept at 390 °C and 410 °C for over 16 hours, no crystallization process is observed. It is natural to conclude that for our g–$GeSe_2$ films the 3D–crystal is very difficult to be formed. The form of $GeSe_2$ crystal in the crystallization processes is strongly related to the preparation of the $GeSe_2$ glasses where their initial states are

considered to be different.

## 4.3 Conclusions

In this chapter, the results lead to the conclusions that:

1. Both in g–, SCL and l–$GeSe_2$, the MRS is implied as a topologically crystalline layer–like fragment. In g–$GeSe_2$, the lone pair Se–Se interaction between the two neighboring layer–like fragments restrains the vibrational intensity of the $A_1^C$ band which relates to the edge-sharing $GeSe_{4/2}$. The fact that the intensity ratio of the $A_1^C$ band to $A_1$ band changes quickly from 1:3 to 1:1 in the SCL is related to a drastic decrease of this interlayer interaction. The onset of the increasing ratio is related to the glass-transition temperature $T_g$.

2. In the TC processes the crystallization tendency, such as the crystalline form and the developing speed of the crystalline nuclei, is closely related to the preparation of the glasses and the crystallization temperature $T_c$. Both the temperatures, at which the velocity of crystalline nuclei growth or that of crystal growth reach to their maxima, are higher than 450 °C.

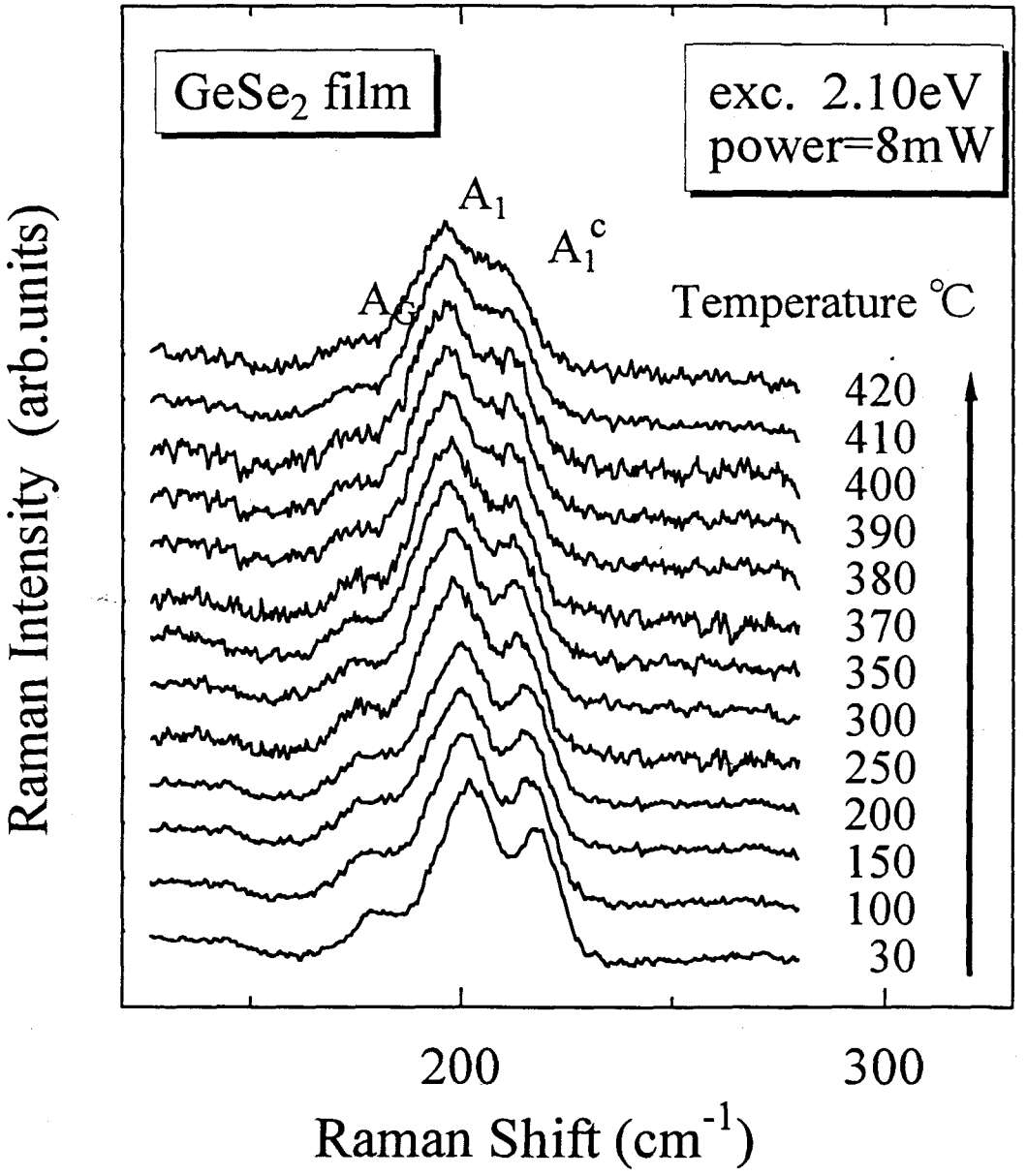


Figure 4.1: Raman spectra of the thin g–$GeSe_2$ film at various temperatures. The arrow indicates the sequence of measurement. Spectra around 200 $cm^{-1}$ at 420 °C are significantly different from those at 30 °C.

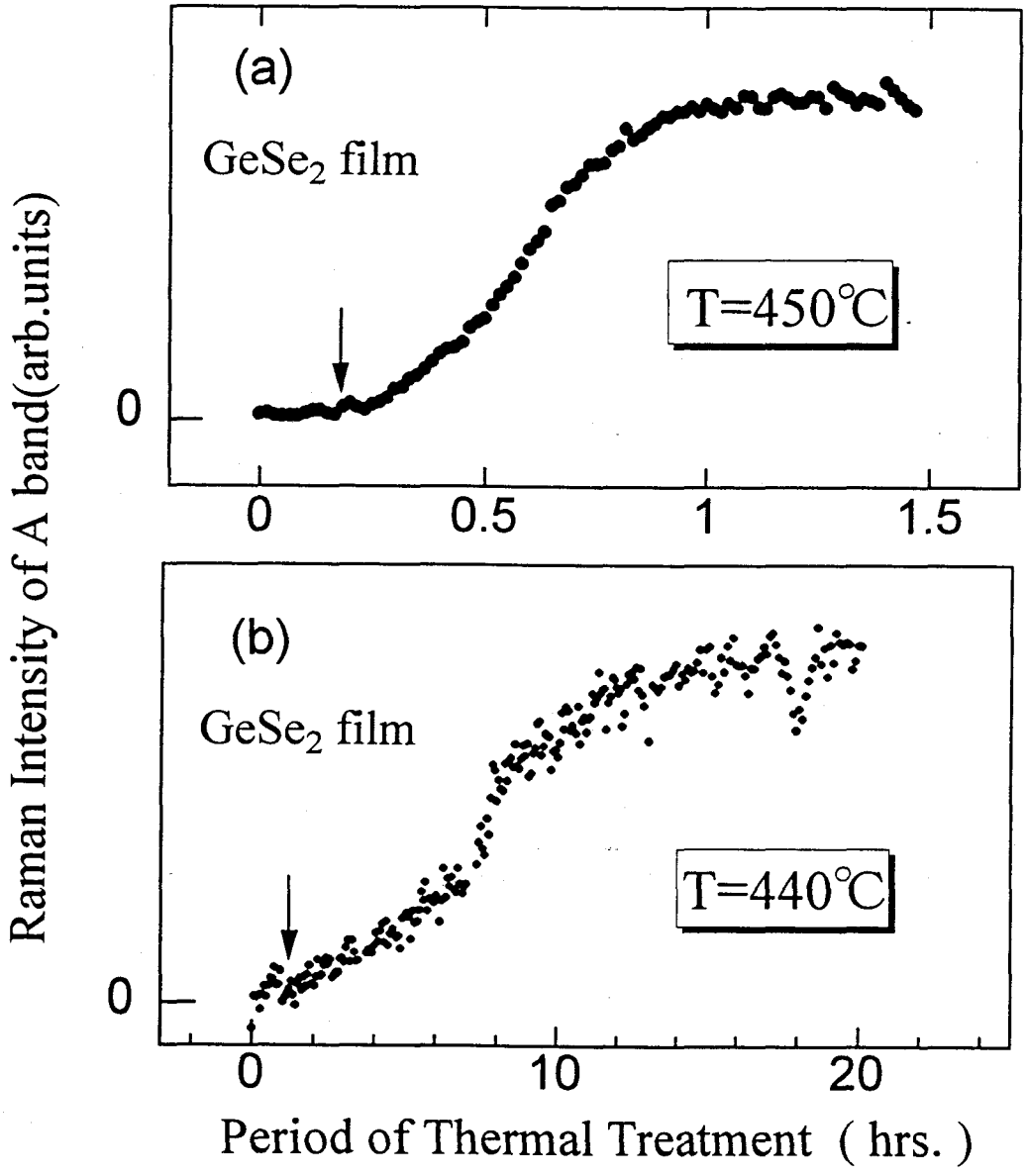


Figure 4.2: Time dependence of the intensity of the crystalline Raman band A for the thermal crystallization processes at 450 °C (a) and 440 °C (b). The arrows qualitatively indicate the starts of crystallization.

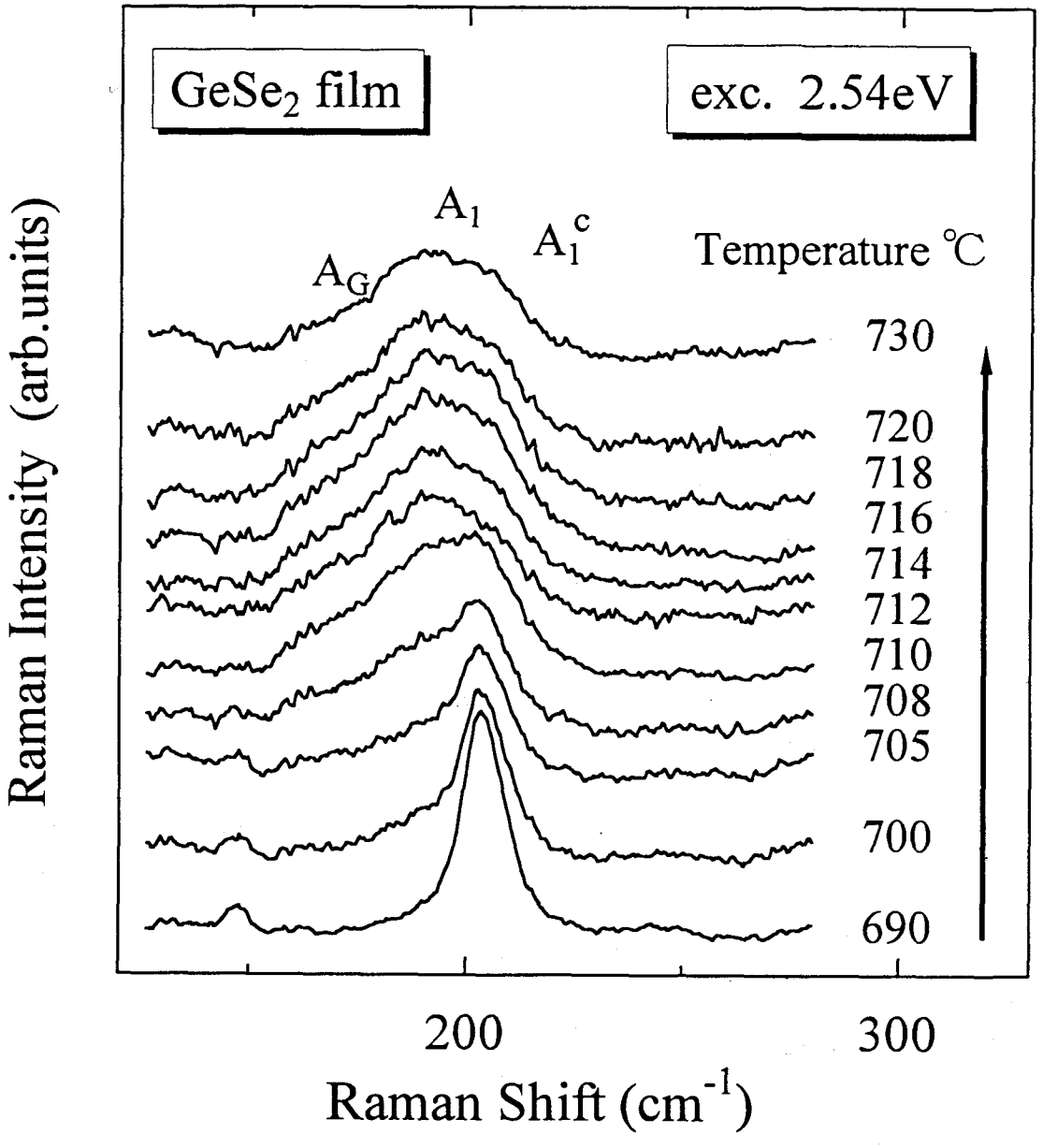


Figure 4.3: Raman spectra of c– and l–$GeSe_2$ at various temperatures. The crystalline vibration A band disappears above 710 °C which is related to the melting temperature $T_m$.

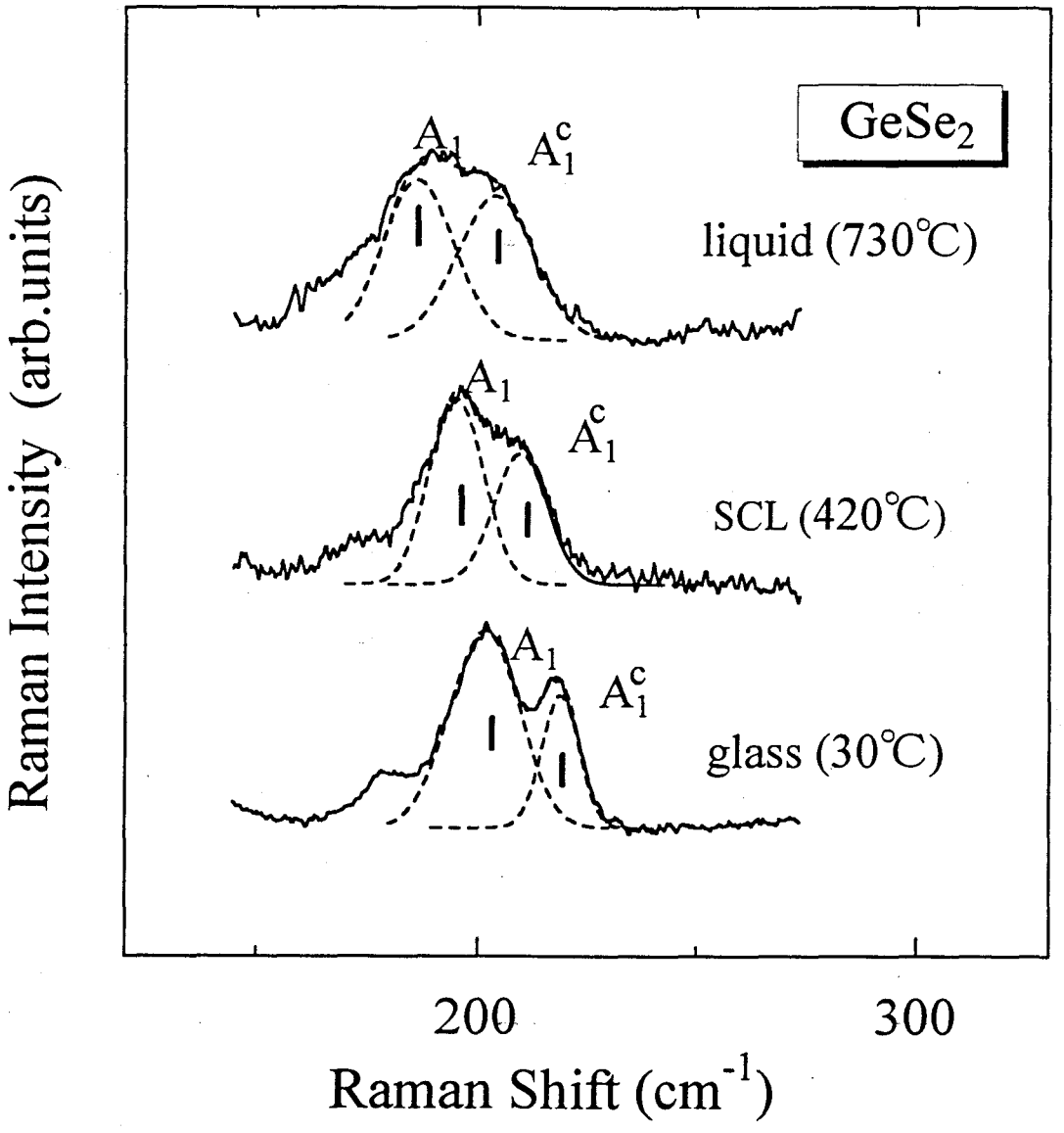


Figure 4.4: Raman spectra of g–$GeSe_2$ at 30 °C, SCL–$GeSe_2$ at 420 °C and l–$GeSe_2$ at 730 °C. The broken lines show the fitted Gaussian curves of the $A_1$ and $A_1^C$ bands.

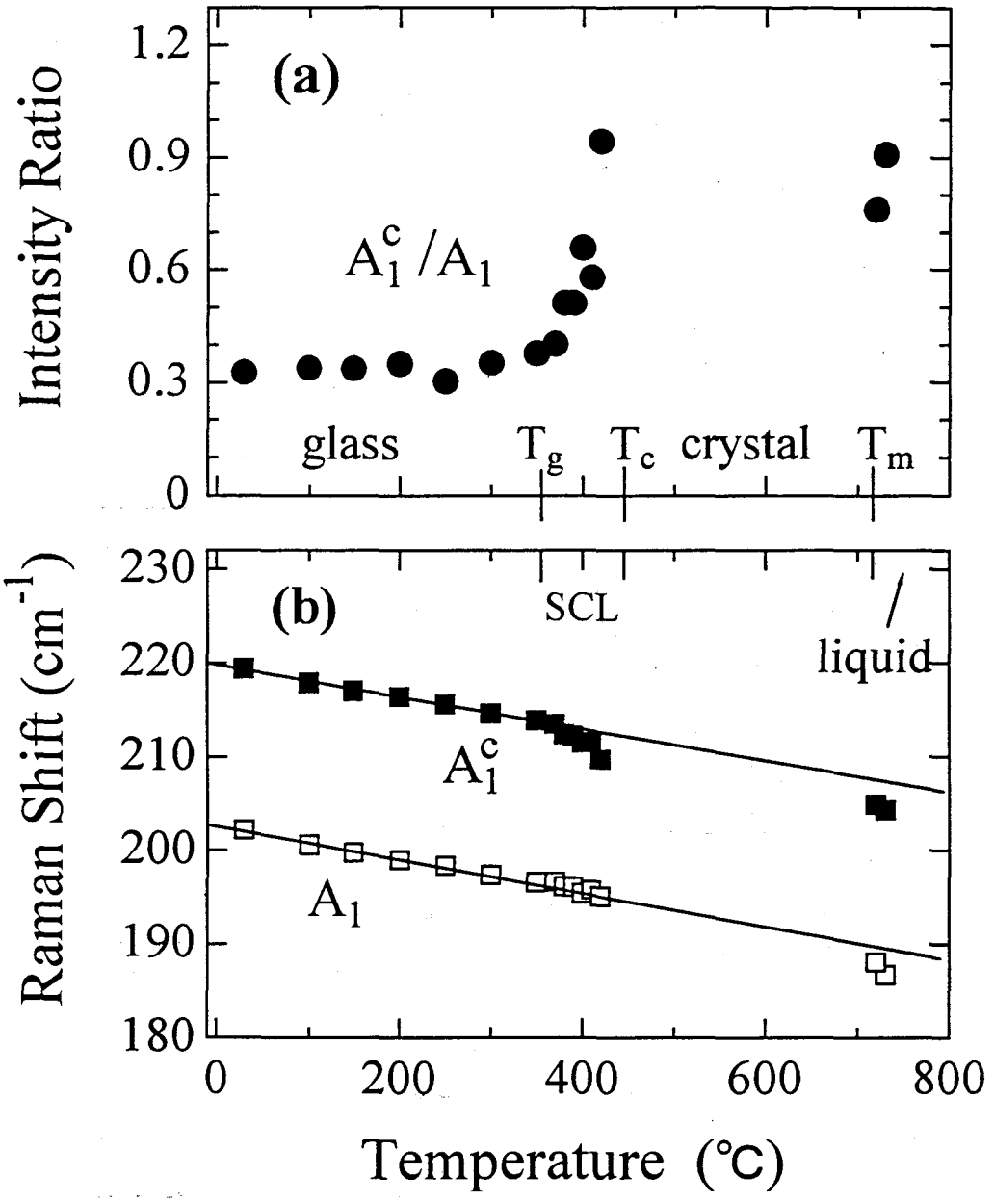


Figure 4.5: Temperature dependence of the vibrational $A_1$ and $A_1^C$ bands in g–, SCL and l–$GeSe_2$; (a) the intensity ratio of the $A_1^C$ and $A_1$ bands, and (b) the peak position of the $A_1$ and $A_1^C$ bands.

# Chapter 5

# Structure and Structural changes in $Ge_xSe_{1-x}$

The $Ge_xSe_{1-x}$ system ($0 \leq x \leq 0.33$) has been paid a great deal of interest in its structure and structural changes [28,32–37,55]. In the previous chapter, the structure and glass transition in $GeSe_2$ have been studied by the temperature dependence of the Raman spectra in glass, super-cooled liquid ( SCL ) and liquid. We expect that the Raman scattering technique will bring important clue to understand the structure and the structural changes in $Ge_xSe_{1-x}$ system. In this system, the structure is changed with varying Ge composition $x$. When the Ge content increases from 0 to 0.33, the structural dimensionality of the glass is supposed to increase since the trigonal ( tc– ) Se has a 1-dimensional chain structure, and crystalline ( c– ) $GeSe_2$ has a 2-dimensional form and a 3-dimensional form. These structural changes relate to the physical properties, such as the glass-transition temperature and the crystallization tendency.

In this chapter, the Raman spectra of $Ge_xSe_{1-x}$ ( $x$ = 0, 0.04, 0.06, 0.07, 0.10, 0.15, 0.18, 0.20 ) have been extensively investigated in a wide temperature range covering the glassy, SCL, crystalline and liquid states ( in chapter 5.1 ). The structure and structural changes are discussed from the view point of the variation of the medium-range structure ( MRS ) ( in chapter 5.2 ).

## 5.1 Results: Temperature and Composition Dependence of Raman Spectra

Thin films of $Ge_xSe_{1-x}$ glasses ( thickness of $\sim$1 $\mu$m, ) are measured by using a low power-density probing light ( $h\nu$ = 2.41 eV ) to avoid an additional temperature rise. The measurements are made in the sequence of increasing temperature. The temperature increasing rate between two successive measurements is 2$\sim$5 °C/min..

Figure 5.1 $\sim$ 5.8 show the typical Stokes Raman spectra at various composition. The measurement temperature in °C is indicated with each spectrum. All the spectra are divided by ( n($\omega$,T)+1 ), where the n($\omega$,T) is the Bose factor, and are normalized to the maximum intensity.

In the Se ( $x$ = 0, Fig. 5.1 ), the change of the spectra shows that the glass crystallizes to tc–Se around 100 °C and then it melts above 200 °C. In the spectra of the glass a peak at 255 $cm^{-1}$ and a shoulder at 235 $cm^{-1}$ are observed. These spectra agree with the common results very well [72,78]. Above 200 °C, the characteristic crystalline peaks at 235 $cm^{-1}$ and 140 $cm^{-1}$ disappear where the melting temperature $T_m$ is empirically estimated as 200 °C. In the liquid state the shoulder is not apparent, but a tail extends to lower energy.

In the $Ge_4Se_{96}$ ( Fig. 5.2 ), the spectra of tc–Se and liquid ( l– ) $Ge_xSe_{1-x}$ are observed in the temperature range between 100 °C and 190 °C. Here, we use the crystalline phase to name the state that the crystal, tc–Se or c–$GeSe_2$, coexists with the l–$Ge_xSe_{1-x}$. The weak band with the peak energy at about 190 $cm^{-1}$ relates to the breathing vibrational mode of the $GeSe_{4/2}$ tetrahedra. The intense band with the peak energy around 255 $cm^{-1}$ implies that the dominant structural species is the $(Se)_n$ chain structure. On the lower energy side of the intense band the weak shoulder with the peak energy at about 235 $cm^{-1}$ is distinguishably observed especially at room temperature. The spectral shape of $(Se)_n$ chain structure related vibrational bands is very similar to that of Se glass at room temperature, however, in the crystalline phase typically at 150 °C the 255 $cm^{-1}$ band remains due to the coexistence of l–$Ge_xSe_{1-x}$.

In the $Ge_6Se_{94}$ ( Fig. 5.3 ) and the $Ge_7Se_{93}$ ( Fig. 5.4 ) neither crystalline form of Se nor of $GeSe_2$ appears in our experimental temperature range. At room temperature the spectral shapes of these two glasses are similar to that of the $Ge_4Se_{96}$ glass, except the intensity ratio between the $GeSe_{4/2}$ related bands and that of the $(Se)_n$ chain structure related bands ( $I_{GeSe4/2}/I_{Se}$ ). With increasing temperature, the spectral shape around

255 $cm^{-1}$ is affected by the increase of the peak width of 235 $cm^{-1}$ shoulder. At higher temperatures, there is an asymmetrical tail at the lower energy side of 255 $cm^{-1}$ band. In addition to the temperature dependence of the spectral shape around 255 $cm^{-1}$, the weak 190 $cm^{-1}$ vibrational band is observed even at high temperature 850 °C.

In the $Ge_{10}Se_{90}$ ( Fig. 5.5 ), there is no crystalline phase in the measurement temperature range. At room temperature the spectral shape around 255 $cm^{-1}$ shows an asymmetrical tail at the lower energy side. Comparing with the intensity ratio $I_{GeSe4/2}/I_{Se}$ at room temperature and that at 200 °C, it is seen that the intensity ratio increases.

In the $Ge_{15}Se_{85}$ ( Fig. 5.6 ), though the crystalline phase has not been observed in the measurement temperature range, the spectral shape and its temperature dependence change obviously comparing with those of the $x = 0.06 \sim 0.10$. At room temperature, two peaks around 190 $cm^{-1}$, where the lower one is called $A_1$ and the higher $A_1^C$, come from the breathing vibration of $GeSe_{4/2}$ tetrahedra [36]. The distinct appearance of the $A_1^C$ band is an essential change for the spectral shape. The two vibrational bands of the $(Se)_n$ chain structure form the spectral shape with the peak at 255 $cm^{-1}$ and an asymmetrical tail at the lower energy side. With increasing temperature, the intensity ratio $I_{GeSe4/2}/I_{Se}$ increases drastically.

In the Raman spectra of the $Ge_{18}Se_{82}$ glass near room temperature ( Fig. 5.7 ), the intensity of the vibrational bands around 255 $cm^{-1}$ and those around 190 $cm^{-1}$ are comparable. Similar to the $Ge_{15}Se_{85}$, the $A_1^C$ band appears. With increasing temperature, the intensity ratio $I_{GeSe4/2}/I_{Se}$ increases. At 320 °C, the typical vibrational bands of c–$GeSe_2$ appear together with the vibrational bands of $(Se)_n$ chain structure around 255 $cm^{-1}$. In this crystalline phase, the c–$GeSe_2$ coexists with the l–$Ge_xSe_{1-x}$. With temperature increasing above 450 °C, the c–$GeSe_2$ bands disappear in the spectra where the crystalline parts are molten. The spectra at 450 °C are very similar to those near room temperature. In the liquid at 850 °C, two broad peaks around 180 $cm^{-1}$ and 245 $cm^{-1}$ are distinguishable.

For the Raman spectra in $Ge_{20}Se_{80}$ glass ( Fig. 5.8 ), near room temperature in the range of 150~300 $cm^{-1}$, a similar spectral shape to that of the $Ge_{18}Se_{82}$ glass implies that the structure of these two glasses are almost same. With increasing temperature, the relation of the total intensity of the vibrations around 190 $cm^{-1}$ and those around 255 $cm^{-1}$ again shows similar variation to that we have observed in $Ge_{18}Se_{82}$ glass. The c–$GeSe_2$ crystal appears above 375 °C together with the $(Se)_n$ chain structure and melts at 475 °C. In the liquid, we also find the two peaks which relate to the $(Se)_n$ chains

and $GeSe_{4/2}$ tetrahedral structures in our experimental temperature range.

Here, we turn to discussing the crystallization and melting in the $Ge_4Se_{96}$, $Ge_{18}Se_{82}$ and $Ge_{20}Se_{80}$ systems where the crystalline phase is observed. The phase diagram of the Ge–Se system has been summarized by Tronc et al. as shown in Fig. 2.25. With increasing temperature above its glass-transition temperature $T_g$, the motions of the $GeSe_2$ and $(Se)_n$ fragments become active. The glass is transformed into super-cooled liquid and these two types of fragments get together to form the crystalline nuclei. For the $Ge_4Se_{96}$ glass at 100 °C, the crystallization of Se occurs. In this work, we name the temperature at which the crystalline spectra appears and disappears as the crystallization temperature $T_c$ and melting point $T_m$, respectively, regardless of whether the system is stoichiometic or not. The $T_c$ and $T_m$ are obtained as 100 °C and 200 °C for the $Ge_4Se_{96}$ system, respectively. According to the phase diagram, one can find that the $Ge_4Se_{96}$ system contains the crystalline Se and l-$Ge_{x'}Se_{1-x'}$ with the Ge composition $x' > 0.04$. For the $Ge_{20}Se_{80}$ glass at 375 °C the crystalline peak of $GeSe_2$ appears and disappears at 475 °C. We can evaluate the $T_c$ and $T_m$ as 375 °C and 475 °C from the spectral changes, respectively. In the crystalline phase the $Ge_{20}Se_{80}$ system contains the c–$GeSe_2$ and l-$Ge_{x''}Se_{1-x''}$ with the Ge composition $x'' < 0.20$. With increasing temperature up to the $T_m$, the c–$GeSe_2$ part enlarges and the Ge composition $x$ of the l-$Ge_xSe_{1-x}$ decreases. In the phase diagram at Ge composition $x = 0.20$, the boundary line between the l-$Ge_{20}Se_{80}$ phase and ( $GeSe_2$ + liquid ) phase indicates the upper limited temperature for the existence of c–$GeSe_2$. We treat this temperature as the $T_m$ of Ref. [55] for $Ge_{20}Se_{80}$ system in Table 5.1. For $Ge_{18}Se_{82}$ system, the $T_m$ and $T_c$ in this work are 320 °C and 450 °C, respectively. In the $Ge_4Se_{96}$ system, the $T_c$ and $T_m$ are similar to those of the Se system ( $x = 0$ ). In the $Ge_{18}Se_{82}$ and $Ge_{20}Se_{80}$ system, both the $T_m$ and $T_c$ increase with increasing the Ge composition $x$. These tendencies agree with the results in Ref. [79] and the phase diagram, Fig.2.25, taken from Ref. [55]. Table 5.1 shows the main results in our $Ge_xSe_{1-x}$ glasses system. Other workers' results in thermal equilibrium are also listed for comparison. In Ge composition $x =$ 0.06~0.15 system, neither tc–Se nor c–$GeSe_2$ has been observed in this work. This will be related to its structure and we will discuss it in the following sections.

Table 5.1: The results of $T_g$, $T_c$, and $T_m$ at various Ge composition in this work and from Refs. [79] and [55]. In Ref. [28], the $T_g$ of $GeSe_2$ is determined as 396 °C by DTA measurement. At the $x = 0.06 \sim 0.15$, no crystalline state appears in our experimental temperature range for the present temperature increasing speed.

| $x$ | $T_g$ ( °C ) | | $T_c$ ( °C ) | $T_m$ ( °C ) | |
|---|---|---|---|---|---|
| ( $Ge_xSe_{1-x}$) | this work | Ref. [79] | | this work | Ref. [55] |
| 0 | unknown | 46 | 100 | 200 | 220 |
| 0.04 | unknown | 55 | 100 | 210 | 215 |
| 0.06 | 130 | 66 | no | unknown | 210 |
| 0.07 | 150 | 75 | no | unknown | 210 |
| 0.10 | 150 | 90 | no | 225 | 260 |
| 0.15 | 200 | 120 | no | 325 | 400 |
| 0.18 | 200 | 159 | 320 | 450 | 520 |
| 0.20 | 250 | 183 | 375 | 475 | 550 |
| 0.33 | 370 | 446 | 440 | 710 | 720 |

## 5.2 Discussion

Now we return to discussing the structure and structural changes from the Raman spectra and spectral changes in the $Ge_xSe_{1-x}$.

### 5.2.1 Medium-range Structure in g– and l–Se

At the $x = 0$, from a tentative fitting of the spectra around 255 $cm^{-1}$ by two Gaussian and a straight line, we plot their full widths at half maximum ( FWHM ) by the squares at the top of Fig. 5.9. The FWHM of the 255 $cm^{-1}$ peak is almost constant in the whole temperature range. However, the FWHM of the 235 $cm^{-1}$ peak in the liquid is approximately twice of that in the glass. In the glass, both the 255 $cm^{-1}$ peak and 235 $cm^{-1}$ shoulder are related to the Se–Se chains stretching vibration [78]. It has been pointed out that the frequency of the Se–Se stretching vibration depends on the interchain distance or an extent of interchain interaction [71]. The weaker interchain interaction leads the higher frequency through the stronger intrachain interaction. We imagine that the glass involves the region where the chains are somewhat parallel and

the region where the chains are oriented randomly to each other. The interchain distance for the former should be shorter than that for the later. Thus we consider that the 235 $cm^{-1}$ shoulder comes from the vibration of the parallel chains and the 255 $cm^{-1}$ peak from non-parallel chains. The relatively narrow peak width of the 235 $cm^{-1}$ band implies that the structural fluctuation is relatively small in the parallel region. On the other hand, in l–Se the increasing configurational freedom removes the above restriction about the parallel region and smears out a quasi-independence of the 235 $cm^{-1}$ band from the 255 $cm^{-1}$ band. The crystallization around 100 °C prevents us from observing the gradual change of the spectra which should have been in the SCL just above the glass-transition temperature $T_g$.

### 5.2.2 Glass-transition, Crystallization and Melt in $Ge_4Se_{96}$

At the $x = 0.04$, Raman spectra in the range of 150~300 $cm^{-1}$ are fitted by three Gaussian curves and one linear line. The vibrational bands with the peak energy at 235 $cm^{-1}$ and 255 $cm^{-1}$ are related to the $(Se)_n$ chain structure. Another vibration band with the peak energy at about 190 $cm^{-1}$ is related to breathing motion of $GeSe_{4/2}$ tetrahedra ( see chapter 2.1 ). In pure Se glass at room temperature, the intense vibrational peak energies of $(Se)_n$ chain structure are at 235 and 255 $cm^{-1}$, while those of the $GeSe_{4/2}$ tetrahedra in the g–$GeSe_2$ are at about 200 $cm^{-1}$. In the $Ge_4Se_{96}$ glass at room temperature, the $(Se)_n$ chain structure related vibrational peak energies are almost same, but the peak energy of the $GeSe_{4/2}$ tetrahedral vibration is shift to the low energy side. At this small Ge composition $x = 0.04$ ( average coordination number $\langle r \rangle = 2.08$ ), the glass is considered to be bond percolated by the $(Se)_n$ chains. Thus, the peak energies of the vibrational bands, which relate to the $(Se)_n$ chain structure, are almost the same as those in the pure Se glass. The low-energy shift of the vibrational band which relates to the $GeSe_{4/2}$ tetrahedra is considered to be caused by the $(Se)_n$ chains surrounding the $GeSe_{4/2}$ tetrahedra. The $(Se)_n$ chain structure is softer than the $GeSe_{4/2}$ tetrahedral structure.

As we have analyzed in pure Se, the fitting results of the intense vibrational bands around 255 $cm^{-1}$ are shown by the squares at the bottom of Fig. 5.9. The FWHM of the 255 $cm^{-1}$ peak is almost constant in the whole temperature range. However, the FWHM of the 235 $cm^{-1}$ peak in the liquid is approximately twice of that in the glass. This temperature dependence of the FWHM for the $(Se)_n$ chain structure related bands is similar to that observed in the pure Se system. The $T_c$ and $T_m$ are also close

to the values we obtained in the Se. The crystallization around 100 °C prevents us from observing the gradual change of the disordered spectra which should have been in the SCL just above the glass-transition temperature $T_g$. From the results that the spectral shape and its temperature dependence, and the crystallization tendency, one can reasonably conclude that the local $(Se)_n$ chain structure is hardly affected by a small population of the $GeSe_{4/2}$.

### 5.2.3 Glass-transition in $Ge_6Se_{94}$ & $Ge_7Se_{93}$

At the $x = 0.06$ and 0.07, Raman spectra in the range of 150~300 $cm^{-1}$ are fitted by three Gaussian curves and one linear line as we analyzed the $Ge_4Se_{96}$ system. The fitting results of the intense vibrational bands around 255 $cm^{-1}$ are shown by the squares in Fig. 5.10. Next we discuss the temperature dependence of the FWHM of the two vibrational bands at 255 $cm^{-1}$ and 235 $cm^{-1}$. For example, in the $Ge_7Se_{93}$ with increasing temperature, the FWHM of the 255 $cm^{-1}$ band again changes little, while that of the 235 $cm^{-1}$ band largely varies. At temperatures above 150 °C, the FWHM of the 235 $cm^{-1}$ band broadens gradually with increasing temperature. In the SCL with increasing temperature, the viscosity decreases quickly to make the molecules and clusters moved easily. This change causes the parallel region of the $(Se)_n$ chains to make large configurational fluctuations which allow to change the spectral shape as in the pure Se. Thus the $T_g$ is estimated to be around 150 °C. In the $Ge_6Se_{94}$ system from the temperature dependence of the FWHM, the $T_g$ is estimated to be around 130 °C.

In this Ge composition $x = 0.06$ and 0.07, another interesting result that with increasing temperature no crystalline state appears in our experimental temperature range. The randomly distributed $GeSe_{4/2}$ tetrahedra terminate the $(Se)_n$ chains to prevent the chains from forming the long-range order or crystallization. In this work, at the temperature lower than the $T_g$ ( 130 °C for $Ge_6Se_{94}$, 150 °C for $Ge_7Se_{93}$ ), the relaxation time for the $(Se)_n$ chains to build the long-range order is much longer than our experiment time periods. At 200 °C or the higher temperature which is above the $T_m$ of the pure Se, the crystallization of the Se is obviously impossible. Though above the $T_g$ 150 °C the $GeSe_{4/2}$ tetrahedra can move easily, the high density of the $(Se)_n$ hinders the tetrahedra in constructing the crystalline nuclei of $GeSe_2$.

With the Ge composition increasing from 0.04 above 0.06, though the spectral shape around 255 $cm^{-1}$ remains, the crystallization tendency is different. In the experimen-

tal temperature range, the absence of $A_1^C$ vibrational mode suggests that the $GeSe_{4/2}$ tetrahedra do not connect each other with their edges.

### 5.2.4 Glass-transition and Melt in $Ge_{10}Se_{90}$ & $Ge_{15}Se_{85}$

In the Raman spectra of the g-$Ge_{15}Se_{85}$ at room temperature, the density of the $GeSe_{4/2}$ tetrahedra is large enough to make the total intensity of the vibrations for the $GeSe_{4/2}$ tetrahedra and those for the $(Se)_n$ chains comparable. In the spectra around 200 $cm^{-1}$, the $A_1^C$ band at higher energy side is also clearly observed in the liquid phase near the $T_m$. This result suggests us that some tetrahedra are connected mutually by sharing their edges in glassy and liquid $Ge_{15}Se_{85}$.

An useful method to analyze the structural change at the glass-transition is to study the spectral shape of both the vibrations of the $GeSe_{4/2}$ tetrahedra and those of the $(Se)_n$ chains. At the $x = 0.10$, Raman spectra in the range of 150~300 $cm^{-1}$ are fitted by at least three Gaussian curves and one linear line as we analyzed in the $x = 0.04$~$0.07$ system. At the $x = 0.15$, Raman spectra in the range of 150~300 $cm^{-1}$ are fitted by four Gaussian curves and one linear line. Two curves around 255 $cm^{-1}$ relate to the $(Se)_n$ chain structure. Two curves around 200 $cm^{-1}$ relate to the $GeSe_{4/2}$ tetrahedral vibrational bands, the $A_1$ and $A_1^C$. The fitting results of the intensity ratio $I_{GeSe4/2}/I_{Se}$ varying with increasing temperature are shown in Fig. 5.11. The intensity $I_{GeSe4/2}$ is defined as the total intensity of two vibrational modes $A_1$ and $A_1^C$, and the intensity $I_{Se}$ is defined as the total intensity of the main vibrational mode at 255 $cm^{-1}$and the lower energy tail.

In the $Ge_{15}Se_{85}$, the intensity ratio $I_{GeSe4/2}/I_{Se}$ begins to take rapid increase in temperature range of 150~300 °C. The possibility of the resonant scattering can be cleaned up by the result, which will be shown in the $Ge_{18}Se_{82}$ system ( chapter 5.2.5 ), that no excitation energy dependence has been found in the temperature where the spectra begin to change. This increase of $I_{GeSe4/2}/I_{Se}$ should relate to the breaking of the Se–Se bonds which makes a fast decrease of the viscosity. At the temperature above the $T_m$ of the tc–Se ( 200 °C ), the Se–Se bonds are easily broken. In the SCL, the c–$GeSe_2$ like fragments easily move and coalesce with each other to form the crystalline embryo. At the temperature in the liquid phase of thermal equilibrium phase diagram Fig. 2.25, the $I_{GeSe4/2}/I_{Se}$ values are similar to those in glassy state which suggests that the population of the $GeSe_{4/2}$ tetrahedra and $(Se)_n$ chains is almost the same both in glassy state and liquid state. Though the population of $GeSe_{4/2}$ tetrahedra and that of

Se–Se bands are almost the same in glassy and liquid states, the increases of $I_{GeSe4/2}/I_{Se}$ is considered as follows:

- In the c–$GeSe_2$ like crystalline embryo the electronic properties localized at $GeSe_{4/2}$ tetrahedra may differ from those in the glassy and normal liquid states.
- We suppose that the local electronic states are similar to those of the crystal which lead the Raman scattering cross section of $GeSe_{4/2}$ to become larger than those in the glassy and normal liquid states.
- The intensity rate $I_{GeSe4/2}/I_{Se}$ takes larger values in temperature region of SCL state due to the coexistence of the c–$GeSe_2$ like crystalline embryo with the l–$Ge_xSe_{1-x}$, no matter whether the population is changed or not.

In the temperature region with the excess intensity ratio $I_{GeSe4/2}/I_{Se}$, the $Ge_xSe_{1-x}$ is in its SCL state, and we estimate that the $T_g$ of $Ge_{15}Se_{85}$ is around 150 °C.

In the $Ge_{10}Se_{90}$ where the $A_1^C$ band is very weak in the spectra in our measurement temperature range, but the increase of $I_{GeSe4/2}/I_{Se}$ in the temperature range of 150~200 °C is related to the c–$GeSe_2$ like crystalline embryo forming. At the Ge composition $x$ between 0.07 and 0.10, the structural changing tendency changes into the $GeSe_2$ like aspect instead of the Se like one. Both in the $Ge_{10}Se_{90}$ and $Ge_{15}Se_{85}$, though the crystalline embryo has been formed, the relaxation time of the crystallization is longer than our experimental time period. Thus, no-crystalline phase appears in these two glass.

In SCL state, with increasing temperature the $I_{GeSe4/2}/I_{Se}$ first shows an rapid increase and then decreases to the usual value as those in glassy and liquid states. These phenomena relate to the crystalline embryo forming of c–$GeSe_2$ in SCL state. With increasing temperature above melting point $T_m$, the crystalline embryo is resolved. In liquid state, the $I_{GeSe4/2}/I_{Se}$ values are similar to those in glassy state which suggests that the population of the $GeSe_{4/2}$ tetrahedra and $(Se)_n$ chains is almost the same both in glassy state and liquid state not so far above $T_m$. The melting point $T_m$ for $Ge_{10}Se_{90}$ and $Ge_{15}Se_{85}$ are obtained as 225 °C and 325 °C, respectively.

### 5.2.5 Glass-transition, Crystallization and Melt in $Ge_{18}Se_{82}$ & $Ge_{20}Se_{80}$

In the Raman spectra of the g–$Ge_{18}Se_{82}$ at room temperature, the $A_1^C$ vibrational band appears obviously. The $A_1^C$ band is also observed in the liquid even at about 800 °C. An essential difference in the structural change between the $Ge_{15}Se_{85}$ and the $Ge_{18}Se_{82}$ is that the crystalline state, c–$GeSe_2$ together with l–$Ge_{x''}Se_{1-x''}$ ( $x'' < 0.18$ ), appears for the later in the range of 320~450 °C but not for the former. Same analysis, which is used in the $Ge_{15}Se_{85}$, was carried out to fit the spectra by four Gaussian curves and one linear line. Figure 5.12 shows the temperature dependence of the intensity ratio $I_{GeSe4/2}/I_{Se}$ in the non-crystalline state. The intensity ratio $I_{GeSe4/2}/I_{Se}$ begins to take rapid increase in temperature range of 200~320 °C. To prove that this increase corresponds to a structural change, we have also measure the Raman spectra with the probing light of 2.54 eV. Same temperature dependence of the intensity ratio $I_{GeSe4/2}/I_{Se}$ has been observed. So the possibility of the resonant scattering can be ruled out by the result obtained by using the different probing light. This rapid increase of $I_{GeSe4/2}/I_{Se}$ should relate to the structural change which makes a fast decrease of the viscosity, as we have discussed in chapter 5.2.4. At the glass-transition where the temperature is not far below the $T_c$, 320 °C, the Se–Se bonds are easily broken since the $T_m$ of the tc–Se is about 200 °C. In the SCL, the c–$GeSe_2$ like fragments easily move and coalesce with each other to form the crystalline nuclei. Now we estimate that the $T_g$ is around 200°C.

At the $x = 0.20$ with increasing temperature, the Raman spectra act in the similar variation as they do at the $x = 0.18$ except that the temperature region of the crystalline state is 375~475 °C. A similar data analysis is also carried out as we have done in the $Ge_{18}Se_{82}$. According to the temperature dependence of the intensity ratio $I_{GeSe4/2}/I_{Se}$, we get the $T_g$ as about 250 °C.

## 5.3 Phase Transition in $Ge_xSe_{1-x}$

To summarize our results of $T_g$, $T_c$ and $T_m$ in the $Ge_xSe_{1-x}$ system, we use the phase diagram shown in Fig. 5.13. The $T_g$ of the $Ge_xSe_{1-x}$ increases monotonically with the Ge composition $x$ increasing. The variation of the $T_g$ agrees with the results in Ref. [79] within our experimental precision.

The $Ge_xSe_{1-x}$ system is considered as a two-component system: one is the $(Se)_n$ chain, the other is the $GeSe_{4/2}$ tetrahedra. In $Ge_xSe_{1-x}$ with the $x$ smaller than the critical composition $x_c$ which is between 0.07 and 0.10, the dominant structural unit is the $(Se)_n$ chains. In the SCL with increasing temperature, the decrease of viscosity causes large configurational fluctuations in the parallel region of $(Se)_n$ chains. The peak width of the vibrational mode which relates to the parallel-chain structure enlarges with increasing temperature above $T_g$. When the Ge composition $x > x_c$, the dominant structural unit changes from the $(Se)_n$ chains to the $GeSe_{4/2}$ tetrahedra. In the SCL with increasing temperature, the breaking of Se–Se bonds, which makes a fast decrease of the viscosity, leads the c–$GeSe_2$ like fragments easily to move and coalesce with each other to form the crystalline embryo.

In the Se-rich crystallizing region ( $0 < x \leq 0.04$ ), it consists of the tc–Se part and the l–$Ge_{x'}Se_{1-x'}$ part whose $x'$ is larger than its original value $x$ in g–$Ge_xSe_{1-x}$. In the Ge-rich crystallizing region ( $0.18 \leq x < 0.33$ ), it consists of the c–$GeSe_2$ part and the l–$Ge_{x''}Se_{1-x''}$ part whose $x''$ is smaller than its original value $x$ of g–$Ge_xSe_{1-x}$. Our $T_m$ agrees well with the results in Fig. 2.25 from the Ref. [55] where the liquidus line indicates the primary crystallizing temperature of c–$GeSe_2$ or tc–Se. In the equilibrium phase diagram, the eutectic point is at $x = 0.08$. In our phase diagram for the $0.04 < x < 0.18$, neither tc–Se nor c–$GeSe_2$ appears in the measurement temperature range. The trend of crystallization is demonstrated by our phase diagram.

When the Ge composition increases above 0.04, the experimental results suggest us that the relaxation time of $(Se)_n$ chains forming the long-range order increases drastically. From the view point of the structure, the population of randomly distributed $GeSe_{4/2}$ tetrahedra, whose structure is rather stable than the $(Se)_n$ chains at the experimental temperature, is large enough to easily prevent the $(Se)_n$ chains from crystallization.

In $Ge_{15}Se_{85}$ though the $GeSe_2$ crystalline embryo may be formed in the SCL, the relaxation time for the c–$GeSe_2$ growth becomes much longer than our measurement time period. With the Ge composition $x$ increases to 0.18, the glass crystallizes as easily as those in the $Ge_{20}Se_{80}$ and $GeSe_2$. The question why the relaxation time for crystallization shows rapid change when $x$ increases from 0.15 to 0.18 should be explained by considering the structure. Basing on the Phillips–Thorpe constraint theory, the rigidity percolation threshold value is at the average coordination number $\langle r \rangle = 2.4$, corresponding to $x = 0.20$ [1,2]. The character of a covalent network undergoes a

qualitative change from being easily deformable at $\langle r \rangle < 2.4$ to being rigid at $\langle r \rangle > 2.4$ [2]. In $Ge_xSe_{1-x}$ system, the relaxation time for crystallization shows an essential change at $x = 0.18$ ( $\langle r \rangle = 2.36$ ) which is apparently very close to the percolation threshold value. It should be noted that such a transition has been observed in the normal and inverse photo-emission spectra that an abrupt change of spectra occurs at $\langle r \rangle = 2.4$ [11].

To declare the relation between our observation and the predictions of the Phillips–Thorpe constraint theory, a combinative study of the experimental and theoretical approach is expectative.

## 5.4 Conclusions

In this chapter, by studying the temperature dependence of Raman spectra, the $T_g$, $T_c$ and $T_m$ have been obtained.

It has been found that in pure Se and Ge-poor $Ge_xSe_{1-x}$ ( $x < 0.07$ ), the dominant structure of glasses is $(Se)_n$ chains where the glassy state involves a parallel Se–Se chain region together with the non-parallel chain region. The low-energy side shoulder 235 $cm^{-1}$ is assigned to the vibration of Se–Se chains in parallel region. In $Ge_xSe_{1-x}$ ( $0.10 \leq x < 0.33$ ), the leading structure units are $GeSe_{4/2}$ tetrahedra which form the c–$GeSe_2$ like crystalline embryo in SCL state.

The relaxation time for crystallization shows an essential change at $x = 0.18$ ( $\langle r \rangle = 2.36$ ) which is apparently very close to the percolation threshold value basing on the Phillips–Thorpe constraint theory.

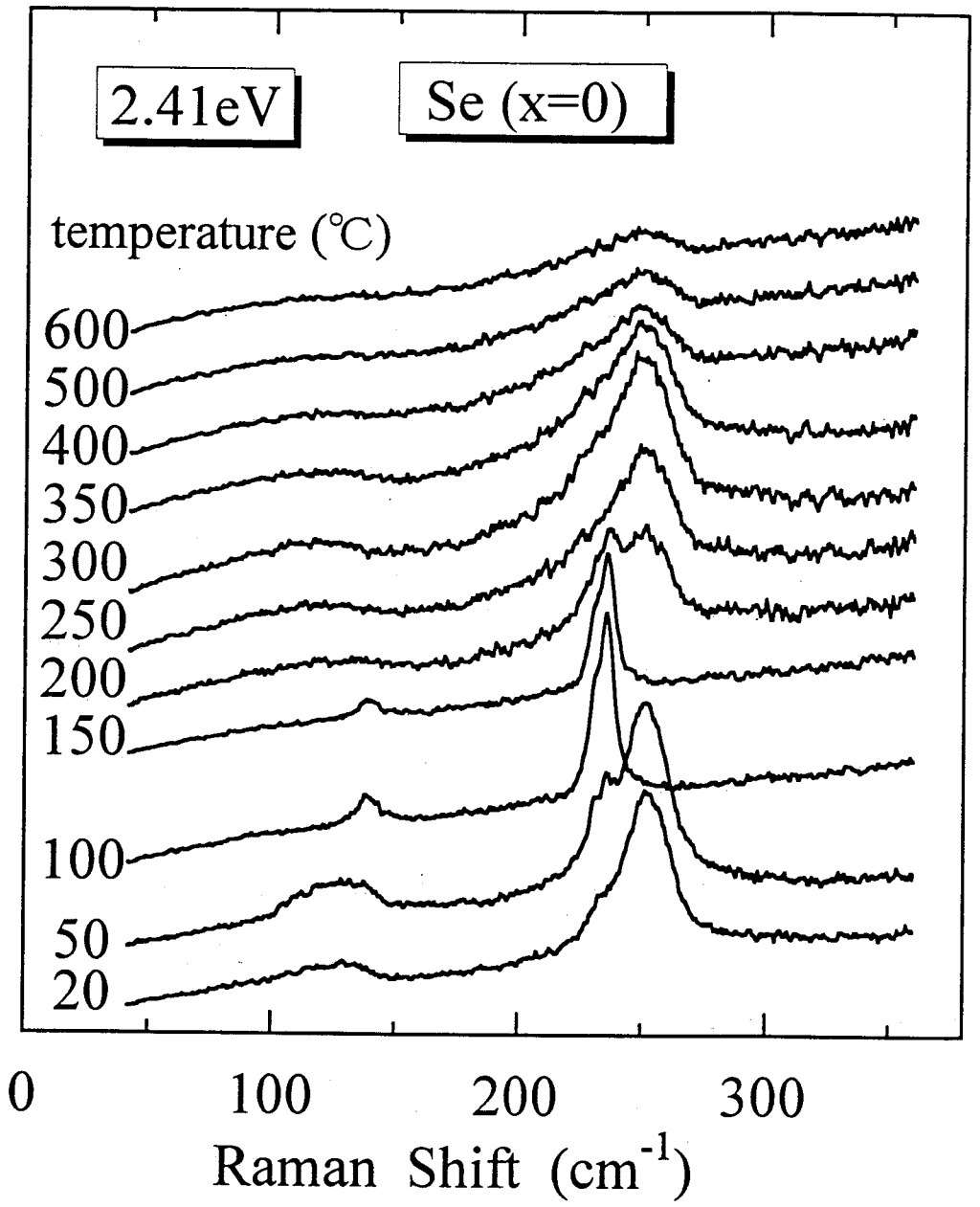


Figure 5.1: Raman spectra of the Se ( $x = 0$ ) at various temperatures which are indicated with the spectra. Raman spectra of tc-Se are observed between 100 °C and 200 °C.

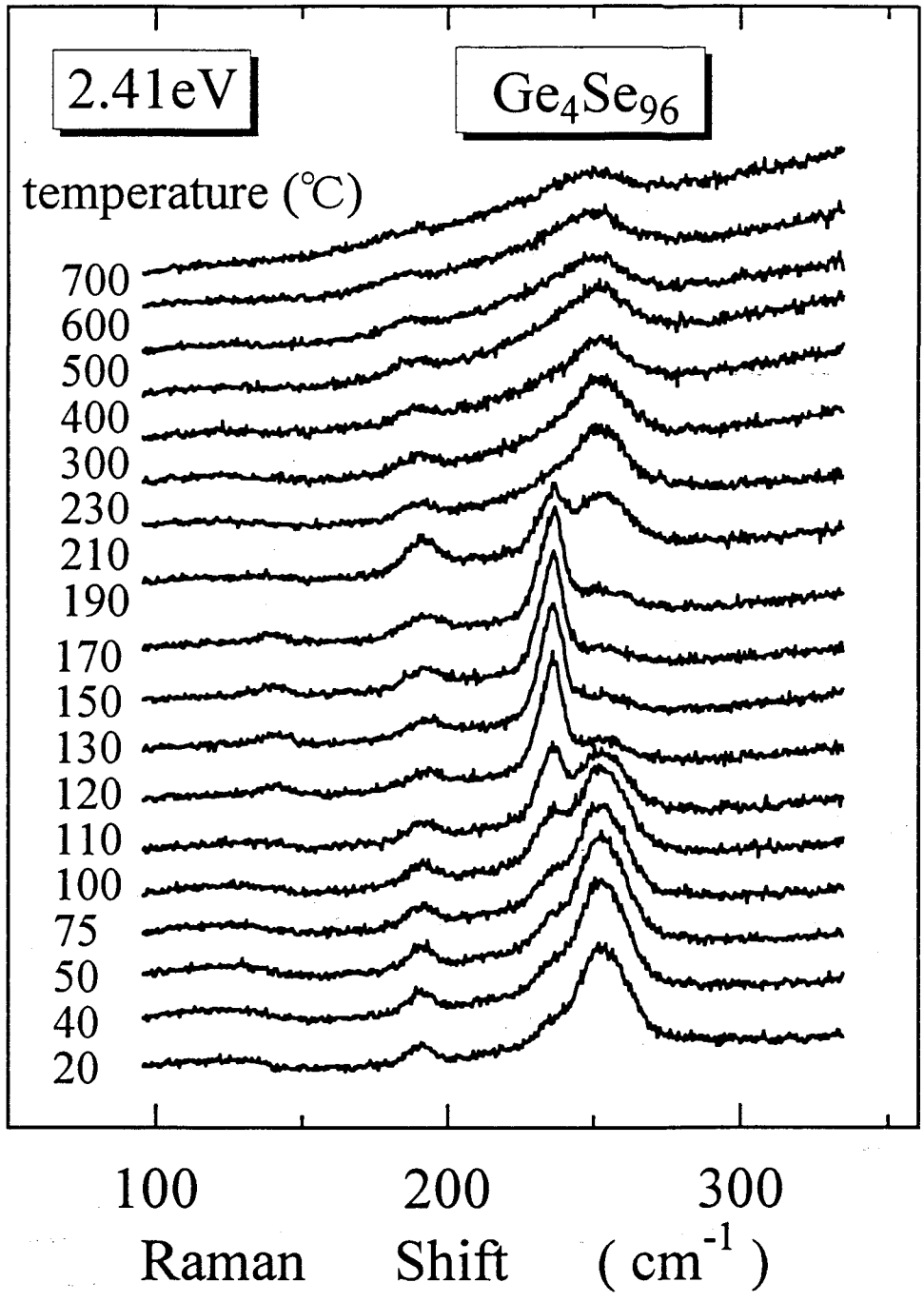


Figure 5.2: Raman spectra of the $Ge_4Se_{96}$ at various temperatures which are indicated with the spectra. The spectra of tc–Se together with those of l–$Ge_xSe_{1-x}$ appear between 100 °C and 190 °C.

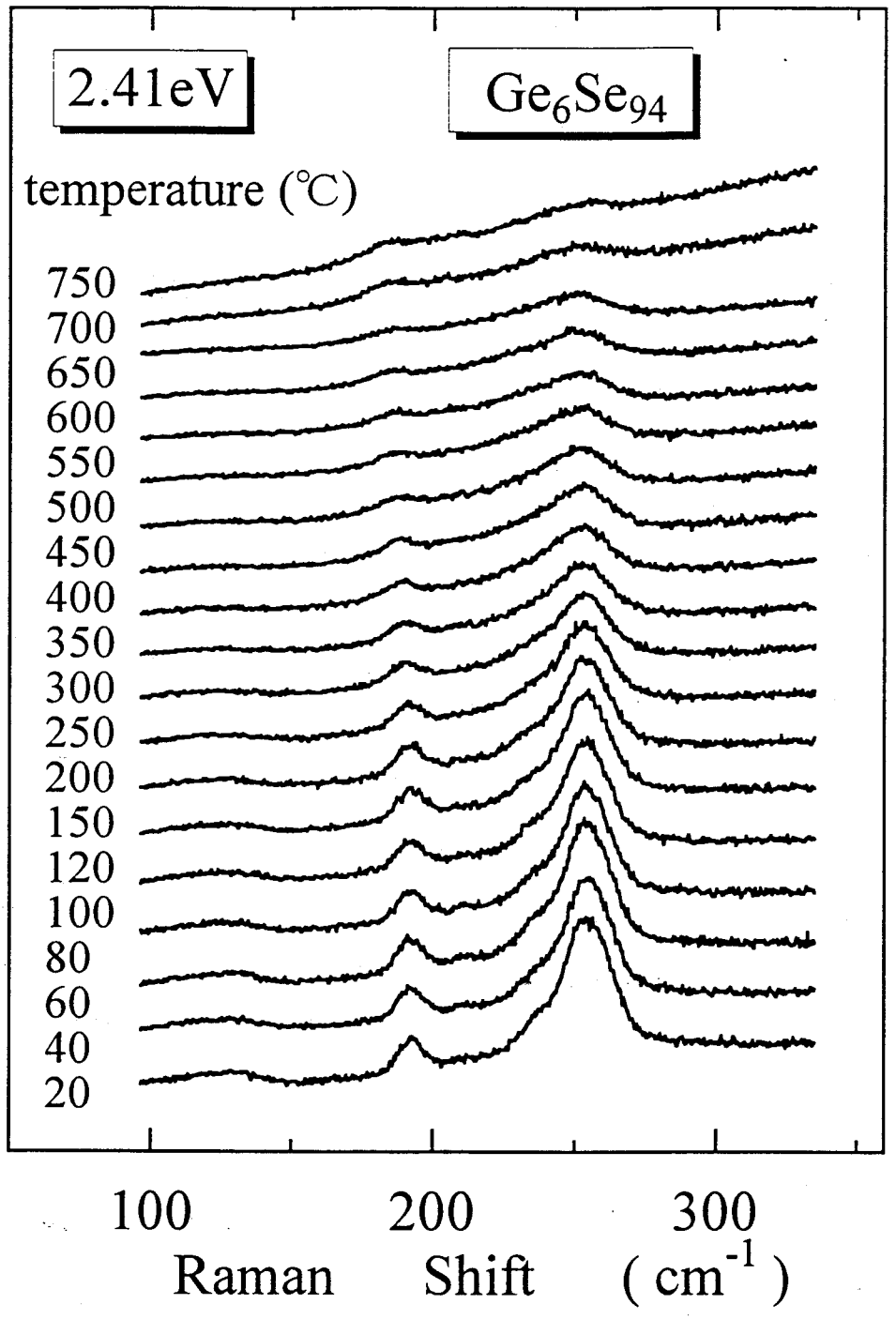


Figure 5.3: Raman spectra of the $Ge_6Se_{94}$ at various temperatures which are indicated with the spectra. There is no appearance of either tc–Se or c–$GeSe_2$ in the experimental temperature range.

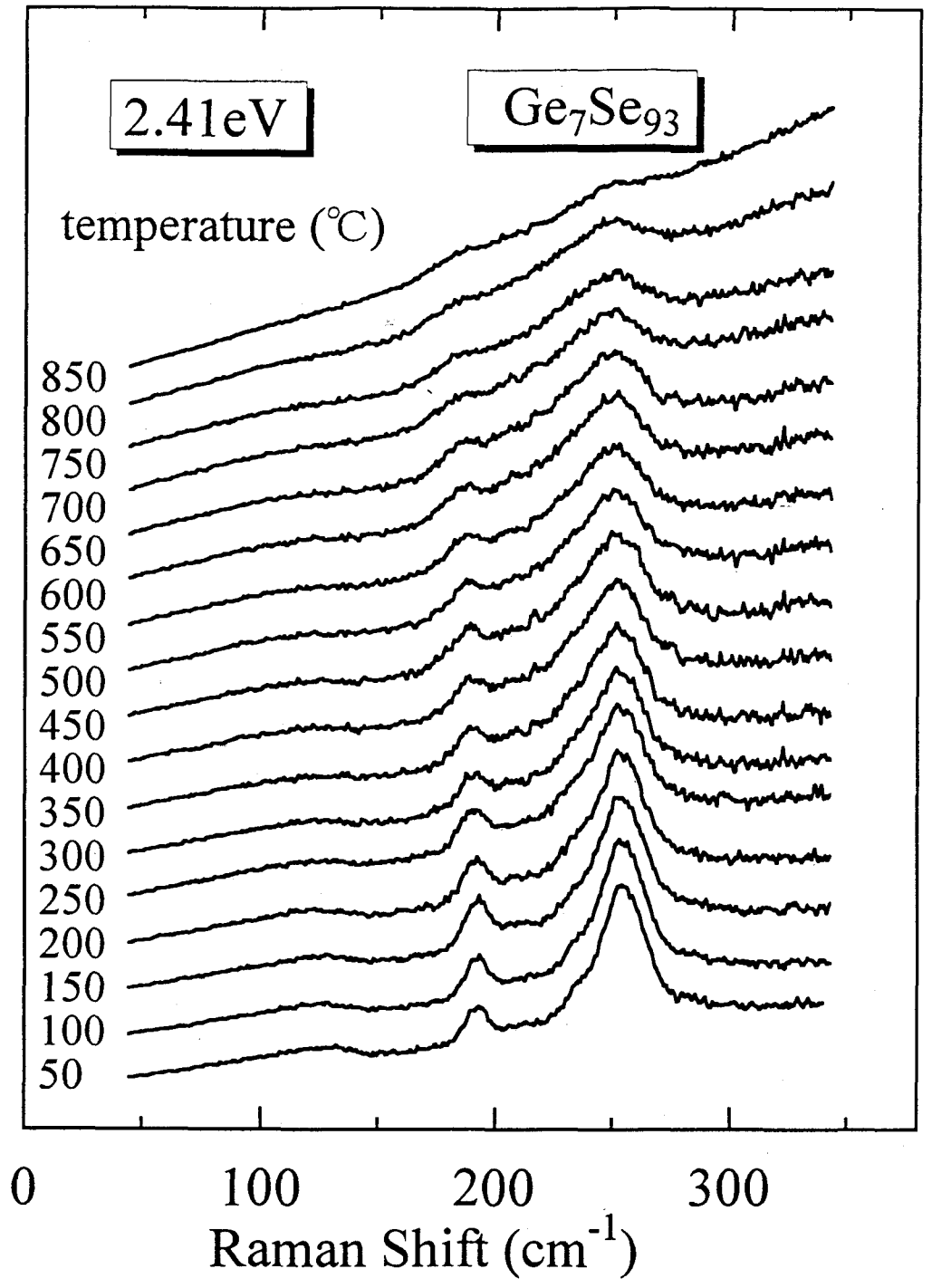


Figure 5.4: Raman spectra of the $Ge_7Se_{93}$ at various temperatures which are indicated with the spectra. There is no appearance of either tc–Se or c–$GeSe_2$ in the experimental temperature range.

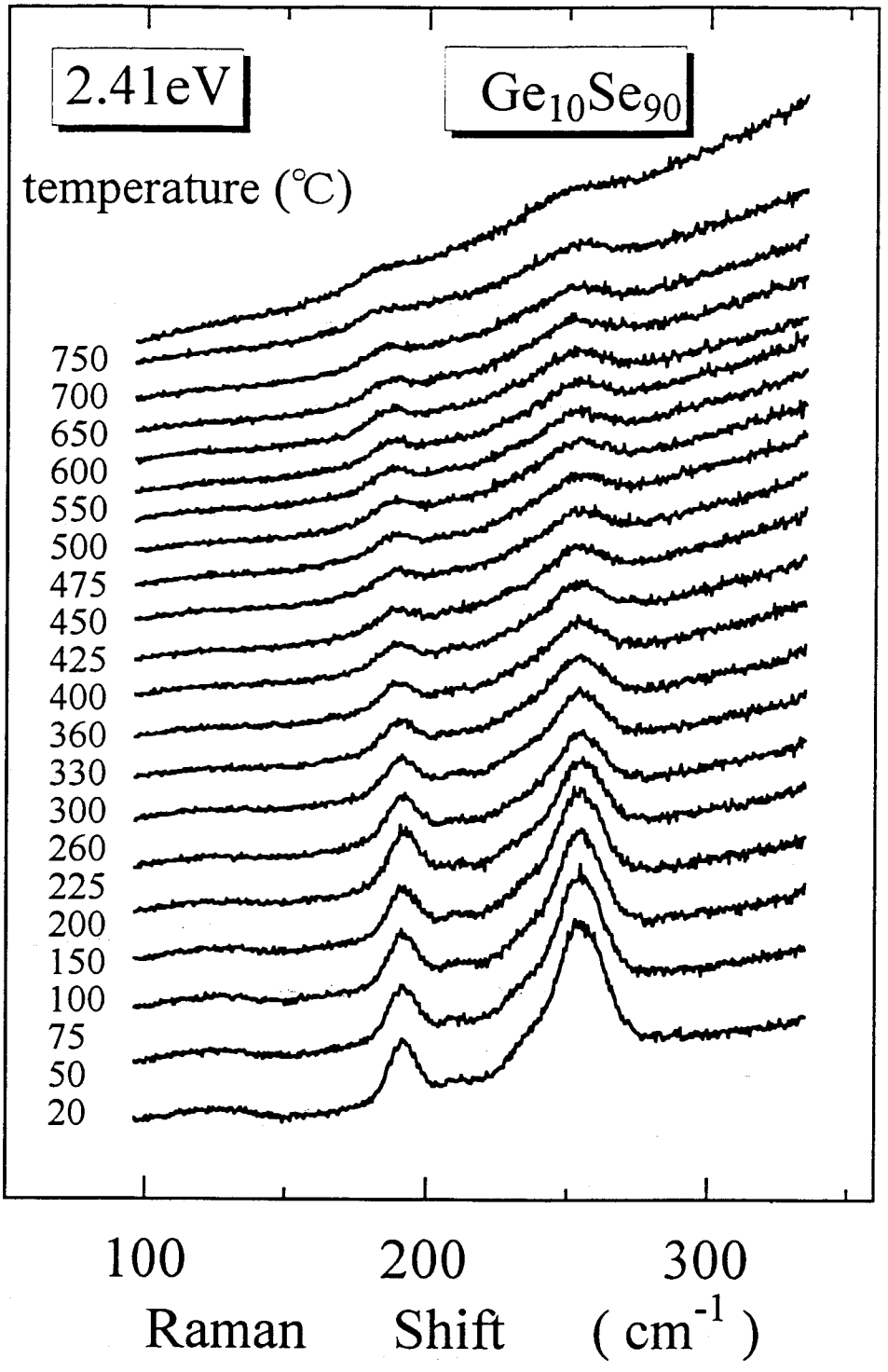


Figure 5.5: Raman spectra of the $Ge_{10}Se_{90}$ at various temperatures which are indicated with the spectra. There is no appearance of either tc–Se or c–$GeSe_2$ in the experimental temperature range.

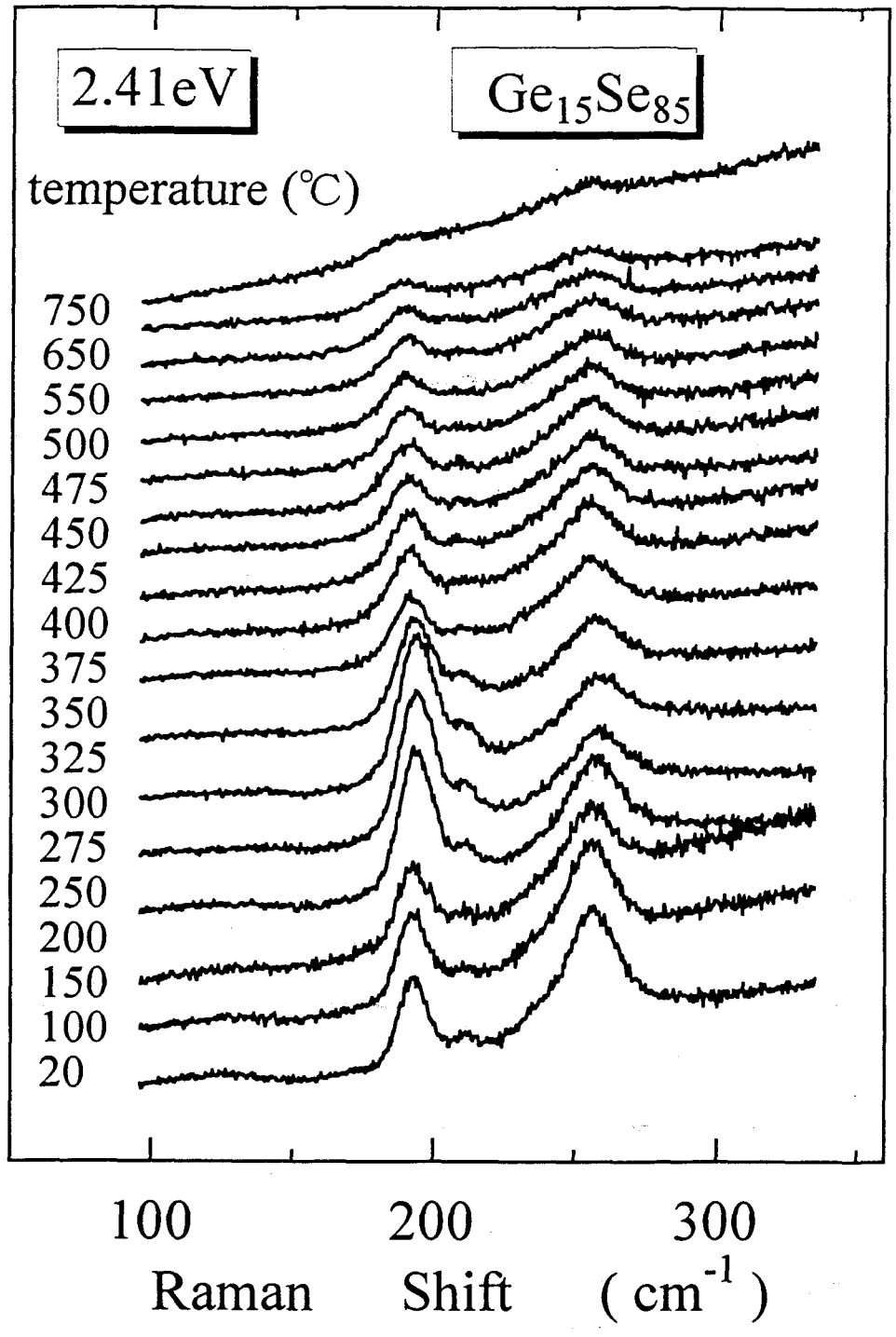


Figure 5.6: Raman spectra of the $Ge_{15}Se_{85}$ at various temperatures which are indicated with the spectra. There is no appearance of either tc–Se or c–$GeSe_2$ in the experimental temperature range. The appearance of the $A_1^C$ band at about 210 $cm^{-1}$ indicates that the glass consists of the part of edge-sharing $GeSe_{4/2}$.

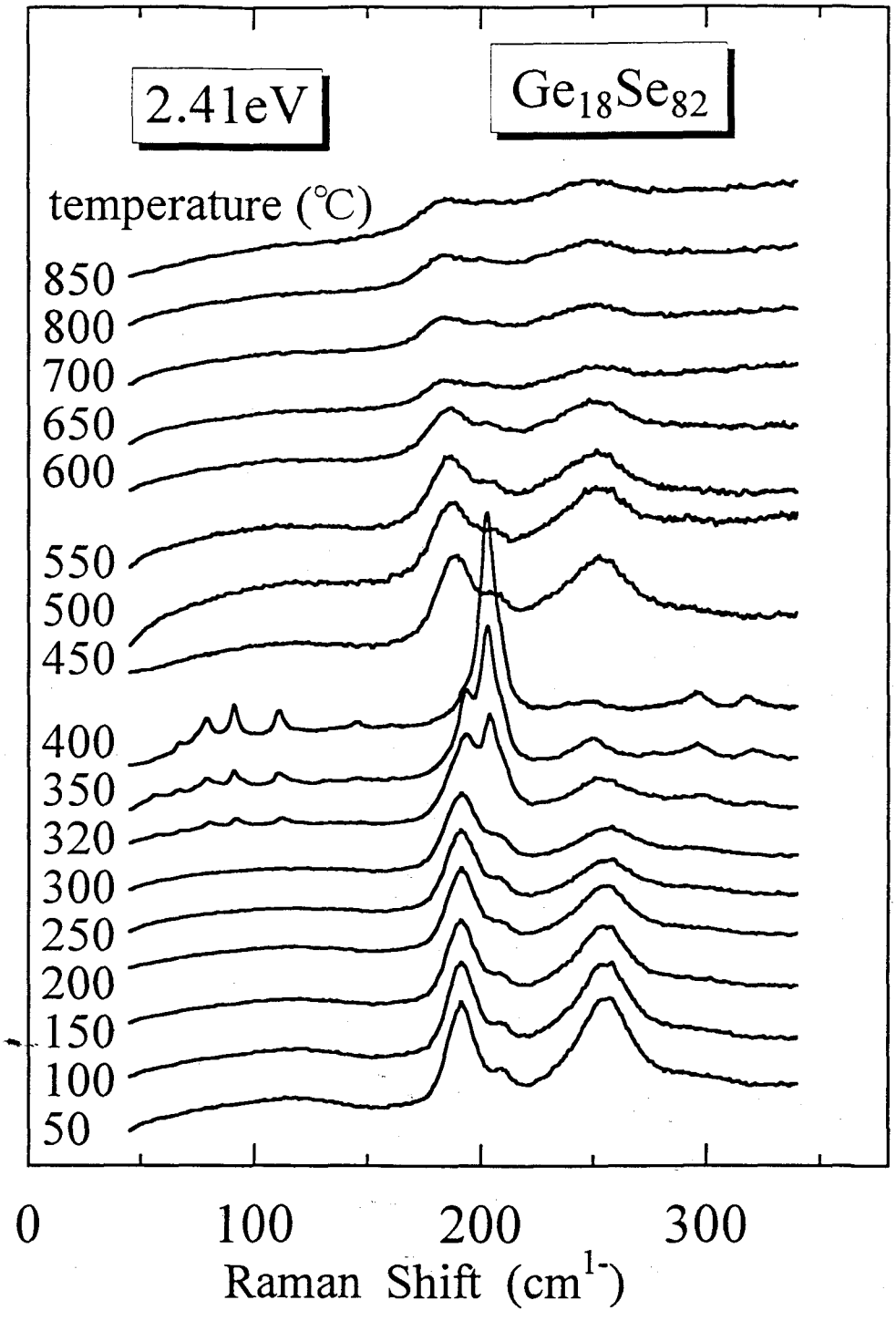


Figure 5.7: Raman spectra of the $Ge_{18}Se_{82}$ at various temperatures which are indicated with the spectra. In the temperature range of 320~450 °C, Raman spectra of c–$GeSe_2$ are observed together with the spectra of l–$Ge_xSe_{1-x}$ ( $x < 0.18$ ).

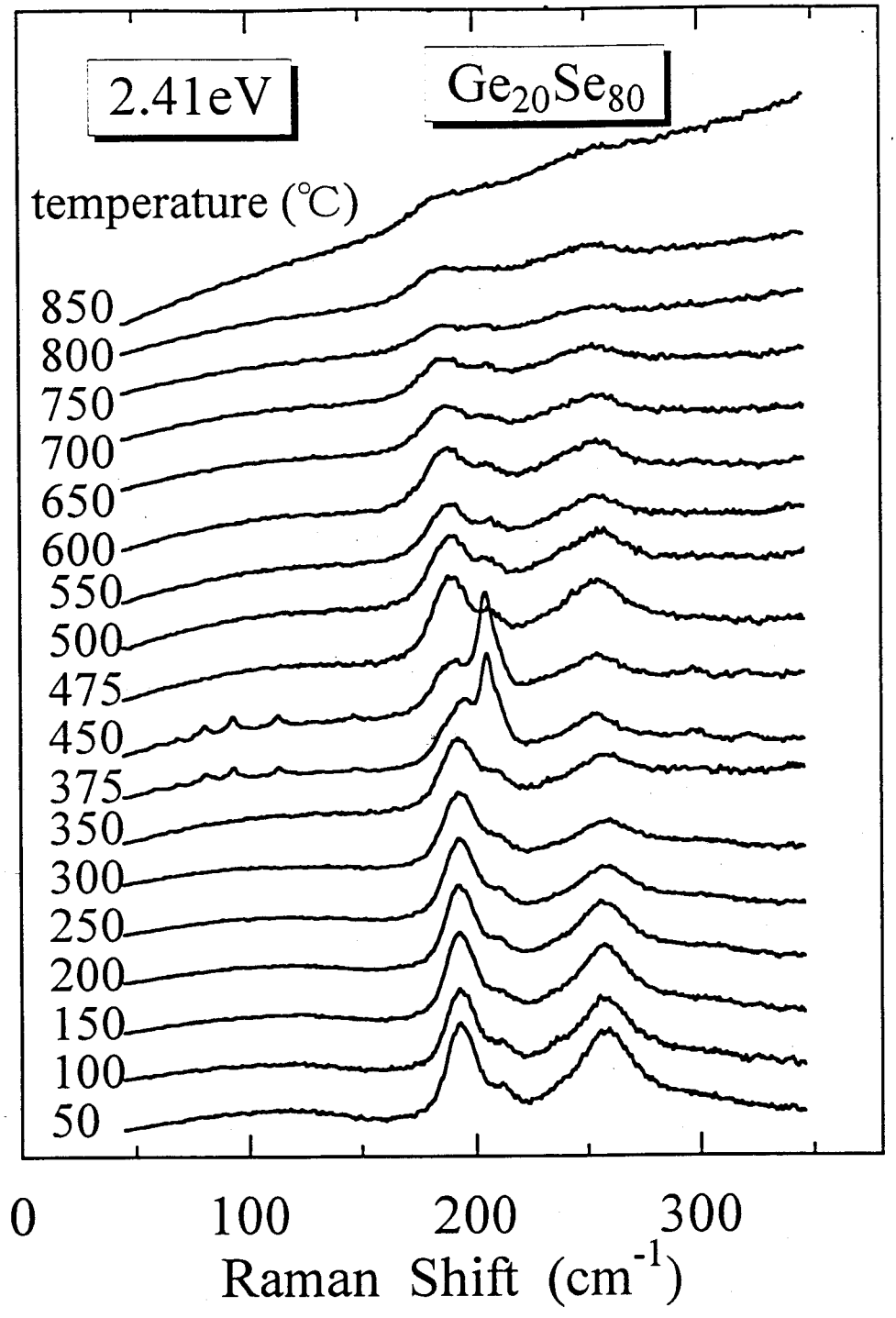


Figure 5.8: Raman spectra of the $Ge_{20}Se_{80}$ at various temperatures which are indicated with the spectra. In the temperature range of 375~475 °C, Raman spectra of c–$GeSe_2$ are observed together with the spectra of l–$Ge_xSe_{1-x}$ ( $x < 0.20$ ) .

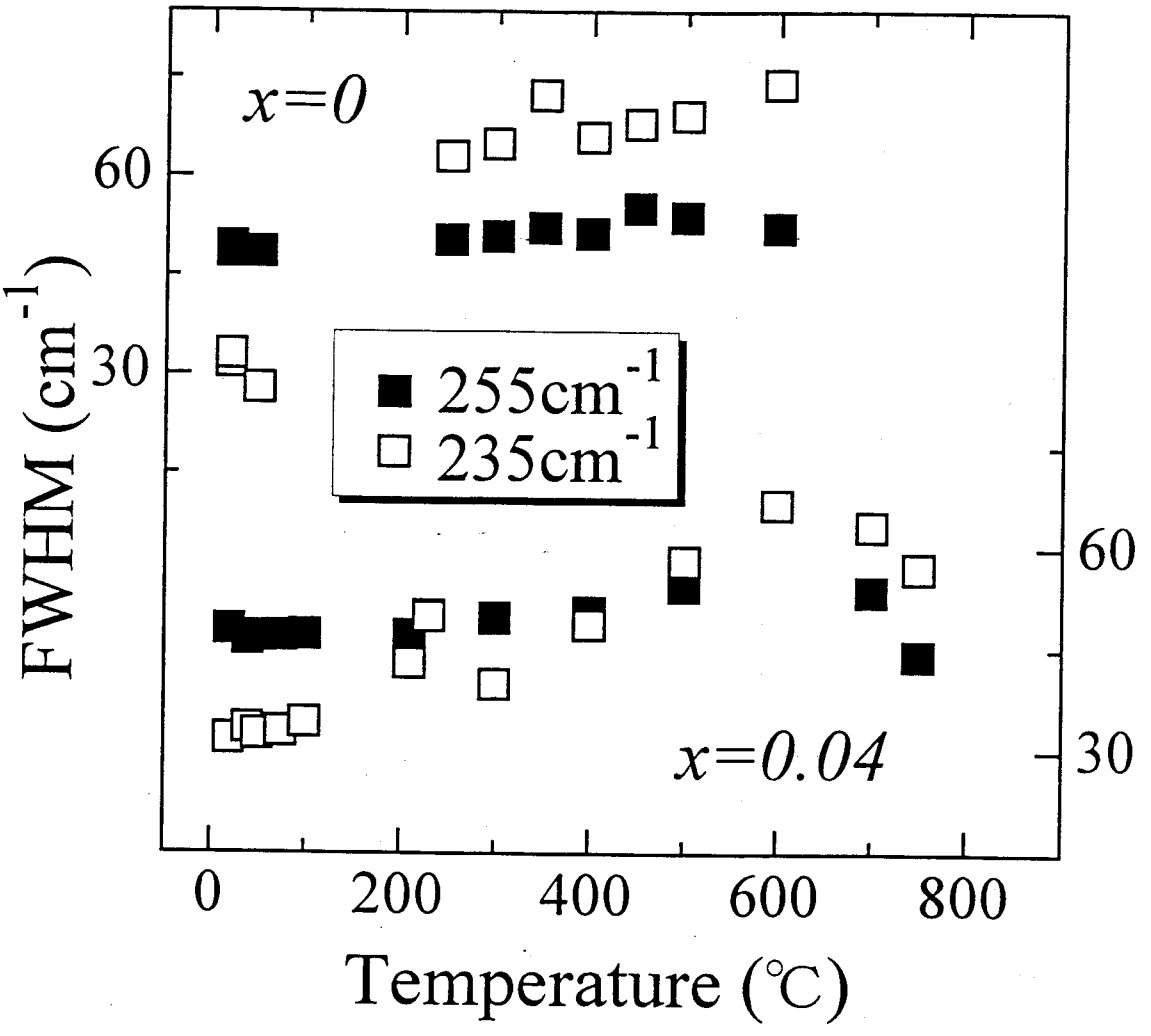


Figure 5.9: The fitting results of FWHM for Se ( $x = 0$ ) are shown in the upper half, and those for $Ge_4Se_{96}$ are shown in the lower half.

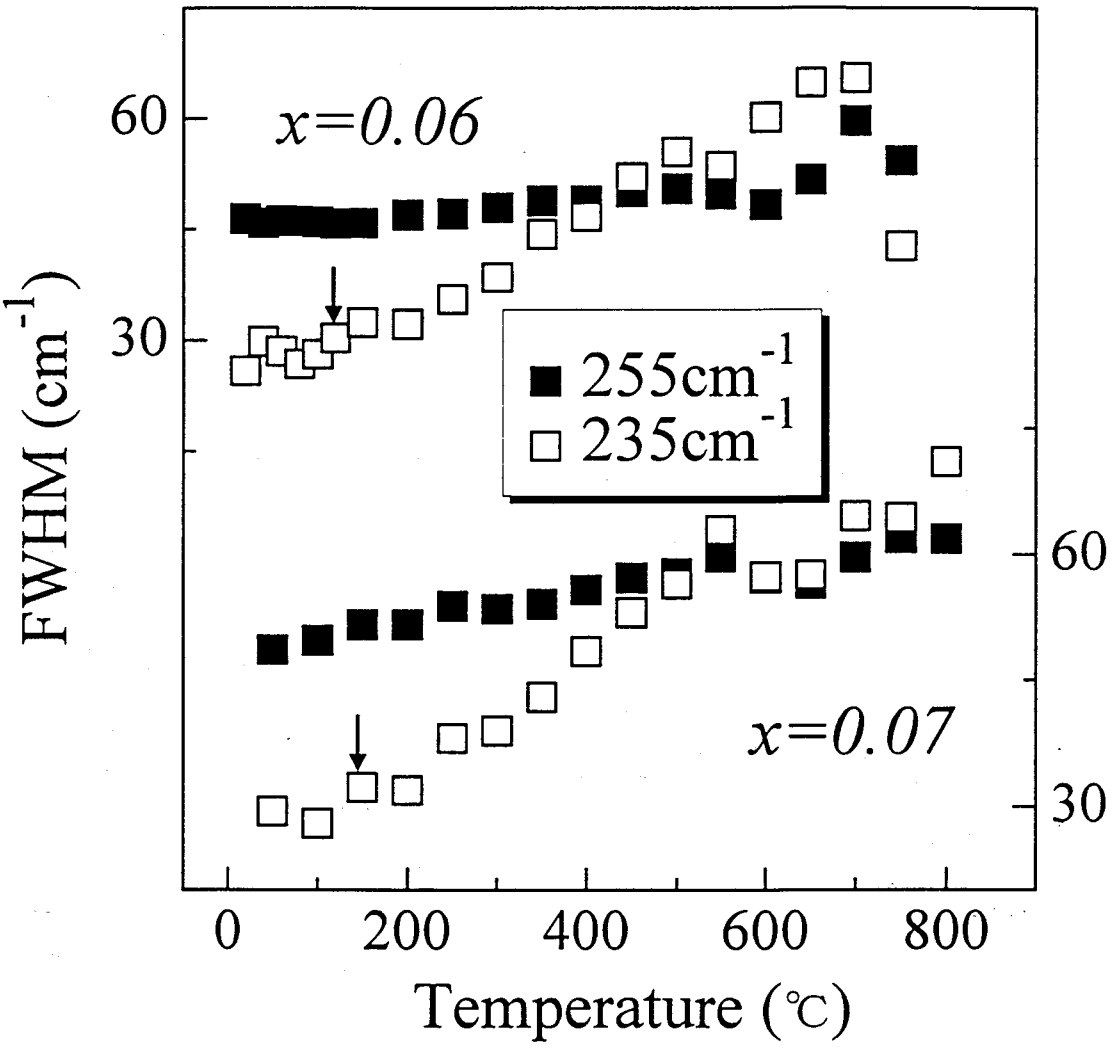


Figure 5.10: The fitting results of FWHM for $Ge_6Se_{94}$ are shown in the upper half, and those for $Ge_7Se_{93}$ are shown in the lower half. The down arrows indicate the glass-transition temperature $T_g$s.

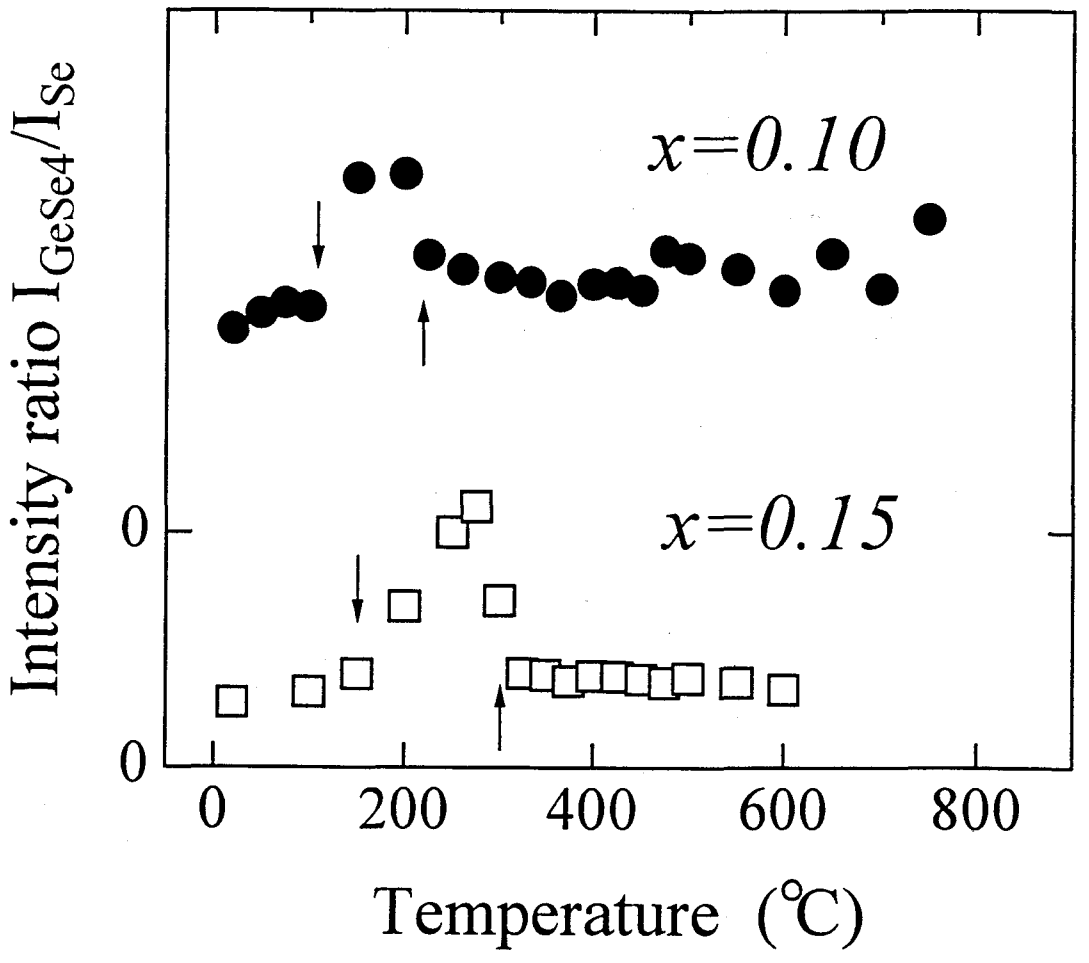


Figure 5.11: The temperature dependence of the intensity ratio $I_{GeSe4/2}/I_{Se}$ in the measurement temperature for the $Ge_{10}Se_{90}$ is shown in the upper half, and that for $Ge_{15}Se_{85}$ is shown in the lower half. The intensity $I_{GeSe4/2}$ is defined as the total intensity of two vibrational modes $A_1$ and $A_1^C$, and the intensity $I_{Se}$ is defined as the total intensity of the main vibrational modes at 255 $cm^{-1}$and the lower energy tail. The down arrows indicate the glass-transition temperature $T_g$s, and the up arrows the melting temperature $T_m$s.

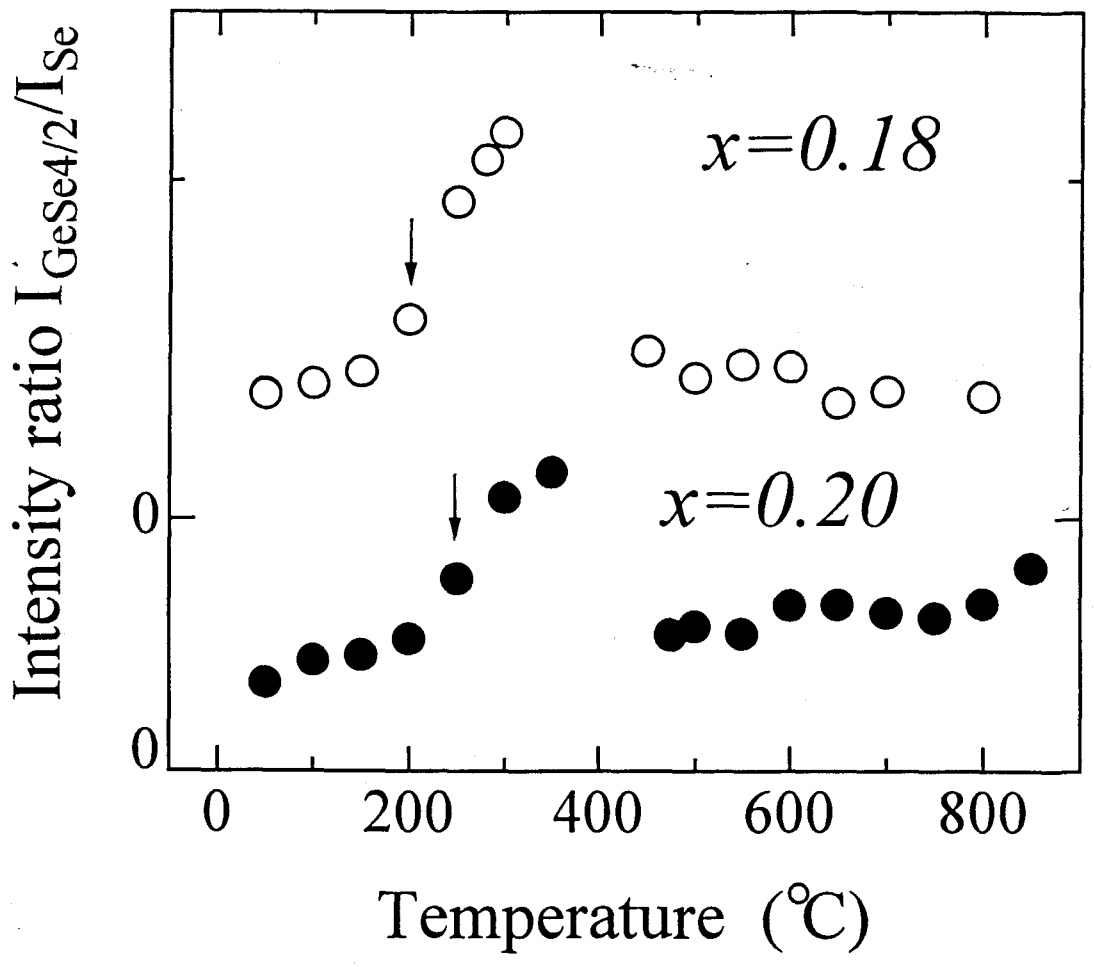


Figure 5.12: The temperature dependence of the intensity ratio $I_{GeSe4/2}/I_{Se}$ in the non-crystalline state for the $Ge_{18}Se_{82}$ in the upper half, and that for $Ge_{20}Se_{80}$ in the lower half. The down arrows indicate the $T_g$s.

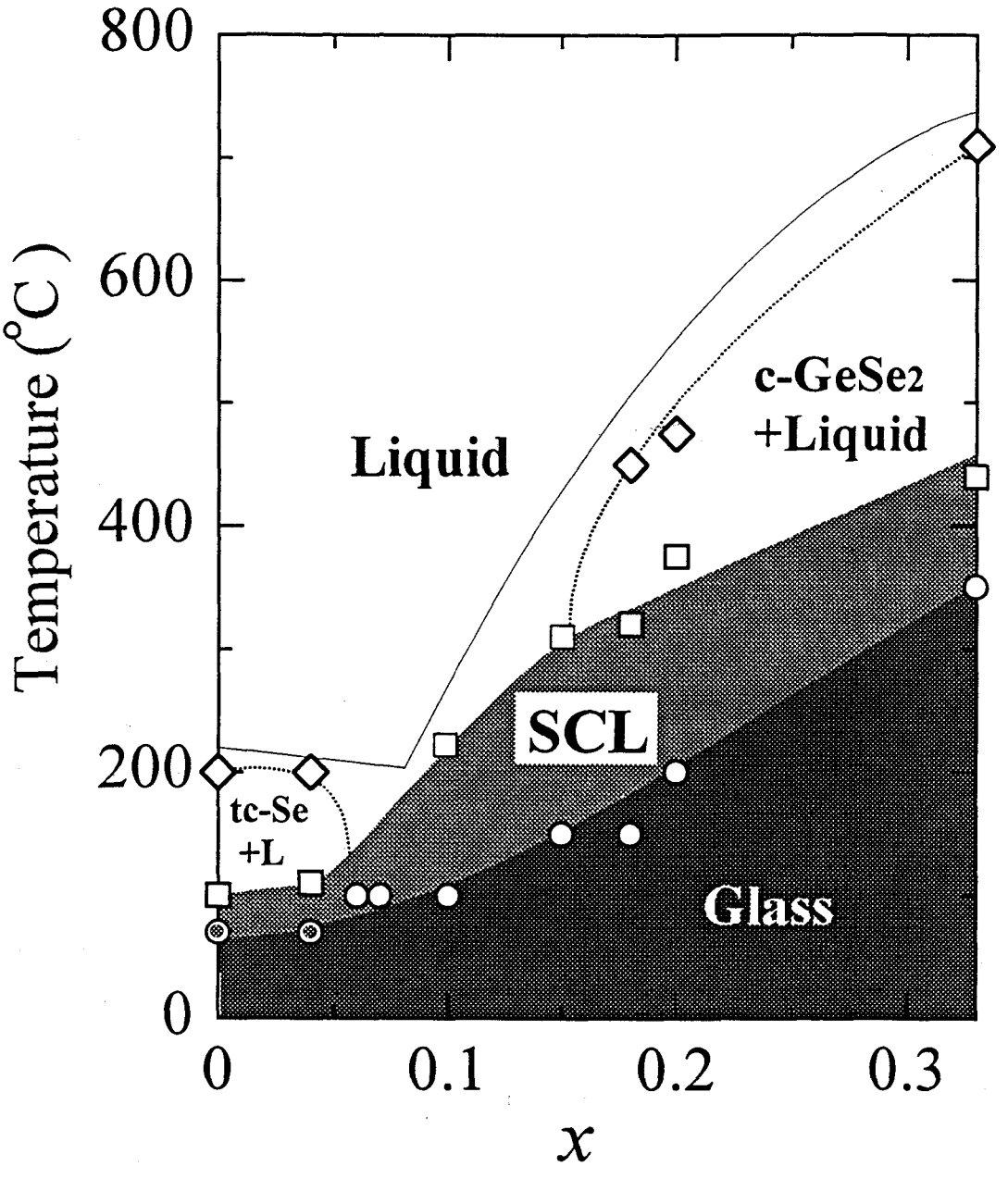


Figure 5.13: A phase diagram of $Ge_xSe_{1-x}$.

# Chapter 6

# PIC Processes in g–$GeSe_2$ Films

The PIC processes in g–$GeSe_2$ films have been studied in three types of films which are prepared by three different cooling rates. The cooling rate dependence of crystallization tendency in the PIC processes is discussed together with that in the TC processes. The variety of glass is determined by the crystallization tendency in the PIC processes.

## 6.1 Results: Cooling Rates Dependence in PIC Processes

In this chapter, we label the g–$GeSe_2$ films of fast, medium, slow cooling rates as F, M, S, respectively ( see chapter 3.1 for detailed preparations ). For the samples S and M, the PIC process has been observed for 60 minutes with the irradiation of an excitation power less than 50 mW. On the other hand, for the sample F, no PIC process has observed within 60 minutes of irradiation with up to 50 mW excitations. In Fig. 6.1, the time resolved Raman spectra of a typical PIC process are shown. Until the first five minutes, there is no observable change in the Raman spectra of g–$GeSe_2$. After five minutes, the line shape around 200 $cm^{-1}$ begins to change, and then the crystalline characteristic $A$ band grows with the prolonged irradiation. There are some weak vibrational bands at lower energy side in the spectra growing simultaneously with the enlargement of the $A$ band.

Fitting the line shape around 200 $cm^{-1}$ by four Gaussian curves which are the bands $A_G$, $A_1$, $A_1^C$ of g–$GeSe_2$, and the crystalline $A$ band, we plot the intensity ( area of the Gaussian curve ) of the A band to obtain a growth curve as shown in Fig. 6.2. The

intensity begins to increase after five minutes of the latent period and almost saturates after 20 minutes of the irradiation. The growth curve is well fitted by the empirical function $I_0[1 - \exp(-k(t - t_0))]$ as in a–$GeSe_2$ vacuum-evaporated films. In a–$GeSe_2$ films, the PIC process is classified into two types, type A and type B, where in the type A case only the 2D form grows, while in the type B case both the 2D and 3D forms grow ( see chapter 2 for details ). However, at present, only type A has been observed in the PIC process of g–$GeSe_2$ films.

Lowering the irradiation light power after the saturation, the peak energy of vibrational band $A$ shifts to higher energy side which relates to the decrease of the temperature under the illuminated portion. As we have discussed in chapter 3, the local temperature of the illuminated portion is estimated by the magnitude of the $A$ peak's shift. The temperature coefficient of the peak energy of the band $A$ is used as -0.01 $cm^{-1}/K$. Figure 6.3 shows the local temperate dependence of the latent period in sample S, and M. In the sample S the crystallization occurs at lower temperature than that in the sample M does. Its threshold temperature for the PIC is approximately 130 °C which is lower than that of the a–$GeSe_2$ film ( ~200 °C ), and is much lower than the thermal crystallization ( TC ) temperature $T_c$ ( ~450 °C ). On the other hand, in the sample M, the threshold temperature is about 430 °C which is almost same as its $T_c$ ( ~450 °C ) for the TC process. For sample F, its $T_c$ has been determined in the chapter 4 as 440 °C. In spite of the fact that the threshold temperatures in sample S and M are quite different, the $T_c$ for their TC processes are almost the same. In the TC processes of g–$GeSe_2$, it should be emphasized that the $T_c$ is almost independent of the cooling rate of the samples in their preparation from the melts. The threshold temperature of the a–$GeSe_2$ film is about 200 °C and is lower than the $T_c$ ~320 °C, which was obtained by annealing the a–$GeSe_2$ in the dark condition. Its $T_c$ is almost 100 °C lower than those of the g–$GeSe_2$.

The results are summarized in Table 6.1. It should be noted again that the threshold temperatures in the photo-induced crystallization in the sample S, M, F vary with the cooling rate in the sample preparation, but the pure thermal crystallization temperature $T_c$ is similar to each other apparently.

Table 6.1: The results of PIC processes in g–$GeSe_2$ films and a–$GeSe_2$ film for comparison. The number of the $\star$ represents the magnitude of the configurational entropy in glasses.

| Sample type | Cooling rate | Threshold T for PIC | $T_c$ | $\Delta S_c(g)$ |
|---|---|---|---|---|
| S | slow | 130 °C | 450 °C | $\star$ |
| M | medium | 430 °C | 450 °C | $\star\star$ |
| F | fast | unknown | 440 °C | $\star\star\star$ |
| a–$GeSe_2$ film | very fast | 200 °C | 320 °C | $\star\star\star\star$ |

## 6.2 Discussion

### 6.2.1 Cooling Rate Dependence of Threshold Temperature

To discuss the relations between the threshold temperature and the cooling rate, it is necessary to consider the cooling process in preparing the glass. During crystallization process, the properties, such as the viscosity $\eta$, entropy $S$, volume $V$ and internal energy $U$, change discontinuously. Though several material properties are reminiscent of solid and liquid behavior below and above a glass-transition temperature $T_g$, no sharp discontinuities are found. Cooling a glass forming liquid its liquid properties are preserved, until the structure becomes frozen in a particular disordered configuration. The configuration represents only one of the many subminima of an extremely rich energetic landscape, for example, the Fig. 2.3. In this situation the system has become incapable of exploring other energetically allowed remote minima in the phase space within finite times. Figure 6.4 shows a typical temperature dependence of the enthalpy H of a material which can either form a glass or crystal. Generally, the specific heat and the thermal expansion coefficient of the glass are observed to be close to those of the crystal. As there is a following relation between the temperature dependence of enthalpy and the $C_p$,

$$dH = C_p dT, \tag{6.1}$$

the slope of the Enthalpy–Temperature ( $H - T$ ) plot in a glass is supposed to be very similar to that in crystal.

Kauzmann has pointed out that the thermodynamic glass transition temperature $T_0$

could be defined by the linear extrapolation of the configurational entropy $\Delta S_{conf}(T)$:

$$\Delta S_{conf}(T) = S_{SCL}(T) - S_{crystal}(T), \tag{6.2}$$

to zero, where $S_{SCL}(T)$ and $S_{crystal}(T)$ are the entropies of the SCL and crystal respectively. In a realistic cooling process, before the SCL reaches to the $T_0$, the SCL is frozen at a glass-transition temperature $T_g$ under which the $\eta$ is too large for the glass to relax toward a more stable state in an observable time scale.

In the glass which is frozen in a slower cooling rate, the $T_g$ is lower than that cooled in a faster cooling rate. The configurational entropy $\Delta S_c(g)$ in the glass has been considered to increase with increasing cooling rate. Though the exact value of the $\Delta S_c(g)$ is difficult to be defined, we may intentionally list the expected $\Delta S_c(g)$ of the sample S, M and F in a sequence from small to large ( Table 6.1 ) by a number of star symbol.

### 6.2.2 Relation Between Structure and Crystallization Tendency

Matsuda et al. [35] have proposed a schematic model of electronic and thermal process in the latent period of the PIC process, where the evolution towards the formation of crystalline nuclei takes place, by using local free energies as shown in Fig. 6.5. After the photo-excitations from the initial glassy states (a), excited electrons relax to the intermediate glassy states (b) by electron-phonon interactions. From the states (b), the system transforms toward the crystalline nuclei with overcoming the energy barrier $U_B$ by the thermal excitation. Thus in the PIC process, the threshold temperature, which is expediently defined as the lowest crystallizable temperature in the 60 minutes of our experimental time period, is related to the height of the energy barrier $U_B$. In the pure thermal process in which the glass transforms from the initial states (a) to the crystalline nuclei (c), the system need to overcome the barrier $U_A > U_B$ by the thermal excitation.

The configurational entropy $\Delta S_c(g)$ is related to the initial energy $U_{ini}$ of the glassy state as shown in Fig. 6.5. For a larger configurational entropy $\Delta S_c(g)$, the initial energy $U_{ini}$ is considered to be higher. In the a-$GeSe_2$ film, the cooling rate is expected to be extremely fast, and the amorphous state is considered to be frozen in a metastable state (a) with a very high initial energy $U_{ini}$ to retain a large configurational entropy $\Delta S_c(g)$. This high $U_{ini}$ metastable state (a) has a barrier $U_A$ toward the crystallization.

To overcome the $U_A$ in the TC process, the a–$GeSe_2$ film system must be thermally excited at a temperature not lower than the crystallization temperature $T_c$ = 320 °C. However, for those g–$GeSe_2$ films, the cooling rates are not so fast as that of the a–$GeSe_2$ film. The slow cooling rate leads the configurational entropy $\Delta S_c(g)$ smaller than that of the a–$GeSe_2$ film. So that the initial energy $U_{ini'}$ of g–$GeSe_2$ at the metastable state (e) is smaller than that of the a–$GeSe_2$ film (a). In the g–$GeSe_2$ films, as we have observed that the $T_c$'s for their TC processes are almost the same ( ~450 °C ), it seems reasonable to suppose that the barrier $U_{A'}$ of sample S, M and F are almost in the same value. According to our quenching rates for preparing the g–$GeSe_2$ samples ( chapter 3.1 ), their initial energy states and the energy barriers are considered to be in almost the same $U_{ini'}$ and $U_{A'}$, respectively. The corresponding $T_c$ for the TC process of this barrier $U_{A'}$ in g–$GeSe_2$ films is about 450 °C. Thus, in two different preparation methods of the samples, vacuum evaporation and quenching melts, we obtain two kinds of samples whose metastable states are accompanied with two different barrier $U_A$ and $U_{A'}$, respectively, where the barrier $U_A$ in the a–$GeSe_2$ film is lower than $U_{A'}$ in the g–$GeSe_2$ films.

Now we return to the point of the influence of the cooling rate in g–$GeSe_2$ films on their PIC processes. In the case of samples S and M, the PIC processes were observed ( chapter 6.1 ). In the sample S, the threshold temperature for the PIC is about 130 °C which is much lower than the $T_c$ ( ~450 °C ) for the thermal crystallization ( TC ) process. However, in the sample M, the threshold temperature ( ~430 °C ) for the PIC is almost the same as the $T_c$ ( ~450 °C ).

After the photo excitation from the initial glassy state (e), the excited electrons relax to the intermediate glassy state (d) as shown in Fig. 6.5. In the sample S, its intermediate glassy state (d) may overcome a low barrier $U_{B'}$ by the thermal excitation. According to the crystallization temperature $T_c$ of the TC process, it is found that the energies ( $U_{ini'}$ ) of initial glassy state (e) are almost the same for the sample S, M and F. Though the initial energies $U_{ini'}$, corresponding the barrier $U_{A'}$ over which the crystallization occurs in the TC process, are almost the same, their intermdiate glassy states (d), corresponding the barrier $U_{B'}$, are quite different. With a slow cooling rate, the sample S can be frozen in the glassy state (e) whose intermediate glassy state (d) only has to overcome a low barrier $U_{B'}$ by the thermal excitation.

By a certain slow cooling rate, a super-cooled liquid is frozen in a low energy state. But for an additionally slow cooling rate, the liquid can be transformed into the crystal.

Though it has not been proved what the critical cooling rate is, it is reasonable to suppose that in the glass prepared by a slower cooling rate the medium-range structure ( MRS ) is topologically more similar to the crystalline nuclei, or easier to transform into crystalline nuclei. Figure 6.6 schematically shows the cooling processes from melt with different cooling rates to make the frozen MRS in various situations. As we have discussed the crystallization process in g–$GeSe_2$ ( chapter 4 ), the two curves in Fig. 6.6 correspond to the appearance frequency $I$ of the crystalline nuclei and the velocity $u$ of the crystal growth. For a simple estimation, we only consider that the curve of $I$ mainly affects the frozen MRS in this quenching process. To obtain the information on how the nuclei formation proceeds, we integrate the appearance frequency $I(T)$ within the quenching time period as follow:

$$M = \int_{T_s}^{T_e} I(T)dt = \int_{T_s}^{T_e} \frac{I(T)}{dT/dt} dT, \tag{6.3}$$

where the $M$ is related to the degree of how the MRS closes to the nuclei; the $T_s$ and $T_e$ are the starting and ending points of the quenching temperature, respectively. If the cooling rate $dT/dt$ is constant, we can get the relation,

$$M = \frac{1}{dT/dt} \int_{T_s}^{T_e} I(T)dT, \tag{6.4}$$

where the $\int_{T_s}^{T_e} I(T)dT$ does not depend on the cooling rate. Obviously, a slower cooling rate leads the MRS closer to the nuclei. Here, this MRS may be named as a near-nuclei glass structure. Acoording to the experimental results that the threshold temperature for the PIC of the sample S is lower than that of the sample M, and the above dedution that a good near-nuclei glass structure is expectative in the sample S, we can conclude that the threshold temperature for the PIC is strongly related to a good near-nuclei glass structure.

Next, we consider the behavior of the sample F. In case of the sample F no PIC process occurs, though for the thermal process the crystallization occurs either at 440 °C after about 8 hours or at 450 °C after about 30 minutes. The results suggest that in the PIC process its intermediate glassy state (d) needs to overcome a high barrier $U_{B'} \sim U_{A'}$ within the experimental time period by the thermal excitation ( ~450 °C ). The probable reasons for the sample F showing the high barrier $U_{B'}$ are considered as follows:

- As the cooling rate from the melt of the sample F is fastest, the glass may be frozen at the temperature which is much higher than those temperatures of the

S and M samples. Certainly, the structure of the sample F may quite differ from those of the S and M samples, particularly in the medium-range structure.

- As we have mentioned the preparation method in the chapter 3 that the glassy films ( thickness $\sim 1\mu$m ) are packed in the quartz cells, during a fast quenching process considerable defects can be remained owing to the difference between the coefficient of thermal expansion of the quartz and that of the $GeSe_2$. These defects may raise the $U_{B'}$ of the intermediate glassy state (d).

## 6.3 Summary and Conclusions

In this chapter, the various structures in g–$GeSe_2$ films, which are quenched from melts with different cooling rates, are investigated by the time-resolved Raman scattering measurement.

The thermal crystallization temperatures of the g–$GeSe_2$ films are higher than those of the vacuum evaporation amorphous $GeSe_2$ films which are prepared with extremely fast cooling rates. This suggests that a fast cooling rate, corresponding to a high energy initial glassy state, leads the thermal crystallization temperature decreased.

In the g–$GeSe_2$ films the energies of initial glassy states are almost the same, however, the threshold temperatures for photo-induced crystallization processes are different. A slow cooling rate lowers the threshold temperature. It is reasonable to considered that in the glass prepared by a slower cooling rate, the medium-range structure is more similar to the crystalline nuclei, or easier to transform into crystalline nuclei. The different local structures in glass affect the crystallization tendency in PIC process, though they do not influence the crystallization tendency in thermal crystallization process.

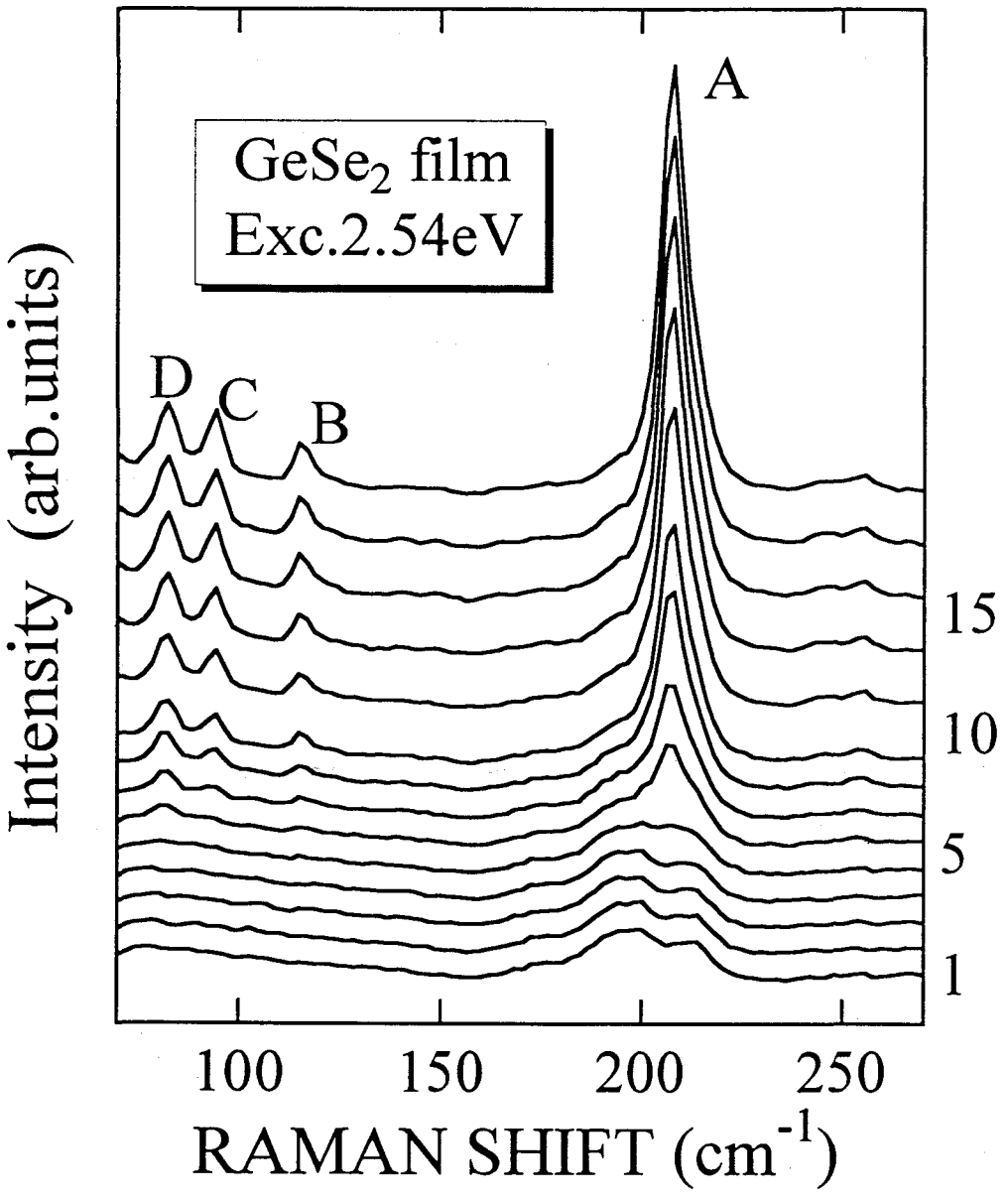


Figure 6.1: Time-resolved Raman spectra during the PIC process in g–$GeSe_2$ film with an excitation power of 20 mW. The characteristic crystalline peaks begin to appear after a latent period of 4 minutes.

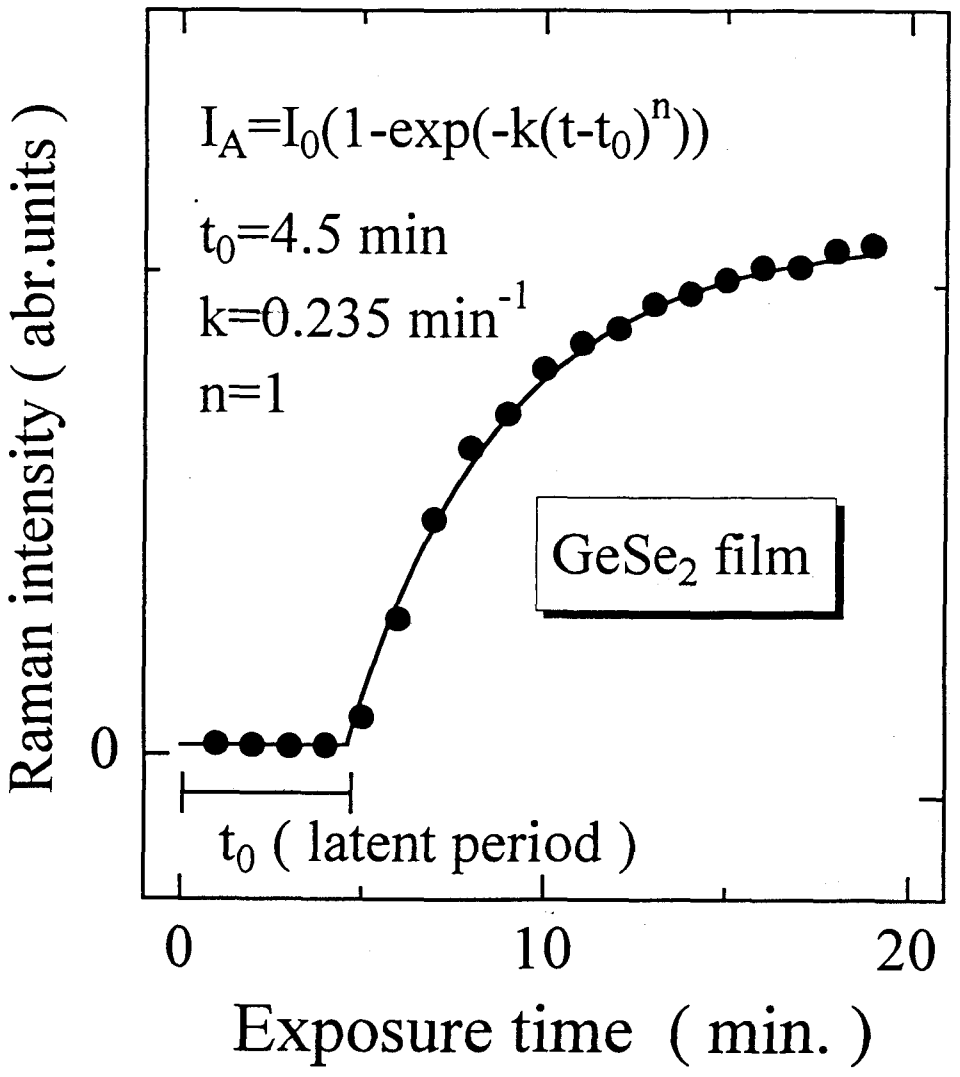


Figure 6.2: Growth curve of the light-induced crystal ( 2D ) in the PIC process by excitation power of 20 mW. The intensity of A band are plotted. Solid lines illustrate the empirical curve $I_0[1-\exp(-k(t-t_0))]$. The $t_0$ is the latent period.

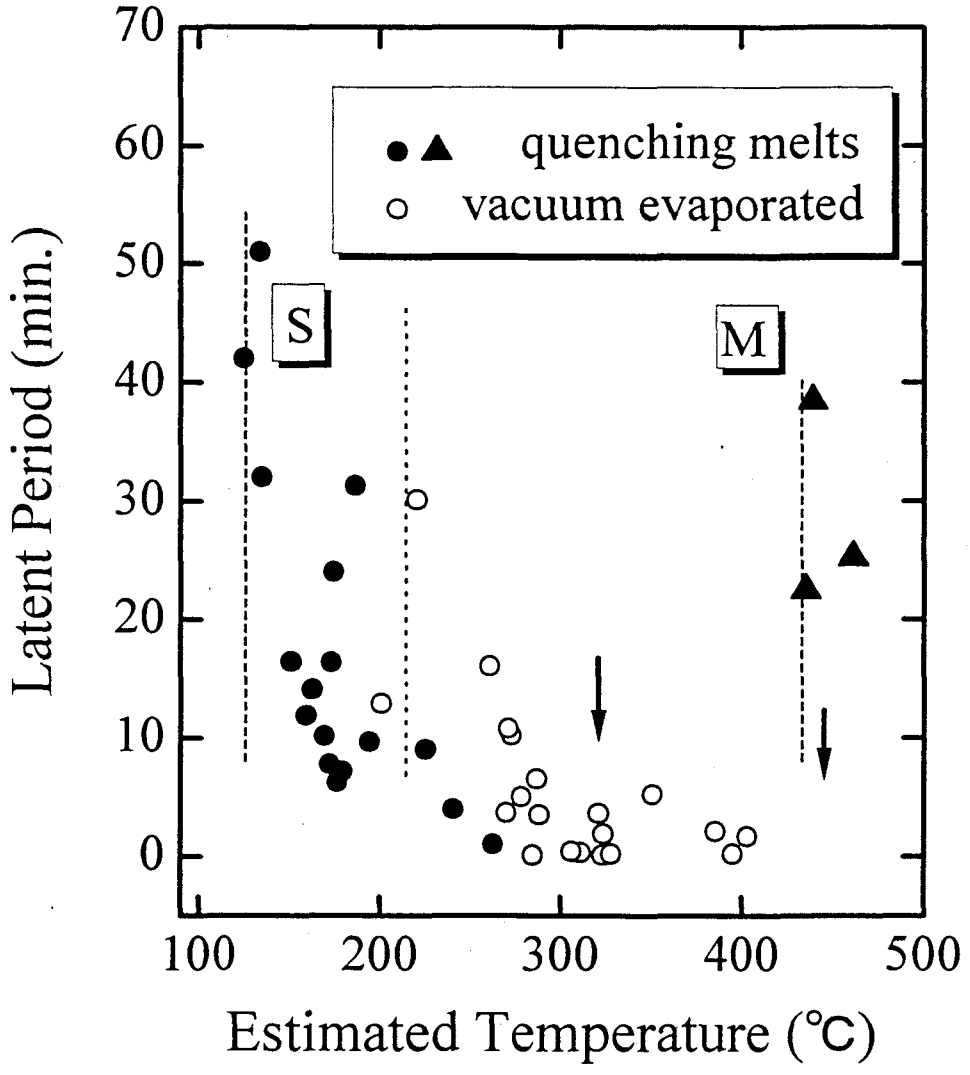


Figure 6.3: Latent period vs. estimated temperature in g–$GeSe_2$ samples S, M, and in a–$GeSe_2$ film. The vertical arrows point the crystallization temperature in a–$GeSe_2$ at 320 °C and in sample g–$GeSe_2$ F at 440 °C.

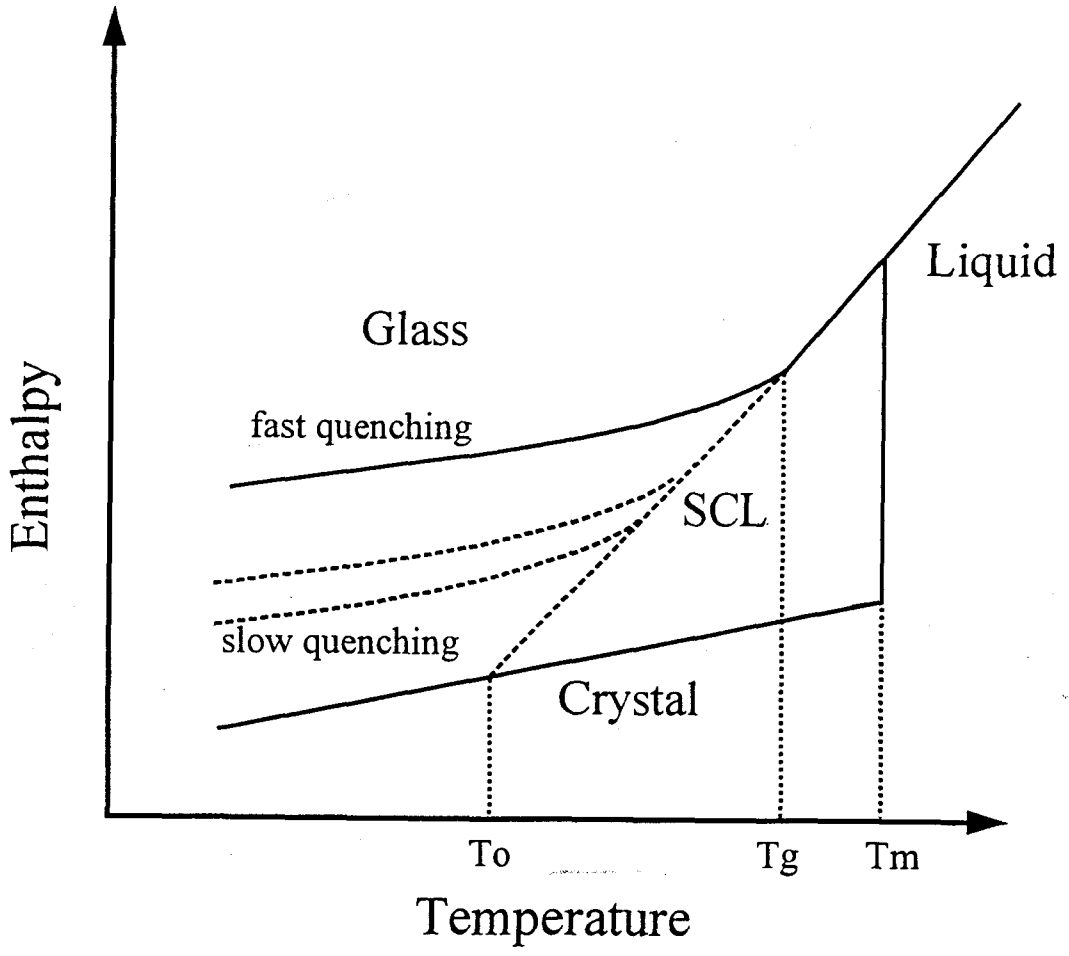


Figure 6.4: Typical schematic temperature dependence of enthalpy of a material which can either form a glass or crystallize. *Solid lines* for $T<T_m$ indicate glass-transition versus crystallization. *Dashed lines* illustrate the effect of decreasing the cooling rate.

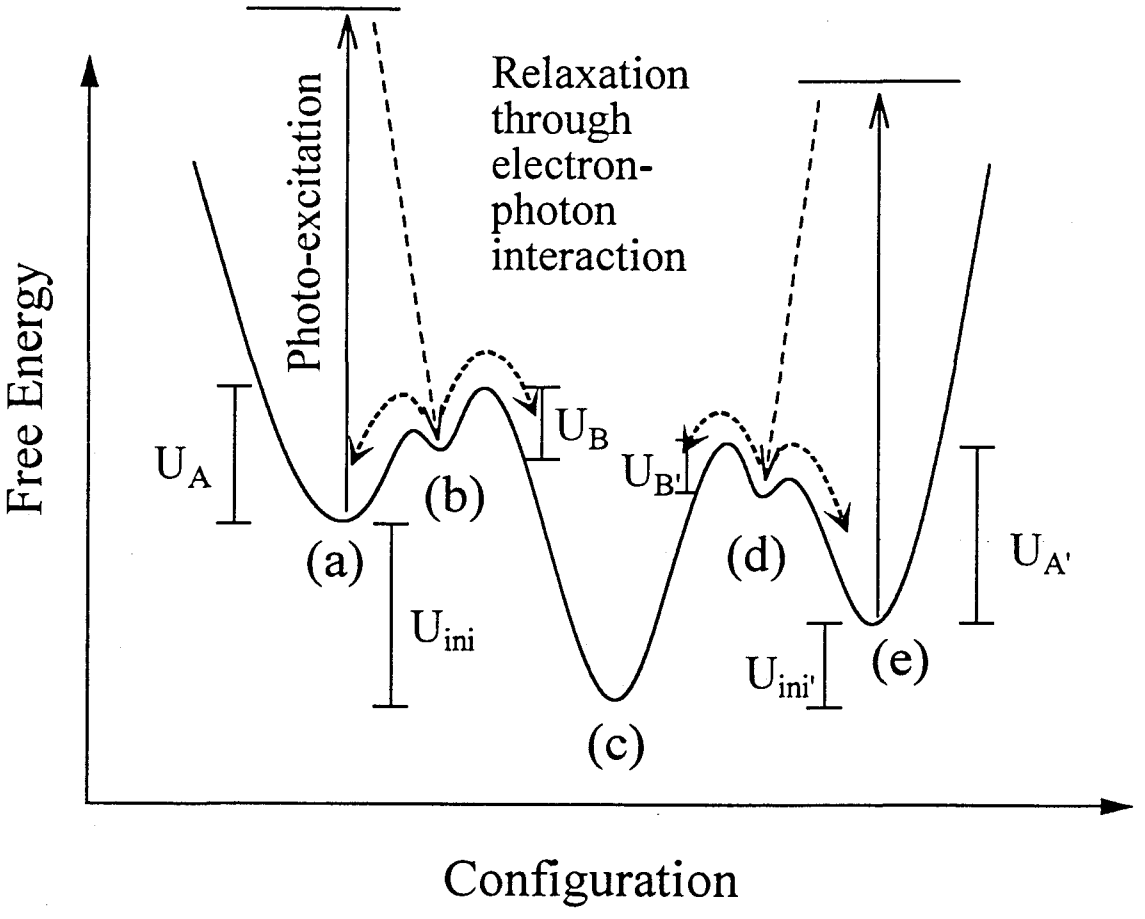


Figure 6.5: The diagram of the electronic and thermal processes during the latent period of the PIC process. The initial glassy states (a) and (e) are obtained by different preparation methods. The former is obtained by vacuum evaporation and the later by quenching melts. The (b) and (d) are the intermediate glassy states and the (c) is the state of crystalline nuclei. For a pure thermal crystallization process the glass must overcome the energy barrier $U_A$ or $U_{A'}$, while in the PIC process it just need to overcome the $U_B$ or $U_{B'}$ by the assistance of the thermal excitation.

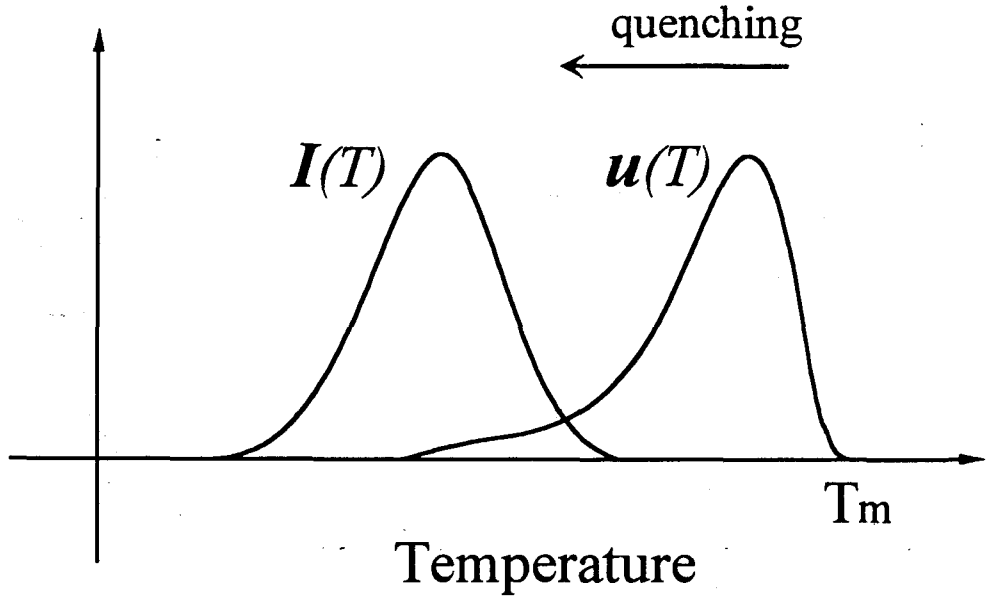


Figure 6.6: The temperature dependence of the nuclei appearance frequency $I(T)$ and the crystal growth $u(T)$. $T_m$ is the melting point.

# Chapter 7

# Photoluminescence in c–$GeSe_2$

In this chapter we report the PL study of c–$GeSe_2$ in the temperature range of 10~250 K and the excitation energy range of 1.9~2.81 eV. The temperature dependence of peak energy, the full width at half maximum ( FWHM ) and the intensity of PL spectra at various excitation energies are analyzed ( chapter 7.1 ). A configurational coordinate energy diagram method is used to interpret the relaxation processes of the photon-excited electrons ( chapter 7.2 ).

## 7.1 Results: Temperature and Excitation Energy dependence

The c–$GeSe_2$ measured in this work is a layer-formed crystal. Here, we report the PL spectra measured with the polarization of the incident light ( $\vec{E}$ ) parallel to the $a$ axis ( $E \parallel a$ ). The only difference between the PL spectra measured in the way of $E \parallel a$ and that of $E \parallel b$ is the intensity. This is related to the difference between the absorption coefficient for $E \parallel a$ and that for $E \parallel b$ [53].

Some characteristic PL spectra of c–$GeSe_2$ which are excited by various excitation energies at 20~55 K are shown in Fig. 7.1. The large Stokes shift ( 1.0~1.2 eV ) which is near the half of the band gap energy and the FWHM ( ~0.33 eV ) observed in each PL spectrum are similar to those in the published papers [41-45]. The PL spectra are fitted very well by a single Gaussian curve except for those excited at 2.41 eV. At excitation energy of 2.41 eV, the PL spectra are fitted by two Gaussian curves Fig. 7.1(b), whose peak energies are about 1.02 eV and 1.25 eV.

The fitting results of peak energies for the PL spectra are shown in Fig. 7.2. Obviously, the peak energies belong to three energy zones. At 20 K the peak energies move around 1.15 eV, 1.02 eV and 1.25 eV in the descendent sequence of excitation energy from 2.81 eV to 2.03 eV. The details are as follows:

1. At the excitation energies of 2.81 eV and 2.71 eV, the peak energies are about 1.15 eV which suggests that a luminescence band ( *P1* ) is associated with a excitation band *E1* which includes 2.71 eV and 2.81 eV.

2. At the excitation energies of 2.54 eV and 2.41 eV, the peak energies are about 1.02 eV. In the same way as we denoting the *P1* and *E1* bands, a luminescence band *P2* with the peak energy around 1.02 eV and a corresponding excitation band *E2* which includes 2.54 eV and 2.41 eV can be obtained.

3. Also from the peak energies of the PL which are caused by the excitation energies of 2.41 ~2.03 eV, we can infer that a luminescence band *P3* with the peak energy around 1.25 eV and a corresponding excitation band *E3* which covers the energy range of 2.41 ~2.03 eV exists.

To summarize the above results at 20 K, a excitation spectrum which is normalized by the incident photon flux as shown in Fig. 7.3 (a) is very useful. At excitation energy of 2.41 eV, the PL spectra are asymmetric since the PL bands *P2* and *P3* are simultaneously excited through the overlapped region of the excitation bands *E2* and *E3*.

Now, we return to Fig. 7.2 to study the temperature dependence of the peak energies. According to the excitation energy, the results are expressed in the next four parts;

1. In the whole experimental temperature range ( 20~250 K ) the excitation energies of 2.71 eV and 2.81 eV belonging to the *E1* band cause the PL of *P1* band peaked near 1.15 eV.

2. At the excitation energy of 2.54 eV, in a lower temperature range ( 20~50 K ) the peak energy is about 1.02 eV, but in higher temperature range ( 100~250 K ) the peak energy is about 1.15 eV. Within each temperature range, the peak energies are independent of temperature. Thus, in the lower temperature range ( 20~50 K ) the *E2* band corresponding to the *P2* band includes 2.54 eV and in the higher temperature range ( 100~250 K ) the *E1* band covers 2.54 eV instead of the *E2* band.

3. At the excitation energy of 2.41 eV the PL spectra are fitted by two Gaussian curves. One with the peak energy about 1.02 eV is related to the *P2* band which is caused by the *E2* band being excited. The other one, whose peak energy is about 1.25 eV, relates to the *P3* band which should be excited by the corresponding excitation band *E3*. Thus, the energy 2.41 eV belongs to both the *E2* and *E3* bands in the whole experimental temperature range.

4. At the excitation energy of 2.13 eV below 150 K and 2.03 eV below 200 K, the PL peak energies are about 1.25 eV which relates to *P3* band. In those two temperature ranges the excitation band *E3* includes 2.13 eV and 2.03 eV. At the excitation energy of 2.13 eV above 150 K and 2.03 eV above 200 K, the PL peak energies are about 1.15 eV. Though according to the peak energies the PL spectra seem to be related to the *P1* band, it is rather inappropriate to imagine that the *E1* band extends over the energy range from 2.81 eV to 2.03 eV at around 150~200 K as described below.

For comparing the temperature dependence of the excitation bands *E2* and *E3*, let us consider the intensities of the resolved PL bands at the excitation energy of 2.41 eV. Although the peak energies of the two resolved PL were independent of the temperature, the shapes of the PL spectra changed and the total luminescence intensity decreased with increasing temperature as shown in Fig. 7.1(b). Here the intensity is represented by the area of the resolved Gaussian curves. In this work at 20 K the intensity which relates to the *P2* band ($I_{P2}$) is about 1/4 of that which is related to *P3* band ( $I_{P3}$ ). With increasing temperature the $I_{P2}$ and $I_{P3}$ become comparable. This result suggests that the decreasing rate of $I_{P2}$ with temperature is different from that of $I_{P3}$ .

The particular temperature dependence of the luminescence bands which are excited by 2.54 eV, 2.13 eV and 2.03 eV can be explained by assuming that the excitation bands shift to lower energies with increasing temperature. At the excitation energy of 2.54 eV, in the lower temperature region the excitation band *E2* is excited, however, with increasing temperature to the higher temperature region the *E2* and *E1* bands shift to lower energies. As a result the *E1* band is excited instead of *E2* in the higher temperature region. At 70 K the peak energy ( 1.08 eV ) which does not belong to any luminescence zones can be interpreted as that both the *E1* and *E2* bands are excited in the nearly equal degree. Later, we will show that at this condition the FWHM takes an abrupt increase at 70 K. At excitation energies of 2.13 eV and 2.03 eV in the

temperature regions above 150 K and 200 K respectively, the *E2* band shifts to the energy region which covers 2.13 eV and 2.03 eV. Both the *E2* and *E3* bands are excited to make the peak energies of PL near $(1.25 + 1.02)/2 \sim 1.15$ eV. Here, the FWHM of the spectra in the higher temperature regions are too wide and the intensity of those are too weak to separate the spectra into two Gaussian curves. The characteristic temperatures at which the *E2* band comes to include the excitation energies of 2.13 eV and 2.03 eV are 150 K and 200 K, respectively. These characteristic temperatures are also consistent with the assumption that the excitation bands shift to the lower energies with increasing temperature.

The main results which have been shown in Figs. 7.1 and 7.2 are summarized by the excitation spectra as shown in Fig. 7.3. The *E1* and *E2* bands shift to lower energies with increasing temperature, however, the *E3* band shows different tendency. Around the excitation energies of 2.13 eV and 2.03 eV at 230 K the excitation spectra are drawn with dashed-lines, because the PL spectra consist of two luminescence which are caused by the *E2* and *E3* bands and those two luminescence are difficult to resolve at 230 K.

The *E1* and *E2* bands have been also observed in the vapor phase grown c–$GeSe_2$ in the previous report [45]. But the *E3* band whose temperature dependence is different from those of *E1* and *E2* bands does not always exist in the different crystalline samples which are prepared even in the same manner. In polycrystalline $GeSe_2$ which are grown with the temperature difference between the two ends of the preparation ampoule larger than 5 °C ( see chapter 3.1 for detail ), we have not found any PL spectra with the peak energies around 1.25 eV. In addition, this type of the PL spectrum does not observed in amorphous $GeSe_2$ ( Ref. [45] or chapter 8 ). It seems that the *E3* band is seldom related to the strain and/or disorder which are generated in the samples during growth process. At present the origin of *P3* and *E3* bands is not clear and we will not discuss about it further in this paper.

The FWHM is another important parameter to study the relaxation processes in the systems with a strong electron–phonon interaction. In Fig. 7.4 the temperature dependence of FWHM at the excitation energies of 2.54 eV, 2.71 eV and 2.81 eV is shown. There is an abrupt increase at 70 K in FWHM of PL whose excitation energy is 2.54 eV. This unusual enlargement of FWHM is explained as that both the *E1* and *E2* bands are excited through their crossover energy region which shifts to lower energies with increasing temperature and comes to cover the excitation energy 2.54 eV at around

70 K.

## 7.2 Discussion

In layer-formed c-$GeSe_2$, it has been reported that there is a peak at 2.854 eV in the absorption spectra of $E \parallel a$ polarization at 4.2 K in Ref. [53], as shown in Figs. 2.8 and 2.9. With increasing temperature. the absorption peak shifts to lower energies and becomes wider ( Fig. 2.9 ). The temperature coefficient of the absorption peak energy has been found as about $-4 \times 10^{-4}$ eV/K. Since this absorption peak is related to the excitons whose energies are lower than that of the band gap and the upper limit energy of our incident light is lower than that of the absorption peak, the final state of the excitation processes should be considered as the excitons in localized states. These excitons involve at least one localized state (gap state) in the excited electron or hole. In this work the excitation and relaxation processes are mainly related to the localized states in the band gap. Though these excitons are only observed at $E \parallel a$ polarization, not difference of the spectral shapes, excitation energy and temperature dependences between the $E \parallel a$ and $E \parallel b$ polarizations has been found except for the intensity. The strong electron–lattice interaction may leads the localized excitons lost their initial polarization during the relaxation processes. In this case the intensity will be different according to the difference between the absorption coefficient for the two polarizations.

Now we turn to discuss why the excitation bands *E1* and *E2* shift to lower energies with increasing temperature while the corresponding luminescence bands *P1* and *P2* are independent of temperature. A configurational coordinate diagram ( CCD ) is often used to interpret the phenomena that the PL spectra have a wide FWHM with a large Stokes Shift [98]. The typical PL radiation processes are shown in Fig. 7.5 schematically.

In the PL radiation processes, we refer to the ground state as that the electronic system is in its ground state but the lattice vibration is not. At rather lower temperature ( ~0 K ) in the ground state, the amplitude of the lattice vibration is small, where the expectation value of the configurational coordinate ( $\bar{Q}(T)$ ) coincides to the position which gives the minimum of the adiabatic potential curve of the ground state. When the electrons/holes are excited optically, the coordinate $Q$ does not change during the excitation according to the Frank–Condon principle. The energy of the absorbed photon is equal to the difference between the two points on the adiabatic potential curves of the ground state and localized state at the same $Q$. Just after the optical excitation

the lattice starts to vibrate around the $Q_l$ which gives the minimum of the curve of the localized state, and at the end of electronic lattice relaxations the PL spectrum with the peak energy of $Ep$ is observed. The peak energy of the excitation band at $T \sim 0$ K is $E(0)$ which is equal to the difference between the two adiabatic potential at $Q = 0$. With increasing temperature the thermal expansion, which is caused by the asymmetrical adiabatic potential of the ground state, becomes to be important when we consider the excitation processes. At $T \neq 0$ in the ground state the averaged position of the lattice vibration is at $\bar{Q}(T) \neq 0$. At this temperature, the absorption band shifts with the peak energy equal to the energy difference between the ground state and the localized state at $Q = \bar{Q}(T)$. This absorption band shift leads the peak energy of the excitation band changes from $E(0)$ to $E(T)$ which is lower than $E(0)$. The fact that the peak energy of a given PL band is not so affected by the temperature suggests that the asymmetric degree of the potential curve of the localized state is less than that of the ground state.

Next we discuss the behavior of the peak energy and FWHM of the PL spectra which are excited by 2.54 eV. In case of having two localized states ( *1*, *2* ) as shown in Fig. 7.5(b), at T $\sim$ 0 K the peak energy of the excitation band which corresponds to the localized state *2* equals to $E_2(0)$. In the temperature range of 20$\sim$50 K after excited by the energy around $E_2(0)$ which includes 2.54 eV, the PL spectra with the peak energies at $E_{P2}$ ( 1.02 eV ) will be observed. With increasing temperature to the higher temperature range of 100$\sim$250 K, the averaged position of the lattice vibration in the ground state changes to $\bar{Q}(T)$, and the peak energy of the excitation band which corresponds to the localized state *1* is $E_1(T)$ whose value is the same as that of the $E_2(0)$. So at these temperatures, the excitation band *E1* is excited by 2.54 eV and the peak energy of the PL becomes $E_{P1}$ ( 1.15 eV ). At 70 K, 2.54 eV is included in both the *E1* and *E2* bands. After the excited electrons/holes releases the energy in the localized states *1* and *2* , the PL spectrum which comes from the two localized states is observed. The peak energy of the PL takes an average value of 1.02 eV and 1.15 eV, and the FWHM shows an unusual increase at 70 K.

Now we turn to discuss the temperature dependence of the FWHM. The calculated values of the FWHM ($\Delta$) are obtained by using the equations

$$\Delta(T) = \Delta(0)(\coth\{\frac{\hbar\omega_{ph}}{2kT}\})^{1/2}, \tag{7.1}$$

and

$$\Delta(0) = 1.7(2W\hbar\omega_{ph})^{1/2}, \tag{7.2}$$

where the FWHM is treated as the result of the electron–phonon interactions ( see chapter 2.4 or Refs. [41,84-88] for details ). Here, $2W$ is the Stokes shift and $\hbar\omega_{ph}$ is the representative phonon energy. The Raman measurement result of $\hbar\omega_{ph} = 24$ meV, which is ascribed to the breathing vibration of $GeSe_{4/2}$ tetrahedra, is used to obtain the $\Delta$. The solid line in Fig. 7.4 is drawn by using the equations ( 7.1 ) and ( 7.2 ) with the experimental results of $2W$ and $\hbar\omega_{ph}$. At low temperature the calculated values are in agreement with the experimental results, however, with increasing temperature the calculated line departs from the experimental results. For example, at 150 K the enlargements of the experimental values are 2~3 times of the calculated value ( $\Delta(T) - \Delta(0)$ ). These big differences which are larger than the experimental error suggest that the PL processes at high temperature can not be interpreted by only considering the effect of electron–phonon interactions.

In the high temperature region, the hot luminescence processes in which the excitons do not reach the thermal equilibrium in the localized states, may directly affect the temperature dependence of the FWHM. The energies of hot luminescence are usually higher than those of the PL with a large Stokes shift ( labeled normal PL ). In case of observing both the hot luminescence and normal PL with comparable intensities, the obtained PL spectrum will be broader than the normal PL spectrum. At the high temperature, as an interpretation of the large broadening of the FWHM as shown in Fig. 7.4, it is probable that the intensity of hot luminescence becomes comparable with that of the normal PL. However, for a complete explanation, a combinative study of the theoretical and experimental approach is expectative. At least the temperature dependence of the decay times for each luminescence bands should be investigated.

By studying the intensity of PL, we also get the information of the way how excited electrons/holes relax. Generally the $I_{PL}$ is described by

$$I_{PL} = I_{in}\,(1-R_{in})(1-R_{PL}) \int_0^D \alpha\,\eta\,e^{-\alpha x}dx = I_{in}(1-R_{in})(1-R_{PL})\,\eta\,(1-e^{-\alpha D}), \tag{7.3}$$

where $I_{in}$ is the incident laser intensity; $\eta$ is the quantum efficiency; $R_{in}$ and $R_{PL}$ are the reflectivity of the incident light and the PL; $\alpha$ is the absorption coefficient for incident light; $D$ is the thickness of the samples. Obviously at the condition that the reflectivity is not sensitive to temperature and the $D$ is large enough to absorb the laser light

completely, equation ( 7.3 ) can be expressed as

$$I_{PL} = C\eta. \tag{7.4}$$

Here $C$ is a constant independent of temperature. In this work at the excitation energy above 2.54 eV in the temperature range of 20~250 K, the $I_{PL}$ directly relates to the quantum efficiency $\eta$ as equation ( 7.4 ).

With increasing temperature the $I_{PL}$ decreases. This thermal quenching is interpreted by the energy level scheme as shown in Fig. 7.6. Here we assume as follows: the non-radiative transition probability $P_{nr}$ relates to a processes where the excitons do not relax to the thermal equilibrium localized states; the $P_r$ with a value of $1 - P_{nr}$ is a transition probability of the excitons relaxing to the thermal equilibrium localized states; the radiative transition probability $q_r$ relates to the processes from the thermal equilibrium localized states to the ground state with emitting photon and the non-radiative transition probability $q_{nr}$ relates to a phonon assisted non-radiation processes from the thermal equilibrium localized states. Then from Fig. 7.6 we get equations

$$\begin{cases} \frac{dN}{dt} = -(P_{nr} + P_r)N + g, \\ \frac{dN'}{dt} = -(q_{nr} + q_r)N' + P_r N, \end{cases} \tag{7.5}$$

where $N$ and $N'$ are the population of excited electrons/holes before the thermal equilibrium and at the thermal equilibrium localized states respectively, $g$ is a generation rate of the excited states. From equation ( 7.5), $N'$ is given as

$$N' = \frac{gP_r}{(P_{nr} + P_r)(q_{nr} + q_r)}, \tag{7.6}$$

where $I_{PL} = q_r N'$. The $q_{nr}$ comes to 0 at T = 0 K . Finally we get the relation

$$\frac{I_{PL}(0)}{I_{PL}(T)} - 1 = \frac{q_{nr}}{q_r}. \tag{7.7}$$

Since the $q_{nr}$ relates to a phonon assisted non-radiative process, it is written in the form of

$$q_{nr} = A\exp(-\frac{E_{th}}{kT}), \tag{7.8}$$

where $A$ is a constant independent of temperature; $E_{th}$ is the thermal activation energy. As for the *P1* band, taking $I_{PL}(10K)$ instead of the $I_{PL}(0)$, good fits to the experimental results are obtained with $E_{th} = 0.1$ eV both at excitation energies of 2.81 eV and 2.71 eV. The experimental results and the fitting lines are shown in Fig. 7.7. The fact that there

is only one activation energy in the *P1* band suggests that the transition probability $P_{nr}$, which relates to the non-radiative transition processes where the excitons not relaxing to the thermal equilibrium localized states, should be independent of temperature. For more information about the activation energies of *P2* and *P3* bands, it is necessary to know the quantum efficiency of the PL from the two bands before using the equation ( 7.5 ).

## 7.3 Summary and Conclusions

In this chapter, the photo-luminescence of c–$GeSe_2$ has been studied in the temperature range of 10~250 K with a excitation energy range of 1.93~2.81 eV. The results can be concluded in the next four parts.

1. There are two intrinsic PL bands *P1* and *P2* with peak energies at 1.15 eV and 1.0 eV respectively. PL band *P3* at 1.25 eV, which is observed at low excitation energy, shows the sample dependence strongly.

2. A configurational coordinate energy diagram method is used to interpret the phenomena that the peak energies of the luminescence bands *P1* and *P2* are independent of temperature while the corresponding excitation bands *E1* and *E2* shift to lower energies with increasing temperature.

3. From the investigation of FWHM at high temperature region of the *P1* band we have found that the PL process is no longer treated with a simple application of the configurational coordinated energy diagram method. The large broadening at high temperature may be related to the hot luminescence processes.

4. With increasing temperature, the decrease of the intensity for *P1* band is a single thermal activation type with the activation energy of $E_{th} = 0.1$ eV.

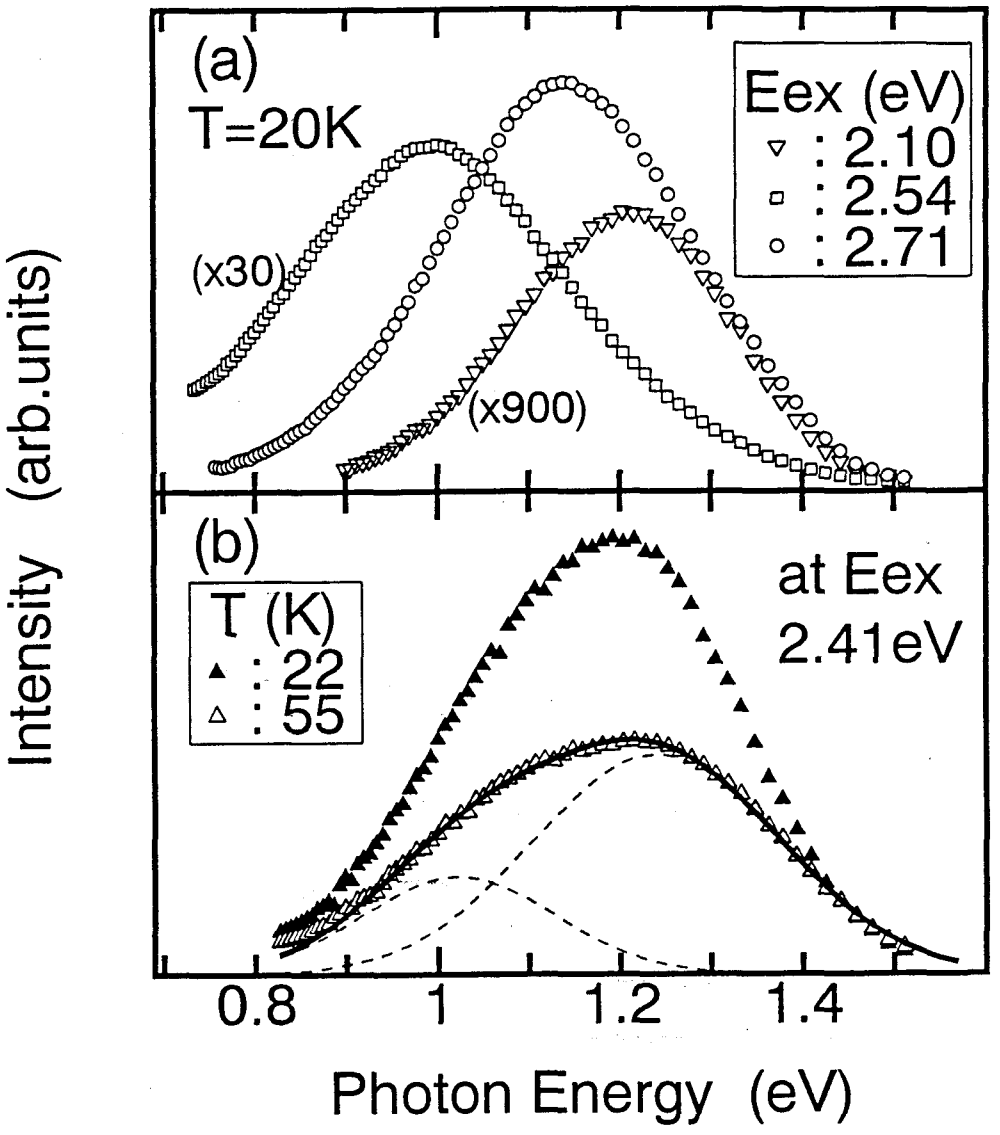


Figure 7.1: (a) The PL spectra of c–$GeSe_2$ at the excitation energies of 2.71 eV, 2.54 eV and 2.10 eV. (b) The asymmetric spectral shape which is fitted by two Gaussian curves ( broken lines ) with peak energy at 1.01 eV and 1.22 eV is excited by 2.41 eV.

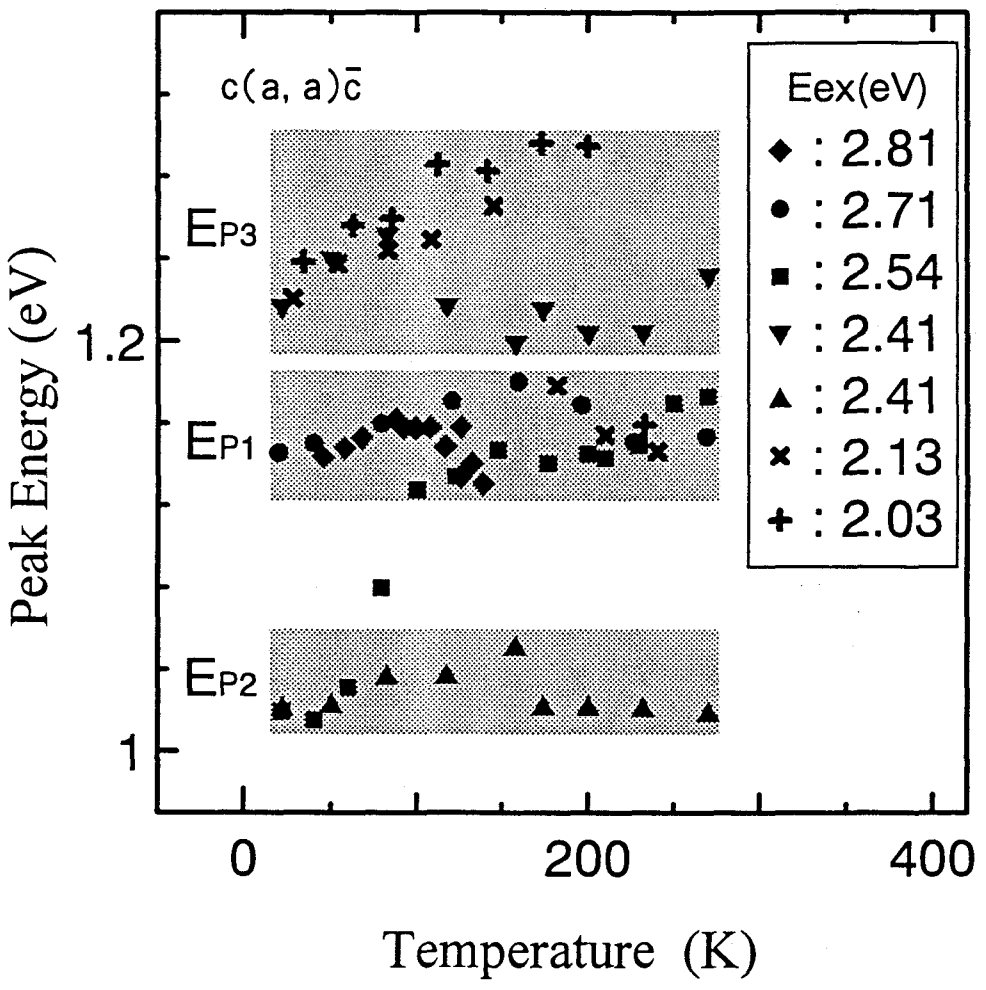


Figure 7.2: Temperature dependence of the peak energies at various excitation energies. The peak energies can be classified into three groups according to the excitation energies. The detail of three groups, ~1.15 eV, ~1.02 eV and ~1.25 eV, is described in the text.

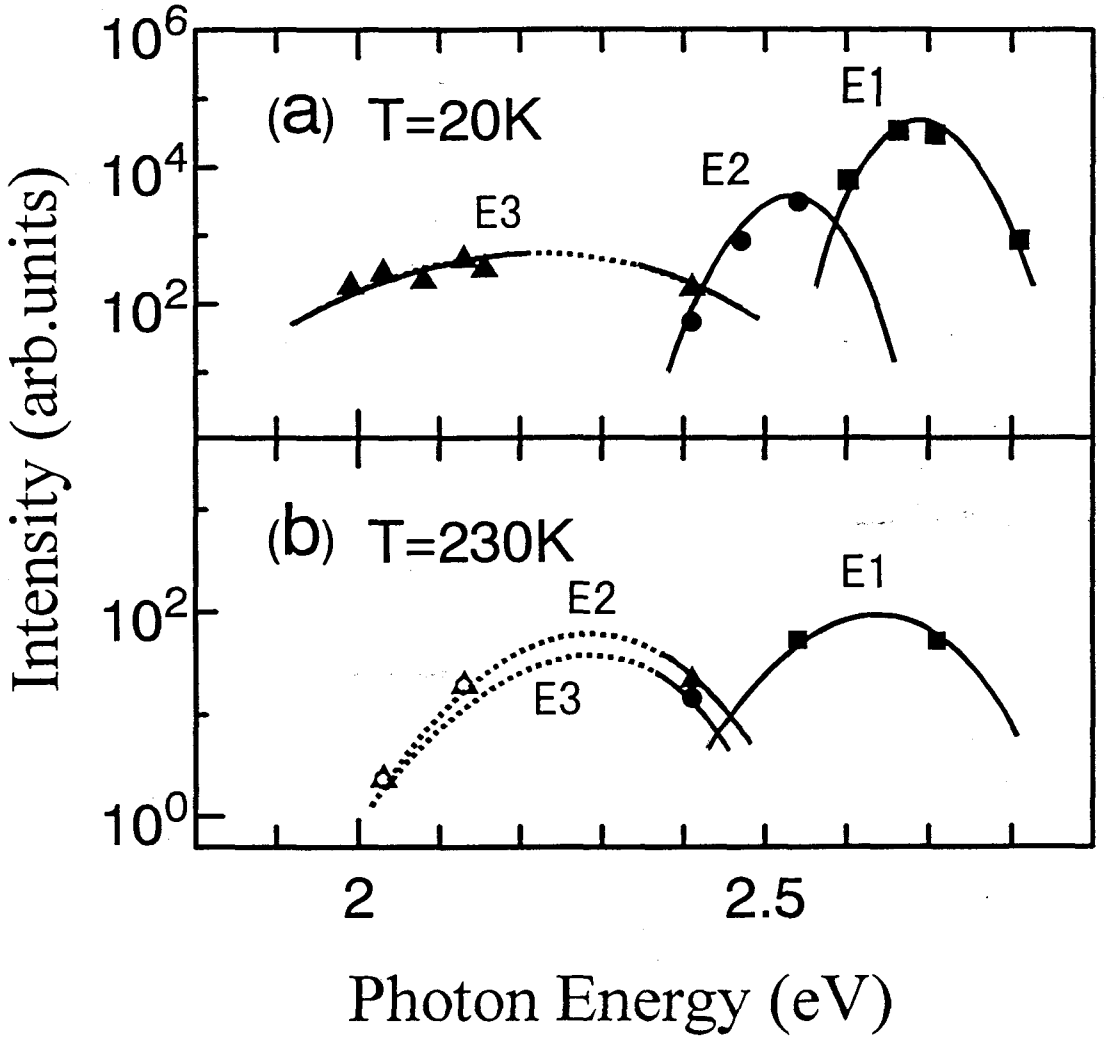


Figure 7.3: The excitation spectra which are normalized by the incident photon flux. Excitation bands *E1* and *E2* shift to lower energies with increasing temperature. Temperature dependence of *E3* is different from those of *E1* and *E2*.

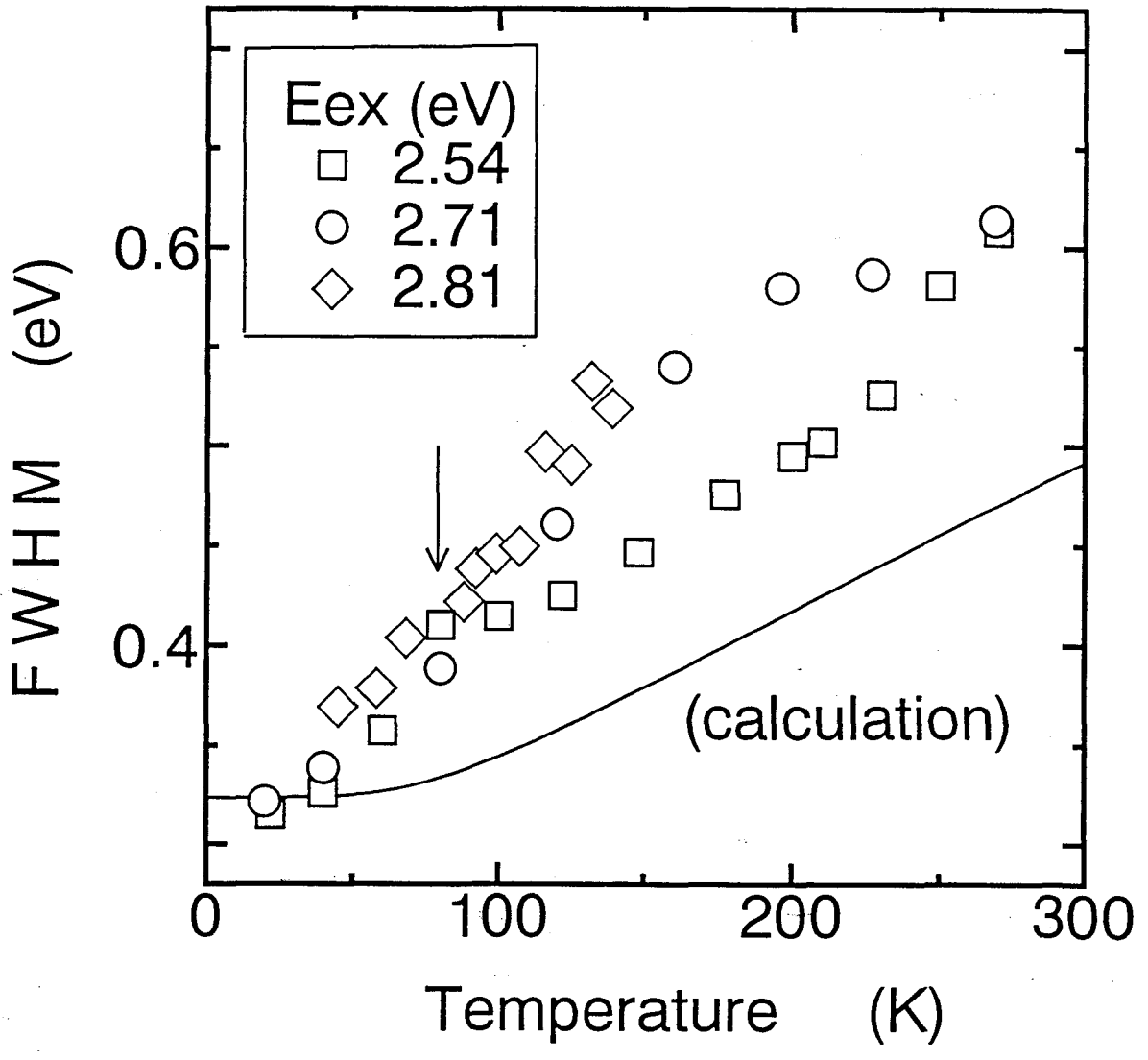


Figure 7.4: Temperature dependence of FWHM. At the high temperature region the calculated line departs from the experiment results. The FWHM of PL excited by 2.54 eV at 70 K is pointed by an arrow takes an unusual increase.

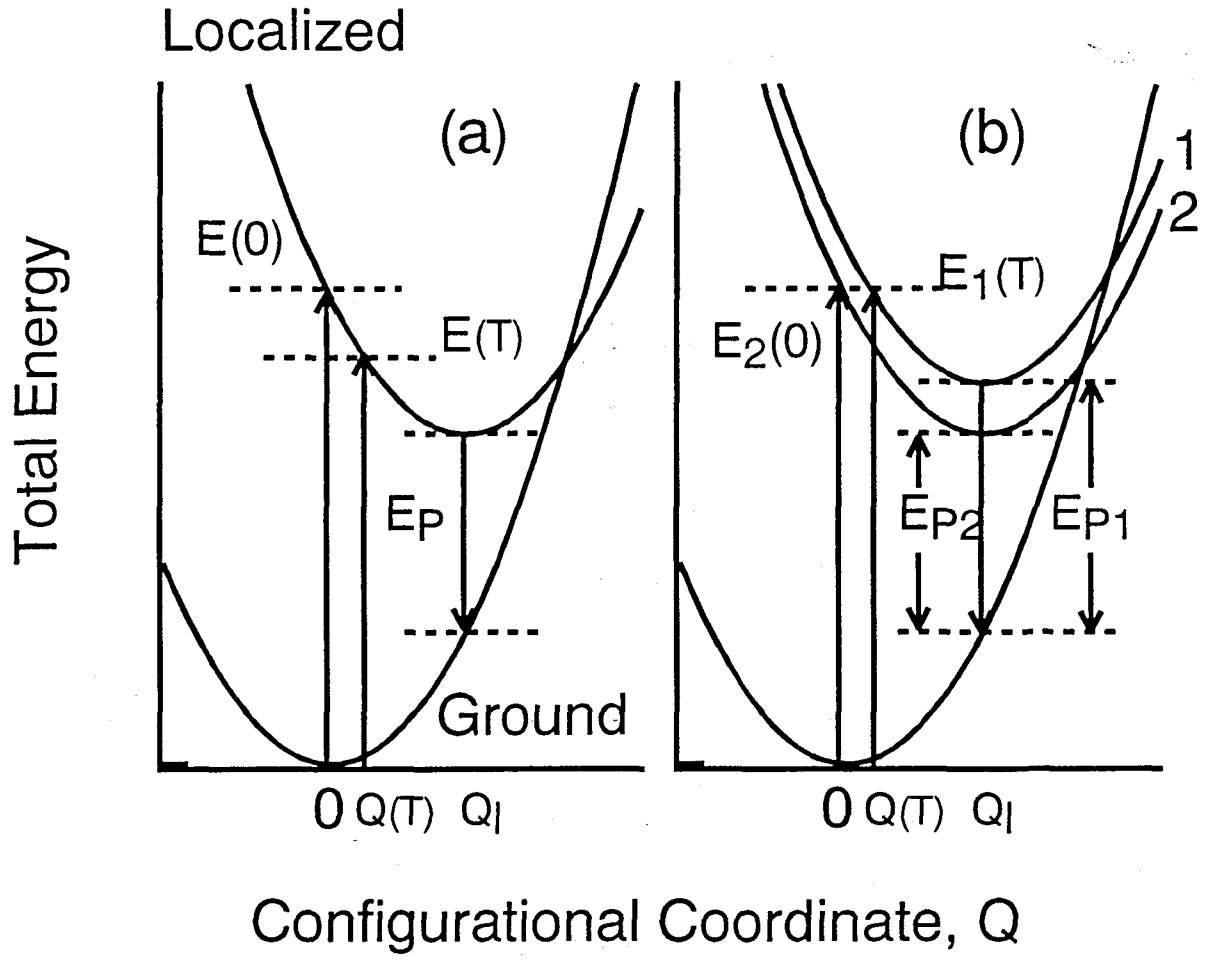


Figure 7.5: (a) The excitation band shifts to lower energies with increasing temperature while the peak energy is independent of temperature. (b) At excitation energy of 2.54 eV which belongs to $E_2(0) = E_1(T)$, with increasing temperature to $T$ the excitation band shifts from *E2* to *E1* which makes the peak energies shift from $E_{P2}$(1.0 eV) to $E_{P1}$(1.15 eV).

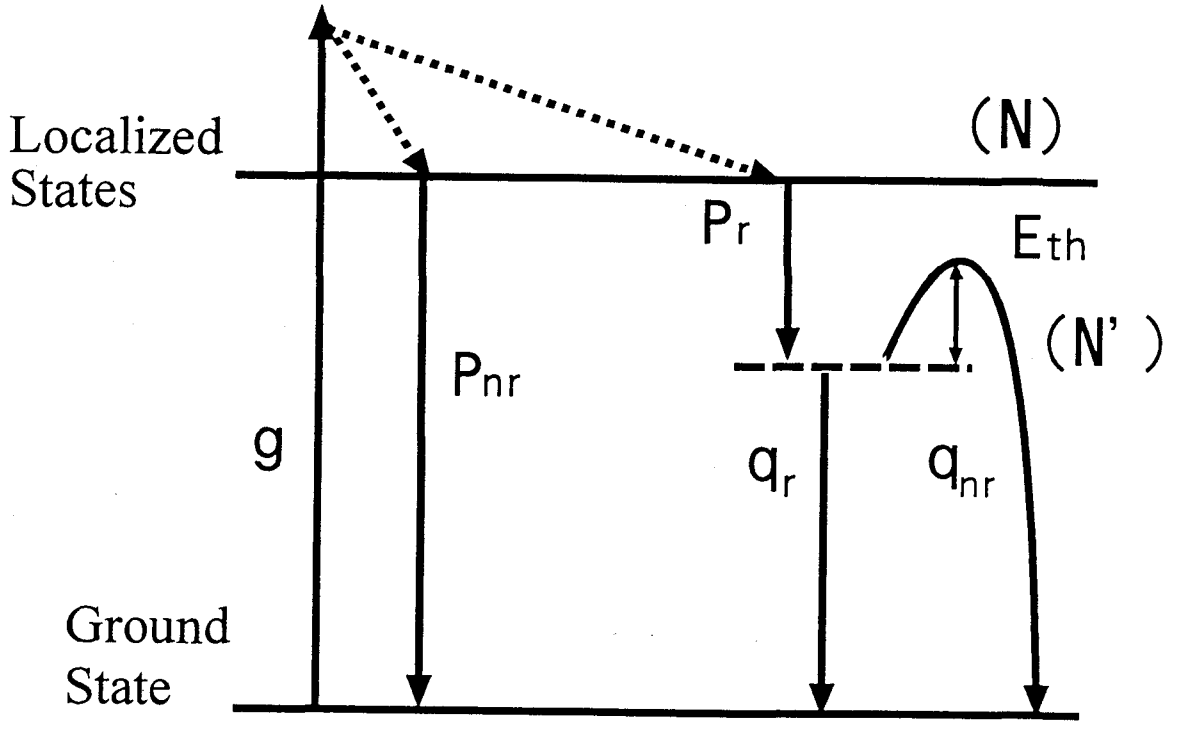


Figure 7.6: A scheme of energy levels in the PL process. $N$ is the population of the excitons before they reach the thermal equilibrium. $N'$ is the population of the localized excitons at the thermal equilibrium states.

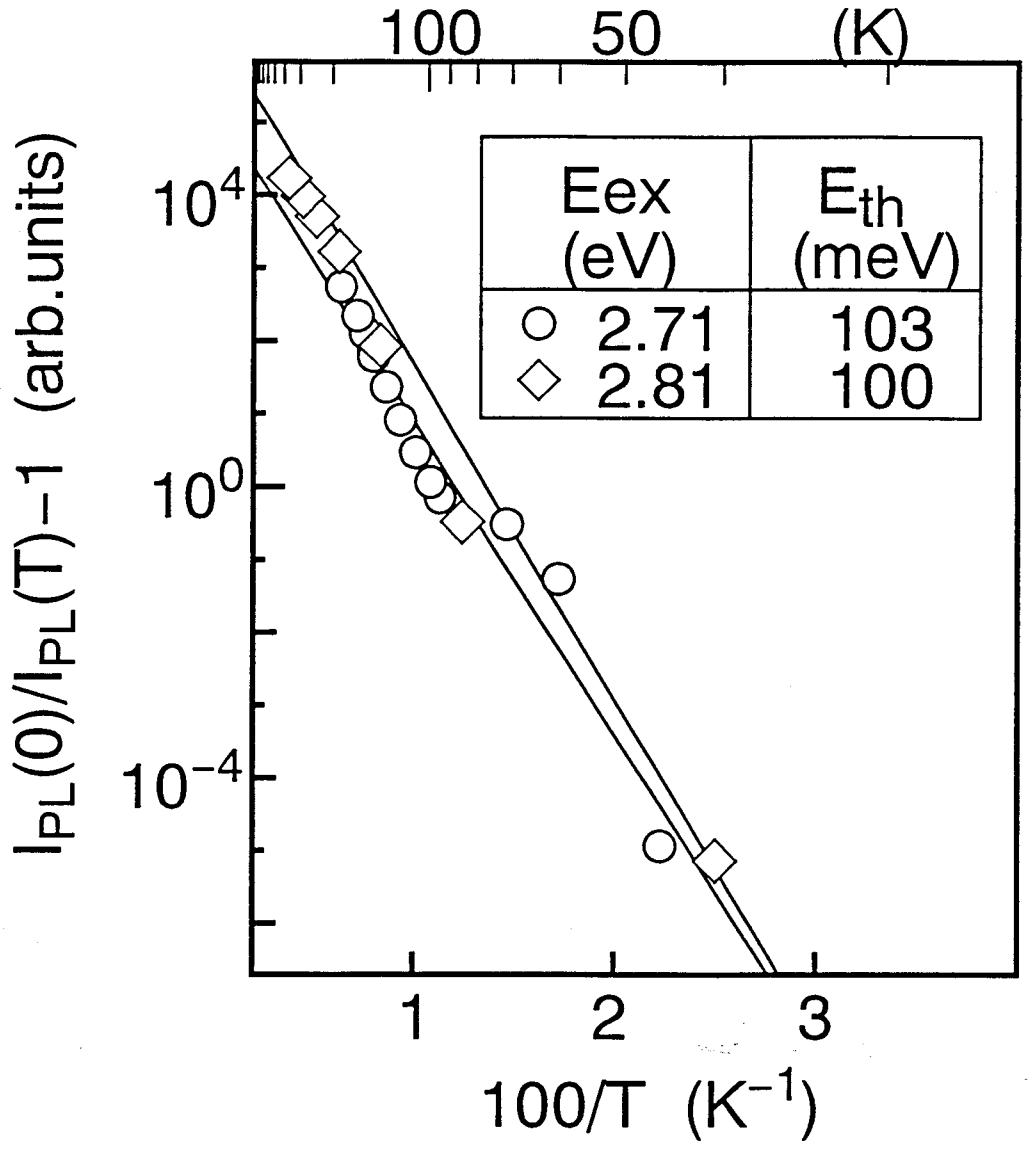


Figure 7.7: Temperature dependence of the $I_{PL}(0)/I_{PL}(T) - 1$.

# Chapter 8

# Photoluminescence in g–$GeSe_2$

In this chapter, we investigate the PL spectra of the glassy $GeSe_2$ ( g-$GeSe_2$ ) in the temperature range of 10~220 K with the excitation photon energy range of 1.93~2.71 eV. The temperature and the excitation photon energy dependence of the PL intensity ( $I_{PL}$ ), of the PL peak energy ( $E_p$ ), and the peak width FWHM ( $\Delta$ ), are measured precisely ( chapter 8.1 ). The results are discussed by considering two different kinds of relaxation processes, one without large lattice distortion and the other with large lattice distortion ( chapter 8.2 ).

## 8.1 Results: Temperature and Excitation Energy Dependence

Figure 8.1 shows some typical luminescence spectra. To get the PL peak energy ( $E_p$ ) and the FWHM, all the PL spectra are fitted by Gaussian curves. In the spectrum of the $GeSe_2$ glass at 10 K with 2.41 eV excitation, for example, $E_p$ and $\Delta$ are 0.99 eV and 0.36 eV, respectively. The obtained values agree with those of the previous works [42,44,99-102]. The fatiguing effect [84] was not remarkable in the sample we used. In Fig. 8.1, changes of the PL spectrum by varying temperature are clearly shown: the lower energy side of the spectrum shifts toward higher energy with increasing temperature, while no notable change is observed on the higher energy side of the spectrum. Consequently, with increasing temperature in this range ( 10~120 K ), $E_p$ increases and $\Delta$ decreases. This behavior has not been reported by other workers. The temperature dependence of the shape of the spectra will be examined more precisely later.

Figure 8.2 shows the variation of $E_p$ and FWHM ( $\Delta$ ) at 18 K in the excitation energy ( $E_{ex}$ ) region from 1.93 eV to 2.71 eV in the upper and lower halfs, respectively. With increasing excitation energy, the peak energy increases in the region of $E_{ex} <$ 2.2 eV and decreases in the region of $E_{ex} >$ 2.4 eV. While the $\Delta$ increases with increasing excitation photon energy monotonically in the whole experimental energy range. In energy region of $E_{ex} >$ 2.5 eV, a faster increasing rate of the $\Delta$ is observed than that in the lower one. The reported data in Ref. [84] well agrees with ours except the decrease of $E_p$ in $E_{ex} >$ 2.5 eV which have been shown in ours as well as data in Ref. [44].

The fitting results of the temperature dependence of the luminescence peak energy at various excitation photon energies are shown in Fig. 8.3. In this work, the relative accuracy of the $E_p$ values in the same excitation energy is generally within 0.01 eV. With increasing temperature, for the curve of $E_{ex} = 2.41$ eV, the peak energy first increases in the region of $T <$ 100 K, and then decreases in the region of $T >$ 100 K. For the curve of $E_{ex} = 2.54$ eV, a similar temperature dependence has been obtained with the turning point at about 120 K. On the other hand, for the curve of $E_{ex} = 2.01$ eV, the peak energy increases monotonically with increasing temperature. Figure 8.4 shows the temperature dependence of the luminescence peak width at various excitation photon energies. At all excitation photon energies, the width first decreases and then increases with increasing temperature. However, the temperature which gives the minimum width varies with the excitation energy; the lowest temperature ( $\sim$ 60 K ) is observed at $E_{ex} = 2.01$ eV among those of the curves shown in the figure. The obtained results are different from those by others. In Ref. [102], with the excitation by broad band light ( 2 $\sim$ 3 eV ) from a Hg lamp, the monotonic increase of $E_p$ and $\Delta$ with increasing temperature has been reported.

Figure 8.5 shows the excitation spectra of PL at 18 K in which the excitation energy dependence of intensity is expressed. Close circles denote the total integration of the emission spectrum normalized to the incident photon flux. The data agree well with those in Ref. [84]. The PL intensity $I_{PL}$ is expressed as follows:

$$I_{PL} = (1 - R_{in})(1 - R_{PL})\, I_{in}\, \eta\, (1 - e^{-\alpha D})$$

which is used in chapter 7.2 ( equation 7.3 ). $I_{PL}$ is proportional to $\eta$ for $\alpha D \gg 1$, while $I_{PL} \propto \eta \alpha D$ for $\alpha D \ll 1$. In the region of $E_{ex} <$ 2.2eV, the sample is considerably transparent. Taking into consideration of non-absorbed light in that energy region, the data points proportional to $\eta$ are plotted as the open circles. In the region of $E_{ex} >$

2.4 eV, the open circles, which are not shown, should be plotted at the same position as the corresponding close circles. The $\eta$ decreases significantly with increasing $E_{ex}$, where the slope of the curve obviously changes between the region of $E_{ex} < 2.2$ eV and that of $E_{ex} > 2.4$ eV.

Figure 8.6 shows the temperature dependence of the PL intensity, which is normalized to the incident photon flux at 18 K. The relation $I_{PL} \propto \exp(-T/T_0)$, which have been pointed out by previous workers, well holds with the value of $T_0 = 30$ K, except for $E_{ex} = 2.01$ eV. In the region of $E_{ex} < 2.2$ eV the absorbed photon flux increases with increasing temperature so that the quantum efficiency $\eta$ must be reduced by the absorption coefficent.

## 8.2 Discussion

In a material with a strong electron-phonon coupling, a PL spectrum generally shows a broad Gaussian line shape with a large Stokes shift. These phenomena were explained by using the configurational coordinate energy diagram in relaxation processes of the excitons in their localized states for c-$GeSe_2$ ( chapter 7, Fig. 7.5 ). The excitons relax and strongly localize with large lattice deformation. In glassy materials, it is also important that, even if there is weak electron-phonon coupling, innumerable localized states ( Anderson localization states ) exist adjacent to the extended states [41,98]. The boundary between the localized states and the extended states is called the mobility edge and the energy difference between the edge in the conduction band and that in the valence band is called the mobility gap. The PL peak energy of the $GeSe_2$ glass first increases and then decreases with increasing excitation photon energy in the present results ( Fig. 8.2 ). Murayama has pointed out that the upper limit of the excitation energy region in which the peak energy increases is related to the mobility gap [44].

With the $E_{ex}$ below the mobility gap in the $GeSe_2$ glass, the exciton is localized as shown in Fig. 8.7 (a). The energy of the innumerable localized states are schematically represented by two adiabatic potential curves in the figure.

The relaxation processes of the excitons are considered in two ways as follows:

1. The excited state loses its energy without large lattice relaxation as in Fig. 8.7 (b). This process contains the transition of the electron from a localized state toward other localized state without varying the coordinate $Q$.

2. The energy of the system is released by lattice relaxation with changing the coordinate $Q$ as in Fig. 8.7 (c). During the change of $Q$, the shape of wave function of the electron becomes to be more localized one.

In the process (1), the exciton is distributed to the localized states within the gap. However, with the process (2) proceeding, the exciton tends to be localized strongly in the localized states to prevent transition in the process (1). The transition ability in the process (1) decreases with the exciton approaches to a self trapped state where the shape of wave function of the electron is strongly localized. When the exciton is self-trapped where the system is in quasi thermal equilibrium, the lattice distortion stops at a certain $Q$ for the excited state with a minimum energy. Numerous self-trapped states are possible corresponding to the localized states in g–$GeSe_2$.

The system relaxes from the self-trapped localized state by radiatively ( Fig. 8.7 (d) ) or non-radiatively and then returns to the initial ground state with recovering the lattice distortion which releases the remainder of the energy. The observed photoluminescence spectra are the superposition of the emission from numerous self-trapped states depending on the distribution profile in the initial localized states.

The result that at the low temperature the PL energy increases with increasing excitation energy is explained as follows: the excitation to the state 1, which needs higher energy than that to the state 2, leads higher emission energy than that in the state 2. The increase of the PL peak energy which is much smaller than that of the excitation photon energy is explained by considering that the redistribution process of the exciton occurs among the localized states before it goes to the self-trapped state which is the initial state of the emission. The increase of the excitation photon energy raises the upper limit of the localized state but it affects the PL peak energy to a lesser extent.

The fact that with increasing the excitation photon energy in the region of below mobility gap the $\Delta$ increases is explained by considering the redistribution of the excited electron among the localized states. Here, we suppose that the process (2) with large lattice distortion dominates the relaxation processes before the quasi thermal equilibrium is reached by the process (1) without large lattice distortion, Thus, the higher the excitation photon energy is, the wider the distribution of the initial localized states are and the higher the upper limit of the distribution is. This leads the $\Delta$ increase.

In the case of above mobility gap excitation, $E_p$ decreases with increasing excitation photon energy in our results as shown in Fig. 8.2. After an electron is excited in the

extended states by the absorption of above mobility gap photon, the initial relaxation process without large lattice distortion is supposed to consist of the transition from the extended state to some localized states. About the transition probability from an extended state to a localized state, the following tendency has to be held: with decreasing the energy of the extended state, it becomes more difficult to make transition from the extended state to a deep initial localized state. This situation is realized by a potential fluctuation as in Fig. 8.8 (a), for example. The high potential barrier around the deep localization site reduces the transition probability from the low energy extended state to the deep localization state. The as-excited extended state with high energy may has a wider distribution of the localized states for its relaxation than that with low energy, particularly, in lower energy region of the localized states. After the distribution in the localized states without large lattice distortion is established, the process of the luminescence is the same as that for the below mobility gap excitation.

The excitation photon energy dependence of $\Delta$ is derived straightforward from above explanation. The schematic view is as follows ( Fig. 8.8 (b) ). The system excited with high energy photon ( $E_A$ ) may relax through the localized state 1 as well as through the state 2, while that with low energy photon ( $E_B$ ) may relax only through the localized state 1. The PL emission band excited with $E_A$ photon is equivalent to that caused by the below band gap excitation to the localized states 1 and 2, while the emission band excited with $E_B$ photon is equivalent to that caused by the excitation to the state 2. Thus $\Delta$ becomes broad with increasing excitation photon energy.

Let us consider the temperature dependence of the PL peak width in detail. In the case of the relaxation of one localized state in the g–$GeSe_2$, the $\Delta_{ph}$ increases with increasing temperature which can be described as $\Delta_{ph}(T) = \Delta_{ph}(0)[\coth(\hbar\omega_{ph}/k_BT)]^{1/2}$ ( chapter 7.2, equation 7.1 ), where $\omega_{ph}$ is the phonon frequency.

In the glassy materials, some additional situation must be considered about the emission band width.

1. Because of the successive energetic distribution of the localized states and the broad absorption band of each localized state, it is impossible to selectively excite the electron to one localized state even if the excitation photon energy was less than the mobility gap and was completely monochromatic.

2. The relaxation process without large lattice distortion tends to broaden the distribution of the initial localized states of the emission further.

Each initial localized state relaxes with large lattice deformation toward the corresponding self trapped state and makes the emission band whose width is $\Delta_{ph}$. The measured PL spectrum is a superposition of the emission bands whose peak energies $E_p'$ are continuously distributed. If the intensity of each emission band is distributed with respect to $E_p'$ as a Gaussian of width $\Delta_D$, the measured PL line width $\Delta$ is given by $\Delta^2 = \Delta_{ph}^2 + \Delta_D^2$ ( chapter 2.4, equation 2.10 ).

The temperature dependence of $\Delta$ and $E_p$ in Figs. 8.4 and 8.3 shows complicated behavior. First we attempt to explain the behavior in low temperature region where $\Delta$ decreases and $E_p$ increases with increasing temperature. The decrease of $\Delta$ should be caused by the decrease of $\Delta_D$ because that the $\Delta_{ph}$ increases with increasing temperature monotonically. The intensity of each emission band corresponding to the localized states is considered to show its own temperature dependence. It is assumed that, with increasing temperature, the emission band from the self trapped state corresponding to the low energy part of the measured PL spectra is quenched faster than the band corresponding to the high energy part of the spectra is. This assumption means that the activation energy for the non-radiative process becomes higher with increasing energy of the related localized state. As a result, with increasing temperature the quench effect of low energy emission band makes the $\Delta$ narrow and leads the $E_p$ of the PL, the superposition of the emission bands, to a slight blue shift.

The temperature coefficient of $\Delta$ in our result of the low temperature region is in opposite sign to the values given by other authors: Koós, Vassilyev and Somogyi [102] obtained the value of $1.1 \times 10^{-4}$ eV/K and Ball, Chamberlain and Instone [99], $2 \times 10^{-3}$ eV/K. The temperature derivative of $\Delta$ ($d\Delta/dT$) is determined by two contributions: $d\Delta_{ph}/dT$ and $d\Delta_D/dT$. As described above, $\Delta_{ph}$ increases and $\Delta_D$ decreases with increasing temperature. Thus the overall temperature dependence of $\Delta$ is based on a subtle imbalance between $\Delta_{ph} \cdot d\Delta_{ph}/dT$ and $\Delta_D \cdot d\Delta_D/dT$.

On the other hand, in the high temperature region of our result, the $\Delta$ increases with increasing temperature. As easily deduced from the equation for $\Delta_{ph}$ above, $d\Delta_{ph}/dT$ increases with increasing temperature. Thus the contribution of $d\Delta_{ph}/dT$ to $d\Delta/dT$ becomes dominant at high temperatures. So the positive sign of $d\Delta/dT$ may be likely to be observed at high temperature measurement. And as we have mentioned in chapter 7.2 that at high temperature region, the hot luminescence effect may not be omitted when we discuss the width.

The decrease of $E_p$ with increasing temperature in the high temperature region

may be attributed to the low energy shift of the distribution profile of the localized states. Increasing thermal energy activates the relaxation process (1) without large lattice distortion and makes possible to relaxes further before the process (2) with large lattice distortion begins.

Now we turn to the quantum efficiency as shown in Fig. 8.5. The quantum efficiency, which is the emission efficiency against an absorbed photon, decreases gradually with increasing photon energy in the region of $E_{ex} < 2.3$ eV and then rapidly in the region of $E_{ex} > 2.4$ eV. According to our model discussed above, the decrease of the quantum efficiency should be attributed to the increase of transition probability to the non-radiative centers in the relaxation process (1) without large lattice distortion, since the relaxation processes after the distribution to the localized states are treated as the same processes for both below and above mobility gap excitation. The details of the energy dependent quantum efficiency have been discussed by Street in Ref. [41]. The next two mechanisms for the changing quantum efficiency were proposed.

1. The probability of exciton ionization may increase at high excitation energies due to the greater initial kinetic energy of the electron and hole. Once excitons ionize, the carriers do not readily reform excitons because of fast trapping.

2. For the radiative recombination to occur, not only the exciton must remain unionized, but it must also be created sufficiently close to the recombination center.

The temperature dependence of the PL intensity has been also discussed in Ref. [41], for the As–Se system. The discussion involved tunneling of the excited state from the localized radiative center to the non-radiative recombination center through the energy barrier by potential fluctuation. The model does not seem to conflict with our explanation described above.

## 8.3 Summary and Conclusions

In this chapter, the PL of g–$GeSe_2$ has been studied in excitation energy range of 1.93~2.71 eV from 10 K to 220 K. The results can be summarized and concluded as follows:

1. With increasing excitation photon energy, the $E_p$ first increases and then decreases while $\Delta$ increases monotonically. The turning point of the $E_p$'s behavior is considered to be the mobility gap. Two relaxation processes are used to qualitatively

explain the $E_p$'s behavior. The process (1), without large lattice distortion, distributes the excitons among the various localized states, and then the process (2), with large lattice distortion, makes the excitons self-trapped. Above the mobility gap, the higher the excited energy is, the bigger the transition ability to the low energy localized state.

2. We find a new temperature dependence of the $\Delta$; with increasing temperature it first decreases and then increases. This behavior can be considered that in the low temperature region the energy distribution of the localized state in which the excited electron is trapped becomes narrow owing to the different quenching activation energy of trapped state. In high temperature region, the broadening of each emissions from the localized states dominates the relaxation processes to broaden the spectra.

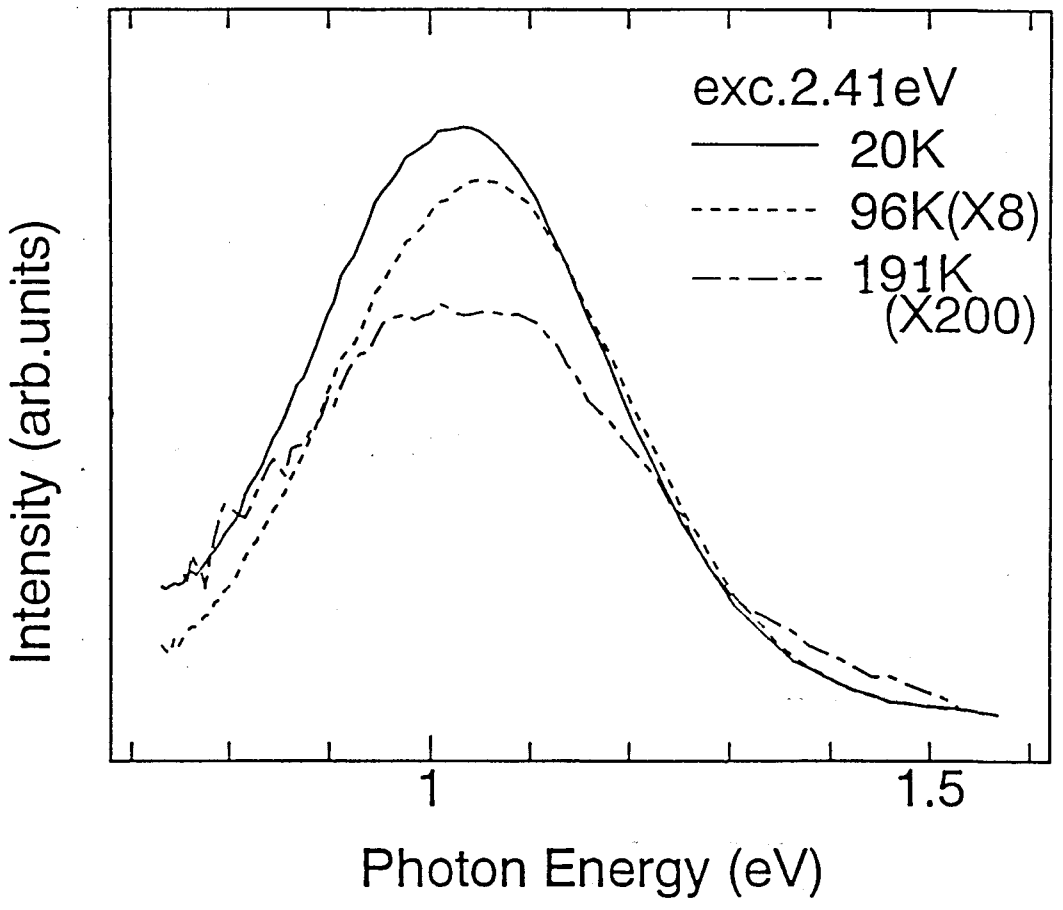


Figure 8.1: Photoluminescence spectra of the $GeSe_2$ glass at various temperature with excitation energy of 2.41 eV. The peak width decreases with increasing temperature.

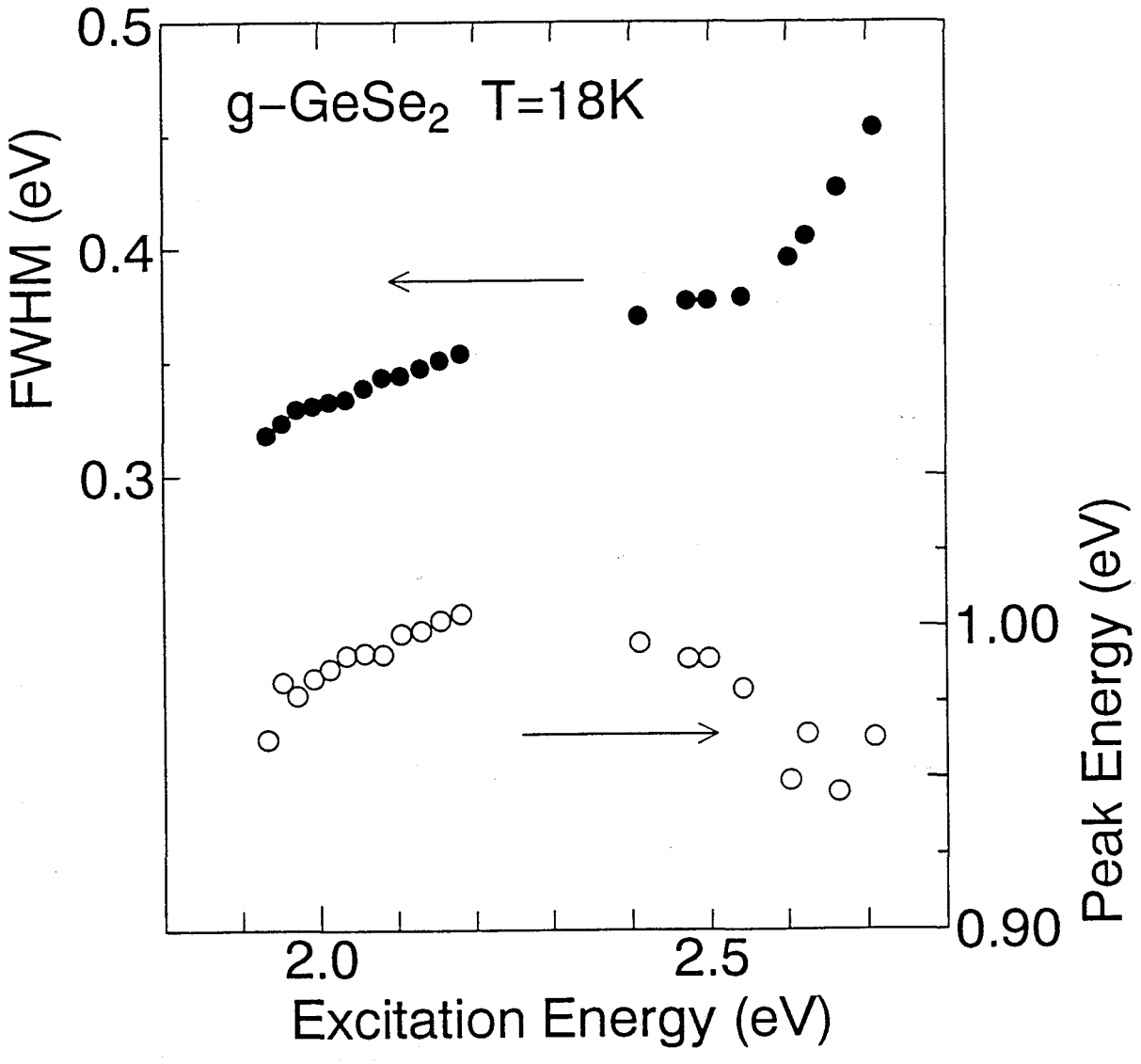


Figure 8.2: Excitation energy dependence of the peak energy ( lower half ) and the full width at half maximum ( upper half ) of the luminescence spectra of the $GeSe_2$ glass at 18 K. With increasing excitation photon energy, the peak energy first increases in the region of excitation energy below 2.2 eV, and then decreases in the region above 2.4 eV. The peak width increases monotonically with increasing excitation photon energy.

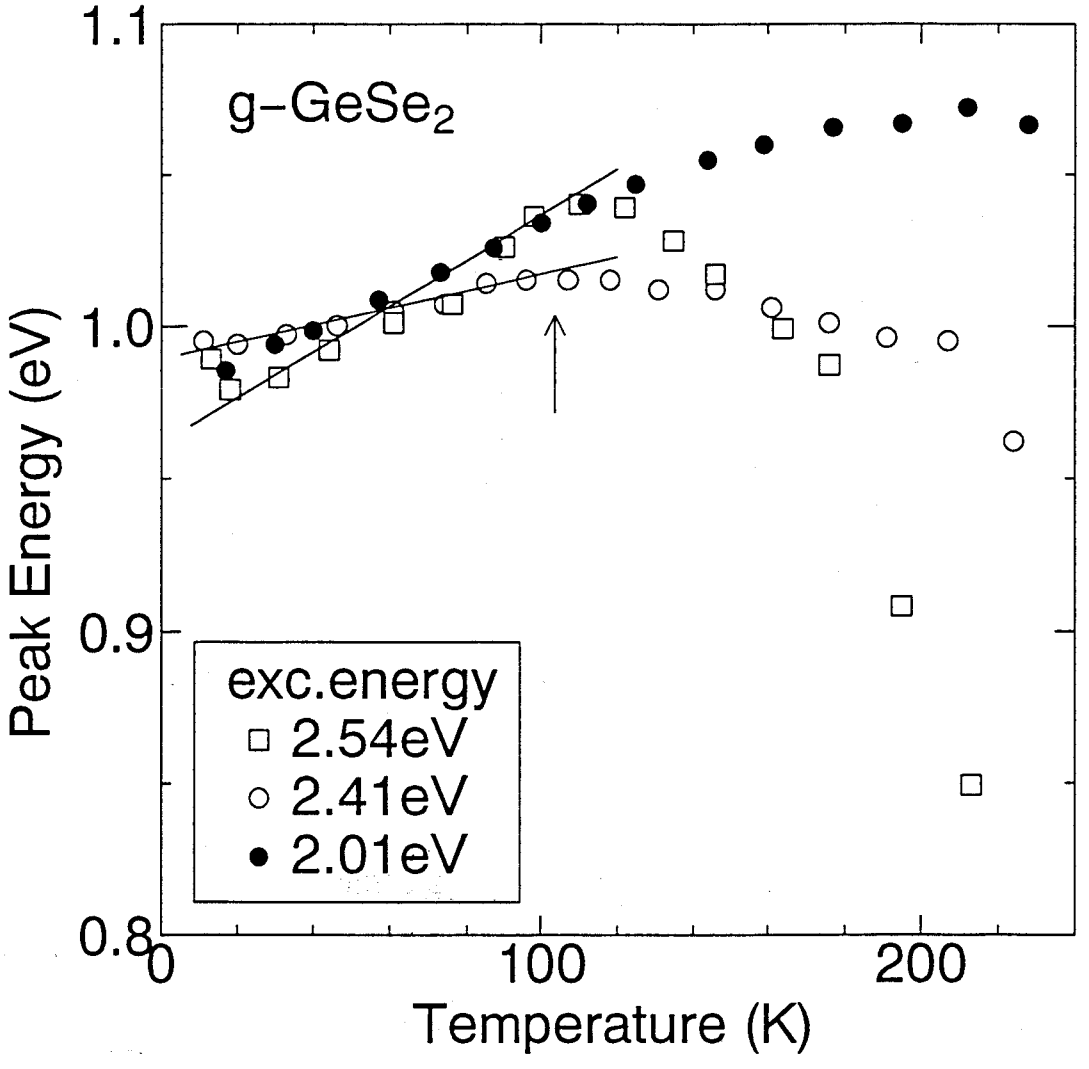


Figure 8.3: Temperature dependence of the luminescence peak energy at various excitation photon energies. With increasing temperature, for the curves of the excitation energies of 2.41 eV and 2.54 eV, the peak energy first increases in the region of temperature below 100 K, and then decreases in the region above 100 K. The lines are guides to the eyes. The up-arrow approximately indicates the turning points of the cures ( 2.41 eV and 2.54 eV ).

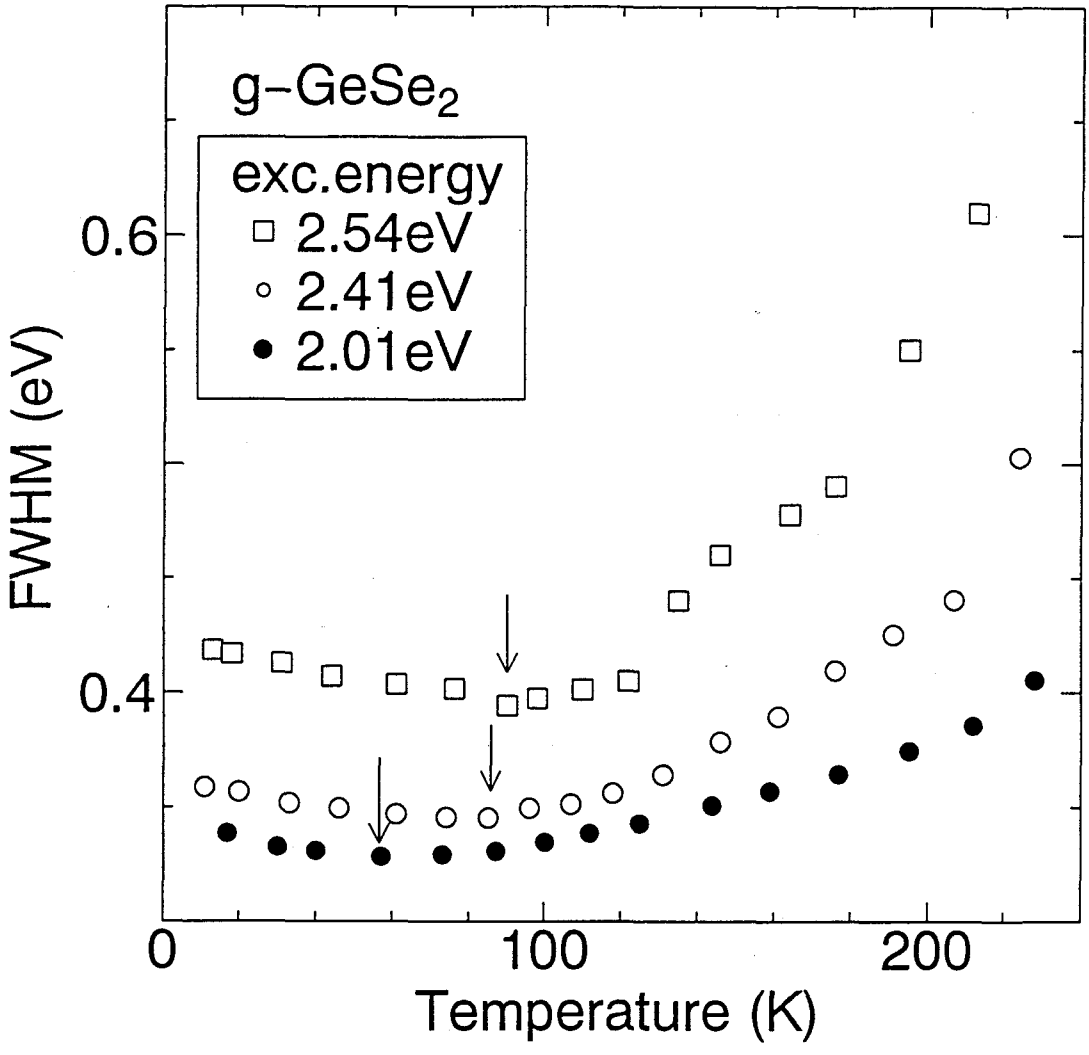


Figure 8.4: Temperature dependence of the luminescence peak width at various excitation photon energies. The peak width first decreases and then increases with increasing temperature for all spectra. The down-arrows approximately indicate the turning points of the cures ( 2.01 eV, 2.41 eV and 2.54 eV ).

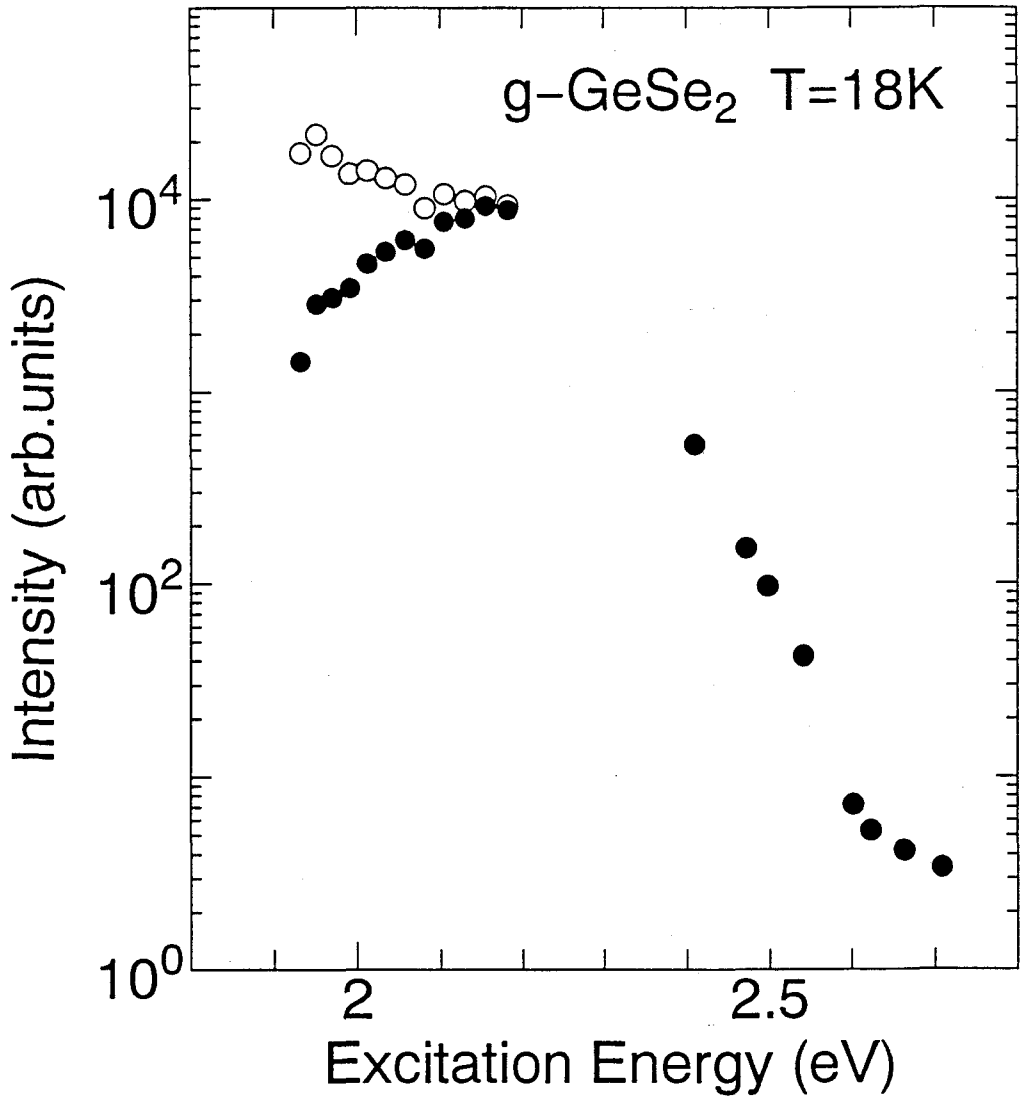


Figure 8.5: Excitation energy dependence of the photoluminescence intensity normalized to the incident photon flux (close circle) and to the absorbed photon flux (open circle) at 18 K. In the region $E_{ex} > 2.4$ eV, the later coincide with the former.

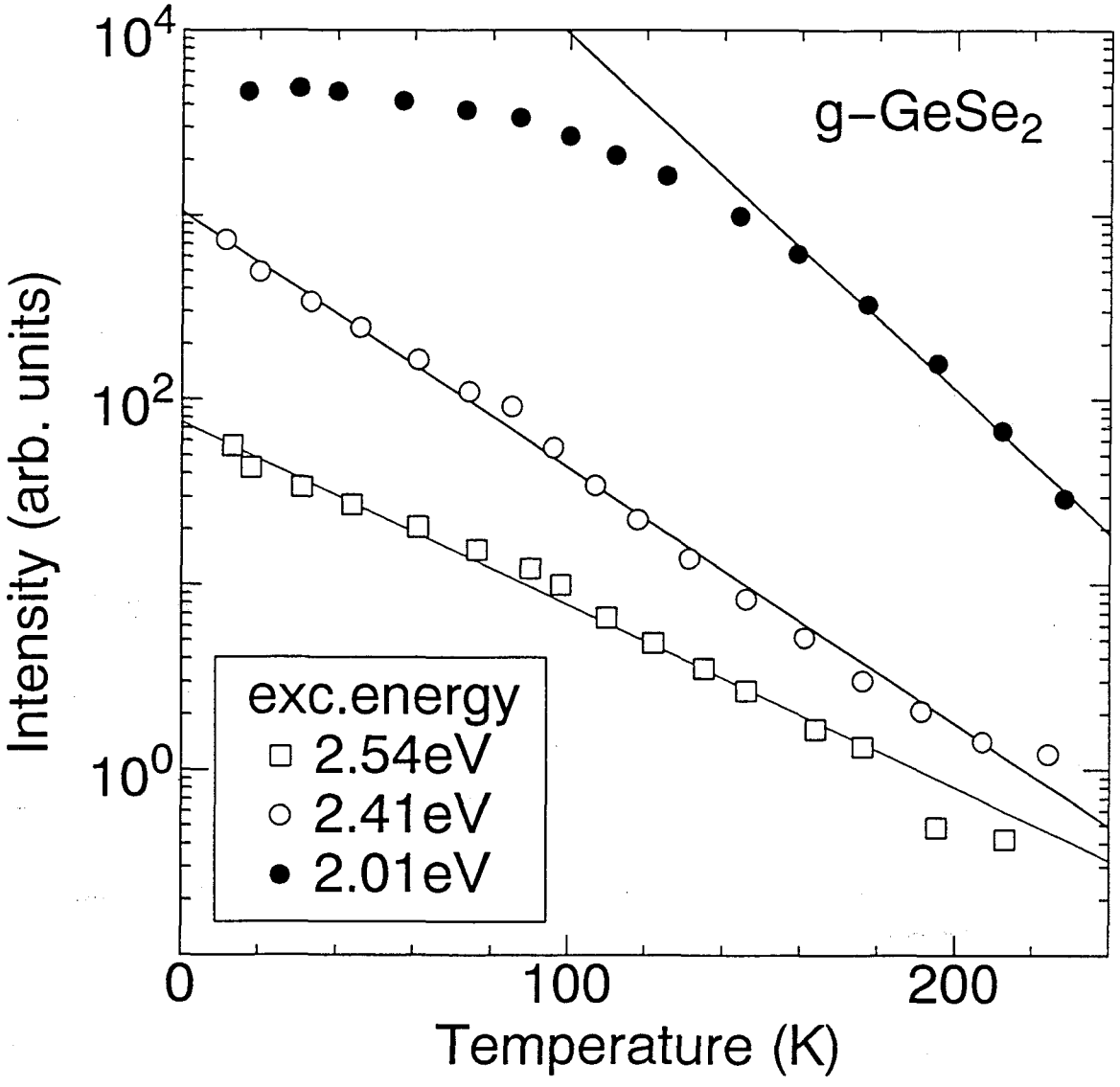


Figure 8.6: Temperature dependence of the luminescence intensity of the $GeSe_2$ glass with the excitation energies described in the figure. The data of 2.41 eV and 2.54 eV excitation follow the relation $I_{PL} \propto \exp(-T/T_0)$ well.

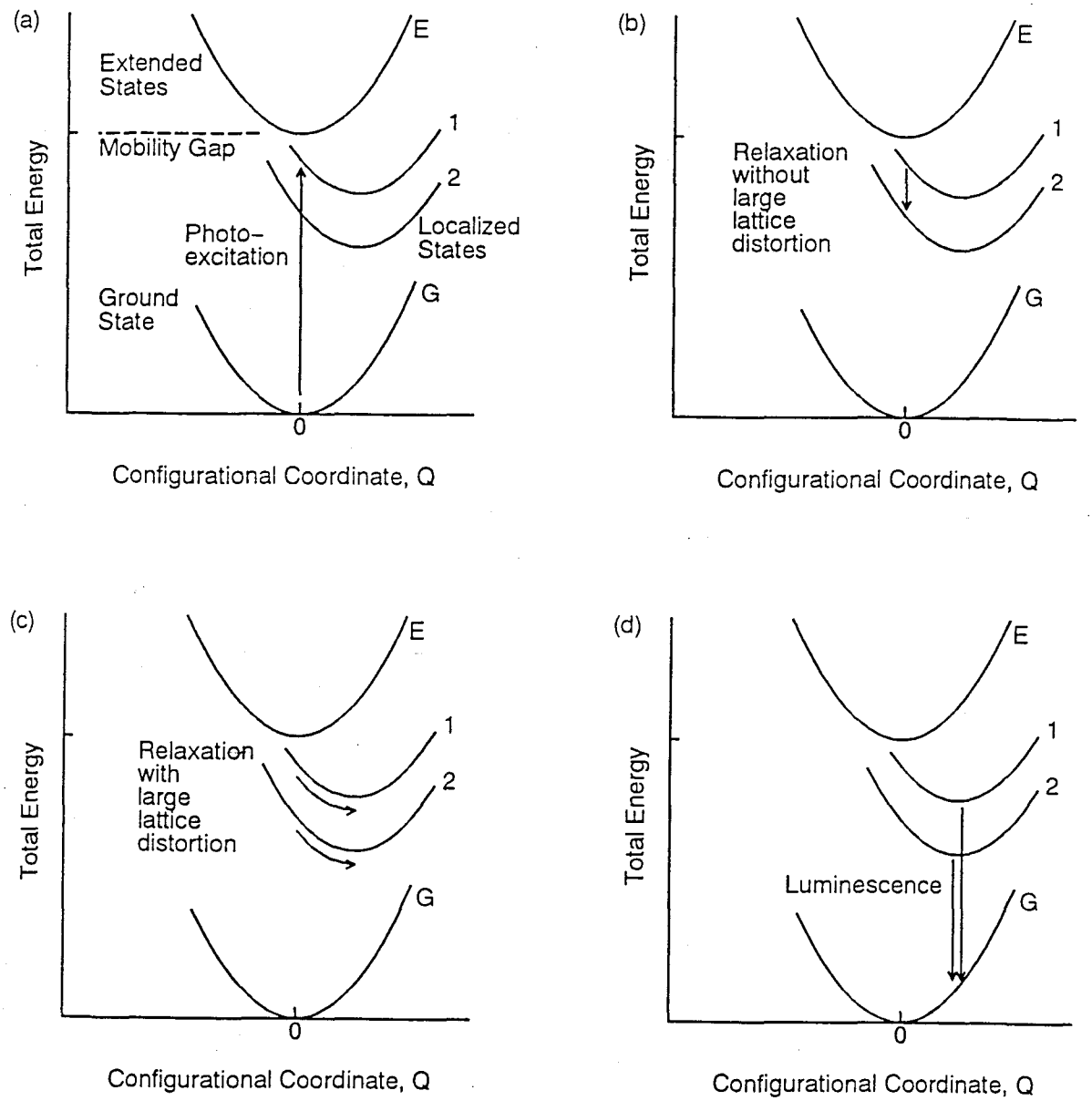


Figure 8.7: The configurational coordinate energy diagram of the system for the below band gap excitation; (a) excitation, (b) relaxation without large lattice distortion, (c) relaxation with large lattice distortion, and (d) emission of luminescence. Innumerable localized states are represented by two states 1 and 2.

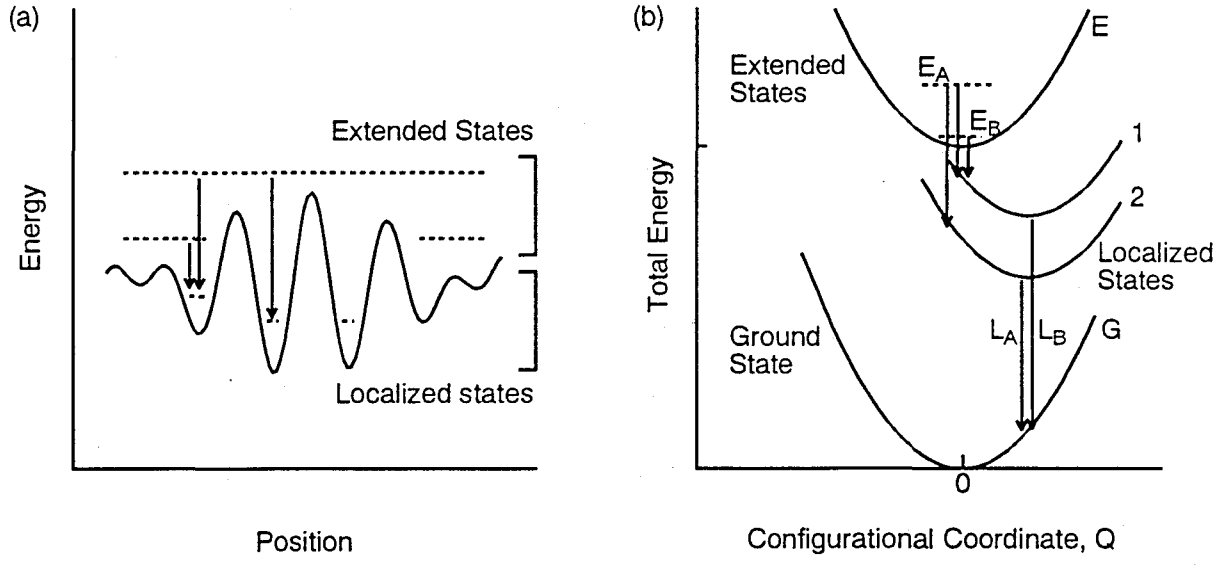


Figure 8.8: (a) The schematic diagram for the potential fluctuation in real space. The dotted lines indicate the energy level and the spatial extent of each state. The energy levels refer to the lattice without large distortion. An extended state with high energy has larger transition probability to a deep localized state than a low energy extended state has, as the arrows show. (b) Configurational coordinate energy diagram for the schematic explanation of the luminescence by above mobility gap excitation. The high energy excitation ($E_A$) leads the emission of $L_A$ and $L_B$, while the low energy excitation ($E_B$) leads the emission only of $L_B$.

# Chapter 9

# Summary and Conclusions

In this thesis, the structure and the structural changes in $Ge_xSe_{1-x}$ system have been mainly studied by using Raman scattering techniques. Three subjects have been investigated.

1. To clarify the structure and structural changes in glassy and liquid $Ge_xSe_{1-x}$, the glass-transition, crystallization and melting in this system have been investigated by measuring the Raman spectra in the temperature range of 20~850 °C.

2. To clarify the structure affected by the sample preparation method, the photo-induced crystallization processes have been interpreted in different g-$GeSe_2$ films which are prepared in different cooling rates.

3. Toward understanding of the relaxation processes of excited electrons in the photo-induced structural changes, the glassy and crystalline $GeSe_2$ have been studied by analyzing the temperature and the excitation energy dependence of the photoluminescence spectra.

In the chapters 4 ( $GeSe_2$ ) and 5 ( $Ge_xSe_{1-x}$ ), the macroscopic phenomena, such as the glass-transition, crystallization and melting, are explained from the view point of the microscopic structural changes.

With increasing temperature at glass-transition, the rapid decrease of the viscosity leads the structural relaxation time shorten fast. In glassy ( g- ) and liquid ( l- ) $GeSe_2$, the medium-range structure ( MRS ) is considered as a topologically crystalline layer-like fragment. In g-$GeSe_2$, the lone pair Se-Se interactions between the two successively stacked fragments restrains the vibrational intensity $A_1^C$ which relates to

the edge-sharing $GeSe_{4/2}$ tetrahedra. The fact that with increasing temperature the intensity ratio of the $A_1^C$ band to $A_1$ band increases quickly from 1:3 to 1:1 in the super-cooled liquid ( SCL ) is related to a drastic decrease of the interaction between the layer-like fragments.

Basing on the temperature dependence of spectral shapes in Se and Ge–poor $Ge_xSe_{1-x}$ ( $x \leq 0.07$ ), it has been found that the dominant structure of the glasses is $(Se)_n$ chains where the glassy state involves a parallel Se–Se chain region together with the non-parallel chain region. The decrease of viscosity causes large configurational fluctuations in the parallel region of $(Se)_n$ chains to broaden the corresponding vibrational band at 235 $cm^{-1}$. In the $Ge_xSe_{1-x}$ ( $0.10 \leq x \leq 0.20$ ), the intensity ratio $I_{GeSe4/2}/I_{Se}$ increases with increasing temperature above glass-transition temperature. The leading structural units are $GeSe_{4/2}$ tetrahedra which easily move and coalesce with each other to form the crystalline embryo in the SCL state. For those $Ge_xSe_{1-x}$ ( $x = 0.10, 0.15$ ) in which no crystalline spectra has been observed, the c–$GeSe_2$ like crystalline embryo is resolved at melting point.

In the Ge composition region of $0.04 < x < 0.18$, no crystallization occurs in the experimental time periods ( $\sim$ 10 hours ) which means that it is shorter than the relaxation time for the crystallization. When the Ge composition increases above 0.04, the population of $GeSe_{4/2}$ tetrahedra, whose structure is rather stable than the $(Se)_n$ chains at the experimental temperature, is large enough to easily prevent the $(Se)_n$ chains from crystallization. Below the $x = 0.18$, though the $GeSe_2$ crystalline embryos are formed in the SCL, the relaxation time for the c–$GeSe_2$ growth becomes much longer than our measurement time period. At the $x = 0.18$, the crystallization of c–$GeSe_2$ occurs easily. The relaxation time for crystallization shows an essential change at $x = 0.18$ ( average coordination number $\langle r \rangle = 2.37$ ) which is very close to the rigidity percolation threshold value $x = 2.0$ ( $\langle r \rangle = 2.4$ ) basing on the Phillips–Thorpe constraint theory.

In the chapter 6, the various structures in g–$GeSe_2$ films, which are quenched from melts with different cooling rates, are investigated by time-resolved Raman scattering measurement. The thermal crystallization temperatures of the g–$GeSe_2$ films are higher than those the vacuum evaporation amorphous $GeSe_2$ films which are prepared with extremely fast cooling rates. This suggests that a fast cooling rate, corresponding to a high initial energy, leads the thermal crystallization temperature decreased. In the g–$GeSe_2$ films the initial energies are almost the same, however, the threshold

temperatures for photo-induced crystallization processes are different. A slow cooling rate lowers the threshold temperature. It is reasonable to considered that in the glass, prepared by a slower cooling rate, the medium-range structure is more similar to the crystalline nuclei, or easier to transform into crystalline nuclei.

In chapters 7 and 8, the relaxation processes of photo-induced electrons in g–$GeSe_2$ and c–$GeSe_2$ have been studied, respectively. In the c–$GeSe_2$, two intrinsic luminescence bands ( 1.02 eV and 1.15 eV ) are independent of temperature, however, the two excitation bands which are related to the two luminescence bands shift to lower energies with increasing temperature. The luminescence band at 1.25 eV, which is observed at low excitation energy, shows the sample dependence strongly. In the g–$GeSe_2$ at low temperature with increasing excitation photon energy, the peak energy first increases and then decreases while the full width at half maximum of the intensity increases monotonically. The turning point of the behavior of the peak energy is considered to be the mobility gap. A new temperature dependence of luminescence width has been found that the FWHM first decreases in the low temperature region and than increases in the high temperature region. A configurational coordinate energy diagram method is used to qualitatively interpret these results. In the g–$GeSe_2$, the relaxation process without large lattice distortion, which distributes the excited system among the various localized states, cooperates with the process with large lattice distortion, which makes the system trapped.

References


1. J.C. Phillips, *J. Non-Cryst. Solids* 43, 37 (1981).
2. M.F. Thorpe, *J. Non-Cryst. Solids* 57, 355 (1983).
3. W. A. Kamitakahara, R. L. Capelletti, P. Boolchand, B. Halfpap, F. Gompf, D. A. Neumann and H. Mutka, *Phys. Rev.* B44, 94 (1991).
4. P. Boolchand, R. N. Enzweiler, R. L. Capelletti, W. A. Kamitakahara, Y. Cai and M. F. Thorpe, *Solid States Ionics* 39, 81 (1990).
5. P. Boolchand, W. Bresser, M. Zhang, Y. Wu, J. Wells and R. N. Enzweiler, *J. Non-Cryst. Solids* 182, 143 (1995).
6. A. Feltz, H. Aust and A. Bleyer, *J. Non-Cryst. Solids* 55, 197 (1983).
7. K. Murase, T. Fukunaga, K. Yakushiji, T. Yoshimi and I. Yunoki, *J. Non-Cryst. Solids* 59 & 60, 883 (1983).
8. K. Murase and T. Fukunaga, *Proc. 17th Int. Conf. on Physics of Semiconductors,* ed. by J. D. Chadi and W. A. Harrison ( Springer–Verlag, New York, 1985), p. 943.
9. K. Murase and T. Fukunaga, *Mat. Res. Soc. Symp. Proc.* ed. by F. L. Galeener, D. L. Griscom and M. J. Weber 61, 101 (1986).
10. M. Tatsumisago, B. L. Halfpap, J. L. Green, S. M. Lindsay and C. A. Angell, *Phys. Rev. Lett.* 64, 1549 (1990).
11. M. Taniguchi, T. Kouchi, I. Ono, S. Hosokawa, M. Nakatake, H. Namatame and K. Murase, *J. Electron Spectroscopy and Related Phenomena* 78, 507 (1996).
12. J. Wong and C. A. Angell, *Glass: Structure by Spectroscopy,* (Marcel Dekker, New York, 1976).
13. C. A. Angell, *J. Non-Cryst. Solids* 73, 1 (1985).
14. C. A. Angell, C. Alba, A. Arzimanoglou, R. Böhmer, J. Fan, Q. Lu, E. Sanchez, H. Senapati and M. Tatsumisago: *Am. Inst. Phys. Conf. Proc.* 253, 3 (1992).
15. R. Böhmer and C. A. Angell, in: *Disorder Effects on Relaxational Processes* , eds. by A. Blumen and R. Richert (Springer-Verlag, Berlin, 1994), p. 11.
16. V. K. Malinovsky, V. N. Novikov, P. P. Parshin, A. P. Sokolov and M. G. Zemlyanov, *Europhys. Lett.* 11, 43 (1990).
17. E. Duval, A. Boukenter and T. Achibat, *J. Phys.: Condens. Matter* 2 10227 (1990).
18. E. Duval, N. Garcia, A. Boukenter and J. Serughetti, *J. Chem. Phys.* 99, 2040 (1993).
19. T. Achibat, A. Boukenter and E. Duval, *J. Chem. Phys.* 99, 2046 (1993).

20. E. Duval, T. Achibat, A. Boukenter, B. Varrel, R. Calemczuk and B. Salce, *J. Non-Cryst. Solids* 190, 258 (1995).
21. L. Claire, G. Nabil, T. Ferial, C. S. Gérard, P. Jacques and V. René, *Phys. Rev.* B51, 8606 (1995).
22. A. P. Sokolov, U. Buchenau, W. Steffen, B. Frick and A. Wischnewski, *Phys. Rev.* B52, R9815 (1995).
23. M. T. Kostyshin, E. V. Mikhailovskaya and P. F. Romanenko, *Sov. Phys.-Solid State* 8, 451 (1966).
24. A. Yoshikawa, O. Ochi, H. Nagai and Y. Mizushima, *Appl. Phys. Lett.* 29, 677 (1976).
25. J. S. Berkes, S. W. Ing. Jr. and W. J. Hillegas, *J. Appl. Phys.* 42, 4908 (1971).
26. S. R. Elliot and A. V. Kolobov, *J. Non-Cryst. Solids* 128, 216 (1991).
27. J. E. Griffiths, G. P. Espinosa, J. P. Remeika, and J. C. Phillips. *Solid State Commun.* 40, 1077 (1981).
28. J. E. Griffiths, G. P. Espinosa, J. P. Remeika, and J. C. Phillips, *Phys. Rev.* B25, 1272 (1982).
29. E. Haro, Z. S. Xu, J. F. Morhange, M. Balkanski, G. P. Espinosa and J. C. Phillips, *Phys. Rev.* B32, 969 (1985).
30. S. Sugai, *Phys. Rev. Lett.* 57, 456 (1986).
31. S. Sugai, *Phys. Rev.* B35, 1345 (1986).
32. K. Murase and K. Inoue, in: *Disordered Semiconductors,* ed. by M. A. Kastner, G. A. Thomas and S. R. Ovshinsky (Plenum, New York, 1987) p.297.
33. K. Inoue, K. Kawamoto and K. Murase, *J. Non-Cryst. Solids* 95&96, 517 (1987).
34. K. Inoue, O. Matsuda and K. Murase, in: *Proc. 19th Int. Conf. on Physics of Semiconductors, Warsaw, Poland,* ed. by W. Zawadzki (Institue of Physics, Polish Academy of Sciences, Poland, 1988), p. 1665.
35. O. Matsuda, H. Oe, K. Inoue and K. Murase, *J. Non-Cryst. Solids* 192&193, 524 (1995).
36. K. Murase, K. Inoue, and O. Matsuda, in: *Current Topics in Amorphous Materials: Physics and technology* , ed. by Y. Sakurai, Y. Hamakawa, T. Masumoto. K. Shirae and K. Suzuki (Elsevier, Amsterdam, 1993), p. 47.
37. Y. Wang, M. Nakamura, O. Matsuda, K. Inoue and K. Murase, *J. Non-Cryst. Solids* 198–200, 753 (1996).
38. R. Azoulay, H. Thibierge and A. Brenac, *J. Non-Cryst. Solids* 18, 33 (1975).

39. K. Inoue, O. Matsuda and K. Murase, *Solid State Commun.* 79, 905 (1991).
40. K. Inoue, O. Matsuda and K. Murase, *Physica B* 219 & 220, 520 (1996).
41. R. A. Street, *Adv. Phys.* 25, 397 (1976).
42. V. A. Vassilyev, M. Koós, and I. Kósa Somogyi, *Solid State Commun.* 22, 633 (1977).
43. M. Koós, I. Kósa Somogyi, and V. A. Vassilyev, *J. Lumi.* 26, 499 (1982)
44. K. Murayama, *J. Non-Cryst. Solids* 59 & 60, 983 (1983).
45. O. Matsuda, T. Nakane, K. Inoue, and K. Murase, in: *Proc. 21th Int. Conf. Phys. Semicond., Beijing*, ed. by P. Jiang, and H. Z. Zheng, (World Scientific Publishers, Singapore, 1992), p.125.
46. H. Fritzsche, *Solid State Commun.* 99, 153 (1996).
47. C. A. Angell et al. in: AIP. Conf. Proc. No. 256 on Slow dynamics in condensed matter, ed. by K. Kawasaki, T. Kawakatsu, M. Tokuyama, (American Institute of Physcis, New York, 1992), p.3.
48. Von. G. Dittmer and H. Schaäfer, *Acta Crystallogr.* B31, 2060 (1975).
49. Von. G. Dittmer and H. Schaäfer, *Acta Crystallogr.* B32, 1188 (1976).
50. Von. G. Dittmer and H. Schaäfer, *Acta Crystallogr.* B32, 2726 (1975).
51. O. Matsuda, K. Inoue, T. Nakane and K. Murase, *J. Non-Cryst. Solids* 150, 202 (1992).
52. K. Inoue, K. Kawamoto and K. Murase, *Solid State Commun.* 79, 905 (1991).
53. S. A. Bioko, D. I. Bletskan, and S. F. Terekhova, *phys. stat. sol. (b)* 90, K49 (1978).
54. Z. V. Popović and A. Breitschwerdt, *Phys. Lett.* 110A, 426 (1985).
55. P. Tronc, M. Bensoussan and A. Brenac, *Phys. Rev.* B8, 5947 (1973).
56. P. Tronc, M. Bensoussan, A. Brenac and G. Errandonea, *J. Phys. (Paris)* 38, 1493 (1977).
57. D. E. Aspnes, J. C. Phillips, K. L. Tai and P. M. Bridenbaugh, *Phys. Rev.* B23, 816 (1981).
58. K. Inoue, T. Katayama, K. Kawamoto and K. Murase, *Phys. Rev.* B35, 7496 (1987). The crystal orientation is mistaken in this literature; replace the ||a with the ⊥a, and the ⊥a with the ||a. The conclusions will not be influenced by this change of the orientation.
59. O. Uemura, Y. Sagara and T. Satow, *phys. stat. sol. (a)* 32, K91 (1975).

60. P. H. Fuoss, P. Eisenberger, W. K. Warburton and A. Bienenstock, *Phys. Rev. Lett.* 46, 1537 (1981).
61. D. E. Sayers, F. W. Lytle and E. A. Stern, in: *Amorphous and Liquid Semiconductors* **1** , *Proc. Int. Conf. Amorphous and Liquid Semiconductor, Garmisch-Partenkirchen, FRG,* ed. by J. Stuke and W. Brenig, (Taylor & Francis Ltd., London, 1974), p.403.
62. O. Uemura, Y. Sagara, D. Muno and T. Satow, *J. Non-Cryst. Solids* 30, 155 (1978).
63. O. Matsuda, K. Inoue and K. Murase, in: *Proc. 20th Int. Conf. Phys. Semicond., Thessaloniki, Greece,* ed. by E. M. Anastassakis and J. D. Joannopoulos, (World Scientific, Singapore, 1990), p.2135.
64. O. Matsuda, K. Inoue and K. Murase, *Solid State Commun.* 75, 303 (1990).
65. O. Matsuda, *Doctorthesis in Graduate School of Science, Osaka University,* 1991.
66. K. Inoue, O. Matsuda and K. Murase, *J. Noc-Cryst. Solids* 150, 197 (1992).
67. O, Matsuda, K. Inoue and K. Murase, *J. Noc-Cryst. Solids* 150, 202 (1992).
68. P. M. Bridenbaugh, G. P. Espinosa, J. E. Griffiths, J. C. Phillips and J. P. Remeika, *Phys. Rev.* B20, 4240 (1979).
69. Z. V. Popović and H. J. Stolz, *phys. stat. sol. (b)* 108, 153 (1981).
70. P. N. Keating, *Phys. Rev.* 145, 637 (1966).
71. F. Gompf, *J. Phys. Chem. Solids* 42, 539 (1981).
72. M. Gorman and S. A. Solin, *Solid State Commun.* 18, 1401 (1976).
73. G. Lucovsky, A. Mooradian, W. Taylor, G. B. Wright and R. C. Keezer, *Solid State Commun.* 5, 113 (1967).
74. G. Lucovsky and F. L. Galeener, *J. Non-Cryst. Solids* 35 & 36, 1209 (1980).
75. G. Lucovsky, *J. Non-Cryst. Solids* 97 & 98, 155 (1987).
76. K. Suzuki, M. Misawa, in: *Proc. of 3rd Int. Conf. on Liquid Metals,* (Inst. Phys. Conf. Ser. No.3, 1977), p.531.
77. M. Misawa and K. Suzuki, *Jpn. J. Phys. Soc.* 44, 1612 (1978).
78. A. A. Baganich, V. I. Mikla, D. G. Semak, A. P. Sokolov and A. P. Shebanin, *Phys. stat. sol. (b)* 166, 297 (1991).
79. M. Koós and I. Kósa Somogyi, *J. Non-Cryst. Solids* 77 & 78, 1145 (1985).
80. S. A. Dembovskii. G. Z. Vinogradova and A. S. Pashinkin, *Ruu. J. Inorg. Chem.* 10, 903 (1963).

81. C. Z. Vinogradova, S. A. Dembovskii and N. B. Sivkova, *Ruu. J. Inorg. Chem.* 13, 1051 (1968).
82. L. Ross and M. Bourgon, *Can. J. Chem.* 47, 2555 (1969).
83. P. Quenez, P. Khodadad and R. Ceolin, *Bull. Soc. Chem. Fr.* 1, 177 (1972).
84. R. A. Street and D. K. Biegelsen, *J. Non-Cryst. Solids* 32, 339 (1979).
85. N. F. Mott, E. A. Davis and R. A. Street, *Phil. Mag.* 32, 961 (1975).
86. N. F. Mott and A. M. Stoneham, *J. Phys.* C10, 3391 (1977).
87. N. F. Mott, *Revue de Phys. Appl.* 12, 619 (1977).
88. K. Huang, and A. Rhys, *Proc. R. Soc.* A204, 406 (1950).
89. S. Hashimoto and M. Itoh *Jpn. J. Appl. Phys.* 27, 726 (1988).
90. S. Susman, K. J. Volin, D. G. Montague and D. L. Price, *J. Non-Cryst. Solids* 125, 168 (1990).
91. I. T. Penfold and P. S. Salmon, *Phys. Rev. Lett.* 67, 97 (1991).
92. W. B. Hillig and D. Turnbull, *J. Chem. Phys.* 24, 914 (1956).
93. D. Turnbull, *J. Phys. Chem.* 66, 609 (1962).
94. D. Turnbull, *Contemp. Phys.* 10, 473 (1969).
95. D. R. Uhlmann, *J. Non-Cryst. Solids* 7, 337 (1972).
96. *New Glass Handbook*, ( Maruzen Press, Tokyo, 1991 ), (Japanese).
97. H. Takeuchi, *Masterthesis in Graduate School of Science, Osaka University*, 1997.
98. Y. Shinozuka, *Jpn. J. Appl. Phys.* 32, 4560 (1993).
99. G. J. Ball, J. M. Chamberlain and T. Instone, *Solid State Commun.* 27, 71 (1978).
100. V. A. Vassilyev, M. Koós and I. K. Somogyi, *Phil. Mag.* B 39, 333 (1979).
101. F. Mollot, Jj. Cernogora and C. B. a. la Guillaume, *Phil. Mag.* B 42, 643 (1980).
102. M. Koós, V. A. Vassilyev and I. K. Somogyi, *Phil. Mag.* B 41, 383 (1980).